12-2014

# GeSn Devices for Short-Wave Infrared Optoelectronics

Benjamin Ryan Conley
*University of Arkansas, Fayetteville*

# GeSn Devices for Short-Wave Infrared Optoelectronics

GeSn Devices for Short-Wave Infrared Optoelectronics

A dissertation submitted in partial fulfillment
of the requirements for the degree of
Doctor of Philosophy in Microelectronics-Photonics

By

Benjamin Ryan Conley
Arkansas Tech University
Bachelor of Science in Physics, 2010
University of Arkansas
Master of Science in Microelectronics-Photonics, 2011

December 2014
University of Arkansas

This dissertation is approved for recommendation to the Graduate Council.

Dr. Shui-Qing Yu
Dissertation Director

Dr. Hameed Naseem
Committee Member

Dr. Magda El-Shenawee
Committee Member

Dr. Greg Salamo
Committee Member

Dr. Rick Wise
Ex-Officio Member

The following signatories attest that all software used in this dissertation was legally licensed for use by Benjamin R. Conley for research purposes and publication.

_____ _____

Mr. Benjamin R. Conley, Student Dr. Shui-Qing Yu, Dissertation Director

This dissertation was submitted to http://www.turnitin.com for plagiarism review by the TurnItIn company's software. The signatories have examined the report on this dissertation that was returned by TurnItIn and attest that, in their opinion, the items highlighted by the software are incidental to common usage and are not plagiarized material.

_____ _____

Dr. Rick Wise, Program Director Dr. Shui-Qing Yu, Dissertation Director

## Abstract

The electronics industry has a large silicon infrastructure for the manufacture of complementary-metal oxide semiconductor (CMOS) based electronics. The increasing density of Si based circuits has set a pace that is now pushing the physical limits of connectivity between devices over conventional wire based links. This has driven the increasing interest in Si based optoelectronics and to use the groundwork already established by the electronics industry for lower cost optical communications. The greatest limitation to this effort has been the incorporation of a Si based laser, which requires integration of a direct bandgap material within this CMOS process.

The $Ge_{1-x}Sn_x$ alloy is one material of interest for this field of Si photonics due to its compatibility on Si CMOS circuits and its direct bandgap for increasing Sn content. The past decade of material development in this field has led to $Ge_{1-x}Sn_x$ films grown on Si with direct bandgaps. The work in this dissertation set out to develop $Ge_{1-x}Sn_x$ based optoelectronics operating in the short-wave infrared (SWIR) region. The fabrication methodology of $Ge_{1-x}Sn_x$ active photonic components such as microdisk resonators, photoconductors, and avalanche photodiodes were developed. A simple, one-mask fabrication method was developed to create $Ge_{1-x}Sn_x$ microdisk resonators on Si, which could serve as a platform for the first on-Si CMOS laser. A study of the noise levels, effective carrier lifetime, and specific detectivity was conducted for the first time on any $Ge_{1-x}Sn_x$ detector.

A systematic study of detectors with Sn content ranging from 0.9 to 10.0% were fabricated and measured for their responsivity and spectral response in the SWIR. A record high responsivity of 1.63 A/W was measured at the 1.55 μm wavelength for a 10% Sn photoconductor at reduced temperature. A long-wavelength cut-off for this device was measured out to 2.4 μm.

Avalanche photodiodes were also developed and tested for devices with $Ge_{1-x}Sn_x$ absorption regions. The low noise operation and high responsivity of these detectors yield a detectivity that is comparable with commercially available detectors. This work established the baseline performance for this technology and demonstrates this material can be used for Si based optoelectronics.

**Acknowledgements**

The work in this dissertation was supported by National Science Foundation under grant number EPS-1003970. Any opinions, findings, and conclusions or recommendations expressed in this material are those of the author and do not necessarily reflect the views of the National Science Foundation. Support is also appreciated from the Arkansas Bioscience Institute and the Defense Advanced Research Projects Agency (DARPA) by Dr. Dev Palmer, Program Manager under project W911NF-13-1-0196. Any opinions, findings, and conclusions or recommendations expressed in this material are those of the author and do not necessarily reflect the views of the Arkansas Bioscience Institute or DARPA. The doctoral fellowship provided by the Department of Defense Science, Mathematics & Research for Transformation (SMART) program is greatly appreciated and allowed me the time needed to complete my research.

Thank you Ken Vickers for all the support and advice you have provided over these past few years. Your wisdom and guidance will be missed. The support by Dr. Rick Wise, Renee Hearon, the entire μEP Graduate Program, and Electrical Engineering Department is greatly appreciated.

Part of this research was made possible through the use of the High Density Electronics Center (HiDEC) at the University of Arkansas, Fayetteville campus. All the hard work Errol Porter and Mike Steger do to in maintaining those facilities and in their dedication to quality are gratefully appreciated. Thanks to Joe Margetis and John Tolle at ASM America for all the $Ge_{1-x}Sn_x$ samples. This work would not be possible without your contributions and hard work.

I express my sincere gratitude to my advisor, Dr. Shui-Qing Yu, for his support, guidance, and teachings. This time spent working with you was a great honor. Thank you Dr.

Wei Du for all your assistance in my experiments, your advice and support was invaluable. Thanks also to my entire dissertation committee for their support and guidance.

I gratefully acknowledge my wonderful wife Steph for all her support of my work. She has supported me through everything from a combat deployment in the Marine Corps to the years of support as I pursued this career. Thanks mom and dad for all the confidence you had in my goals and your support throughout my life.

## Table of Contents


Chapter 1: Introduction ..... 1

1.1 Motivation ..... 1

1.2 $Ge_{1-x}Sn_x$ Optoelectronics ..... 2

1.3 Organization ..... 8

Chapter 2: Thermal Stability of $Ge_{1-x}Sn_x$ under CMOS Processing ..... 9

2.1 Rapid Thermal Annealing Experimental Design ..... 10

2.2 High Temperature Sn Segregation Limit ..... 12

2.3 Rapid Thermal Annealing at CMOS Compatible Temperatures ..... 18

Chapter 3: $Ge_{1-x}Sn_x$ Microdisk Resonator for Si-based Laser ..... 22

3.1 Microdisk Background ..... 24

3.2 Modeling of Microdisk Resonator using Finite Difference Time Domain (FDTD) ..... 26

3.3 $Ge_{1-x}Sn_x$ Microdisk Fabrication on Si ..... 33

3.3.1 Dry Mesa Etching ..... 34
3.3.2 Microdisk Undercut Etching with KOH ..... 38
3.4 Micro-Photoluminescence of $Ge_{1-x}Sn_x$ Microdisks ..... 44

Chapter 4: CMOS Compatible Photodetectors for Infrared Detection ..... 47

4.1 Photodetector Applications in the Short-Wave Infrared ..... 48

4.1.1 Short-Wave Infrared Detection ..... 48
4.1.2 High Speed Optical Communication ..... 51
4.1.3 Focal Plane Array ..... 52
4.2 Photodetector Structures ..... 54

4.2.1 Photoconductor ..... 54
4.2.2 Avalanche Photodiode (APD) ..... 57
4.3 Photodetector Figures of Merit ..... 67

4.3.1 Spectral Response ..... 68
4.3.2 Responsivity and Photoconductor Gain ..... 69
4.3.3 Effective Carrier Lifetime ..... 71
4.3.4 Photodetector Noise ..... 74
4.3.5 Specific Detectivity ($D^*$) ..... 77

Chapter 5: Fundamental Study of $Ge_{1-x}Sn_x$ Photoconductors ..... 80

5.1 Experimental Setup ..... 80

5.1.1 $Ge_{1-x}Sn_x$ Growth and Device Fabrication ..... 80
5.1.2 Characterization and Measurement Setup ..... 84
5.2 Background Carrier Activation Energy ..... 85
5.3 Long-Wavelength Cut-off of $Ge_{1-x}Sn_x$ Photoconductors ..... 91
5.4 Responsivity ..... 97
5.5 Effective Carrier Lifetime ..... 105
5.6 Specific Detectivity ($D^*$) ..... 107
Chapter 6: Advanced Photoconductive Devices with Interdigitated Electrodes ..... 114
6.1 Interdigitated Electrode Device Fabrication ..... 114
6.2 Enhanced Photoconductive Gain ..... 120
6.3 $Ge_{1-x}Sn_x$ Bulk Lifetime ..... 121
Chapter 7: $Ge_{1-x}Sn_x$ Avalanche Photodiode ..... 125
7.1 Fabrication ..... 125
7.2 Electrical Characterization ..... 128
7.3 Optical Characterization ..... 132
Chapter 8: Summary and Future Work ..... 137
8.1 Summary ..... 137
8.2 Future Work ..... 140
References ..... 143
Appendix A: Description of Research for Popular Publication ..... 152
Appendix B: Executive Summary of Newly Created Intellectual Property ..... 154
Appendix C: Potential Patent and Commercialization Aspects of listed Intellectual Property Items ..... 155
C.1 Patentability of Intellectual Property (Could Each Item be Patented) ..... 155
C.2 Commercialization Prospects (Should Each Item Be Patented) ..... 155
C.3 Possible Prior Disclosure of IP ..... 156
Appendix D: Broader Impact of Research ..... 157
D.1 Applicability of Research Methods to Other Problems ..... 157
D.2 Impact of Research Results on U.S. and Global Society ..... 157

D.3 Impact of Research Results on the Environment ..... 157
Appendix E: Microsoft Project for MS MicroEP Degree Plan ..... 158
Appendix F: Identification of All Software Used in Research and Dissertation Generation ..... 159
Appendix G: All Publications Published, Submitted and Planned ..... 160
G.1 List of peer reviewed published works ..... 160
G.2 List of conference proceedings and publications ..... 161
G.3 List of submitted works ..... 162
G.4 List of planned works ..... 162
Appendix H: Device Fabrication Methods and Recipes ..... 163
H.1 Thin Film Processing ..... 163
H.2 Fabrication Methods ..... 164
H.3 Gold Bold Ball Bonding to Metal on BCB ..... 165
Appendix I: Design of Experiments Matrix and Results of Rapid Thermal Annealing ..... 167
Appendix J: Copyright Permissions ..... 169

## List of Figures

Figure 1: Si-Ge-Sn ternary lattice and band gap space calculated from ref [9]. Other well-known semiconductors and their binary combinations are also plotted. Dotted lines signify indirect bandgap materials and solid lines mark direct bandgap materials. ..... 3

Figure 2: $Ge_{1-x}Sn_x$ research publications from 1990 to 2013 have an increase after 2004 as a result of the stable growth using $SnD_4$ gas on Si via CVD. Data obtained from Web of ScienceTM Thomson ReutersTM. ..... 4

Figure 3: $Ge_{1-x}Sn_x$ technology overview from early precursor development in 2002 up to the most recent advancements in 2014. The progress made in this work is highlighted with dashed boxes. ..... 6

Figure 4: Focal plane arrays with $Ge_{1-x}Sn_x$ pixels could allow imaging in the SWIR on both, vehicle mounted and man portable applications. The use of Si CMOS processing would allow for lower cost and higher density arrays in this spectrum. Image taken by Benjamin Conley used with permission. ..... 7

Figure 5: (a) XRD 2θ - ω rocking curves for $Ge_{0.968}Sn_{0.032}$, with a film thickness of 76 nm are plotted for different annealing temperatures. (b) Reciprocal space maps of the as-grown show strained, almost pseudomorphic $Ge_{0.968}Sn_{0.032}$ epi-layer grown on top of the relaxed Ge buffer. (c) Annealed at 550 °C for 10 seconds, the GeSn peak in the RSM transitions from compressively strained towards relaxed. Reproduced by permission of The Electrochemical Society [31]. ..... 13

Figure 6: (a) The rocking curve spectra for $Ge_{0.94}Sn_{0.06}$ measure the out-of-plane lattice decreasing for increased annealing temperatures. (b) Reciprocal space map taken of the as

grown and (c) after rapid thermal annealing at 550 °C for 10 seconds. Reproduced by permission of The Electrochemical Society [31]. ..... 14

Figure 7: (a) The XRD rocking curves for $Ge_{0.93}Sn_{0.07}$ represent the lattice constant change for 30 seconds at 550 °C and for 10 seconds at 550 °C compared to the as grown sample. Reciprocal space maps of the (b) as grown and (c) sample annealed at 550 °C for 30 seconds show $Ge_{1-x}Sn_x$ film transition from partially relaxed to a reduced Sn mole fraction and relaxed film. Reproduced by permission of The Electrochemical Society [31]. ..... 15

Figure 8: In-plane strain measured for each RTA temperature shows a decreased level of strain and Sn incorporation as temperature increased..... 16

Figure 9: Measured Raman spectra of the Ge-LO peak locations (squares) are plotted for the Sn mole fraction of each sample. Predicted Raman peak location (stars) was determined based on Sn composition and the measured in-plane strain from XRD 2θ scans using Equation 2.5. ..... 18

Figure 10: Photoluminescence spectra of a $Ge_{0.94}Sn_{0.06}$ thin film due to RTA at (a) 400 °C and (b) 450 °C. The change in PL intensity (c) and PL peak location (d) from the as-grown are plotted versus total RTA time for each annealing temperature. ..... 21

Figure 11: Experimental setup and boundary conditions for (a) 2D and (b) and 3D FDTD simulation within the CAD environment. The boundary of the simulation (purple outline) in (a) was set as a perfectly matched layer condition..... 26

Figure 12: First order Bessel function plotted for mode distance used to determine the Bessel Zero for n = 1 and the corresponding m = 35, 50. ..... 28

Figure 13: (a), (c), (e) Computed mode profile for a $Ge_{0.94}Sn_{0.06}$ microdisk with 25, 10, and 4 μm diameters, respectively. (b), (d), (f) Resonant optical modes within the microdisk show decreasing FSR with decreasing disk diameter..... 30

Figure 14: (a) Enlarged view of n = 1 axial mode for a 4 μm diameter $Ge_{0.94}Sn_{0.06}$ microdisk within the measured PL emission range. (b) The enlarged view allows for Q-factor of this resonator to be determined..... 32

Figure 15: Process flow for fabricating $Ge_{1-x}Sn_x$ microdisk on Si had four central steps: (1) Spin coat with photoresist, (2) pattern photoresist with optical photolithography, (3) reactive ion etching of the mesas, and (4) undercut etch the Si substrate using potassium hydroxide. ... 34

Figure 16: Sidewall etch profile of $Ge_{0.974}Sn_{0.026}$/Ge films on Ge within a $CF_4$ dry etch. All etches were performed at 250 mtorr. Etch parameters for each image is listed in Table 5. . 35

Figure 17: SEM images after $Ge_{0.974}Sn_{0.026}$ sample was etched with an optimized dry etching recipe. (a) Top view of a 100 μm $Ge_{0.974}Sn_{0.026}$ mesa etched down to the Si substrate. (b) Sidewall profile shows moderate undercut of the Ge buffer layer. (c) SEM image of the $Ge_{0.974}Sn_{0.026}$ mesa analyzed with EDX for elemental study in (d)-(f) for Ge, Si, and Sn presence, respectively. ..... 37

Figure 18: Variation of KOH etch rate based on concentration for (100) Si, (110) Si, and thermally grown $SiO_2$ for a 60 °C solution..... 39

Figure 19: Simulation of 30% KOH solution on Silicon with a 100 μm diameter mask (grey outline). A negative mask was used in (a) and (b) for 15 and 45 minutes, respectively to simulate the (111) termination planes for a convex pattern. A positive mask was used in (c) and (d) for 15 and 45 minute, respectively that showed the nonterminating etch under the mask to form a Si pedestal..... 40

Figure 20: (a) SEM image of a $Ge_{1-x}Sn_x$/Ge thin film whereby a convex pattern was created and subsequently etched with KOH. (b) Enlarged view shows the undercut etch terminating along the (111) planes. ..... 41

Figure 21: (a) $Ge_{0.974}Sn_{0.026}$/Ge microdisk etched for 12 minutes within a 30% KOH solution at 60 °C. (b) The expanded view of one disk shows the initial undercut due to the KOH etch. ..... 42

Figure 22: SEM image of $Ge_{1-x}Sn_x$/Ge microdisk etched for (a) 20 minutes and (b) 10 minutes shows the lateral etch for increased etch time within the RIE using the GeSn_ET recipe. Both samples were subsequently undercut etched within 30% KOH solution. ..... 42

Figure 23: $Ge_{0.974}Sn_{0.026}$/Ge microdisks with nominal diameter of 12 to 15 μm. Images (a)-(d) are enlargements of the same sample. Sample was etched in 30% KOH at 60 °C for 20 minutes, 15 seconds. ..... 43

Figure 24: $Ge_{0.974}Sn_{0.026}$/Ge microdisk with a nominal diameter of 25 μm. Sample was etched in 30% KOH at 60 °C for 30 minutes. ..... 44

Figure 25: Power dependent photoluminescence at 10 K for the $Ge_{0.94}Sn_{0.06}$ (a) bulk and (b) 12 μm diameter microdisk. The dotted lines in (b) mark the resonant peaks in the PL due to the WGM resonance. ..... 45

Figure 26: Spectral detectivity ($D^*$) of available detectors operating in the SWIR. Plotted from data in ref. [78]. ..... 50

Figure 27: The spectral detectivity for different composition InGaAs detectors at room temperature with detector cut-offs at 1.6, 1.9, 2.2, and 2.6 μm. Plotted from data in ref. [79]. ..... 51

Figure 28: Schematic representation of a $Ge_{1-x}Sn_x$ photoconductor grown on Ge buffered Si. ... 55

Figure 29: Energy-wave vector (E-k) diagram of the electron (solid) and hole (empty) carrier dynamics as a result of impact ionization within a semiconductor..... 58
Figure 30: Schematic cross section of a separate absorption and charge multiplication (SACM) avalanche photodiode. The energy and electric field profiles for each layer highlight the multiplication regions. ..... 62
Figure 31: Band diagram for a SACM avalanche photodiode schematically shows the band offset and band bending for semiconductors with a type-I band alignment. ..... 62
Figure 32: (a) Large band offset in the valence band ($\Delta E_v$) scatters high energy holes, but does not affect the electron. (b) Graded heterostructure reduces the overall energy step for the hole..... 65
Figure 33: Parameters used in the short diode approximation of a separate absorption and charge multiplication avalanche photodiode. ..... 67
Figure 34: Noise current of a photoconductor with 10 μA and 10 nA dark current plotted for the device resistance and temperature..... 77
Figure 35: Relative effects of device noise, responsivity, and area have on the detectivity ($D^*$). 79
Figure 36: Process flow for fabrication of $Ge_{1-x}Sn_x$ photoconductors grown on Ge buffered Si. 82
Figure 37: Top view optical image of a fabricated $Ge_{1-x}Sn_x$ photoconductor. This image of the 0.5 and 1.0 mm mesas was taken after the metal lift-off process. ..... 82
Figure 38: Top view optical image of the transmission line structure fabricated on the photoconductor die..... 83
Figure 39: Dark I-V measurements of a 2 mm photoconductor for each $Ge_{1-x}Sn_x$ sample at (a) 300 K and (b) 77 K. ..... 85

Figure 40: Temperature dependent dark I-V of the (a) $Ge_{0.93}Sn_{0.07}$ and (b)$Ge_{0.9}Sn_{0.1}$ 2 mm photoconductors showed a decreasing metal-semiconductor barrier with decreasing temperature. ..... 86

Figure 41: Dark resistance of each 2 mm $Ge_{1-x}Sn_x$ photoconductor measured for varying temperature. Regions 1, 2, and 3 defined the regions of changing slope for each detector set. ..... 88

Figure 42: Natural logarithm of the 2 mm photoconductor dark resistance [ln(R)] plotted for 1/T. The slope of each separate region corresponds to the corresponding carrier activation energy ($E_A$)..... 90

Figure 43: Normalized spectral response of the (a) 0.9, 3.2, and (b) 7.0% Sn photoconductors for different temperatures as a function of wavelength shows the shifting absorption edge for increased Sn composition. © 2014 Optical Society of America [92]..... 92

Figure 44: Absolute spectral response temperature profile of the 7.0% Sn photoconductor shows increasing response intensity for decreased temperature. The absorption edge power factor (m) indicates either direct or indirect absorption. © 2014 Optical Society of America [92] 93

Figure 45: Temperature dependent long-wavelength spectra of $Ge_{1-x}Sn_x$ photoconductors with Sn composition 8.0 – 10.0%. ..... 94

Figure 46: Detector cut-off plotted for each measured temperature and fitted using the Varshni relationship. The Ge-direct line was plotted from ref. [99] and is shown here for comparison. ..... 95

Figure 47: Zero Kelvin bandgap of $Ge_{1-x}Sn_x$ alloys extracted from the temperature dependent photoconductor long wavelength cut-off. ..... 97

Figure 48: Responsivities of the 0.9 and 3.2% Sn photoconductors measured at 1.55 μm and plotted for the DC bias voltage. The photoconductor mesa size was 2 mm. ..... 98
Figure 49: Responsivity of the 7.0% Sn photoconductor at 1.55 μm plotted for the lowest measured temperatures. The photoconductor mesa size was 2 mm. ..... 99
Figure 50: Responsivity of the 2 mm photoconductor mesas with 8.0, 9.0, and 10.0% Sn were measured as a function of applied bias, and across different temperatures. ..... 100
Figure 51: Responsivity at 1.55 μm for the 8.0% Sn photoconductor measured as a function of temperature and applied bias voltage and plotted in a 3D contour plot. This measurement was conducted on 0.5, 1.0, and 2.0 mm square mesas. ..... 101
Figure 52: Effect of mesa size on responsivity at 1.55 μm compared for the 9.0 and 10.0% Sn photoconductors at 77 K. ..... 103
Figure 53: High voltage bias effect on responsivity was measured for 10.0% Sn photoconductor at 77 K. The measurement was made using a 1.55 μm laser source. ..... 104
Figure 54: Effective lifetime of the 10.0% photoconductor with 1.6 mm electrode spacing (2 mm square mesa) calculated for each measured temperature. ..... 106
Figure 55: Effective lifetime for the 10.0% Sn photoconductor measured at 77 K versus the photoconductor electrode spacing. Two separate detectors with 1.6 mm spaced electrode spacing were measured. ..... 107
Figure 56: Detectivity at 1.55 μm for the 0.9, 3.2, and 7.0% Sn photoconductors as measured versus the applied bias voltage. The values were for the temperatures with the maximum detectivity of each device. ..... 108
Figure 57: Specific detectivity of the 2 mm photoconductors with 8.0, 9.0, and 10.0% Sn. Measurement conducted using a 1.55 μm laser source. ..... 109

Figure 58: Detectivity of 10.0% Sn photoconductor at 77 K for the 2.0, 1.5, 1.0, and 0.5 mm square mesa sizes measured at 1.55 μm. ..... 110
Figure 59: Spectral detectivity for the 2 mm square photoconductors with 8.0, 9.0, and 10.0% Sn composition. Each measurement was conducted with a 10 volt applied bias..... 112
Figure 60: Spectral $D^*$ of the 8.0, 9.0, and 10.0% Sn photoconductors at 77 K plotted versus wavelength. Also plotted are the $D^*$ values of currently available detectors in the SWIR. The $D^*$ of InGaAs, extended-InGaAs, Ge, InAs, and PbS are plotted using data from references [78, 79]..... 113
Figure 61: Fabrication process flow for fabricating a $Ge_{1-x}Sn_x$ photoconductor with interdigitated electrodes used a photoactive BCB layer as a dielectric and passivation. ..... 115
Figure 62: Current-voltage measurement before and after ball wire bonding on a 500 nm thick Au pad with (a) 500 nm and (b) 1000 nm thick $SiO_2$ passivation layer. ..... 116
Figure 63: SEM image of a metal trace test structure going up a vertical $SiO_2$ passivation layer with (a) 500 nm and (b) 1000 nm $SiO_2$ thickness. ..... 117
Figure 64: SEM image of fabricated interdigitated photoconductor with BCB passivation layer. Image (b) is a zoomed in view of the metal trace transition down to the device surface from the highlighted red box in (a) the device full view perspective. ..... 117
Figure 65: (a) Top view optical image of a fabricated $Ge_{0.93}Sn_{0.07}$ photoconductor with interdigitated electrodes. (b) SEM image measured the electrode dimensions of a fabricated device with expected 3 μm electrode width and 6 μm spacing. ..... 118
Figure 66: Current-voltage measurement of the (a) co-planar and (b) interdigitated electrode photoconductors at 77 K. ..... 119

Figure 67: Dark resistance of the (a) co-planar photoconductors and (b) interdigitated electrodes were plotted for each measured temperature. ..... 120

Figure 68: Responsivity measured for the $Ge_{0.93}Sn_{0.07}$ interdigitated photoconductor devices at 1.55 μm for device temperatures of 300, 260, 100, and 77 K. ..... 121

Figure 69: Effective carrier lifetime for the $Ge_{0.93}Sn_{0.07}$ photoconductor measured per interdigitated electrode spacing. ..... 122

Figure 70: Inverse of effective carrier lifetime plotted against the inverse of the squared electrode spacing at (a) 77 K and (b) 300 K. Linear fitting was performed for the 0.5 and 1.0 mm mesas. ..... 123

Figure 71: Cross section of the $Ge_{1-x}Sn_x$ avalanche photodiode shows the final fabricated detector with a top illuminated design. ..... 126

Figure 72: Top view SEM image of (a) 250 μm diameter $Ge_{1-x}Sn_x$ APD shows the top signal contact on the $Ge_{1-x}Sn_x$ epilayer and the ground ring contact on the Si n-type substrate. (b) Enlarged view shows the metal trace across the BCB to $Ge_{1-x}Sn_x$ interface. ..... 127

Figure 73: SEM image the $Ge_{1-x}Sn_x$ APD after mesa dry etching. (a) Side view of a device and (b) cross sectional view allows the total etch depth to be determined. ..... 128

Figure 74: Energy dispersive x-ray spectroscopy of the APD device cross section identifies the elemental presence defining the epitaxial layers with Sn (blue), Ge (green), or Si (red). .. 128

Figure 75: Dark I-V measurement of the (a) 100 μm, (b) 250 μm, and (c) 500 μm diameter $Ge_{1-x}Sn_x$ APDs measured for temperatures from 340 to 77 K. ..... 130

Figure 76: Breakdown voltage for each measured temperature plotted for the $Ge_{1-x}Sn_x$ 100, 250, and 500 μm diameter APDs. The right axis is the corresponding ionization coefficient. .. 131

Figure 77: (a) Current-voltage measurement of the Ge APD at room temperature. (b) Current-voltage of a 500 μm diameter Ge APD at 77 K under dark and 1.55 μm laser illumination. ..... 132

Figure 78: Spectral response of a 500 μm diameter $Ge_{1-x}Sn_x$ APD measured for varying device temperatures from 77 to 340 K. ..... 133

Figure 79: Dark and 1.55 μm laser illuminated I-V of a $Ge_{1-x}Sn_x$ APD with a 500 μm diameter. ..... 133

Figure 80: (a) Spectral response of a 500 μm diameter $Ge_{1-x}Sn_x$ APD measured at room temperature for different applied bias near the breakdown voltage. (b) Peak intensity from each spectrum plotted for each applied voltage. ..... 134

Figure 81: Dark (solid lines) and white light (dashed lines) I-V were measured for $Ge_{1-x}Sn_x$ APDs with 100, 250, and 500 μm diameters at 77, 140, 200, and 300 K. ..... 135

Figure 82: Experimentally multiplication gain of $Ge_{1-x}Sn_x$ APDs measured per applied bias. Devices with diameters of 100, 250, and 500 μm were measured at temperatures of 300, 200, 140, and 77 K. ..... 136

Figure 83: Design for monolithic integration of epitaxial $Ge_{1-x}Sn_x$ pixels with a Si read out integrated circuit (ROIC). Not drawn to scale. ..... 141

Figure 84: Cross sectional side view of a multi-spectral detection design using $Ge_{1-x}Sn_x$ films can be accomplished by increasing the Sn content of each subsequent film. This design would be back-side illuminated. Top view of the pixel shows a simple geometry for the metal contacts of each layer. Not drawn to scale. ..... 142

Figure 85: $Ge_{1-x}Sn_x$ ring formed by etching punch through of the photoresist within the RIE process. ..... 164

Figure 86: Actual vs predicted plot of the PL Peak location using standard least squares on DOE matrix of variables and measured outputs in Table 16. ..... 168

## List of Tables

Table 1: Strain, composition, and thickness of as-grown Ge1-xSnx samples prior to annealing. 10

Table 2: Design of experiments input and measured parameters. Reproduced by permission of The Electrochemical Society [31]. ..... 19

Table 3: Effect of annealing parameters through a DOE analysis using standard least squares .. 20

Table 4: Calculated Q and Purcell factor for a 4 μm microdisk with a $Ge_{0.94}Sn_{0.06}$ active layer.. 32

Table 5: Experimental parameters for RIE of $Ge_{1-x}Sn_x$ thin films etched at 250 mTorr ..... 35

Table 6: Resonant modes from microPL measurement of 12 μm diameter microdisk ..... 46

Table 7: Summary of Ge, $Ge_{1-x}Sn_x$, and $Si_{1-x-y}Ge_ySn_x$ photodetectors at room temperature..... 48

Table 8: Sn composition and film thickness of $Ge_{1-x}Sn_x$ photoconductors ..... 80

Table 9: Carrier and trap activation energy for 2 mm $Ge_{1-x}Sn_x$ photoconductors ..... 89

Table 10: Fitting parameters for $Ge_{1-x}Sn_x$ temperature dependent bandgap..... 96

Table 11: Bulk lifetime and minority carrier diffusion of $Ge_{0.93}Sn_{0.07}$ thin films at 77 K..... 124

Table 12: Plasma enhanced chemical vapor deposition recipes used for $SiO_2$ and $Si_3N_4$ thin film deposition ..... 163

Table 13: Reactive ion etch recipes used to remove $Ge_{1-x}Sn_x$ and $Si_3N_4$ thin films ..... 163

Table 14: Gold ball bond settings for wire bonding to thin Au/Cr pads on BCB..... 165

Table 15: Global settings on the ball bonding tool for samples with thin film metal contacts .. 166

Table 16: Design of Experiments Matrix for Rapid Thermal Annealing of $Ge_{1-x}Sn_x$ Thin Films ..... 167

# Chapter 1: Introduction

## 1.1 Motivation

The short-wave infrared (SWIR) region of the electromagnetic spectrum from 1.5 to 3.0 μm is an area of increased detection interests. The blackbody spectrum given off by ambient objects is too cool, and have too long of wavelength to affect detection in this region. Thus the interaction of light in the SWIR is of a specular nature and requires a light source, i.e. the sun, an IR emitter, starlight, etc. The significance of this implies that there is a large unused band of the electromagnetic spectrum that is both unaffected by thermal radiation and not seen by humans or other visible light sensors, such as Si charge coupled devices (CCD) or complementary metal oxide semiconductor (CMOS) detectors. Communications (free-space or fiber based), covert security, enhanced night vision, 3D cameras, and gas sensing are a few of the applications that would rely on or could benefit from SWIR detection.

One particular commercial application is focal plane arrays (FPA) operating in the SWIR band for applications in security and digital night vision. Currently fielded FPAs in the SWIR have high costs that usually only permit their practical deployment on large scale optics platforms such as vehicles. To obtain better IR coverage on a man portable level, future optoelectronic devices will need to be more mass producible and should also be uncooled for lower power consumption and weight. This would allow individuals and mobile units to rely less on vehicle or other equipment assets in order to access these spectral bands. The current technologies heavily relied upon for SWIR use the InGaAs material system. These InGaAs cameras are smaller density pixel arrays as compared to the ultra-high definition Si sensors used for visible detection due to the decreased substrate size and increased fabrication costs.

Incorporation of Si-based optoelectronics would be a revolutionary achievement not only for data communication and FPAs, but it would also open up the SWIR spectrum to sensing, lab on a chip, and medical imaging that are out of reach due to a lack of cost effective devices. Direct incorporation of III-V semiconductors on Si or flip chip bonding of these optoelectronics have disadvantages that limit such solutions from being mass producible. The added steps of bonding or machine transfer for III-V growth adds material cost, fabrication complexity, and potentially introduces contamination to Si CMOS chips. Additionally, there is an increased apprehension with direct integration of III-V on Si due to possible auto-doping from those III-V materials into the Si electronics. Incorporating photonics with an off-chip design presents further problems as well, such as coupling losses for waveguides across dies, complex alignment procedures, and differing thermal responses [1, 2]. Development of Si compatible photonics would enable existing Si foundries and automated fabrication facilities to be quickly adapted for fabrication of photonic integrated circuits (PIC) in tandem with their microelectronic counterparts.

### 1.2 $Ge_{1-x}Sn_x$ Optoelectronics

It was first suggested by R. Soref in 1993 to use all Group IV elements for a complete Si based optoelectronics platform [3]. Since then, Ge (direct band gap of 0.8 eV at 300 K) has been considered a candidate material for incorporation of group IV materials with the telecom 1.55 μm band to compete with the more expensive InGaAs based detectors. This Si based photonic motivation has driven much research towards developing Ge on Si optoelectronics with the eventual success of high responsivity Ge detectors around 1 A/W with GHz level bandwidths [4]. Another great success in this area of Ge optoelectronics was the first Ge on Si laser using high n-type doped, tensile strained Ge as the gain medium [5]. Although Ge showed initial

success in photonic active devices, its indirect band gap ultimately limits the performance and light emission efficiency. For example, Ge lasers require either 2% tensile strain or n-type doping levels in upwards of $7\times10^{19}$ $cm^{-3}$ in order to achieve gain [6].

The proposed solution for a Si based optoelectronic platform is the $Ge_{1-x}Sn_x$ material system. Tin is a semi-metal with a diamond cubic allotrope that can offer band gap and lattice tuning when incorporated with Si and Ge materials. The direct gap of Ge is 140 meV above the indirect L point ($E_g$ = 0.66 eV) and Sn alloying allows for a crossover from an indirect to direct semiconductor with 8 – 10% Sn incorporation [7, 8]. Thus an alloy of $Ge_{1-x}Sn_x$ can have direct bandgap emission without doping or induced tensile strain. The band gap versus lattice constant for the Si-Ge-Sn system shown in Figure 1 illustrates how expansive this material can be for the SWIR to the mid-wave infrared (MWIR) regions.

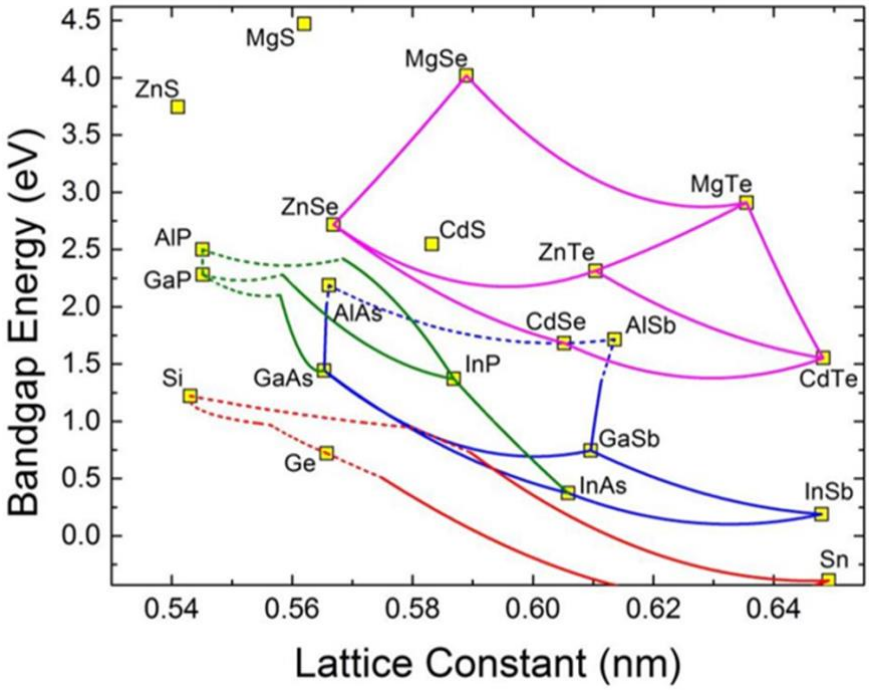


Figure 1: Si-Ge-Sn ternary lattice and band gap space calculated from ref [9]. Other well-known semiconductors and their binary combinations are also plotted. Dotted lines signify indirect bandgap materials and solid lines mark direct bandgap materials.

$Ge_{1-x}Sn_x$ alloys are grown using either chemical vapor deposition (CVD) or molecular beam epitaxy (MBE). Crystalline $Ge_{1-x}Sn_x$ alloys were first deposited on Si and $SiO_2$ using an ultra-high vacuum chemical vapor deposition (UHV-CVD) reactor in 2001 using stannane ($SnD_4$) as the Sn precursor [10]. Figure 2 shows the increased interest in the $Ge_{1-x}Sn_x$ field as a result of these first successful film growths.

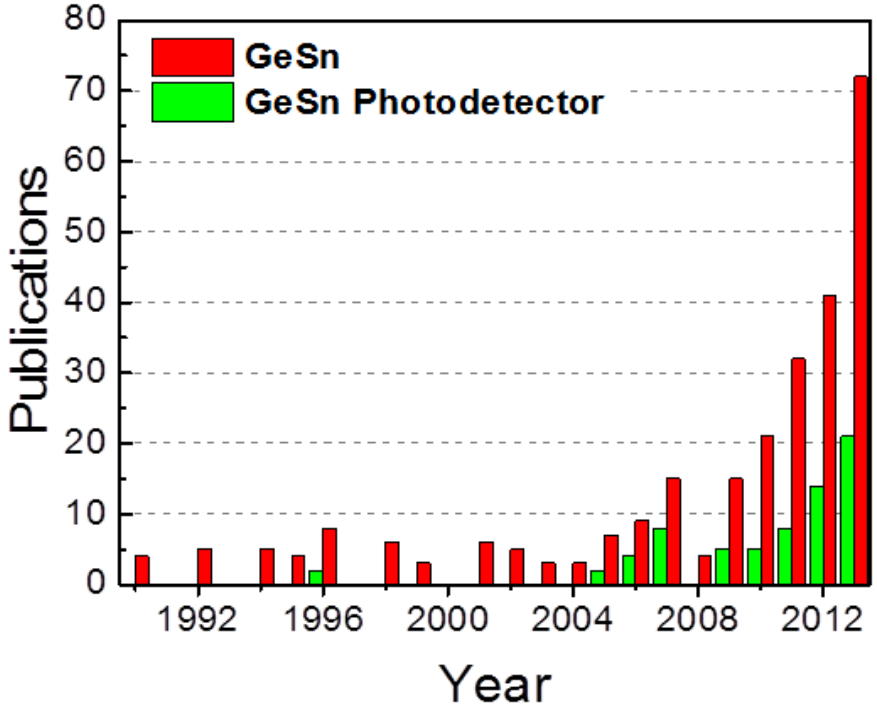


Figure 2: $Ge_{1-x}Sn_x$ research publications from 1990 to 2013 have an increase after 2004 as a result of the stable growth using $SnD_4$ gas on Si via CVD. Data obtained from Web of ScienceTM Thomson ReutersTM.

The diamond cubic allotrope of Sn, known as α-Sn (or grey Sn), only exist in a stable form below 13° C [11]. Thermodynamically this limits the solid solubility of Sn in Ge to 0.5% and also decreases the thermal stability of the films above the growth temperatures. Despite these limitations, the deposition of $Ge_{1-x}Sn_x$ alloys on Ge-buffered Si and directly on Si using different variations of CVD and MBE have been explored and growth recipes are well documented [12-

17]. Upwards of 26% Sn composition has been demonstrated [11], but alloys with measurable band gaps have been observed with up to 14% Sn composition [7].

In this work the $Ge_{1-x}Sn_x$ films were grown on Si via CVD using commercially available hydride based precursors and dopant gases. The non-equilibrium growth conditions of CVD allow for suppression of Sn segregation even for high Sn compositions well above the 0.5% solubility limit. Low temperature growth confines the Sn atoms within the substitution lattice sights. This non-equilibrium growth can be achieved in low temperature environment (< 500 °C) of a UHV-CVD or RP-CVD reactor. The clean environment of an Ultra High Vacuum (UHV) chamber reduces the amount of contaminants within the chamber, but has a reduced throughput. The growth of $Ge_{1-x}Sn_x$ using commercially available CVD reactors and precursors has also been demonstrated by several groups using ASM Epsilon [15, 18], ASM Polygon [19], and Axitron Tricent reactors [20]. The Sn precursor used in these reactors is the commercially available and stable $SnCl_4$. The material development and characterization roadmap for $Ge_{1-x}Sn_x$ and $Si_{1-x-y}Ge_xSn_y$ materials, presented in Figure 3, outlines the technology progression of this material. The device research in this work is included in the roadmap and is highlighted by the dashed boxes.

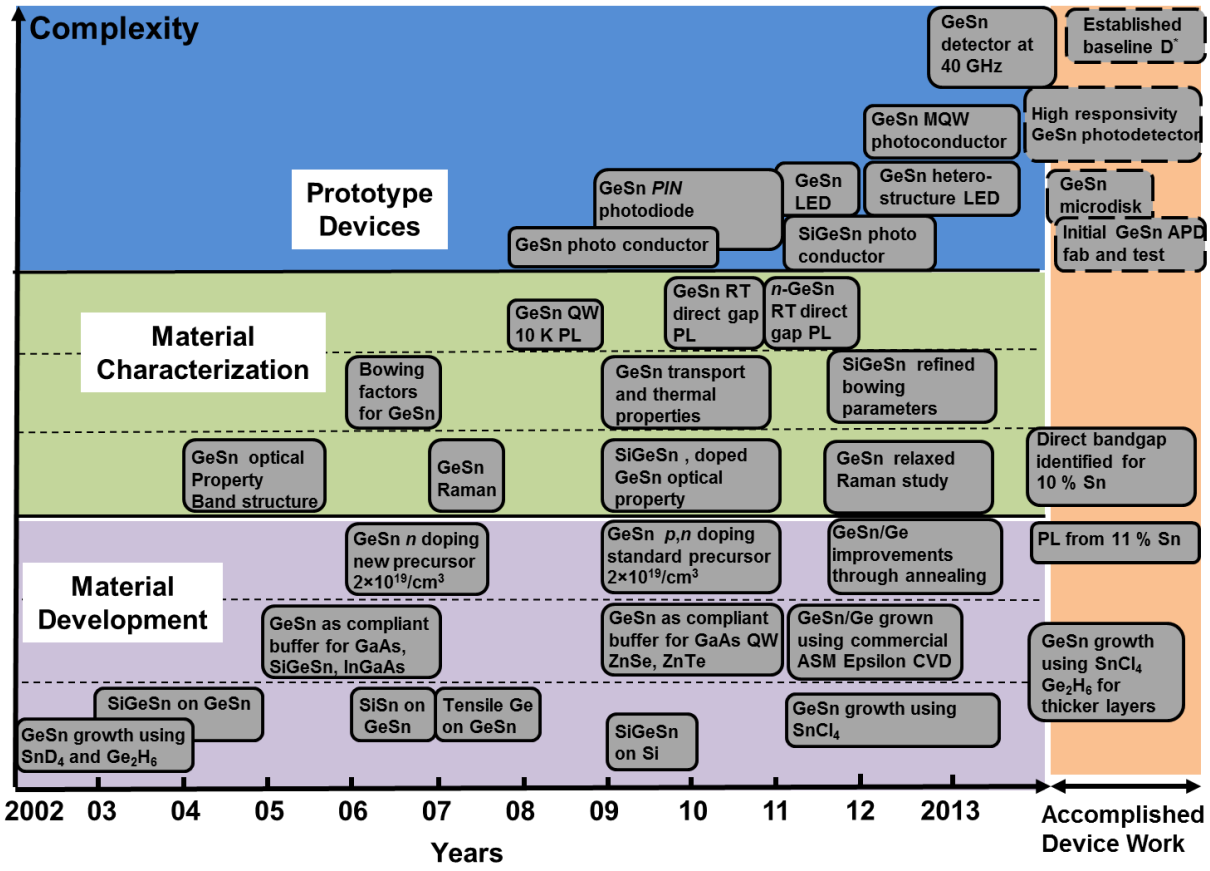


Figure 3: $Ge_{1-x}Sn_x$ technology overview from early precursor development in 2002 up to the most recent advancements in 2014. The progress made in this work is highlighted with dashed boxes.

The initial motivation for $Ge_{1-x}Sn_x$ and the ternary Si-Ge-Sn materials was for optical communication via Si photonic integration. The outlook was to replace long wire (>1km) interconnects and to augment current 1.55 μm long haul fibers using SWIR optical fiber around the 2 μm wavelength band [21]. The 2 μm band is a feasible optical transition within a $Ge_{1-x}Sn_x$ or $Si_{1-x-y}Ge_xSn_y$ alloy system as the addition of Sn will shift the band gap of pure Ge towards longer wavelengths. Although development of a Si based laser is one field where $Ge_{1-x}Sn_x$ could be a revolutionary achievement, the driving motivation for the devices in this work is the Si-integrated FPA for the SWIR spectrum as highlighted in Figure 4. These $Ge_{1-x}Sn_x$ based FPAs would allow imaging in the SWIR on an almost equivalent scale and cost to Si visible imagers.

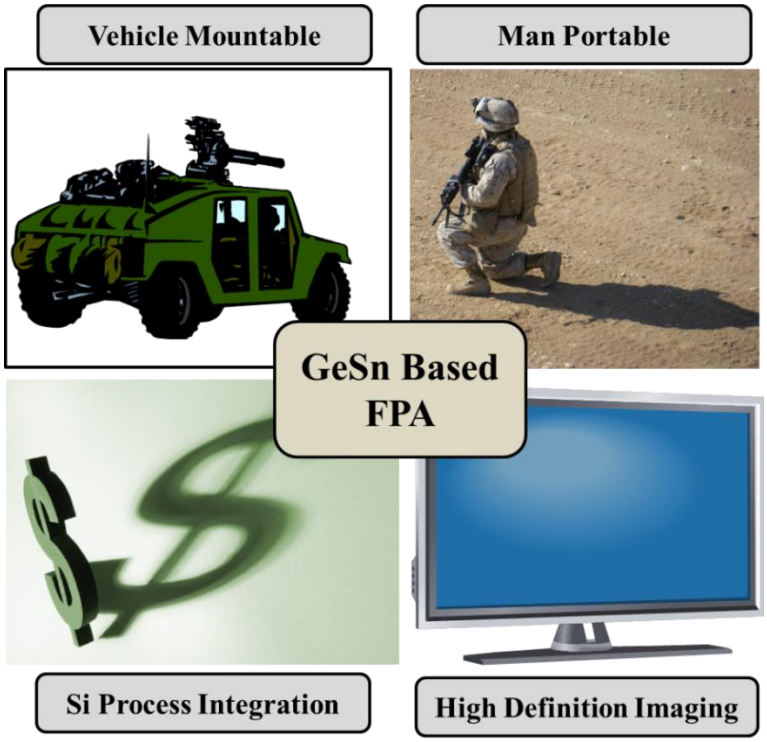


Figure 4: Focal plane arrays with $Ge_{1-x}Sn_x$ pixels could allow imaging in the SWIR on both, vehicle mounted and man portable applications. The use of Si CMOS processing would allow for lower cost and higher density arrays in this spectrum. Image taken by Benjamin Conley used with permission.

In this work, $Ge_{1-x}Sn_x$ active devices were studied for their application as a new low cost optoelectronic platform in the SWIR spectral range. Thus far, $Ge_{1-x}Sn_x$ detectors have only been considered for application in Si photonics applications. The use of this material in a FPA requires research into material parameters such as carrier lifetime, noise, and temperature dependent spectral response. Prior to this work, none of those parameters had been investigated. The baseline for these material parameters was established across a broad range of Sn compositions, from 0.9 to 10.0% Sn. As a result, detector fabrication and testing methodologies were developed that will allow continued work in this area. Fabrication and simulation for $Ge_{1-x}Sn_x$ microdisk resonators were also developed. Wet chemical undercut etching and smooth sidewall mesa etching requirements of 5 μm diameter disks led to the development of etch recipes compatible with these films.

## 1.3 Organization

The experimental and theoretical experiments are organized into six different chapters. Chapter 2 covers the material stability of the $Ge_{1-x}Sn_x$ films under thermal conditions that these thin films might experience in a CMOS processing facility. Although the growth of $Ge_{1-x}Sn_x$ films was previously established as CMOS compatible, it has yet to be determined if CMOS processing temperatures up to 450 °C are compatible with the as-grown films. This chapter explores the thermal stability of the films at temperatures above and below 450 °C.

The fabrication and modeling of a $Ge_{1-x}Sn_x$ microdisk resonator is covered in Chapter 3. This chapter covers the initial fabrication methods used in fabricating $Ge_{1-x}Sn_x$ devices. The fabrication concepts outlined in this chapter are also applied to the $Ge_{1-x}Sn_x$ photodetectors discussed in Chapters 5-7. The finite difference time domain (FDTD) modeling and the fabrication results are covered in this chapter.

The background information for photodetector physics, measurement methods, and relevant figures of merit are covered in Chapter 4. This chapter also covers a brief review of current detector technologies operating in the same wavelength spectrum. Chapters 5-7 will explore the fabrication and results of $Ge_{1-x}Sn_x$ photodetectors. The temperature dependent analysis and performance of $Ge_{1-x}Sn_x$ photoconductors are explored in Chapter 5. The effective carrier lifetime of the $Ge_{1-x}Sn_x$ thin films and the enhanced photoconductor gain due to an interdigitated design is explored in Chapter 6. Finally, $Ge_{1-x}Sn_x$ and Ge avalanche photodiodes grown on Si are fabricated and tested with their results presented in Chapter 7.

A summary and the conclusions of this entire work is covered in Chapter 8 along with the future work.

## Chapter 2: Thermal Stability of $Ge_{1-x}Sn_x$ under CMOS Processing

Growth of $Ge_{1-x}Sn_x$ thin films on Si substrates using the CVD process is accomplished with one of two Sn based precursors: deuterated stannane ($SnD_4$) or stannic chloride ($SnCl_4$). Photonic quality films grown using $SnD_4$ were demonstrated to be compatible with direct growth on Si [22] and are expected to also be compatible with growth on a Ge buffer layer. However, $SnD_4$ is an unstable gas and decomposes at room temperature [23]. To reduce the number of misfit dislocations propagating through the film due to the large $Ge_{1-x}Sn_x$/Si mismatch, post-growth rapid thermal annealing (RTA) process was used [24, 25].

The other precursor known well for $Ge_{1-x}Sn_x$ growth, as previously discussed in Chapter 1, is $SnCl_4$. This chemical exists as a liquid at room temperature, has long term room temperature stability, and is already widely used throughout the microelectronics industry. The growth mechanisms for $SnCl_4$ require balancing the Sn deposition with HCl etching that occurs as a byproduct of the film synthesis reaction. One method to ensure Sn incorporation into the Ge lattice is the growth of a Ge buffer layer on Si prior to the $Ge_{1-x}Sn_x$ film growth [20]. This Ge buffer layer is grown beyond the critical thickness, thus causing it to relax at the Ge/Si interface. The Ge buffer, now fully relaxed acts as a virtual substrate for subsequent film growth. The smaller lattice constant difference between Ge and $Ge_{1-x}Sn_x$ allows growth of fully pseudomorphic to relaxed $Ge_{1-x}Sn_x$ thin films. This variation in initial strain and the interface difference from that of previously documented RTA on $Ge_{1-x}Sn_x$/Si films indicate further study is needed to analyze the thermal effect on the $Ge_{1-x}Sn_x$/Ge. Initial thermal stability and RTA studies for these films were either done on select Sn compositions, or those studies did not achieve full film relaxation [26, 27]. Additionally, it was concluded that RTA is detrimental to a $Ge_{1-x}Sn_x$ film that has already been optimized within the growth process [27].

This chapter analyzes the effect of RTA processing on $Ge_{1-x}Sn_x$ films with varying Sn compositions from 0.9 to 7.0%. Additionally, these films have varying initial strains due to the different Sn compositions and film thickness. This work seeks to decouple these effects and answer two questions. (1) What is the thermal stability of the films at high temperatures? (2) Can the film quality can be improved by RTA? The Sn composition and strain were analyzed using x-ray diffraction (XRD) while the material quality was correlated through photoluminescence measurements (PL).

### 2.1 Rapid Thermal Annealing Experimental Design

The $Ge_{1-x}Sn_x$ thin films were grown on Ge buffered Si by ASM America using an ASM Epsilon reduced pressure chemical vapor deposition (RPCVD) reactor. The growth process was done below 450 °C for all samples, maintaining a CMOS compatible thermal budget. Each sample was measured after growth (as-grown) and again following the annealing treatment by a Philips X'Pert PRO XRD. The 2θ scans were measured for each sample to determine the out-of-plane lattice constant. Since the out-of-plane lattice constant measurement can change due to a change in strain or Sn composition, select samples were measured by reciprocal space mapping (RSM). RSM measures both the in-plane and out-of-plane lattice constants simultaneously. The Sn composition, thickness, and in-plane strain for each sample in this experiment are listed in Table 1. Positive values for the in-plane strain of the samples listed in Table 1 indicate compressive strain, while a negative value would indicate a tensile strained film.

Table 1: Strain, composition, and thickness of as-grown Ge1-xSnx samples prior to annealing

| Sample | Sn Composition (%) | $Ge_{1-x}Sn_x$ Thickness (nm) | As-Grown Strain $\epsilon_{\parallel}$ |
|---|---|---|---|
| B | 2.7 | 173 | 0.0009 |
| C | 3.2 | 76 | 0.0018 |
| E | 6.0 | 45 | 0.0063 |
| F | 7.0 | 211 | 0.0035 |

The XRD 2θ scans measured the amount of reflected x-rays that meet the Bragg reflection criteria for the given angle of the sample. This means the overall intensity of the x-ray counts/second (y-axis) is related to both the film thickness and material quality (amount of identical planes). However, direct correlation of the counts/second to film quality is difficult to interpret between samples due to the variation in optical alignment per sample. The angle of these Bragg reflections corresponds directly with the out-of-plane lattice constant of the crystal,

$$2d\sin(\theta) = n\lambda \tag{2.1}$$

where d is the vertical spacing between planes, θ is the measured diffraction angle, n = 1 for first order diffraction, and λ = 1.540562 nm is the x-ray wavelength. These films, which are all diamond cubic crystals, have lattice constants equal to four times the plane spacing d. When the out-of-plane lattice ( $a_\perp$ ) constants are known, the in-plane and out-of-plane strain can be found,

$$\epsilon_\perp = \frac{a_\perp - a_o}{a_o} \tag{2.2}$$

$$\epsilon_\parallel = \epsilon_\perp \Big/ \left( 2\frac{C_{12}}{C_{11}} \right) \tag{2.3}$$

where $C_{12}/C_{11}$ is the film elastic ratio, and $a_o$ is the relaxed lattice constant. The relaxed lattice constant is calculated based on the interpolation of Ge and Sn lattice constant (Vegard's law) and an appropriate bowing factor [28]. More accurately the relaxed lattice constant is directly calculated from RSM data, but this data is not available for every annealed sample. For $Ge_{1-x}Sn_x$ films, the elastic ratio is taken as [29],

$$\frac{C_{12}}{C_{11}} = 0.3738 + 0.167x - 0.0296x^2 \tag{2.4}$$

where x is the Sn mole fraction of the film.

The RTA experiments were carried out in a HeatPulse 210 oven with a nitrogen purged chamber. The RTA heat up rate was not modified between experiments. The rapid heating rate was measured to vary from 45 to 55 °C/second. The set temperature was maintained by a feedback loop pyrometer and thermocouple system with an observed 2 °C accuracy. The RTA chamber was actively cooled with a water chiller and $N_2$, causing the samples to cool down below the growth temperature within 5 seconds after completion of the set annealing time.

Raman spectra were collected for each as-grown sample and after RTA treatment. A 632 nm HeNe laser was used as the excitation source. A grating spectrometer with 0.025 nm resolution and a CCD Si sensor were used to acquire the spectra and determine the Raman shift. The resolution of a Raman system is dependent upon the excitation wavelength, spectrometer resolution, and center wavenumber of interest. For this setup, a 632 nm laser was sufficient to provide acquisition of the Ge-Ge and Ge-Sn longitudinal optical (LO) phonon. The Ge-Ge and Ge-Sn LO phonons have wavenumbers of 300 and 260 $cm^{-1}$, respectively [30].

### 2.2 High Temperature Sn Segregation Limit

Three of the samples listed in Table 1 (Samples C, E, F) were chosen for their varying Sn compositions. High temperature RTA processing was conducted on these samples to assess the thermal stability limit. Each sample was subjected to the same RTA cycle, then XRD was used to measure the change in the film strain. Select samples were measured by RSM to confirm total Sn concentration incorporated within the lattice.

Sample C was RTA processed at 550, 650, and 700 °C for 30 seconds each. An additional RTA was performed at 550 °C for 10 seconds. The measured XRD 2θ scans in Figure 5 (a) show the diffraction peak due to the $Ge_{0.968}Sn_{0.032}$ film shifting to lower angles caused by a reduction in the out-of-plane lattice constant when annealed at 650 °C. Prior to this temperature,

the diffraction peak reduces in intensity, indicating a reduction in film quality for both the 550 °C (10 second and 30 second) annealing cycles. The RSM data in Figure 5 shows the almost fully strained $Ge_{1-x}Sn_x$ film on Ge for the as-grown [Figure 5 (b)] shift slightly right, away from the pseudomorphic line for the 550 °C, 10 second annealed sample [Figure 5 (c)]. Relaxation of the film without Sn segregation was observed at 550 °C. Subsequently a shift toward lower diffraction angles for increasing temperature indicated relaxation of the film occurred up to 650 °C. The lack of a discernable $Ge_{0.968}Sn_{0.032}$ peak for the 700 °C anneal indicated that Sn segregation out of the film has occurred.

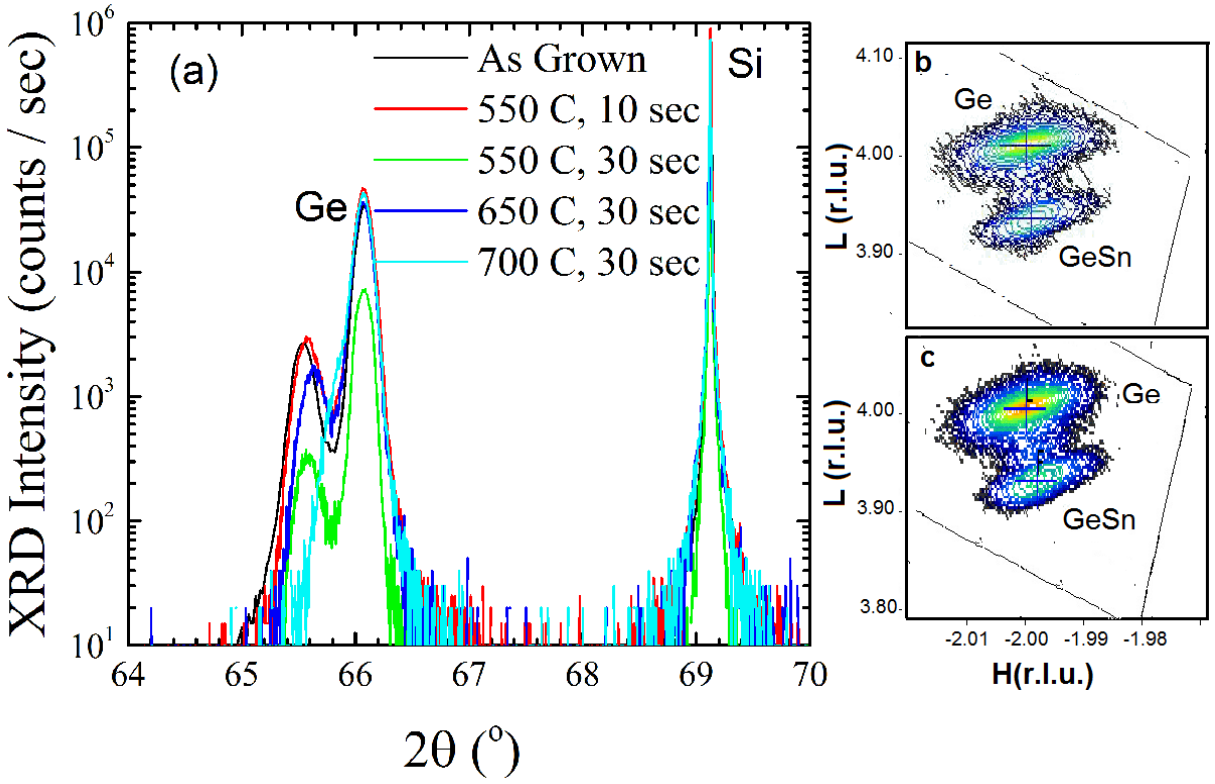


Figure 5: (a) XRD 2θ - ω rocking curves for $Ge_{0.968}Sn_{0.032}$, with a film thickness of 76 nm are plotted for different annealing temperatures. (b) Reciprocal space maps of the as-grown show strained, almost pseudomorphic $Ge_{0.968}Sn_{0.032}$ epi-layer grown on top of the relaxed Ge buffer. (c) Annealed at 550 °C for 10 seconds, the GeSn peak in the RSM transitions from compressively strained towards relaxed. Reproduced by permission of The Electrochemical Society [31].

The 45 nm thickness of the $Ge_{0.94}Sn_{0.06}$ film caused it to remain fully pseudomorphic after grown, with an in-plane lattice constant matching that of the Ge buffer. This is evident by the $Ge_{0.94}Sn_{0.06}$ peak residing directly below the Ge peak in the as-grown RSM of Figure 6 (b). The fringes in this RSM scan between the Ge and $Ge_{0.94}Sn_{0.06}$ peak for the as-grown scan are interference fringes due to the highly abrupt $Ge_{0.94}Sn_{0.06}$/Ge interface. This sample relaxed and degraded following the RTA process. The XRD scans indicate the material quality degraded for all temperatures applied. The XRD scans in Figure 6 (a) show the shifting $Ge_{0.94}Sn_{0.06}$ peak moved towards higher angles due to the film relaxation and reduced Sn content. The RSM of the 550 °C RTA for 10 seconds in Figure 6 (c) illustrates the spreading of the $Ge_{0.94}Sn_{0.06}$ peak due to a decreased uniformity in the Sn lattice spacing. Additionally, this RSM peak shifted towards being relaxed and no longer has a highly abrupt film interface with the Ge buffer.

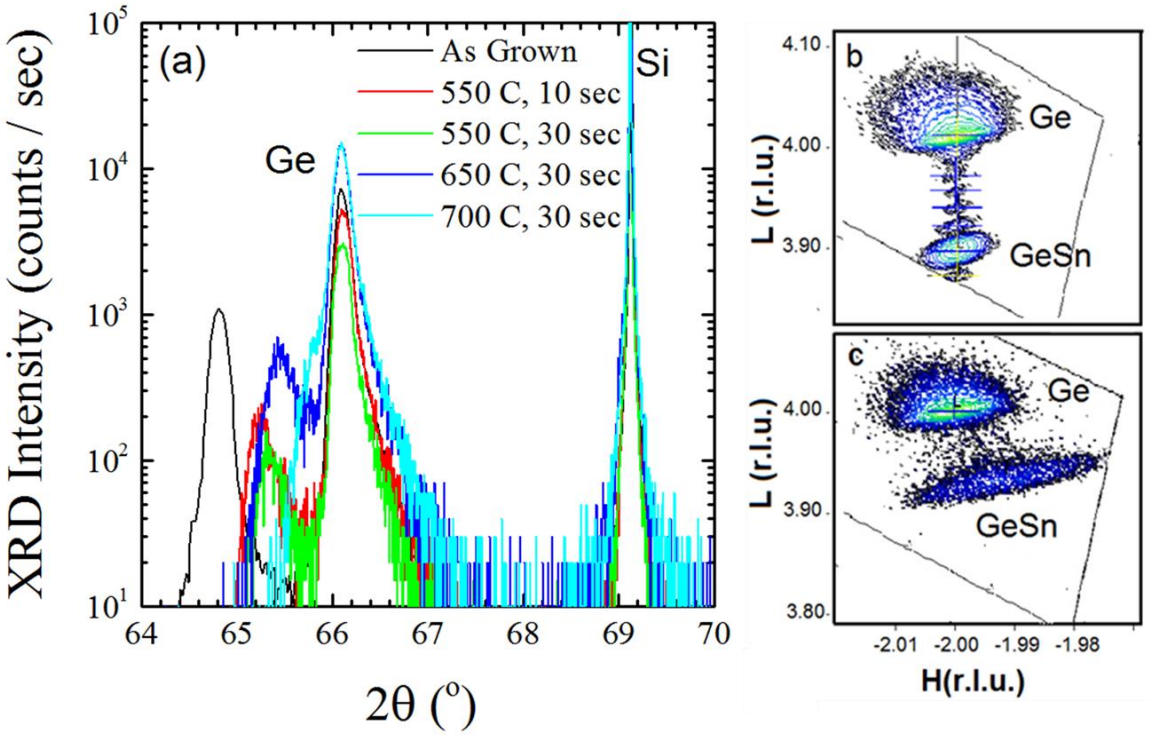


Figure 6: (a) The rocking curve spectra for $Ge_{0.94}Sn_{0.06}$ measure the out-of-plane lattice decreasing for increased annealing temperatures. (b) Reciprocal space map taken of the as grown and (c) after rapid thermal annealing at 550 °C for 10 seconds. Reproduced by permission of The Electrochemical Society [31].

The increased Sn content of sample F resulted in a lower thermal budget before Sn segregation was observed. The 2θ scans of this sample in Figure 7 (a) resulted in an undiscernible $Ge_{0.93}Sn_{0.07}$ peak after a 30 second RTA at 550 °C. The RSM scans for the as-grown in Figure 7 (b) showed that this film lied along the diagonal relaxation line, indicating it was almost fully relaxed. After annealing at 550 °C for 30 seconds the RSM in Figure 7 (c) shows that the film fully relaxed and the Sn content lowered significantly as the two Ge and $Ge_{0.93}Sn_{0.07}$ peaks were almost merged.

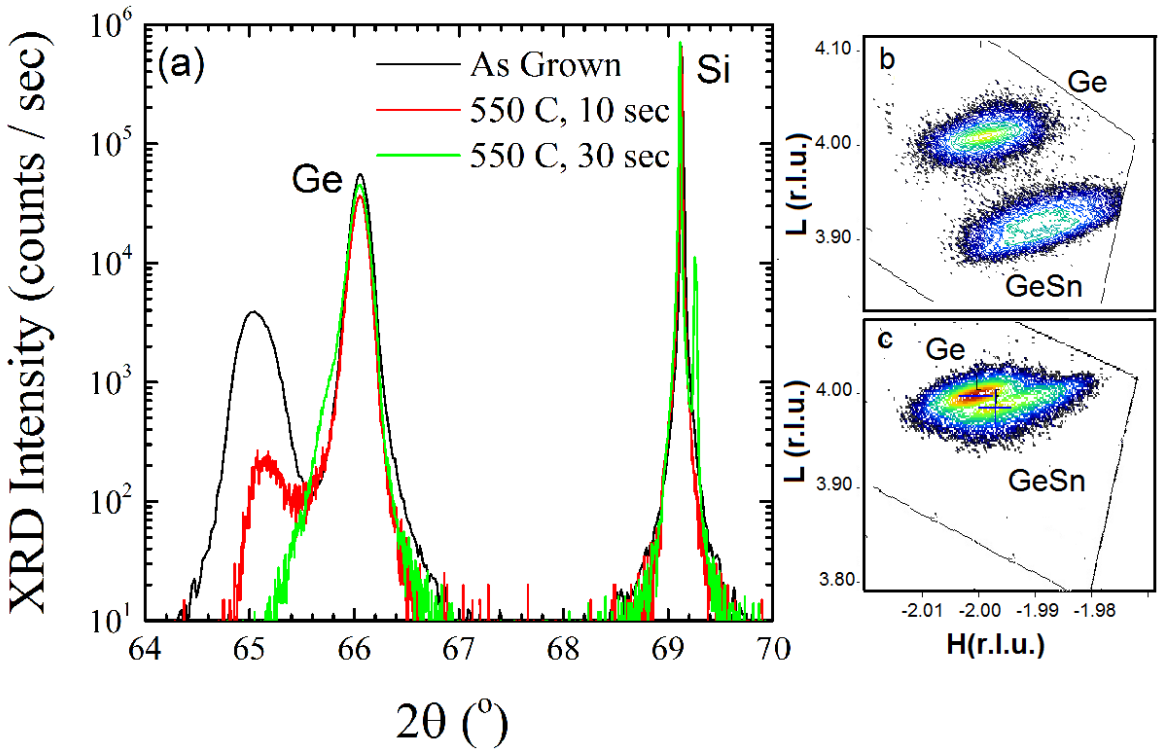


Figure 7: (a) The XRD rocking curves for $Ge_{0.93}Sn_{0.07}$ represent the lattice constant change for 30 seconds at 550 °C and for 10 seconds at 550 °C compared to the as grown sample. Reciprocal space maps of the (b) as grown and (c) sample annealed at 550 °C for 30 seconds show $Ge_{1-x}Sn_x$ film transition from partially relaxed to a reduced Sn mole fraction and relaxed film. Reproduced by permission of The Electrochemical Society [31].

Using Equations 2.1 - 2.4 the in-plane strain of Samples C, E, and F was calculated from the XRD 2θ scans and plotted in Figure 8. Since the 2θ scan measured the out-of-plane lattice

constant, a negative value for in-plane strain could be due to tensile strain or a decrease in the total amount of Sn incorporation. The dashed line at a strain of zero marks the relaxation line. From this plot it was concluded that the increased Sn content samples have a reduced thermal budget compared to lower Sn samples. For each sample processed with RTA above the growth temperature, the effect of high temperature annealing cycles was detrimental to the film quality compared to the as-grown samples.

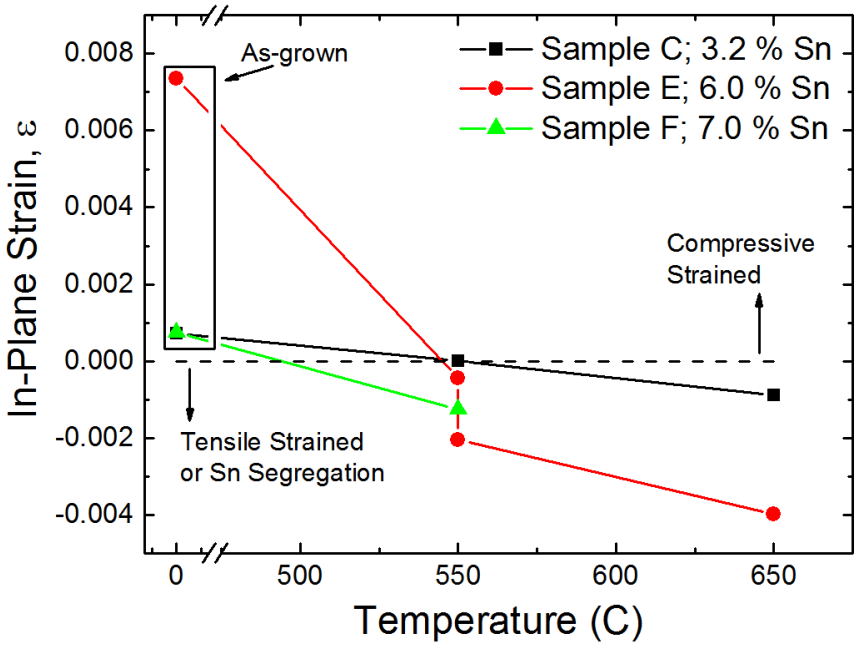


Figure 8: In-plane strain measured for each RTA temperature shows a decreased level of strain and Sn incorporation as temperature increased.

The Raman shift of Samples C, E, and F were measured and the location of the Ge-Ge LO (Ge-LO) phonon peak was extracted and plotted in Figure 9. A relaxed Ge film without Sn has a known Ge-LO Raman shift peak at 300 $cm^{-1}$. A red-shift in this peak occurs when the energy of this bond is decreased either by incorporation of Sn atoms ($\omega_{alloy}$), or by in-plane compressive strain ($\omega_{strain}$). The total Raman shift ($\omega_{total}$) is a linear combination of these two factors,

$$\omega_{total} = \omega_{strain} + \omega_{alloy} . \quad 2.5$$

The alloy disorder dependence was determined by Cheng *et al.* [32] to be, $\omega_{alloy} = -83.11x\ \text{cm}^{-1}$, where x is the Sn mole fraction. That work also extrapolated an estimated $\omega_{strain} = -374.53\epsilon\ \text{cm}^{-1}$, with $\epsilon$ being the in-plane strain.

The expected Raman peak location based on the expectation of constant Sn concentration and the calculated in-plane strain from the XRD 2θ scans was plotted in Figure 9 (stars) as comparison with the measured Raman peak location (squares). The predicted Raman peak location fell within the margin of error for 3.2% Sn sample. However the 6.0 and 7.0% Sn was outside this expected range. The difference for the Raman peak location for the as-grown samples cannot be concluded from this work. The error between the measured and predicted 6.0 and 7.0% Sn gave an indication for the Sn segregation point of the film. Since the expected location of the Raman peak is calculated based on zero loss of Sn from the film, these values are determined directly from the in-plane strain values. However, the higher Sn composition samples showed a blue-shift to higher wavenumbers for the measured values that indicated a reduction in Sn composition. This annealing condition leads to a reversal in the experimental measured trend compared to the expected location. This divergent trend marks the point for Sn segregation. No such point occurs for the 3.2% Sn sample. The Sn segregation, as measured by this method, occurred for the 30 second RTA of the 6.0% Sn and 10 seconds RTA for the 7.0% Sn samples at 550 °C each.

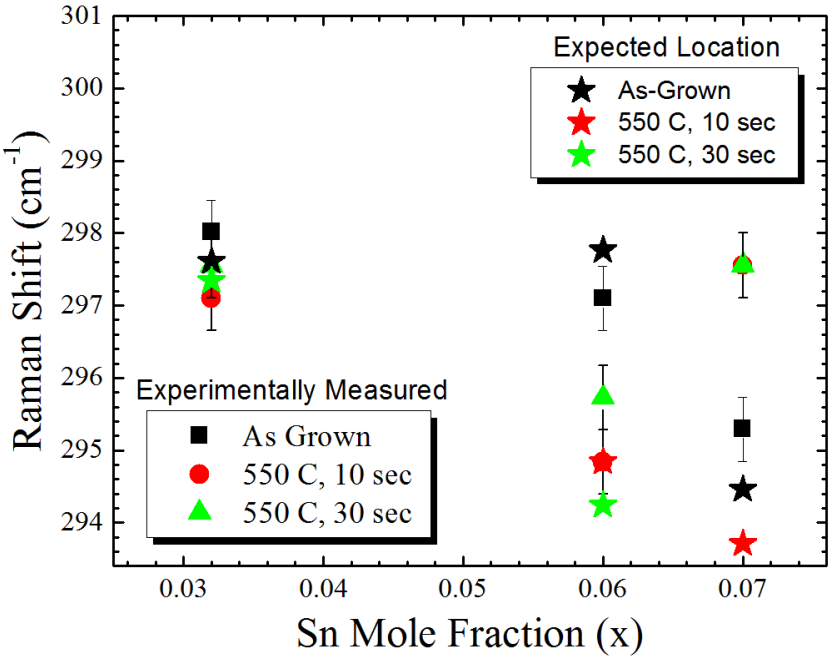


Figure 9: Measured Raman spectra of the Ge-LO peak locations (squares) are plotted for the Sn mole fraction of each sample. Predicted Raman peak location (stars) was determined based on Sn composition and the measured in-plane strain from XRD 2θ scans using Equation 2.5.

### 2.3 Rapid Thermal Annealing at CMOS Compatible Temperatures

Growth of $Ge_{1-x}Sn_x$ films is a CMOS compatible process due to the growth temperature being below 450 °C for all ranges of Sn concentrations. However, as previously shown, the increased levels of Sn led to a reduction in the thermal stability of the $Ge_{1-x}Sn_x$ films. For a material to be readily integrated on a CMOS level, it will be subject to multiple thermal process steps for varying temperature and duration. As such, it has yet to be explored what effect such cycling will have on $Ge_{1-x}Sn_x$ thin films. Since most of these CMOS level processing steps are proprietary and unknown, a design of experiments (DOE) matrix was used to explore the expected upper limit of these heat budgets. The DOE used here assumes short temperature annealing steps below 450 °C are possible for several cycles and for different lengths of time. Annealing was done at 400 or 450 °C on $Ge_{1-x}Sn_x$ samples with 0.026, 0.06, and 0.07 Sn mole fractions. The length of time for annealing was set to 30 or 120 seconds in length. An additional

parameter was added to account for the possibility of a single process going through multiple high temperature processes. This was done by allowing the number of cycles for each anneal to be 1, 3, or 5 total cycles. The full input parameters and measured quantities of this DOE are summarized in Table 2.

Table 2: Design of experiments input and measured parameters. Reproduced by permission of The Electrochemical Society [31].

| Input | | Measured |
|---|---|---|
| Sn Mole Fraction | 0.026, 0.06, 0.07 | Photoluminescence FWHM (nm) |
| Time of each cycle (sec) | 30, 120 | Photoluminescence Peak Location (nm) |
| Temperature (°C) | 400, 450 | Photoluminescence Intensity (μV) |
| Number of Cycles | 1, 3, 5 | |

Following each anneal experiment within the DOE matrix, the photoluminescence was measured at room temperature to quantify changes to the material quality compared to the as-grown samples. Before each PL spectra was collected the optical alignment was verified using a reference Ge sample mounted next to the measured sample. From the measured PL spectra, the full width half max (FWHM), peak location, and PL intensity were extracted for analysis within the DOE matrix. The full DOE matrix and an example predicted plot vs actual plot associated with these results are presented in Appendix I.

The results of this DOE presented in Table 3 were determined using a standard least squares fit with an emphasis on effect leverage. This method produced an analysis of the input variables with respect to individual measured quantities. This provided a probability of the factors having a significant outcome on the result. The level of significance was set to the standard value of 5%. The time per cycle and number of cycles analyzed the effect of individual RTA cycle events compared to the total time parameter in Table 3, which was the combined total time a sample experienced at the elevated temperature. The results in Table 3 indicate that only the Sn mole fraction had a significant effect on the PL FWHM and PL peak location. However,

the PL intensity showed a level of significance below 0.05 for the time per cycle and total time. This implies that the time spent at an elevated temperature and not on the number of cycles was a relevant factor. This result is expected as atomic and defect diffusion within a crystal film has an activation energy dependence [33], related only to the total input energy.

Table 3: Effect of annealing parameters through a DOE analysis using standard least squares

| Parameter | Photoluminescence FWHM (Prob > F) | Photoluminescence Peak Location (Prob > F) | Photoluminescence Intensity (Prob > F) |
|---|---|---|---|
| Temperature (°C) | 0.1306 | 0.8122 | 0.2076 |
| Time per Cycle (sec) | 0.0926 | 0.2548 | 0.0488 |
| Sn Mole Fraction | <.0001 | <.0001 | 0.1217 |
| Number of Cycles | 0.366 | 0.461 | 0.064 |
| Total Time (sec) | 0.2117 | 0.2919 | 0.0447 |

The PL spectra for the sample with 0.06 Sn mole fraction is plotted in Figure 10 (a) and (b) for annealing temperatures at 400 and 450 °C, respectively. The statistical insignificance of the number of cycles allowed these spectra to be plotted for a combined annealing time. The extracted change in peak intensity (μV) and location (nm) of the PL spectra are plotted in Figure 10 (c) and (d), respectively. The change in intensity for both temperatures initially decreased due to annealing, followed by an increase with increased time. This was due to the film first relaxing and forming defects at the interface, thereby reducing the radiative recombination rate. Continued annealing allows for defect diffusion and a reduction in the number of dangling bonds. This hypothesis was supported by the red-shift in the PL peak intensity within Figure 10 (d) for increased time. A red-shift in the $Ge_{0.94}Sn_{0.06}$ peak due to RTA could only be a result of a reduced compressive strain. The blue-shift in the 400 °C anneal for 600 seconds occurred as an onset of Sn segregation of the film.

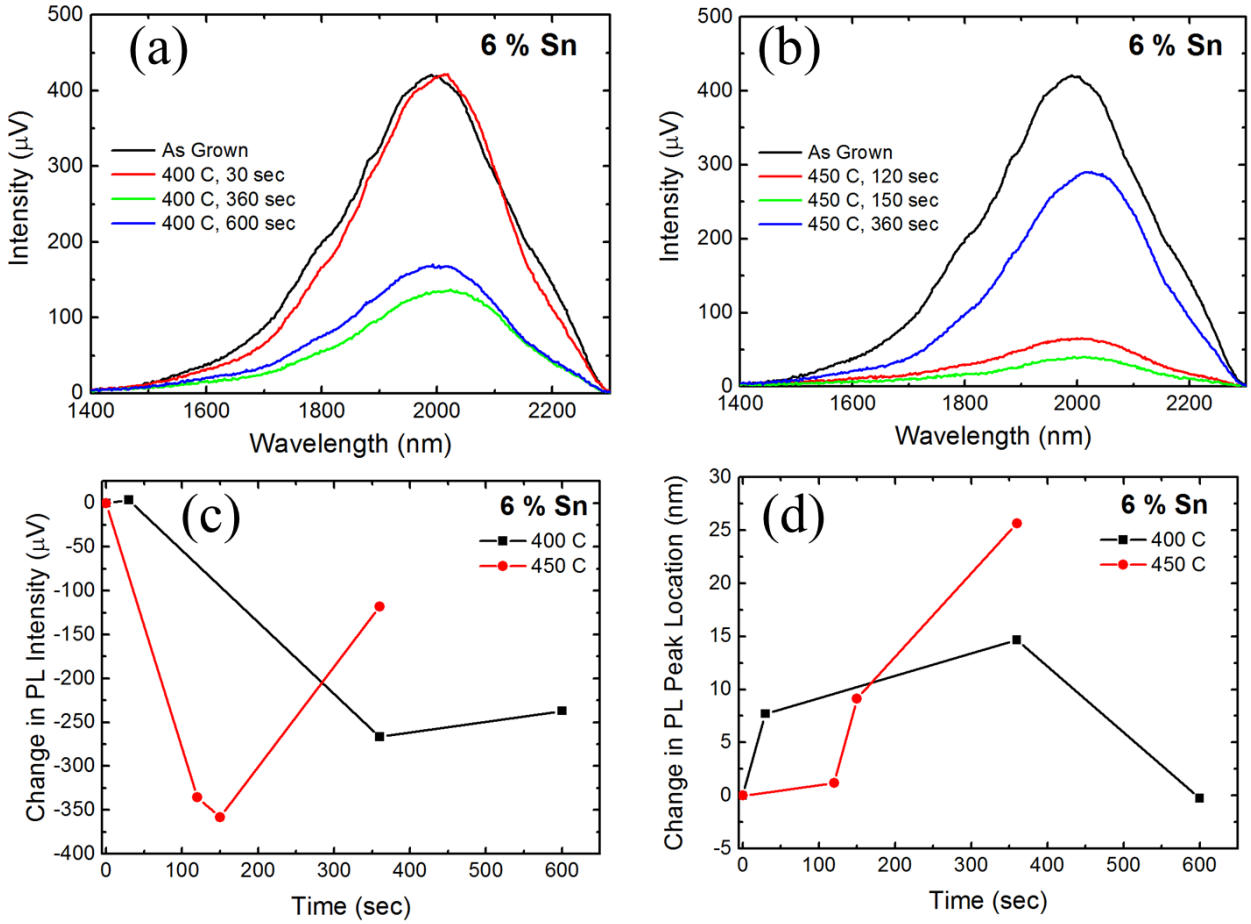


Figure 10: Photoluminescence spectra of a $Ge_{0.94}Sn_{0.06}$ thin film due to RTA at (a) 400 °C and (b) 450 °C. The change in PL intensity (c) and PL peak location (d) from the as-grown are plotted versus total RTA time for each annealing temperature.

## Chapter 3: $Ge_{1-x}Sn_x$ Microdisk Resonator for Si-based Laser

The most sought after goal in Si photonics is a monolithic laser on Si [34-36]. This is because the infrastructure and low cost fabrication of Si CMOS based devices would allow for high density optical communications to surpass wire connections in cost per bit. High density data transmission for long distances (>1 km) has been largely satisfied by optical fiber using III-V lasers lattice matched to InP substrates, and InGaAs or Ge detectors [34, 37, 38]. These technologies traditionally have been deployed as stand-alone products mounted on printed circuit boards. In the past decade these have been moving to hybrid or Si die bonding to reduce the cost and increase overall speed by adding more channels [2]. Short distance links from substation to homes, server-to-server, rack-to-rack, and down to the chip level are connected via wires due to the currently lower cost of these connections compared to optical links when prices are compared for Gbit/dollar. However, these copper based connections have been predicted to have a fundamental limit of 100 Gbit/s/m while single mode and multimode optical links have $10^6$ and $10^3$ Gbit/s/m, respectively [39]. Beyond just higher data rates, optical links have on average 100 times less energy usage per bit than equivalently length wire connections.

Development and research into the components required for photonic integrated circuits (PIC) on Si has already been of interest in the community [3]. Si PIC components such as waveguides [40], add/drop lines [41], modulators [42, 43], multiplexers/de-multiplexers [44, 45], on/off chip coupling [46-48], and photodetectors [4] have all been addressed in varying degrees of interest. The last primary component for this system is an on Si laser source [34]. Wafer bonding [2] and hybrid integration [49] of existing semiconductor laser technology (III-Vs such as InGaAsP) is one approach that has been explored, but the lack of CMOS compatibility and component level integration does not solve the overall cost and scalability problem. Therefore,

using CMOS compatible group IV elements such as Ge, $Ge_{1-x}Sn_x$, or $Si_{1-x-y}Ge_xSn_y$ is a cost effective and scalable active photonic solution.

The indirect bandgap of Si and Ge results in non-radiative recombination of the injected carriers to phonon assisted transitions from the indirect conduction bands. However, the small difference between the Γ and L valleys of 140 meV for Ge is small enough that high n-type doping and moderate biaxial tensile strain in a Ge film would result in Γ valley population [6]. The first Ge on Si laser was demonstrated in 2010 using optical pumping at room temperature [5], and an electrically pumped Ge laser was demonstrated shortly thereafter [50]. Those devices however required the combination of high n-type doping ($>1x10^{19}$ $cm^{-3}$) and tensile strain of 0.25% in order to achieve population inversion within the direct Γ valley. The problems with this approach are a reduction in device performance and large current densities due to the large free carrier absorption loss mechanism and non-radiative recombination at the indirect L valley.

To circumvent these high doping and strain requirements, a $Ge_{1-x}Sn_x$ active region with sufficient amount of Sn could be used. Double heterostructure [51] and multi-quantum well (MQW) [52] designs for $Ge_{1-x}Sn_x/Si_{1-x-y}Ge_xSn_y$ devices were proposed by Sun *et al.* for an electrically pumped laser diode on Si. The large gain volume of this design makes these structures more competitive with longer distance communication links and other discrete photonic applications. The proposed MQW laser diode was theoretically shown to have modal gain at room temperature and a 2.3 μm emission spectrum [52]. The carrier confinement for this device has reduced Auger recombination and a tolerable current density of 3 $kA/cm^2$. Additionally, the long mesa of the device forms a strip waveguide, with light confinement occurring due to the reflective facets as a result of cleaving. This device assumes a type-I band

alignment within the MQW for carrier confinement calculation. To date, MQW $Ge_{1-x}Sn_x$ emitters have not yet been grown to test this design experimentally.

The mirror facet losses and lower Q-factor of a Fabry-Perot cavity require higher quality gain mediums. This work investigates the prospect of a $Ge_{1-x}Sn_x$ laser using a high Q-factor microdisk in parallel with the work done by others seeking to improve the material quality. The combination of a high Q-factor microdisk structure, direct bandgap $Ge_{1-x}Sn_x$ active medium, and high optical pumping could allow demonstration of the first $Ge_{1-x}Sn_x$ on Si laser.

### 3.1 Microdisk Background

Microdisk laser resonators are disks with a size on order with the free space wavelength and are optically isolated by materials of lower refractive index along the edges of the disk [53]. The comparable wavelength size, curvature, and refractive index confinement between the semiconductor and dielectric (usually air) causes whisper gallery modes (WGM) to propagate along the inside circumference of the disk. At the location of these whisper gallery modes are regions of high optical intensity where stimulated emission can occur. Microdisks have high optical confinement (high Q-factor) but their mode volume is small compared to edge emitting Fabry-Perot semiconductor lasers. This smaller size limits their emission range and application. The integration of an electrically pumped InP microdisk laser on Si-on-insulator (SOI) was previously explored by others [54]. The electrical injected carriers were confined within the active layer of the disk and the stimulated emission within the WGM was evanescently coupled to the buried SOI waveguide (WG) beneath the disk.

Germanium microdisks previously demonstrated the selective fabrication capabilities of Ge on Si, and a Q factor of 700 for 1575 nm was measured [55]. That work however, did not show lasing and the cause is believed to be the result of free carrier absorption within the Ge

active layer. Additionally, tensile strained 4 μm Ge microdisks grown on GaAs with silicon nitride as a stressor were investigated as a means to enhance the Γ population for possible stimulus emission [56]. The unstrained Ge microdisk had a PL emission with Fabry-Perot modes embedded in the PL spectra for bulk Ge, while the nitride stressed disk had a PL that was red-shifted by 445 nm and only one resonant mode around 1990 nm was observed. The indirect bandgap limits the Γ transition probability within the Ge active region, thus population inversion was not achieved.

$Ge_{1-x}Sn_x$ alloys provide the engineering freedom to create a direct bandgap active region without the need for tensile strain or high doping. A $Ge_{1-x}Sn_x$ microdisk structure grown on GaAs substrate with InGaAs buffer showed absorption spectrum characteristic of resonating modes within the disk [57]. That work did not produce any luminescence out of the disk nor was $Ge_{1-x}Sn_x$ on Si explored in that work.

$Ge_{1-x}Sn_x$ growth on Ge buffered Si has two separate confinement situations that could be fabricated. This could be achieved by either selectively etching the Ge buffer leaving an air/$Ge_{1-x}Sn_x$/air interface or the Si substrate or the Si could be selectively undercut leaving an air/$Ge_{1-x}Sn_x$/Ge/air interface. The chemical reactivity of $Ge_{1-x}Sn_x$ close to that of Ge does not allow for a good selectivity between these two using wet chemical etching methods [32]. The highest reported selectivity in that work was 8 for $Ge_{0.923}Sn_{0.077}$ on Ge using a $H_2O_2$:$NH_4OH$:$H_2O$ solution. The method developed in this work uses the high etch selectivity of potassium hydroxide between Ge and Si [58] and a high lateral Si etch rate. This allowed for $Ge_{1-x}Sn_x$/Ge microdisk on a Si pedestal to be fabricated.

### 3.2 Modeling of Microdisk Resonator using Finite Difference Time Domain (FDTD)

The simulation of the resonant WGM in the microdisks was performed using the finite difference time domain (FDTD) method with Rsoft software. The microdisk structure was designed in the CAD environment using available n and k data on $Ge_{1-x}Sn_x$ [7], Ge, and Si as shown in Figure 11. The boundary conditions used in all the simulations were perfectly matched layers (PML). This boundary condition sets the electric and magnetic conductivities such that the impendence of the waves at the boundary are equal, thus giving no reflected wave and all the energy is absorbed at the boundary.

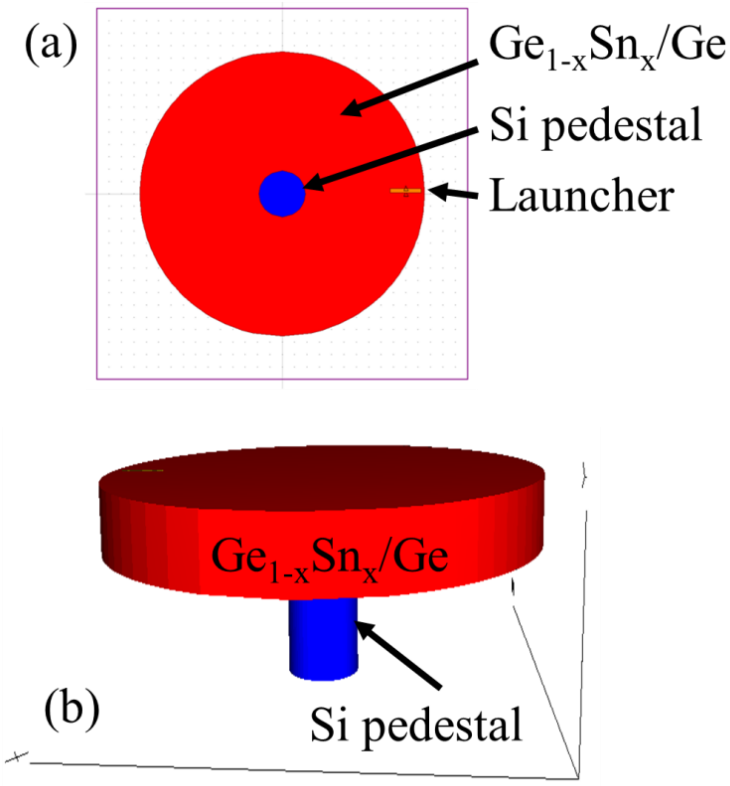


Figure 11: Experimental setup and boundary conditions for (a) 2D and (b) and 3D FDTD simulation within the CAD environment. The boundary of the simulation (purple outline) in (a) was set as a perfectly matched layer condition.

The $Ge_{1-x}Sn_x$ sample chosen for the initial microdisk fabrication and testing is ASM7007, which is a fully pseudomorphic $Ge_{0.94}Sn_{0.06}$ film on Ge buffered Si. This sample had the highest

photoluminescence (PL) peak amongst available $Ge_{1-x}Sn_x$ samples at the time and with moderate Sn incorporation, had potential for direct Γ valley population under high injection conditions. The temperature-dependent PL in Figure 10 shows a peak wavelength overlap between 1900 and 2000 nm for 300 K.

Using this PL emission wavelength range, the FDTD modeling parameters were chosen to optimize a structure with a high Q-factor. The initial free space wavelength used was determined based on the available WGM [53],

$$m\frac{\lambda_m}{n_g} = 2\pi R \tag{3.1}$$

where m is the azimuthal number, λ is the free space wavelength for a given m, $n_g$ is the material refractive index, and R is the disk radius. The azimuthal number, m, is the number of waves that fit within the circumference of the microdisk for a given wavelength. Higher order radial modes, n, are also possible within microdisks. This modal number, n, starts at 1 for the outer most circumference and are numbered inward. The more accurate determination of the WGM profile and emission wavelength is done by finding zero order of the corresponding Bessel function. Bessel function of the first kind are used for the n = 1 case, second kind for n = 2, and so on. A plot of the Bessel function for the radial mode, m, of interest vs mode distance, x, allows for one to extract the corresponding zero for that m value. This zero order Bessel function value is applied in the modified Equation 3.1,

$$BesselZero_n(m,x)\frac{\lambda_m}{n_{eff}} = 2\pi R \tag{3.2}$$

where $n_{eff}$ is the effective refractive index. The $BesselZero_1(50,x)$ in Figure 12 occurs at 57.11, and $BesselZero_2(50,x)$ is at 53.51, yielding a blue-shift in the initial mode prediction compared to when m = 50 is used.

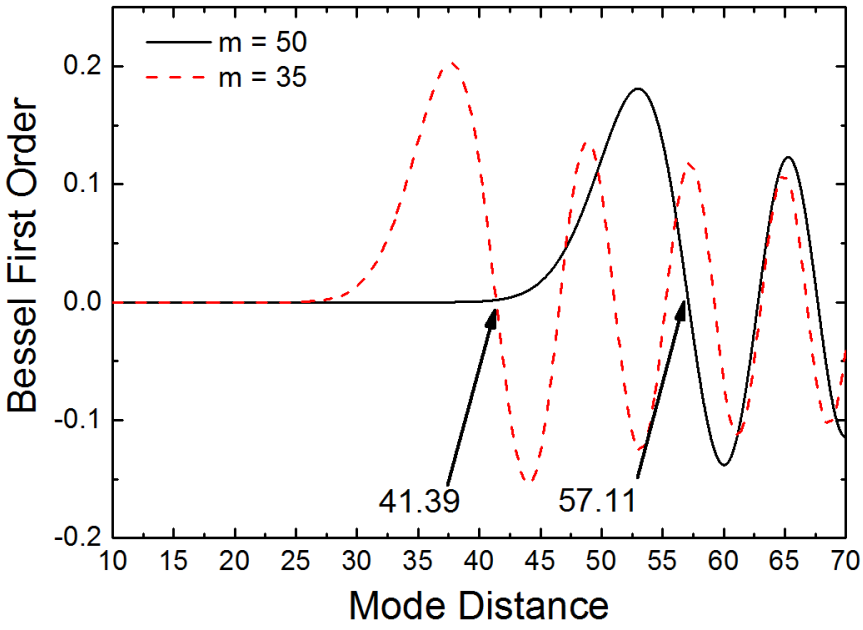


Figure 12: First order Bessel function plotted for mode distance used to determine the Bessel Zero for n = 1 and the corresponding m = 35, 50.

For stimulus emission, only the dominant mode is of interest, thus each subsequent calculation takes only the n = 1 case. For thin microdisks the transverse electric (TE) mode will dominate and only one vertical mode is allowed. The existence of only one vertical mode allows for these FDTD simulations to be performed in 2D, excluding the z-dimension, thus saving time and computing resources. Further simulation time and resources can be saved using symmetric boundary conditions by dividing the simulation space into four quadrants [59]. The real and imaginary refractive index, n = 4.281 and k = 0, was used for the $Ge_{1-x}Sn_x$ layer based on data from Ref [60] at $\lambda = 2$ μm.

A Gaussian impulse was used to stimulate the simulation medium which subsequently determined the optical field profile and available modes. For each size microdisk, Equation 3.1 was used to determine the initial free space wavelength. Upon completion, one of the mode solutions within the PL emission range of this 6.0% Sn sample was used to calculate the final

optical mode profile within the disk for its given size. The modeled microdisks diameters were chosen for decreasing size of 25, 10, and 4 μm to match those of the fabrication conditions. Although it is expected from Equation 3.1 that the free spectral range (FSR) will be larger for smaller disks, the larger disks are considered here due to the reduced fabrication requirements. By examination of Equation 3.1, the FSR (Δλ) can be estimated based on the disk radius,

$$\Delta\lambda = 2\pi R n_g \left( \frac{1}{m_s} - \frac{1}{m_f} \right) \tag{3.3}$$

where $m_s$ and $m_f$ represent the starting and final mode of interest, respectively. The mode profiles for disks with 25, 10, and 4 μm diameter in Figure 13 (a), (c), and (e), respectively shows the computed mode profile for a 2D $Ge_{0.94}Sn_{0.06}$ disk. The decreasing size of the microdisk has a corresponding decrease in the FSR as noted in the available resonant modes in Figure 13 (b), (d), and (f). The electric field profile and resonant wavelength modes within the 10 and 4 μm diameter $Ge_{1-x}Sn_x$ microdisk show the two axially resonant modes (n = 1 and n =2) due to the higher confinement. These secondary modes also showed up in Figure 13 (f). The larger intensity peaks correspond to radial mode n = 1 while the lower intensity peaks correspond to the inner radial mode n = 2. Each pair of peaks are those of increasing axial modes (m).

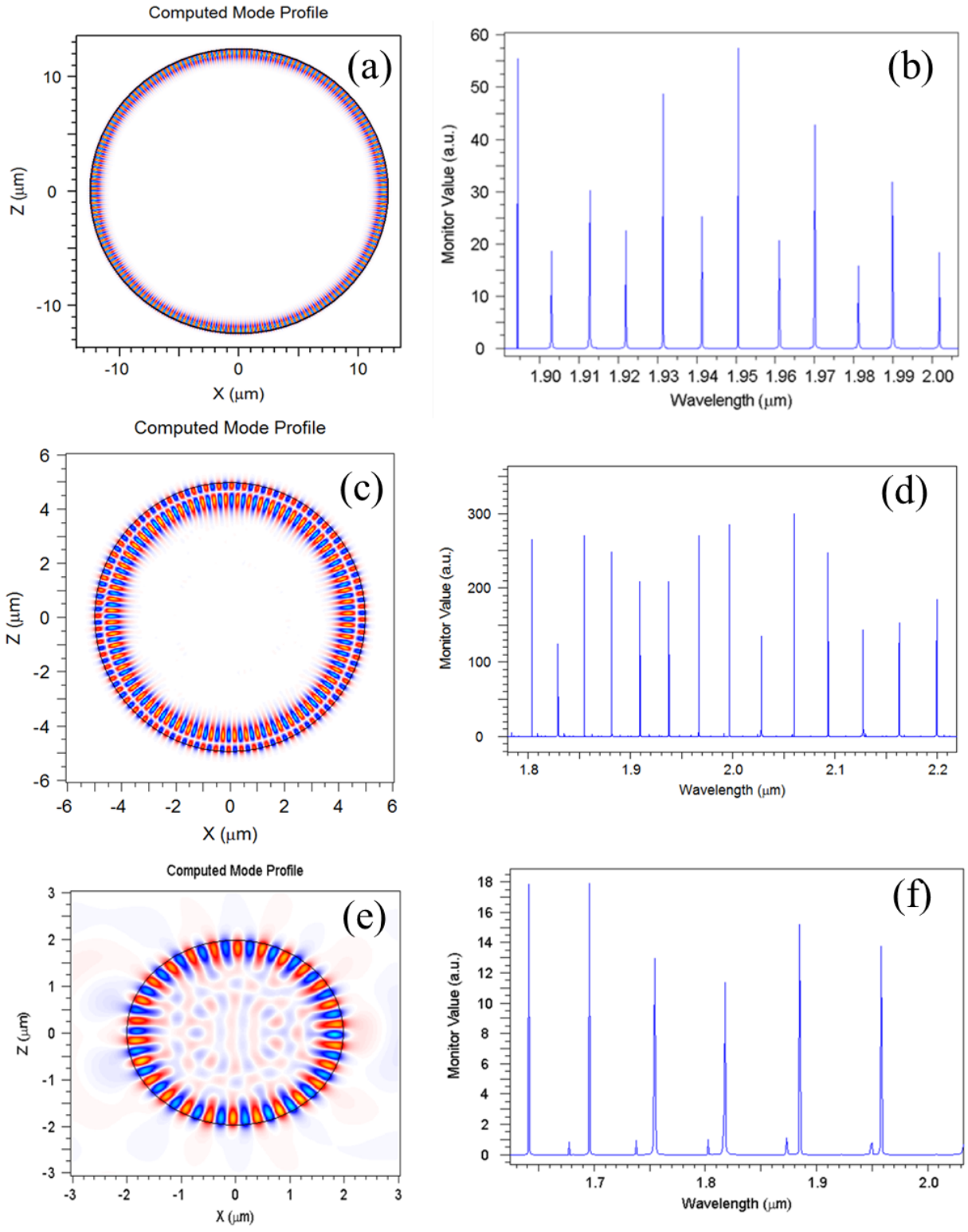


Figure 13: (a), (c), (e) Computed mode profile for a $Ge_{0.94}Sn_{0.06}$ microdisk with 25, 10, and 4 μm diameters, respectively. (b), (d), (f) Resonant optical modes within the microdisk show decreasing FSR with decreasing disk diameter.

Based on the emission PL of the 6% Sn, the resonant wavelength modes that could have stimulus emission are around 1.9 μm. By examination of the 4 μm diameter disk modes, the two dominant wavelengths with n = 1 near this range are 1.818 and 1.885 μm as shown Figure 14 (a). The optical mode confinement within a resonant cavity is quantified with the ratio of the energy stored within the cavity to the power lost per cycle [61]. This is approximated with the relationship for the center wavelength (λ) and the full width at half max of that mode (Δλ),

$$Q \approx \frac{\lambda}{\Delta\lambda} \ . \tag{3.4}$$

The expanded view of a n = 1 mode in the 4 μm diameter $Ge_{1-x}Sn_x$ microdisk in Figure 14 (b) allows for the Q-factors for these two modes to be determined. The calculated Q-factors for this simulation are summarized in Table 4. These calculations used FWHM of 0.0005 and 0.001 μm for the 1.818 and 1.885 μm modes, respectively. These Q-factors are expected to be an underestimation because the simulation resolution limits the width of the FWHM. The spontaneous emission rate can be approximated using the Purcell factor,

$$F_p = \frac{3Q}{4\pi^2 V_{eff}} \left( \frac{\lambda}{n} \right)^3 \tag{3.5}$$

where $V_{eff}$ is the gain volume. For the Q-factors determined for the 4 μm microdisk, assuming an optimal gain overlap of the $Ge_{0.94}Sn_{0.06}$ active region, and letting $V_{eff}$ equal the active region volume (3.52 $\mu m^3$), then the Purcell factor for these resonators was calculated. The Purcell factors for the two corresponding Q-factors previously discussed are listed in Table 4. The key factors in Equation 3.5 that can be affected by fabrication and film growth are the Q-factor, since theoretical Q calculated here does not account for surface roughness, film growth defects, and absorption loss.

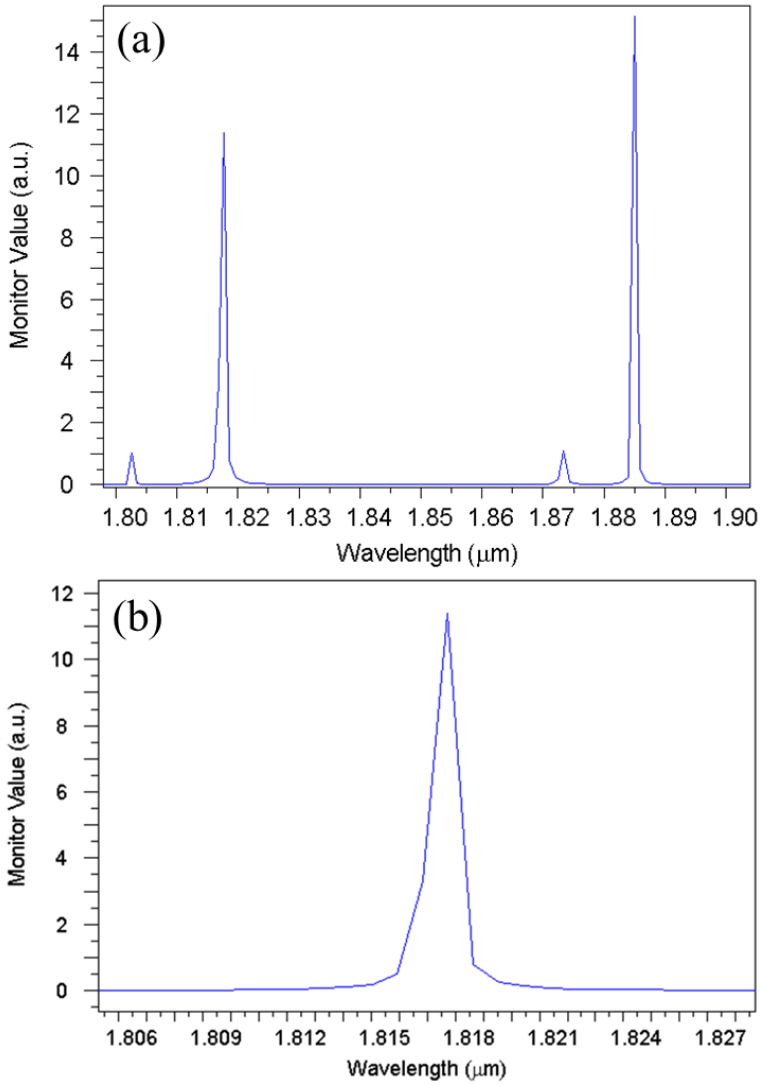


Figure 14: (a) Enlarged view of n = 1 axial mode for a 4 μm diameter $Ge_{0.94}Sn_{0.06}$ microdisk within the measured PL emission range. (b) The enlarged view allows for Q-factor of this resonator to be determined.

Table 4: Calculated Q and Purcell factor for a 4 μm microdisk with a $Ge_{0.94}Sn_{0.06}$ active layer

| Resonant Wavelength (μm) | Q-factor | Purcell Factor |
|---|---|---|
| 1.818 | 2363 | 3.91 |
| 1.882 | 1885 | 3.13 |

The Q-factor in a material is the combination of the material absorbance, scattering loss, and intrinsic impedance of the TE or TM mode of interest,

$$Q^{-1} = Q_{abs}^{-1} + Q_{scatt}^{-1} + Q_{intr}^{-1}. \qquad 3.6$$

The intrinsic impendence is the optical interference of the standing wave. Absorbance loss is due to the band-to-band, free-carrier, and Auger losses within the material. Scattering loss occurs at the edge of the disk due to the roughness of the mesa etching. The loss due to scattering becomes dominated by curvature loss for small disk diameters smaller than ~2 μm and is dominated by edge roughness for diameters larger than this [62]. For this reason the dominant focus of the fabrication work was to establish a stable $Ge_{1-x}Sn_x$/Ge mesa etch recipe with reduced surface roughness, and a selective undercut recipe that does not chemically react with the $Ge_{1-x}Sn_x$ film surface.

### 3.3 $Ge_{1-x}Sn_x$ Microdisk Fabrication on Si

The $Ge_{1-x}Sn_x$ microdisk fabrication process flow is outlined into four main steps in Figure 15. (1) Photoresist was spin coated onto the sample using an appropriate thickness and resist based on resolution and etch time. The photoresist AZ4110 was used with a nominal thickness of 1.8 μm which allowed microdisks to be resolved down to a diameter of 5 μm. This thickness is also sufficiently thick to withstand any wet chemical or 30 minutes of dry etching. (2) The disk pattern was then transferred to the photoresist using standard UV lithography and a chromium/glass mask. (3) Mesa etching of the $Ge_{1-x}Sn_x$/Ge layers was conducted to expose the underlying Si substrate. (4) Selective undercut etching using potassium hydroxide (KOH) etched the Si anisotropically to produce the desired undercut etch profile.

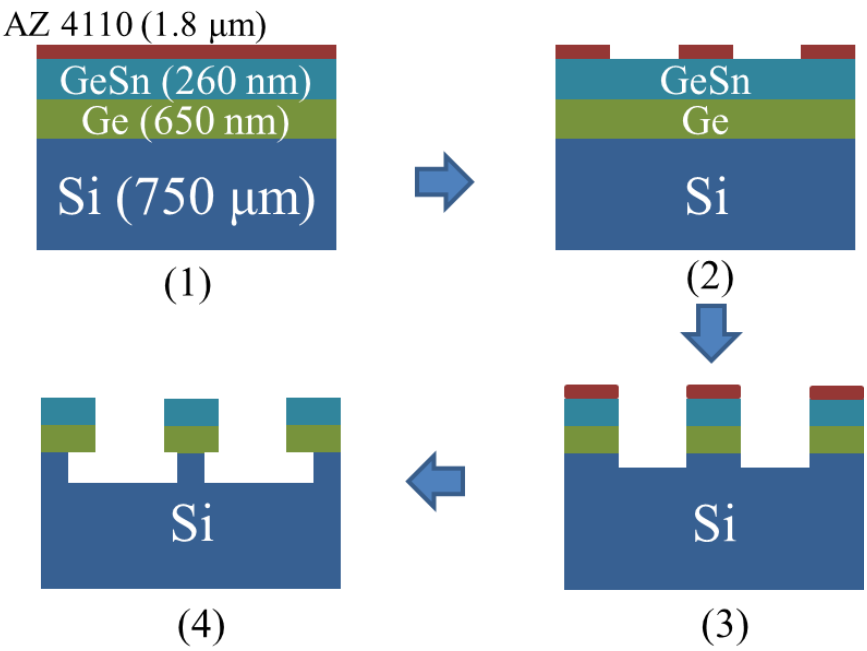


Figure 15: Process flow for fabricating $Ge_{1-x}Sn_x$ microdisk on Si had four central steps: (1) Spin coat with photoresist, (2) pattern photoresist with optical photolithography, (3) reactive ion etching of the mesas, and (4) undercut etch the Si substrate using potassium hydroxide.

### 3.3.1 Dry Mesa Etching

The available dry etching tool was a parallel plate reactive ion etcher (RIE) with two fluorine based gases available, $CF_4$ and $SF_6$. Prior smooth etching profiles of Ge by $CF_4$ [63], and a slower more controlled etch rate of $CF_4$ compared with $SF_6$ [64, 65] led to the choice of developing an RIE recipe based only on $CF_4$. The experimental parameters outlined in Table 5 list the etch parameters explored in optimizing a smooth $Ge_{1-x}Sn_x$ sidewall dry etch. The pressure and etch time were held constant for each experiment at 250 mtorr and 5 minutes, respectively. The SEM images of the resulting etch for each sample listed in Table 5 is shown in Figure 16. From the SEM images a trend was observed that decreasing $CF_4$ flow rate lead to a smoother sidewall profile. This was clear in samples A, B, and C which only varied by $CF_4$ flow rate. The decreased $CF_4$ flow rate lowers the chemically active $F^-$ radicals in the plasma,

reducing the lateral attack of the $Ge_{1-x}Sn_x$ film. Little to no difference was discernable between samples C and D, which differ by the amount of applied RF power. This small change in relative RF power did not improve the film sidewall smoothness. For all these samples, the 5 minute etch time resulted in complete etch through the $Ge_{1-x}Sn_x$/Ge film to the Si substrate.

Table 5: Experimental parameters for RIE of $Ge_{1-x}Sn_x$ thin films etched at 250 mTorr

| Sample | $CF_4$ Flow Rate (sccm) | Power (W) |
|---|---|---|
| A | 100 | 200 |
| B | 80 | 200 |
| C | 60 | 200 |
| D | 60 | 175 |

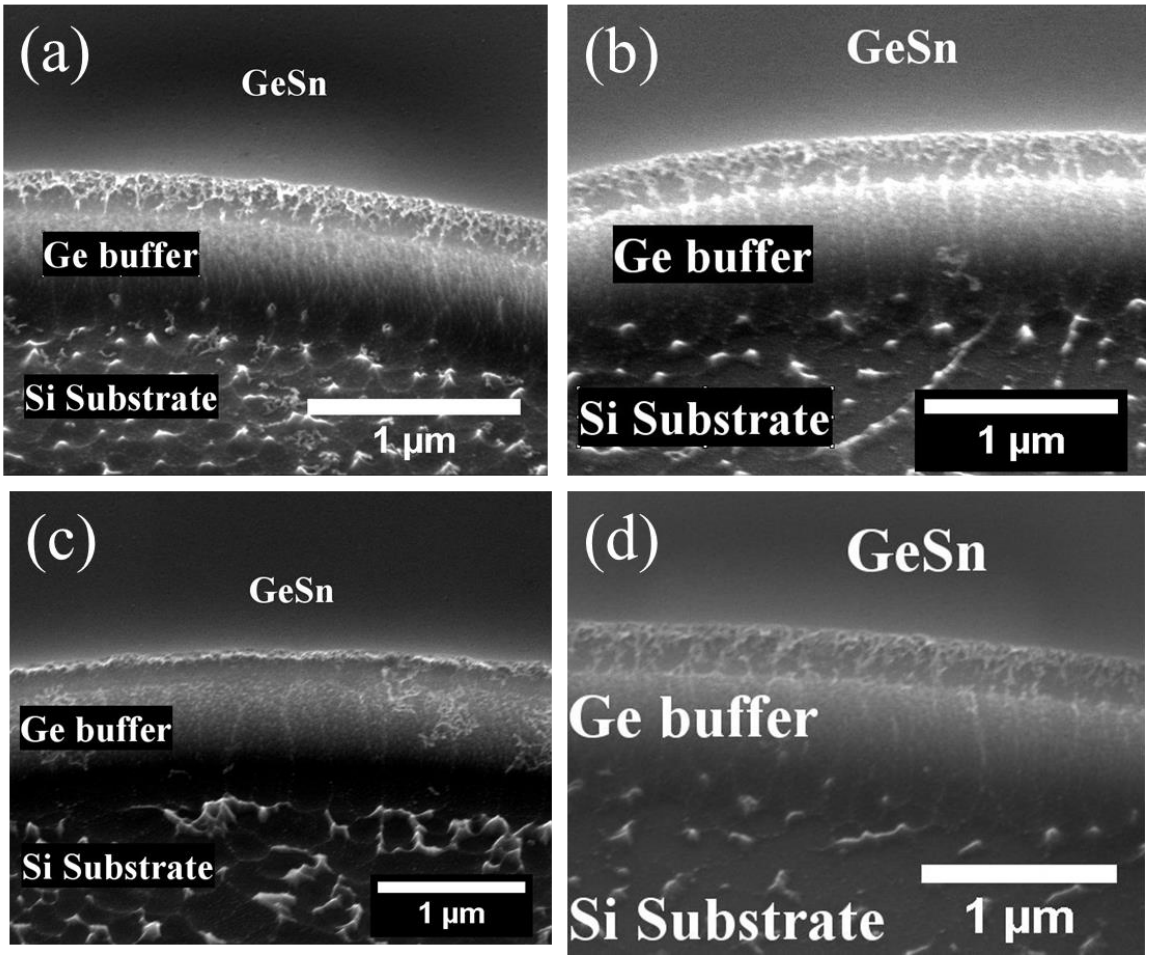


Figure 16: Sidewall etch profile of $Ge_{0.974}Sn_{0.026}$/Ge films on Ge within a $CF_4$ dry etch. All etches were performed at 250 mtorr. Etch parameters for each image is listed in Table 5.

To increase the anisotropic etch profile, i.e., increase the vertical etch rate compared to the horizontal attack of the film, Ar gas was added in equal parts to the $CF_4$ gas. Additionally, the pressure was reduced to allow higher ion bombardment and lower the chemical based etching. A reduction in applied RF power was implemented to reduce surface damage as a result of the increased ion milling based etching. The resulting etch parameters, 30 sccm $CF_4$, 30 sccm Ar, 100 watts power, and a pressure of 200 mTorr left a satisfactory smooth sidewall as shown in the SEM image of Figure 17. These parameters are referred to as the GeSn_ET recipe for the remainder of this dissertation. Figure 17 (a) shows the top view image of a 100 μm disk fabricated with a $Ge_{0.974}Sn_{0.026}$ film. Figure 17 (b) and (c) show the sidewall profile due to this dry etch recipe. Figure 17 (d-f) are energy dispersive x-ray (EDX) spectroscopy mapping of the resulting etch. This mapping profile confirms that etching of the films down to the Si substrate has occurred by measuring the x-ray signature of the elements exposed to the electron beam.

The effective etch rate of the combined $Ge_{1-x}Sn_x$/Ge layers was observed to vary from 40 to 70 nm/min. No distinguishable trend for this variation was linked to Sn composition or sample pre-treatments of the bulk $Ge_{1-x}Sn_x$/Ge films. This variation is likely due to equipment cleanliness and locally varying electric fields within the RIE that caused differing regions of high and low ion bombardment. The samples were deliberately over etched in the RIE process to ensure the Si substrate was exposed. The etch rate of this recipe on Si was observed to be 40±10 nm/min.

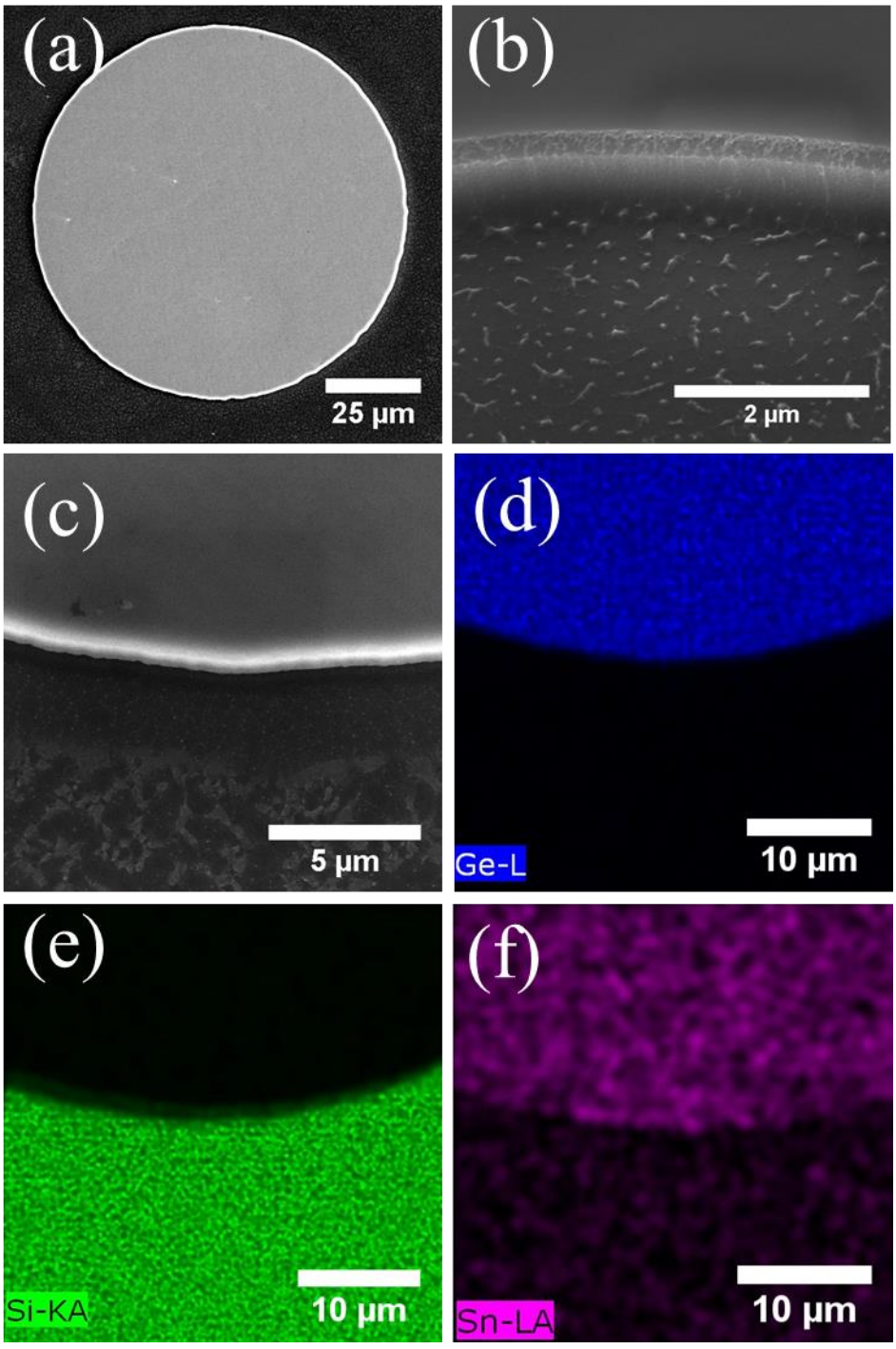


Figure 17: SEM images after $Ge_{0.974}Sn_{0.026}$ sample was etched with an optimized dry etching recipe. (a) Top view of a 100 µm $Ge_{0.974}Sn_{0.026}$ mesa etched down to the Si substrate. (b) Sidewall profile shows moderate undercut of the Ge buffer layer. (c) SEM image of the $Ge_{0.974}Sn_{0.026}$ mesa analyzed with EDX for elemental study in (d)-(f) for Ge, Si, and Sn presence, respectively.

### 3.3.2 Microdisk Undercut Etching with KOH

Potassium hydroxide (KOH) was used to selectively etch the Si substrate without appreciably etching the $Ge_{1-x}Sn_x$/Ge layers. The etch rate for this KOH solution on Si has dependence on the crystal orientation with a general etch rate for each orientation as, (100) > (110) > (111) [66]. This trend of decreasing etch rate based on crystal orientation is due to decreasing density of the $SP^3$ hybridized bonds that are chemically available on each of the crystal planes. However, the etch rate for the Si (100), Si (110), and $SiO_2$ plotted at 60 °C in Figure 18 show that the Si (110) direction has a higher rate than (100). While the (110) does have fewer dangling surface bonds than (100), there is an increased number of back-bonded Si atoms for the (110) surface giving an overall lower bond energy. Additionally, channeling of water molecules is expected to be slightly higher in (110) than for (100) adding to the higher reactivity.

In this work a 30% KOH to water solution was used giving an expected etch selectivity of 1.5 for Si (110) to (100). This solution was prepared by mixing KOH solid pellets by weight with deionized water by weight in a glass beaker. Heat was applied by hot plate and the temperature monitored by a glass thermometer. The chemical reaction process for KOH etching on Si proceeds as follows,

$$Si + 2(OH)^- + 2H_2O \rightarrow SiO_2(OH)_2^{--} + 2H_2 \qquad 3.7$$

where the final resulting silicate is water soluble and removed from the surface. The etch rate can be reduced and an etch stop engineered by use of p-type doping in Si. The excess hole concentration at the surface captures the free electrons liberated by the multistep reaction, thereby slowing or stopping the reaction. In contrast, the Ge native oxide is already water soluble and can be etched in a solution with an increased oxygen content, such as hydrogen peroxide.

Within a caustic solution, such as KOH, the Ge surface bonds react with the hydroxyl groups to form a non-water soluble compound,

$$Ge + 2(OH)^- + H_2O \rightarrow GeO_3H_2 + 2H_2 \qquad 3.8$$

This explains the reduced reactivity for Ge in KOH.

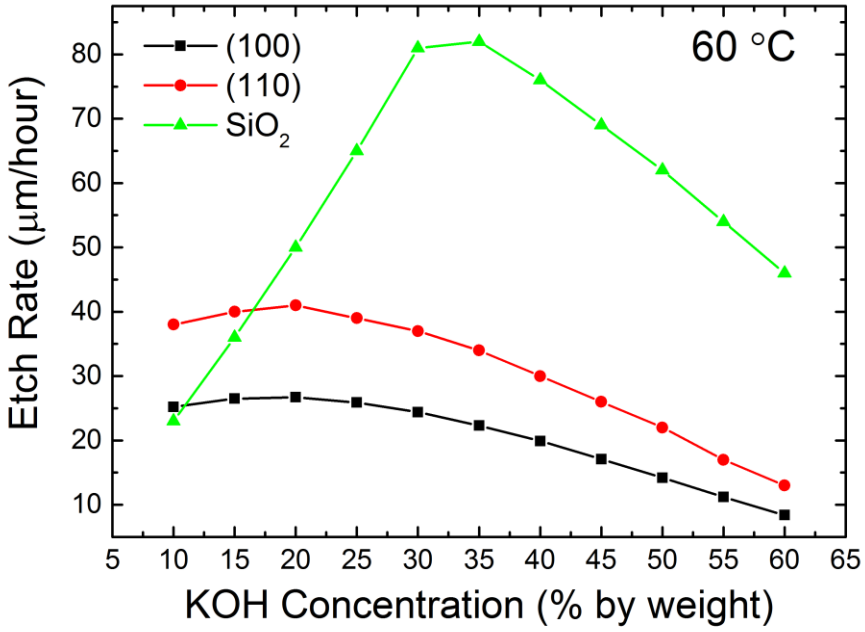


Figure 18: Variation of KOH etch rate based on concentration for (100) Si, (110) Si, and thermally grown $SiO_2$ for a 60 °C solution.

The typical application for KOH etching on bulk Si is to create pyramid structures terminated at the (111) faces to enhance light confinement. For convex patterns or openings with fixed sidewalls, KOH will etch along the (110) direction until two intersecting (111) planes are reached. To investigate this, a simulation using the ACES open source program was done to simulate a 30% KOH etch on a (100) Si substrate with (110) side orientation. A 100 μm diameter circular mask was used with both a positive and negative polarities. Figure 19 (a) and (b) show the results of this simulation after 15 and 45 minutes, respectively. After 15 minutes the (111) planes are observable and by 45 minutes the etch has terminated in the (110) direction. The simulation in Figure 19 (c) for a positive circular mask shows that a 15 minute KOH begins to

undercut the mask pattern. A total of 45 minutes etch simulation in Figure 19(d) shows the desired undercut Si pedestal, with an etch unterminated by any specific crystal plane. The mask in the Figure 19 simulations is marked by the grey line. The terminated etch for an opening in a $Ge_{1-x}Sn_x$ film with underlying Si substrate was experimentally tested and the SEM image in Figure 20 shows the beginning of this (111) termination.

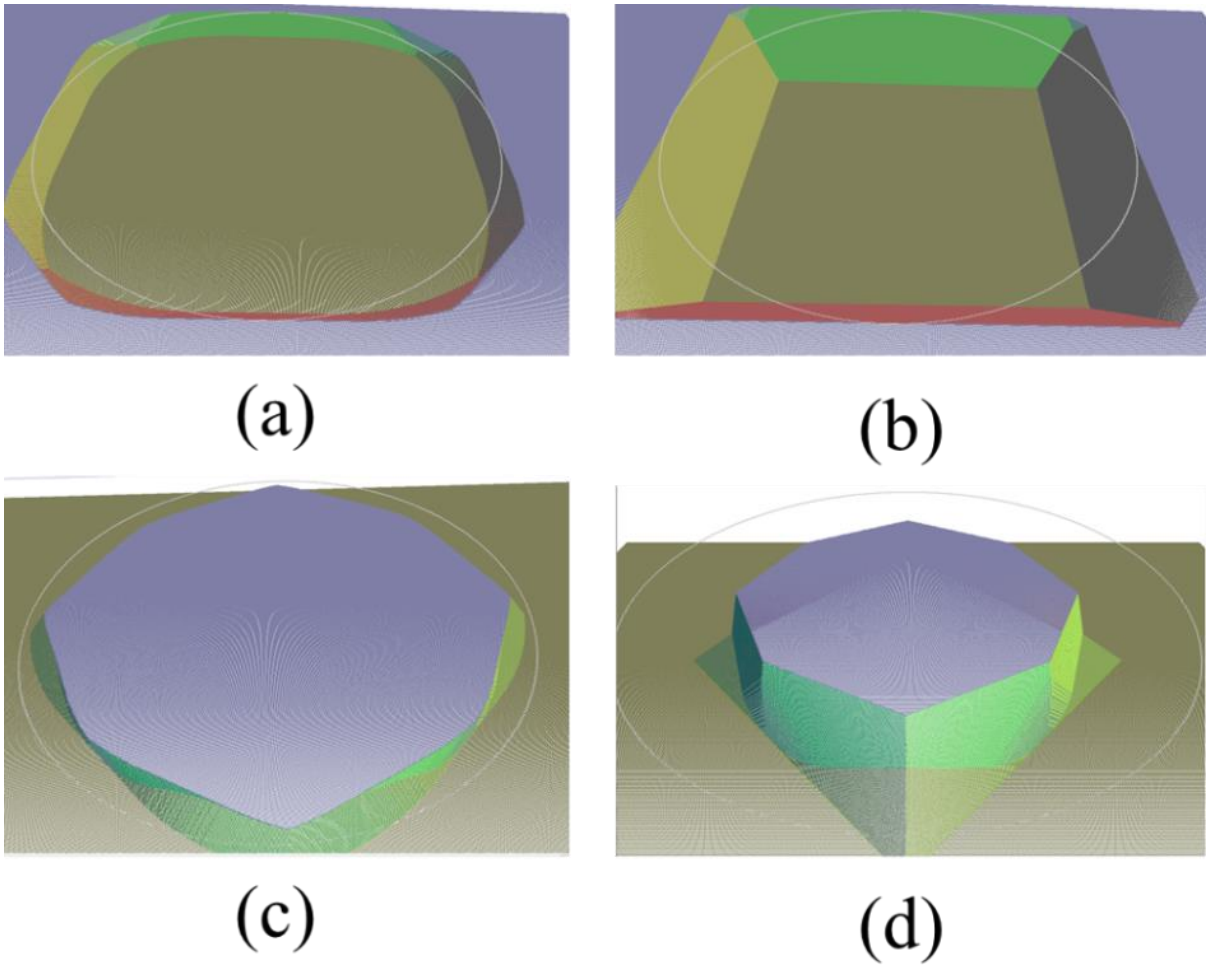


Figure 19: Simulation of 30% KOH solution on Silicon with a 100 μm diameter mask (grey outline). A negative mask was used in (a) and (b) for 15 and 45 minutes, respectively to simulate the (111) termination planes for a convex pattern. A positive mask was used in (c) and (d) for 15 and 45 minute, respectively that showed the nonterminating etch under the mask to form a Si pedestal.

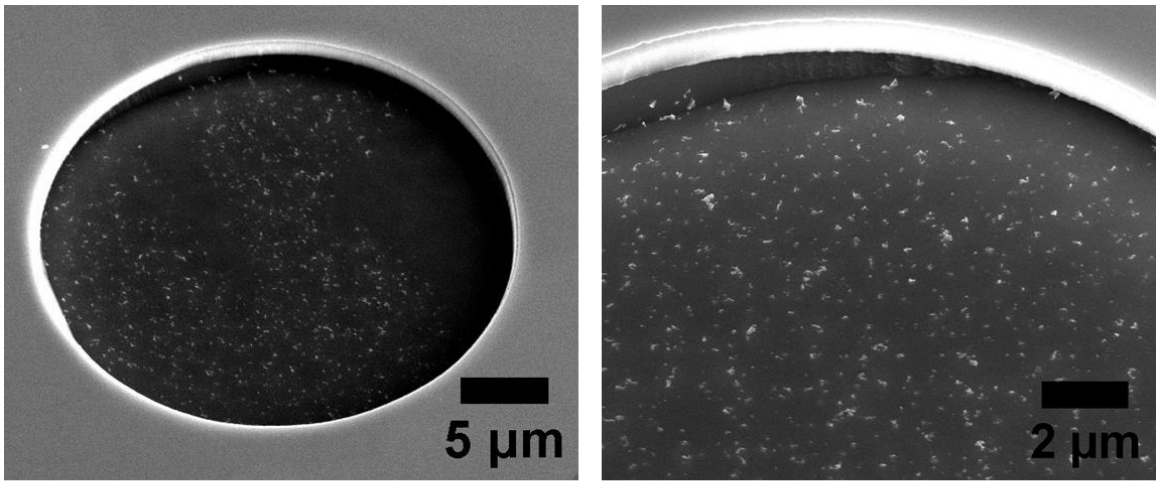


Figure 20: (a) SEM image of a $Ge_{1-x}Sn_x$/Ge thin film whereby a convex pattern was created and subsequently etched with KOH. (b) Enlarged view shows the undercut etch terminating along the (111) planes.

For concave patterns, such as disks, an undercut of the pattern will result without any self-termination on a particular crystal orientation. This allowed a Si pedestal to form under the $Ge_{1-x}Sn_x$/Ge disks with pedestal widths dependent only on the etch rate and time used. A 30% KOH solution in water heated at 60 °C was used to etch $Ge_{0.974}Sn_{0.026}$/Ge sample after the RIE mesa etching exposed the underlying Si substrate. After 12 minutes of etching the beginning of this undercut was observed in Figure 21. The diameter of these disks was measured at 12 µm. The difference between this and the 15 µm mask diameter was due to limitations of the photoresist and the chemical lateral etching within the RIE process. To compare this lateral effect on smaller microdisks, two samples were patterned and etched for different times using the same RIE recipe. Figure 22 shows a 7% Sn sample that was etched for (a) 20 minutes compared to a 2.6% Sn sample that was etched using the standard GeSn_ET recipe for (b) 10 minutes. Each sample in Figure 22 was then etched for 12 minutes in the same 30% KOH solution at 60 °C. The depressions around the disks that have a higher vertical etch compared to the bulk Si between disks [Figure 21] was etched faster initially due to the lateral Ge removal around these

features within the RIE. This prepared Si surface can be seen in Figure 17 (c) that was taken after the RIE process. Increasing the etch time produced a uniform bulk etch profile on the Si substrate. This increased Si surface preparation also explains the increased KOH undercut etch between the samples in Figure 22, which vary only be RIE etch time.

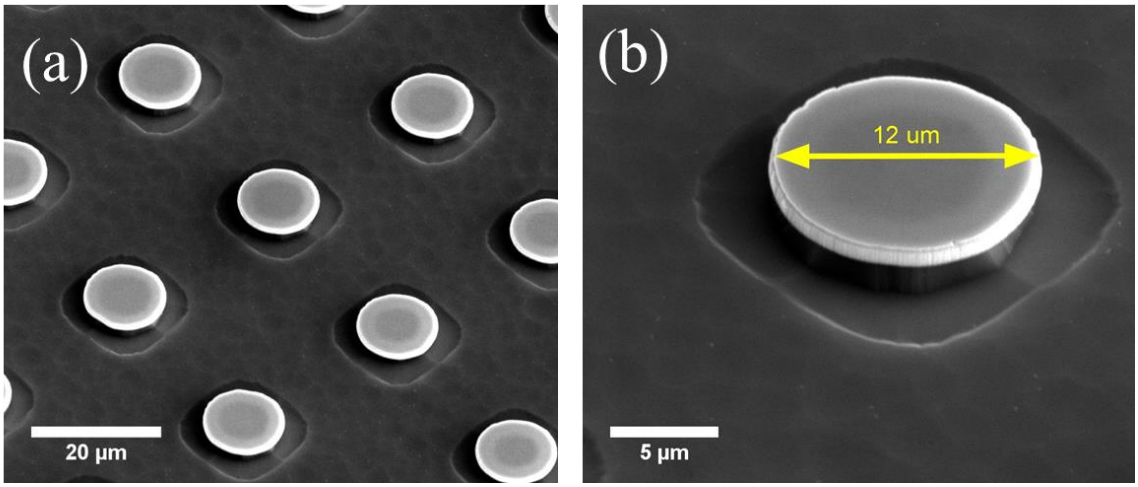


Figure 21: (a) $Ge_{0.974}Sn_{0.026}$/Ge microdisk etched for 12 minutes within a 30% KOH solution at 60 °C. (b) The expanded view of one disk shows the initial undercut due to the KOH etch.

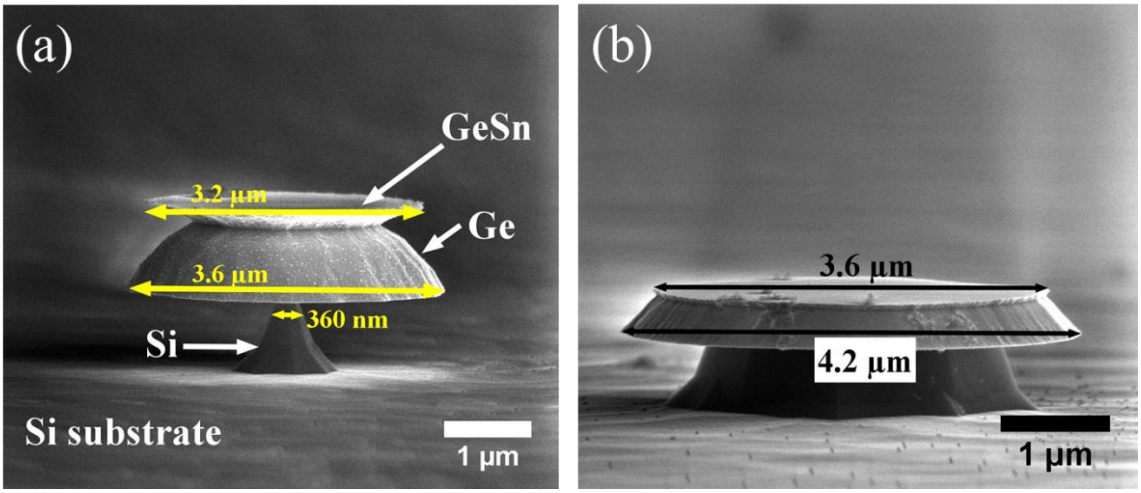


Figure 22: SEM image of $Ge_{1-x}Sn_x$/Ge microdisk etched for (a) 20 minutes and (b) 10 minutes shows the lateral etch for increased etch time within the RIE using the GeSn_ET recipe. Both samples were subsequently undercut etched within 30% KOH solution.

An increased KOH etch time to 20 minutes and 15 seconds resulted in an ideal undercut of the 12 µm diameter microdisks on a Si pedestal. The SEM images in Figure 23 show the

zoomed out image of the microdisk array (a) and increases in magnification through image (d). A 25 μm diameter microdisk was etched in KOH at 60 °C for 30 minutes. The SEM image of this sample in Figure 24 show an ideal undercut. The $Ge_{1-x}Sn_x$/Ge sidewall profile compared to the sidewall due to the RIE have smoothed, indicating a slight etch of the $Ge_{1-x}Sn_x$/Ge films within KOH solution. It is known that $GeO_2$ is soluble in water, and though the KOH solution does not have an oxidation agent to readily form $GeO_2$, the solubility of $GeO_2$ increases for increasing pH.

The fabrication procedures and results described here were found to be directly applicable to other samples with different Sn compositions. No known variation was found due to the amount Sn within a film.

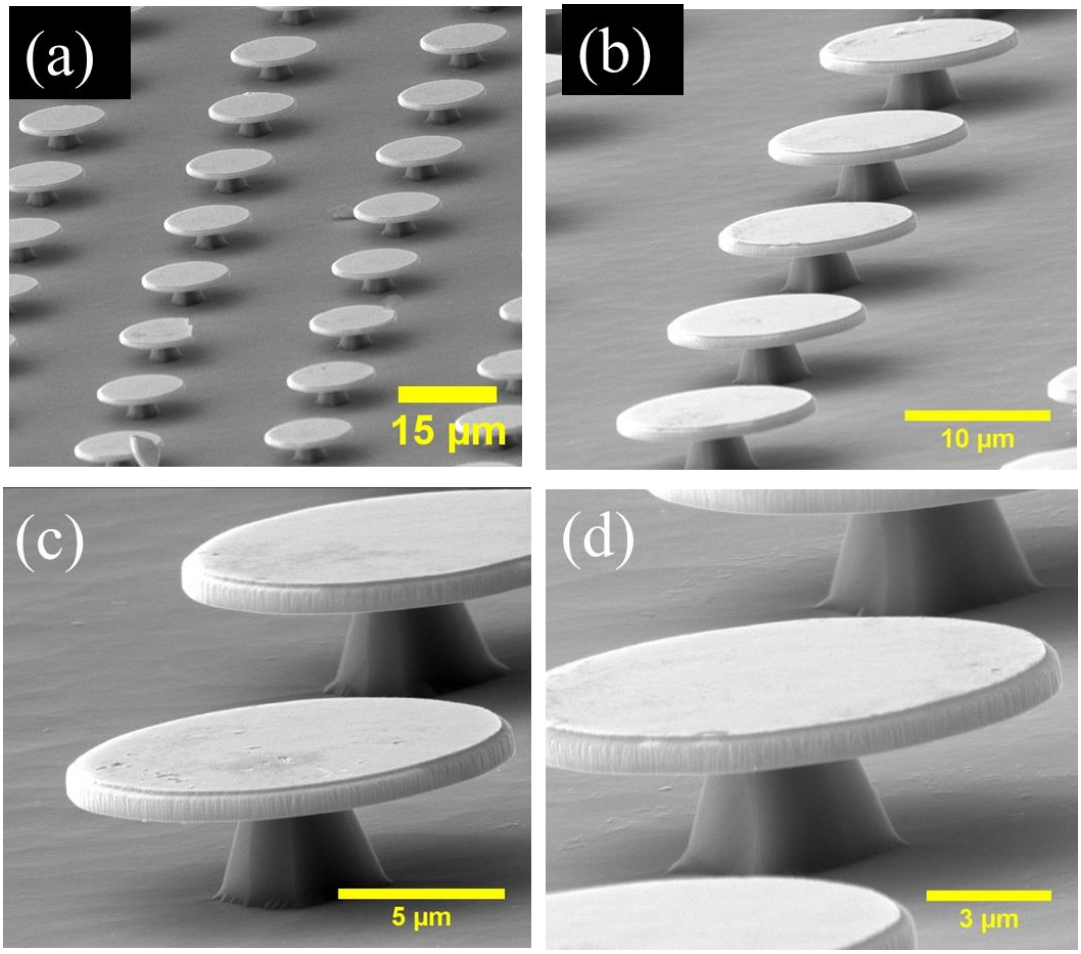


Figure 23: $Ge_{0.974}Sn_{0.026}$/Ge microdisks with nominal diameter of 12 to 15 μm. Images (a)-(d) are enlargements of the same sample. Sample was etched in 30% KOH at 60 °C for 20 minutes, 15 seconds.

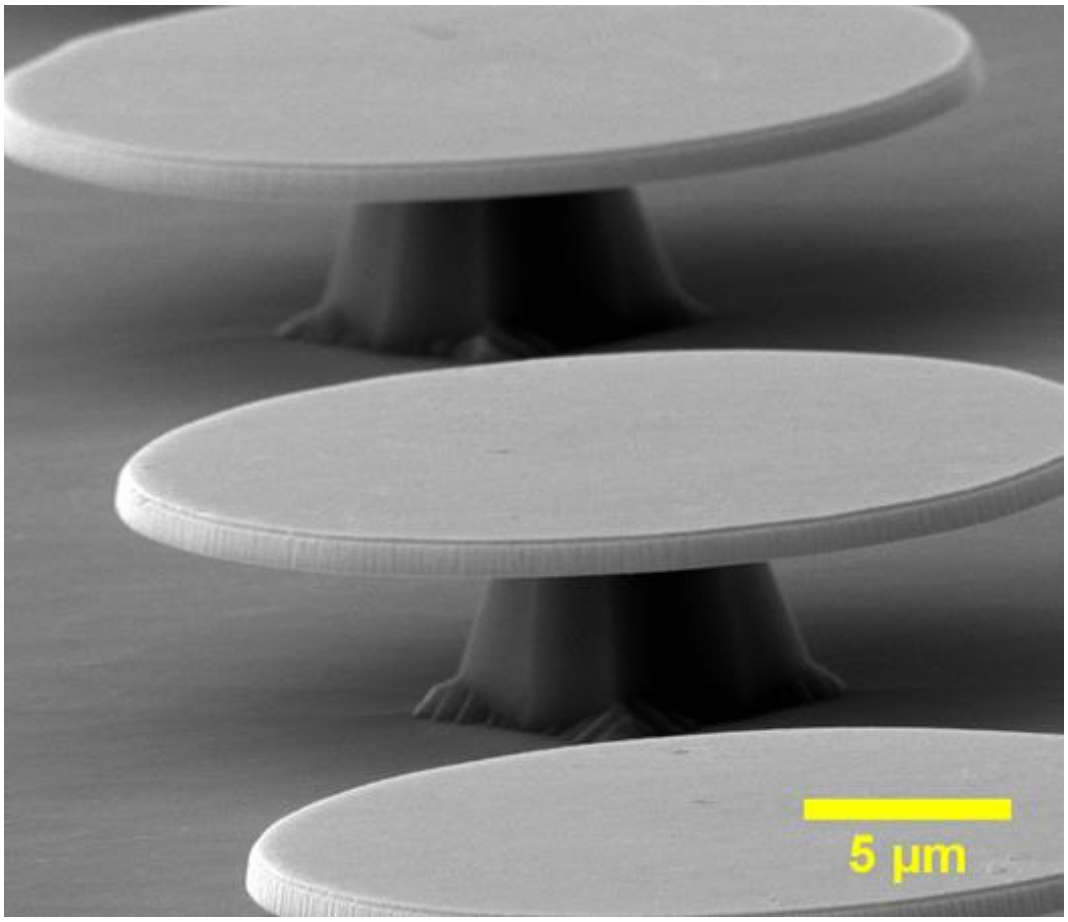


Figure 24: $Ge_{0.974}Sn_{0.026}$/Ge microdisk with a nominal diameter of 25 µm. Sample was etched in 30% KOH at 60 °C for 30 minutes.

### 3.4 Micro-Photoluminescence of $Ge_{1-x}Sn_x$ Microdisks

Microdisks were fabricated with the $Ge_{0.94}Sn_{0.06}$/Ge thin film sample on Ge using the fabrication process described in Section 3.3. The samples were mounted in a short working distance cryostat and cooled using liquid helium with a closed loop heater and Si sensor to maintain temperature control. A femtosecond pulse Ti:sapphire laser with a 700 nm wavelength was used as the excitation source to achieve high pumping density on the samples. A reflective objective lens in combination with a CCD camera system was used to align the pump laser and light collection optics on one microdisk. The pumping laser beam was then focused onto one microdisk with an on-axis configuration. This microPL setup collected the PL emission light also

at normal incidence. A long pass filter was used to remove the pump laser light from the collection path and the final spectrum was directed into a grating spectrometer and liquid nitrogen cooled extended InGaAs detector. The microPL was collected for both the as-grown $Ge_{0.94}Sn_{0.06}$/Ge thin film sample and a fabricated 12 μm diameter microdisk. A power dependent microPL measurement of the sample was conducted to allow filling of all the conduction band states and confirm that direct bandgap states were populated.

The emission spectra in Figure 25 show the power dependent PL spectra at 10 K (a) for the as-grown sample and (b) for the 12 μm diameter microdisk sample. The microPL emission spectra for the as-grown sample was a smooth, Gaussian peak as expected for band-to-band radiative recombination. The emission peak from the microdisk sample had a reduced intensity, possibly due to localized heating, and has periodic peaks and valleys in the PL spectra. These peaks were noticeable above 80 mW pumping power, and dominant at high pumping power.

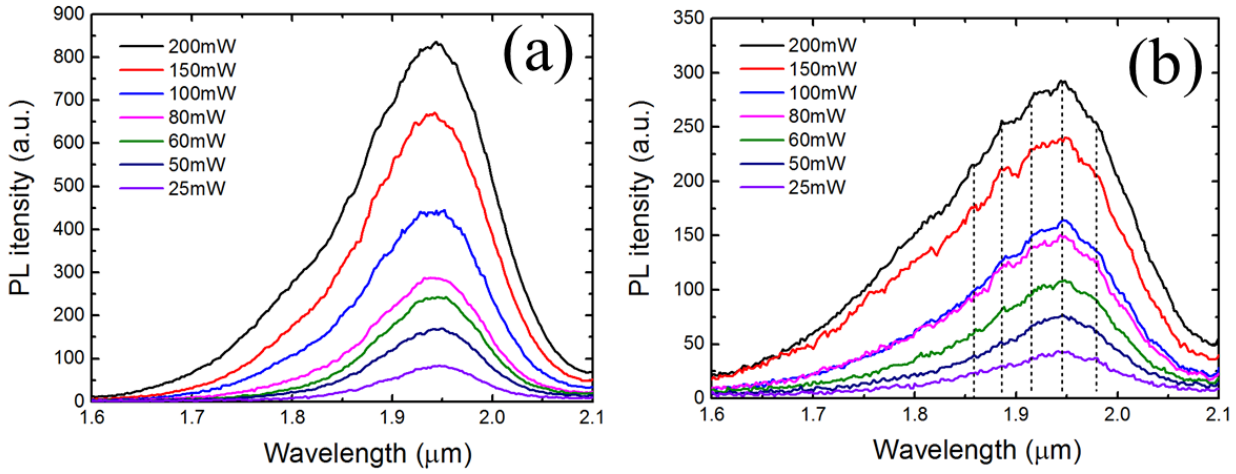


Figure 25: Power dependent photoluminescence at 10 K for the $Ge_{0.94}Sn_{0.06}$ (a) bulk and (b) 12 μm diameter microdisk. The dotted lines in (b) mark the resonant peaks in the PL due to the WGM resonance.

The separate peak and valley spacing within the PL of the microdisk sample were attributed to mode resonance of a WGM within the microdisk. The location of resonance within

the spectrum and expected mode is listed in Table 6. Equation 3.3 was used to calculate these expected modes using the microdisk diameter and refractive index. The 0.4 error listed in the expected mode was due to the accuracy of the wavelength identification within the PL spectrum. This error of ±5 nm corresponded to an error in the mode number of ±0.4. Internal interference of the propagating wave due to a rough sidewall may be causing the spacing of three between measured resonant modes. The wavelength spacing between these resonant wavelengths in Table 6 corresponded to decreasing mode number for increasing wavelength as expected.

Table 6: Resonant modes from microPL measurement of 12 μm diameter microdisk

| Count | Wavelength (μm) (±5 nm) | Expected WGM (±0.4) |
|---|---|---|
| 1 | 1.857 | 174 |
| 2 | 1.886 | 171 |
| 3 | 1.915 | 169 |
| 4 | 1.945 | 166 |
| 5 | 1.977 | 163 |

Microdisks with diameters smaller than 12 μm were also fabricated, but the microPL measurement showed no IR emission from the $Ge_{1-x}Sn_x$ films. There are three possible reasons for this: (1) the microPL setup focus and alignment is not sufficient to accurately resolve these small microdisks within the laser spot. (2) As mentioned above, the smaller microdisks have increased light emission loss due to the larger curvature angle. This implies the fabrication conditions need to be better controlled to fabricate microdisks with a more uniform circular shape. (3) Emission is occurring for these smaller disks, but the light was emitted tangentially from the microdisk, and thus not collected by the normal incidence microPL collection optics.

## Chapter 4: CMOS Compatible Photodetectors for Infrared Detection

The Ge photodetector has been progressing over the past decades from basic photoconductors and metal-semiconductor-metal (MSM) structures to p-i-n diodes, quantum wells (QW), and avalanche photodiodes (APD). This motivation has come from the increased material quality of epitaxial Ge on Si as a lower cost solution to III-V based detectors. Although Ge is an indirect bandgap material, the direct bandgap at 0.8 eV could be used for optical communication at 1.55 μm. Waveguide (WG) Ge photodetectors have an efficiency that is expected to reach as high as 90% due to higher waveguide coupling and longitudinal light absorption. The device structures, deposition methods, and fabrication steps previously developed for the Ge on Si industry can be transferred and modified for $Ge_{1-x}Sn_x$ photodetectors on Si. A summary of recent Ge, $Ge_{1-x}Sn_x$, and $Si_{1-x-y}Ge_xSn_y$ photodetectors grown on Si is listed in Table 7. This summary includes device architecture, responsivity, dark current ($I_{Dark}$), and the 3 dB frequency cut-off for each device at room temperature.

The summary in Table 7 highlights the primary motivation of group IV photonics, which is for low cost, on and off-chip optical communication. However, the potential of this material system and its CMOS transferability can be extended to low cost and high density focal plane arrays (FPA) as well. To meet this application need the fabrication and testing standards of the photodetectors must be modified. The key figure of merit for comparing detectors in low light environments is the specific detectivity ($D^*$). This value is a combination of the responsivity, detector active area, and noise level within the device. This advanced level of characterization, based on signal noise ratio, has yet to be explored for $Ge_{1-x}Sn_x$ on Si devices.

Table 7: Summary of Ge, $Ge_{1-x}Sn_x$, and $Si_{1-x-y}Ge_ySn_x$ photodetectors at room temperature

| Year | Structure | Responsivity $\lambda = 1.55$ μm @-1 V bias (A/W) | Responsivity $\lambda > 1.55$ μm @-1 V bias (A/W) | $I_{Dark}$ (mA) | 3 dB Electrical Bandwidth (GHz), (Bias) | Sn% Si% | Ref. |
|---|---|---|---|---|---|---|---|
| 2007 | MSM-WG | 1 | - | 0.13 | 25, -6V | - | [67] |
| 2007 | PIN-WG | 1.08 | - | 0.001 | 7.5, -3V | - | [68] |
| 2007 | PIN-WG | 1.16 -2 V bias | 0.41 @ 1.61 μm | $2x10^{-4}$ | 31, -2V | - | [69] |
| 2009 | PIN | 0.47 | - | $4x10^{-5}$ | 33, -3V | - | [70] |
| 2009 | APD | 0.6 -10 V bias | - | 0.01 | 11.5 | - | [71] |
| 2010 | APD | 0.15 | - | - | 34, 1.1V | - | [72] |
| 2011 | APD | 5.6 -22 V bias | - | $\sim10^{-4}$ | - | - | [73] |
| 2011 | PIN | 0.23 | 0.12 @1.64 μm | 0.1 | - | 3% Sn | [74] |
| 2011 | PIN | 0.113 | 0.09 @1.6 μm | 1 A/cm$^2$ | - | 2% Sn | [75] |
| 2012 | PIN | - | - | 1mA/cm$^2$ | - | 2% Sn, 7% Si | [76] |
| 2012 | PIN | 0.2 | 0.171 @1.6 μm | $10^4$ A/cm$^2$ | - | 4% Sn | [13] |
| 2012 | QW | 1 -5 V bias | 0.1 @ 2.2 μm | - | - | 9% Sn | [77] |
| 2013 | PIN | 0.2 | 0.165 @1.6 μm | - | - | 4% Sn | [14] |

## 4.1 Photodetector Applications in the Short-Wave Infrared

### 4.1.1 Short-Wave Infrared Detection

Spectral operation in the SWIR band of the electromagnetic spectrum is ideal in the high atmospheric transmission windows of 1.5 – 1.8 μm and 2.0 – 2.5 μm, also known as the H and K bands, respectively. These transmission regions allow eye-safe laser interaction ($\lambda$>1.4 μm), scientific applications, environmental monitoring, 3D imaging through time of flight technique, and astronomical observation. The detection of eye safe lasers indicates that these detectors can

be used for ranging, guidance, or communication without harm or interference with human vision. Further advantages of this band come from direct use of traditional glass lenses and windows as $SiO_2$ transmits IR up to 2.5 μm. This allows for reduced cost optics similar to those already used for visible detection. Additionally, the spectral region from 1.0 to 1.3 μm, known as the 'night glow' region, is the spectral range of highest night time illumination. This provides an added advantage for security or covert imaging applications where passive night time illumination is required.

Several common material systems are currently available for detection in the SWIR region such as; InGaAs, PbS, Ge, PbSe, HgCdTe, and InAs. Each of these is nominally operated as photovoltaic except PbS and PbSe, which are available as photoconductors only. Photodiodes operated in photovoltaic mode have a reduced noise component and thus have higher $D^*$ values compared to photoconductors. The $D^*$ will be discussed in more detail in Section 4.3.5. A plot of each of these detectors and their operating temperature is plotted in Figure 26 using data from ref [78]. The InGaAs material system has the highest $D^*$ in this range due to its direct bandgap absorption, lattice matched growth, and low leakage current fabrication methods. The InGaAs based p-i-n diode is also the basis for currently available FPA that operate in this range. As the development of the $Ge_{1-x}Sn_x$ binary parallels that of the high $D^*$ InGaAs technology, it is worth a short review to note the operating spectral range and performance of InGaAs detectors.

The standard InGaAs has a composition of $In_{0.53}Ga_{0.47}As$. The lattice constant of this alloy is lattice matched to InP substrates and has a spectral coverage from 1.0 to 1.6 μm [79]. The first growth of this composition grown lattice matched to InP was in 1976 [80]. Since that development, this composition has since been referred as standard InGaAs. Substrates of InP are now commercially available up to 100 mm diameter, making it the dominant substrate for

growth of this material. Extending the absorption edge beyond this 1.6 μm cut-off requires increasing the indium content, which increases the lattice constant away from the lattice matched condition. The $D^*$ of some commercially available InGaAs detectors in Figure 27 shows a decreasing signal-to-noise ratio as the long-wavelength cut-off is increased (increased indium content). This decrease in $D^*$ is due to the increased defects in the film as a result of lattice mismatched growth.

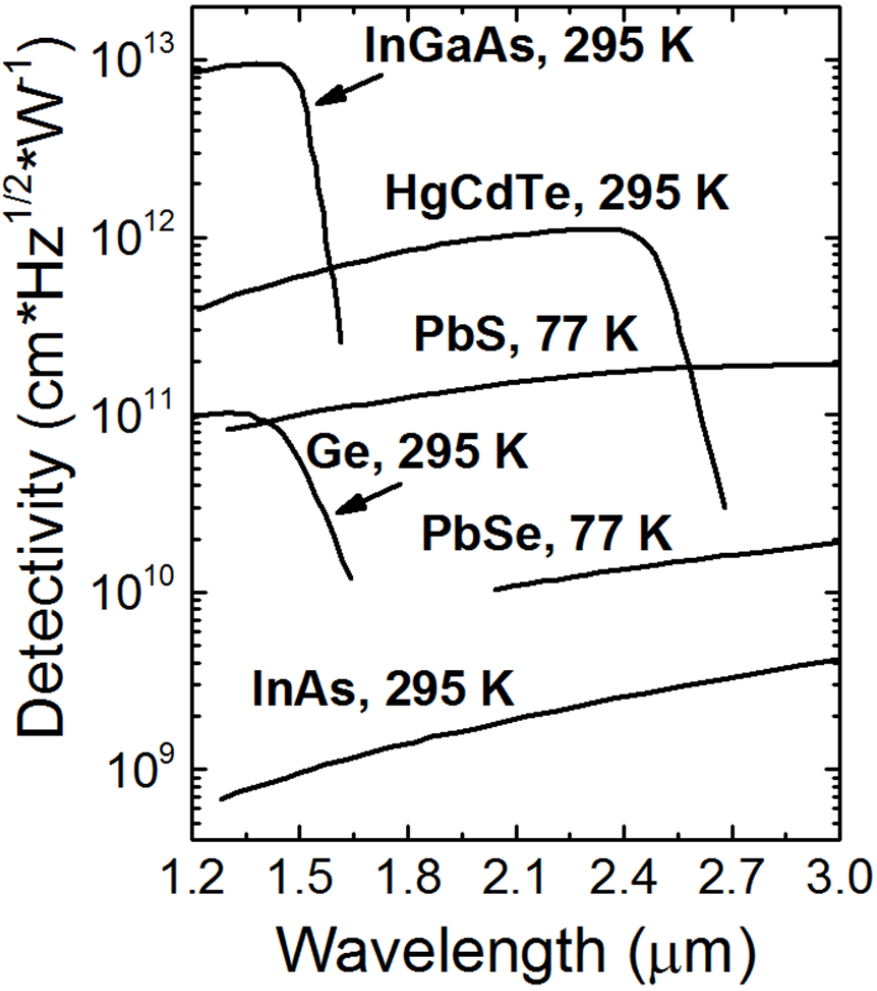


Figure 26: Spectral detectivity ($D^*$) of available detectors operating in the SWIR. Plotted from data in ref. [78].

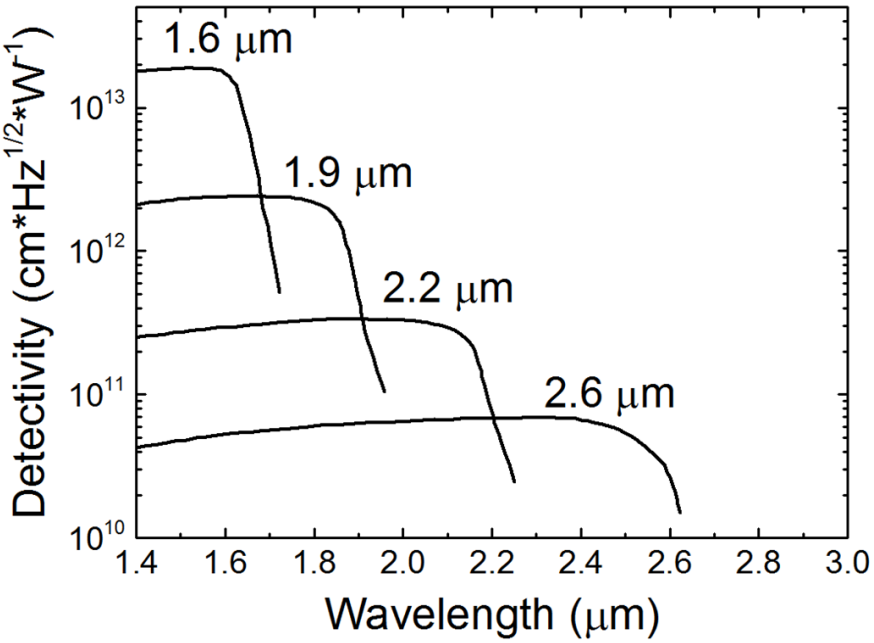


Figure 27: The spectral detectivity for different composition InGaAs detectors at room temperature with detector cut-offs at 1.6, 1.9, 2.2, and 2.6 μm. Plotted from data in ref. [79].

To be competitive with detectors already dominant in this spectral region, a new CMOS compatible material will need to demonstrate comparable signal-to-noise ratio as Ge and PbS, whilst remaining a lower cost solution to the higher performance III-V detectors.

### 4.1.2 High Speed Optical Communication

CMOS compatible photodetectors for off die or off package communication need to have basic requirements of at least 0.4 A/W responsivity, bandwidth of 20 Gb/s at 1 V, and operation up to 100° C [81]. For emitters the requirements depend more on operation conditions but they should have around a 1 W operation, wavelength stable, and reliable at operating temperature. A target for transmission of data is to have less than $10^{-12}$ bit error rate (BER). As a reference of performance, Intel's 50 Gbps Si link has a BER of $3x10^{-15}$ over a 5 meter distance.

### 4.1.3 Focal Plane Array

A focal plane array (FPA) is a collection of individual detector elements, called pixels, in an array that electronically combines the individual signal from each pixel into an image. The array can be a linear array of pixels that mechanically scans the second dimension, or a 2D array that electronically scans each pixel spatially to form the final image. This proceeding discussion will focus only on the application of 2D arrays, sometimes referred to as staring arrays.

The accumulated charge at each pixel due to the detected light is combined by an integrated circuit, called a readout integrated circuit (ROIC) or multiplexing unit. Visible Si detectors use monolithic incorporation of the detector element and ROIC into a single die, reducing cost. The two most common implementations of this are Si CCD and CMOS imagers. For a detecting element that is epitaxial grown onto a Si die, the CMOS readout method will allow for deposition of the active material over top of the buried transistors followed by deposition of the metal stack [82]. This method leaves an optical path for the signal to travel through the opening in the metal stack to the active pixel.

Operation in the SWIR benefits pixel density and resolution from the shorter wavelength operation over thermal detection (long wavelength IR). The pixel pitch and size limitation within a FPA is limited by the wavelength of light being detected. This is because the smallest diameter (d) the light can be focused is limited by the f-number of the optics and the size of the first Airy disk, which is wavelength ($\lambda$) dependent,

$$d = 2.44\lambda f \ . \tag{4.1}$$

As an example, common f/2.0 optics and a detector operating in the 5 μm wavelength has a minimum detector size of 24.4 μm. However, the same optics for a detector operation at 2.2 μm can use detector pixels as small as 11 μm. This reduced size allows for faster (lower capacitance) and higher density arrays to be fabricated.

There are two different forms of noise within an image array, temporal and spatial noise. Temporal noise is largely described using figures of merit such as noise equivalent temperature difference (NEP) and specific detectivity ($D^*$). Noise of this type is due to shot noise, Johnson-Nyquist (thermal) noise, and 1/f noise. These different noise mechanisms are bandwidth dependent in the time domain and are characterized per pixel within an array, or on single element detectors. Spatial noise describes the uniformity of light detection between pixels and is characterized as fixed pattern noise or non-uniformity correction factors. The detection of an object at long distances or through a heavily attenuated atmosphere limit the performance of the FPA within the temporal domain. The performance of the imaging system to identify this object is limited by the $1/R^2$ relationship of the number of photons arriving and being detected by the imaging system. For less attenuated atmospheres, or for reduced range imaging, the object image has a signal-to-noise ratio (SNR) above 1. In this case, the performance limitation of the imaging system is limited by the fixed pattern noise, or noise uniformity across all the detection pixels. This leads to specification tradeoffs in IR imaging that either rely on a high $D^*$ detection platform for long range use, or an array with higher uniformity that has a lower signal-to-noise ratio within a wavelength detection window.

Current material systems used in the SWIR such as InGaAs and InAs have increased costs due to a lack of manufacture scaling, higher material costs, and ROIC mounting costs which are all higher compared to Si CCD or Si CMOS imaging arrays. The $Ge_{1-x}Sn_x$ material system, which has shown to be Si CMOS compatible, can be monolithically grown and processed on Si taking advantage of these large scale processing and fabrication methods. In addition to higher production scalability, the maturity of Si processing will ultimately lead to an infrared imaging array with higher pixel-to-pixel uniformity reducing spatial noise. That puts this

system at the forefront of short-range applications where a higher uniformity is desired over lower photon flux applications.

## 4.2 Photodetector Structures

There are three dominant photodetector structures commonly used for both single element and 2D FPA. These are photoconductors, photodiodes, and avalanche photodiodes. Since photodiodes were not the focus of this work they were not directly covered here. However, many background concepts building up to the behavior of an APD directly correlate with the standard photodiode theory.

### 4.2.1 Photoconductor

Light is detected by a photoconductor by measuring the change in conductance of the device due to the increase in optically generated carriers. The increase in conductance of the device is due to electron-hole pairs generated as a result of the absorbed light. The change in the conductance ($\Delta\sigma$) of the device can be derived from the drift diffusion model of conductance for a semiconductor dependent on the electron (n) and hole (p) concentrations,

$$\sigma = q(n\mu_n + p\mu_p) \tag{4.2}$$

where q is the electron charge, $\mu_e$ and $\mu_h$ are the electron and hole mobilities, respectively. For a constant and uniform light source the optical generation rate becomes, $G = \delta p / \tau_p$ with $\delta p$ being the excess carrier concentration and $\tau_p$ the carrier lifetime. The change in carrier concentration can occur by absorption of light by a trap state within the bandgap, called an extrinsic photoconductor, or by an interband transition, called an intrinsic photoconductor. This work focuses only on intrinsic photoconductors and thus only interband transitions are considered. For

optical interband transitions the excess hole and electron concentrations are equal, $\delta n = \delta p$. Thus, the optical photoconductivity is defined as,

$$\Delta\sigma = Gq\left(\mu_n\tau_n + \mu_p\tau_p\right). \tag{4.3}$$

Under an applied bias the photocurrent is,

$$\Delta I = \Delta\sigma\frac{A}{L}V = Gq(\mu_n\tau_n + \mu_p\tau_p)\frac{A}{L}V \tag{4.4}$$

where A=w*t is the device cross section, L is the length between metal contacts, and V is the applied bias. The schematic of a $Ge_{1-x}Sn_x$/Ge photoconductor under optical illumination in Figure 28 shows the optical generation of an electron-hole pair being seperated by the appliced electric field.

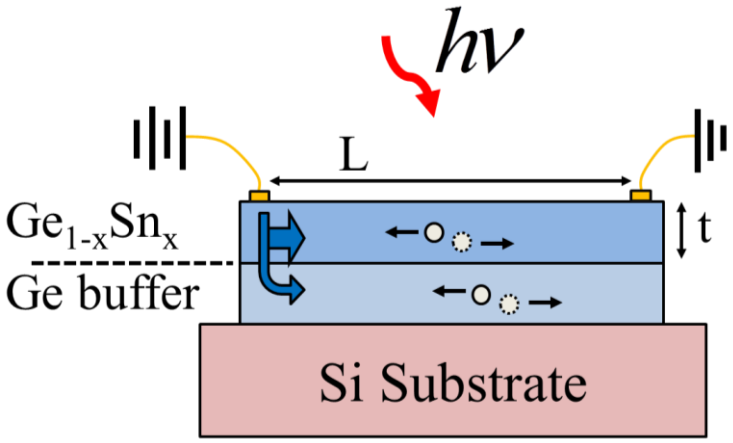


Figure 28: Schematic representation of a $Ge_{1-x}Sn_x$ photoconductor grown on Ge buffered Si.

A large majority carrier mobility allows Equation 4.4 to be reduced to,

$$\Delta I = Gq(\mu_p\tau_p)\frac{A}{L}V\,. \tag{4.5}$$

The carrier transit time between metal contacts is $\tau_{tr} = L^2/\left(\mu_p V_B\right)$, then rearranging and combining with Equation 4.5 becomes,

$$\Delta I = GqAL\frac{\tau_p}{\tau_t}. \tag{4.6}$$

The photoconductive gain is then defined as,

$$Gain \equiv \frac{\tau_p}{\tau_t}. \tag{4.7}$$

From this expression, it is observed that the photocurrent can be increased by reduction of the transit time or by increase of the lifetime. This gain behavior and how it relates to responsivity will be further discussed in Section 4.4.2.

The ideal photoconductor has an infinite recombination velocity at the metal contacts (Ohmic contacts) and a low contact resistance. For a photoconductor, the optimum device has a high sheet resistance ($R_{sh}$) and low contact resistance ($R_c$). As a new material system is developed, the metals and contact methods may not produce this optimum low resistance condition, and thus must be determined per fabrication condition. The total resistance of the photoconductor is a summation of the total resistances within the device,

$$R_T = R_{sh}\left(\frac{L}{w}\right) + R_d + R_w + 2R_C \tag{4.8}$$

where, L is the distance between contacts, w is width of the mesa, $R_d$ is the resistance due to current crowding, and $R_w$ is a width correction for contacts less than w [83]. However, to determine the contact and sheet resistance, the total resistance is measured for varied contact spacing, L. This technique is called the transmission line method and reduces Equation 4.8 to [84],

$$R_T = R_{sh}\left(\frac{L}{w}\right) + 2R_C. \tag{4.9}$$

A plot of the total resistance vs the contact spacing, L, allows determination of $R_{sh}$ and $R_c$ from the slope and intercept, respectively.

The advantages of photoconductors are the simpler fabrication methods, undoped active layer, and the photoconductive gain. Since the photoconductor device benefits from low background doping, then there is reduced development cost for forming p-n junctions by doping. The intrinsic nature also allows for an unambiguous study of the intrinsic material parameters, such as mobility and lifetime. The photoconductive gain behavior can allow for quantum efficiencies above 100% due to the multiple transits a single optical generated majority carrier can make within the circuit. This gain can be a lower noise method of signal amplification compared to electronically amplified signal due to a lower Johnson-Nyquest noise mechanism. There also exist some disadvantages of the photoconductor design. The intrinsic material and large drift volume allows for a higher recombination rate of minority carriers compared to a p-n junction. This recombination creates a noise component within a photoconductor device that is $\sqrt{2}$ greater than a device with a built in space charge region. Since the lowest level of dark conductivity for a photoconductor is achieved for a purely intrinsic semiconductor, then the dark resistance has an upper limit. This intrinsically limited impendence limits the application of photoconductors for FPAs because on-chip ROIC designs require high impendence matching.

### 4.2.2 Avalanche Photodiode (APD)

Low optical powers are difficult to detect without gain or amplification. The internal gain mechanism in avalanche photodiodes (APD) produces an amplified signal with reduced external amplifier circuits. The amplified signal is a quantum process and not subject to external electronic interference. The small junction and high field also allow for fast switching. Common applications of APDs include laser range finding (LADAR) and optical communication. The

[Gain x bandwidth] product of an APD is higher than a p-i-n detector with external low noise amplifier. This is because even for an ideal external amplifier circuit, the electronic amplifier multiplies the noise in addition to the signal. Commercial APD devices can achieve better S/N ratio higher than this ideal p-i-n device/amplifier pairing.

The process of multiplication within an APD occurs as a result of impact ionization. Carriers that gain more energy higher than the bandgap through acceleration within an electric field can stimulate impact ionization. This occurs under high electric fields such as a high reverse biased photodiode. The energy-wave vector diagram of this process is illustrated in Figure 29. The electron (solid circle) at $E_i(k_i)$ is accelerated under the high electric field and impacts an electron still in the valence band, $E_v(k_1)$. The initial electron after impact ionization, $E_c(k_3)$ now has reduced E and a change in k. The impacted electron, $E_c(k_2)$, has gained energy leaving a hole at $E_v(k_1)$. Any change in wave vector is compensated by emission of a phonon. Although $E_c(k_3)$ and $E_c(k_2)$ are not always equal, average energy transfer often occurs this way. This is due to the requirements of ionization [85]: (1) Total energy of the final carriers must be minimized for a given wave vector, k. (2) Energy and momentum must be conserved.

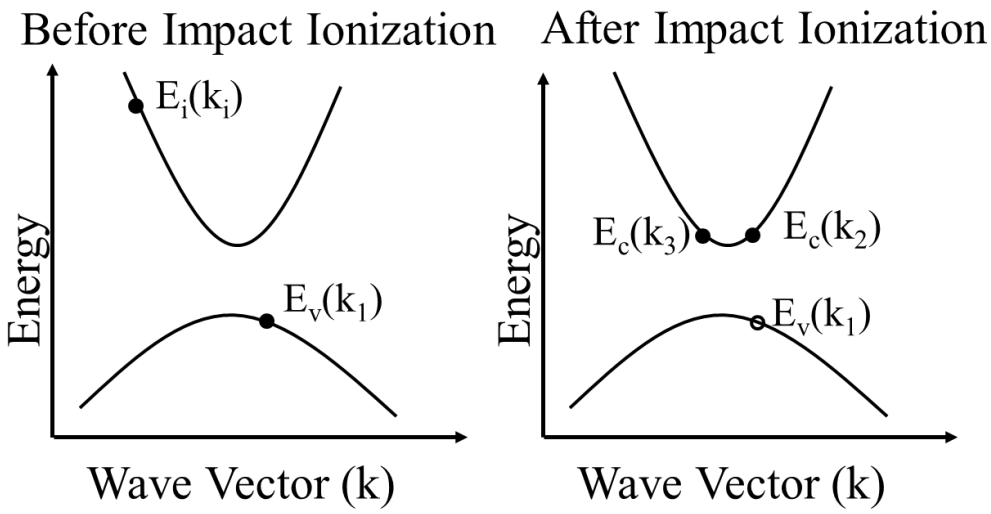


Figure 29: Energy-wave vector (E-k) diagram of the electron (solid) and hole (empty) carrier dynamics as a result of impact ionization within a semiconductor.

To fully understand the breakdown mechanisms within an APD, the impact ionization and carrier transport velocities must be derived. From Figure 29 the final energy and momentum can be written as,

$$E_F = E_c(k_3) + E_c(k_2) - E_v(k_1)\,, \tag{4.10}$$

$$K_f = k_3 + k_2 - k_1\,. \tag{4.11}$$

Applying requirement 1 ($dE_f=0$ and $dK_f=0$) to Equations 4.10 and 4.11, and applying the definition of group velocity ($v_g = \nabla E(k)/\hbar$), then solving by substation yields,

$$dk_2(v_2 - v_3) + dk_1(v_3 - v_1) = 0\,. \tag{4.12}$$

The values $dk_1$ and $dk_2$ are independent of each other, thus the only solution to Equation 4.12 is that $v_1 = v_2 = v_3$. To satisfy requirement 2, the total energy before and after impact ionization must equal, $E_f(k_f)=E_i(k_i)$. Thus, a band with an energy state $E_i$ with energy equal to the total $E_f$ is required for ionization. This energy availability creates windows of ionization within a material. For ionization between two parabolic bands the ionization energy of a carrier is,

$$E_{ionize} = E_g\left[\frac{2+\gamma}{1+\gamma}\right] \tag{4.13}$$

where $\gamma$ is the ratio of effective masses, $m_e/m_h$ for electron initiated ionization and $m_h/m_e$ for hole initiated ionization. This equation assumes ionization occurs for the lowest energy threshold and lowest effective masses. A special case of $m_e=m_h$ leads to the common empirical relationship for the ionization energy,

$$E_{ionize} = \frac{3}{2}E_g \tag{4.14}$$

where $E_g$ is the bandgap of the ionization material. A more thorough treatment of the required ionization energy should include the split-off band [85]. For materials with a split-off energy

close to $E_g$, the total energy needed for hole initiated ionization is reduced. The probability of ionization at $E_i$ is ~ 0, but increases exponentially as energy increases.

The avalanche behavior and ionization probability can be better understood by analysis of the basic drift and current density equations within a semiconductor. The electron and hole drift current density,

$$\begin{aligned} J_n &= -qnv_n \\ J_p &= qpv_p \end{aligned} \qquad 4.15$$

where q is the elementary charge, $v_n$ and $v_p$ are the electron and hole velocities, respectively. Applying the ionization coefficient, $\alpha_e = 1/(|v_n|\tau_n)$, for n and p respectively ($\tau_n$ and $\tau_p$ represent the impact ionization time between events) into the differential equation for current density throughout the material as a function of distance, x,

$$\begin{aligned} \frac{dJ_n}{dx} &= \alpha_e(x)J_n(x) + \alpha_h(x)J_p(x) \\ -\frac{dJ_p}{dx} &= \alpha_e(x)J_n(x) + \alpha_h(x)J_p(x) \end{aligned} \quad . \qquad 4.16$$

In Equation 4.16, x is the distance from 0 to W, where W is the multiplication region width. This expression assumes that the electric field $\overrightarrow{E(x)}$ is constant throughout this region. Finally, the continuity equation and rate equation under steady state condition are applied yielding the final carrier concentration for the multiplication region,

$$\begin{aligned} \frac{dn}{dx} &= \alpha_e n + p\left(\alpha_h \frac{v_p}{v_n} - \frac{1}{v_n}\left[\frac{dv_p}{dx}\right]\right) \\ \frac{dp}{dx} &= \alpha_h p + n\left(\alpha_e \frac{v_n}{v_p} - \frac{1}{v_p}\left[\frac{dv_n}{dx}\right]\right) \end{aligned} \qquad 4.17$$

A device with pure electron (or hole) injection and with impact ionization as the only source of carrier generation within the multiplication region then, $J_n(0) \neq 0$ and $J_p(\mathrm{W}) = 0$. The multiplication gain under this scenario then becomes,

$$M_e = \frac{J_n(W)}{J_p(0)}$$
$$M_h = \frac{J_p(0)}{J_n(W)} \qquad 4.18$$

where $M_e$ is for electron injection and $M_h$ is for hole injection.

Longer wavelength infrared response requires a narrower bandgap semiconductor than visible detection. Smaller bandgap materials have an increased tunnel current under increased reverse bias. The separate absorption and charge multiplication (SACM) design shown in Figure 30 solves this issue. A charge layer separating the absorption and multiplication region isolates the high field region to the wider band gap material. The avalanche process in a SACM proceeds as follows:

1. Photons are absorbed in the narrow band material.
2. The generated carriers drift under the applied electric field to the charge layer.
3. The p-i-n doping profile between the charge, multiplication, and N contact layer forces the largest potential across this multiplication region.
4. Sufficient reverse bias widens the depletion region from this N contact layer to the P charge layer.
5. Carriers reach saturation velocity and gain enough kinetic energy to break additional carriers free upon striking stationary lattice sites (impact ionization).
6. These secondary carriers are also accelerated under the electric field to saturation velocity and further impacts ionize additional carriers.

This process has a saturation velocity determined by the kinetic energy and impact ionization rate within the multiplication material.

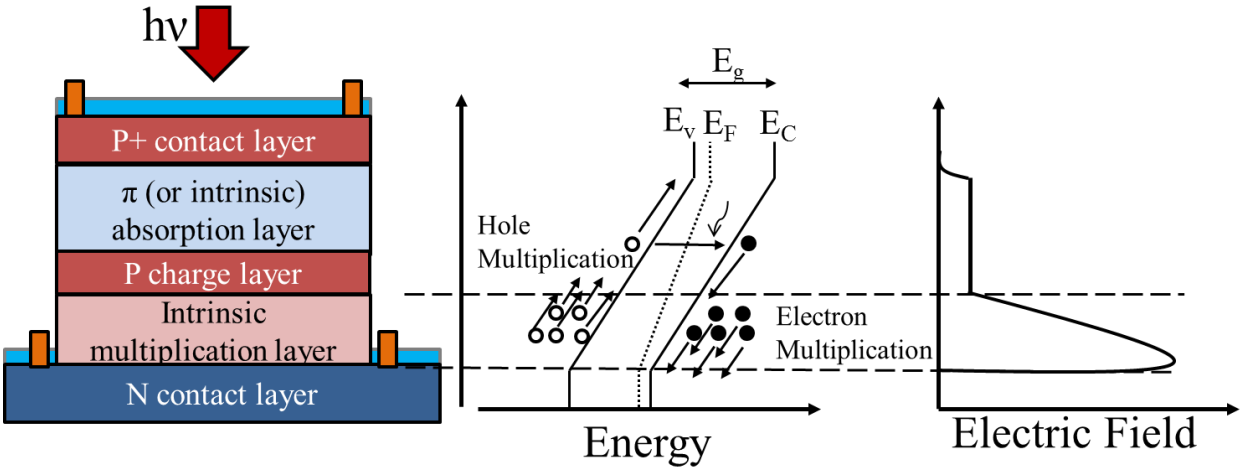


Figure 30: Schematic cross section of a separate absorption and charge multiplication (SACM) avalanche photodiode. The energy and electric field profiles for each layer highlight the multiplication regions.

A schematic representation of the band diagram for a Ge/$Ge_{1-x}Sn_x$/Ge/Si APD in Figure 31 shows the expected band offsets and band bending under equilibrium conditions with a valence band offset for Ge (100) on Si of 0.22 eV [86].

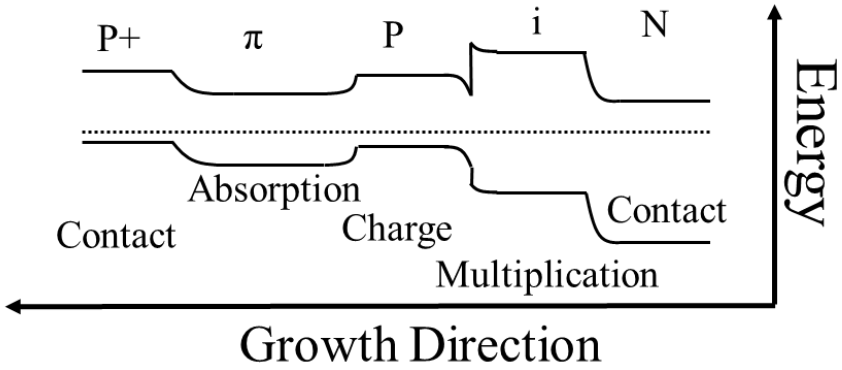


Figure 31: Band diagram for a SACM avalanche photodiode schematically shows the band offset and band bending for semiconductors with a type-I band alignment.

The design of an APD structure should consider the absorption and multiplication materials, desired doping profile, and thickness of each layer. Each of these parameters

subsequently affects the spectral response, responsivity, noise factor, multiplication, and bandwidth of the device. A summary of some commercially available APDs and their specifications are listed in reference [87]. Wavelength spectral response and quantum efficiency determine overall conversion rate of photons to generated carriers at a specific wavelength. Both Si and Ge are indirect band gap materials with reduced absorption near the band edge. $In_{1-x}Ga_xAs$ has a tunable direct band gap depending on the x mole fraction of the film. However, the Si APD has the highest gain and gain product bandwidth (100 to 400 GHz) due to its higher multiplication factor. This will be discussed in more detail later, but the combination of an infrared absorption layer for detection in the SWIR combined with the higher Si multiplication factor would yield an optimal SACM combination.

Examine now the multiplication factor and the mechanism for high gain within an APD. This examination is treated in more detail in references [85, 88]. The DC multiplication factor (M) is determined by the ionization coefficient, α, of electrons/holes and length of the space charge region, L,

$$M_{DC} = \frac{1}{1 - \int_0^L \alpha(x) dx} \tag{4.19}$$

The frequency dependent multiplication is,

$$M(\omega) = \frac{M_{DC}}{\sqrt{1 + (\omega M_{DC} k \tau)^2}} \tag{4.20}$$

where ω is the frequency of operation, k is ionization ratio, and τ is the carrier transit time across the multiplication region. The accepted empirical formula for M as a function of the applied voltage, V, and breakdown voltage, $V_B$,

$$M = \frac{1}{1-\left(\frac{V}{V_B}\right)^n}. \qquad 4.21$$

The exponent, n, in this expression is a fitting parameter that depends on the material and doping profile. The multiplication can also be expressed in terms of the ionization coefficient, α, and the depletion width, $W_D$,

$$M = \frac{1}{\left(1-\alpha W_D\right)}. \qquad 4.22$$

The two empirical expressions for the multiplication of an APD allow extraction of the physical parameters within the device, or for known parameters to predict the multiplication. One parameter in particular is the ionization coefficient, α, which is one over the distance needed to cause an ionization event by an electron or hole. This is dependent upon the multiplication material, doping profile, and applied electric field. However, a general form for the ionization coefficient is a simple exponential fit dependent upon the applied electric field, E, [87]

$$\alpha = a\exp\left(-\left[\frac{b}{E}\right]^c\right) \qquad 4.23$$

where a, b, and c are fitting parameters. For most materials ionization does not occur for electric fields below $10^5$ V/cm. For Si and InGaAs, the electron ionization coefficient is higher than for holes, but this is reverse for Ge.

Heterostructure growth interface barriers represent a potential scattering site for carriers with high drift velocities. This has the effect of reducing ionization events from carriers that encounter a barrier upon entering the multiplication region. The diagram in Figure 32 (a) shows the propagation of electrons (solid circle) unaffected by the energy offset, but the holes (empty

circle) experiences increased scattering at this interface. A graded heterostructure barrier can be included in the layer growth to reduce this effect [Figure 32 (b)].

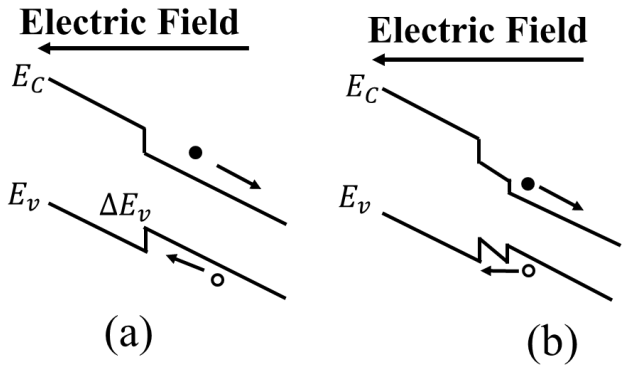


Figure 32: (a) Large band offset in the valence band ($\Delta E_v$) scatters high energy holes, but does not affect the electron. (b) Graded heterostructure reduces the overall energy step for the hole.

The breakdown voltage ($V_B$) within an APD occurs when the product of the multiplication region and ionization coefficient equal 1, $W_D\alpha = 1$. Recall the depletion width approximation for an abrupt, one sided p-n junction, at thermal equilibrium,

$$W_D = \sqrt{\frac{2\epsilon_s}{qN}\left(V_{bi} - V - \frac{2kT}{q}\right)} \qquad 4.24$$

where N is the concentration of the heavy doped region, k is Boltzmann constant, T is the absolute temperature, $\epsilon_s$ is the material permittivity, V is the applied reverse bias voltage, and $V_{bi}$ is the built in junction potential. For a non-degenerate semiconductor the built in potential is approximated as,

$$V_{bi} = \frac{kT}{q}\ln\left(\frac{N_D N_A}{n_i^2}\right) \qquad 4.25$$

with $n_i$ being the intrinsic carrier concentration of the multiplication region, and $N_D$ and $N_A$ are the donor and acceptor concentrations at the abrupt interface.

Applying breakdown voltage condition and substituting Equation 4.25 into Equation 4.24 yields the avalanche breakdown voltage for an abrupt $N^+$ junction with a lightly doped avalanche region,

$$V_B = -\frac{kT}{q}\ln\left(\frac{N_A N_D}{n_i^2}\right) + \frac{qN_D}{2\alpha_n^2\epsilon_s} + \frac{2kT}{q}. \quad 4.26$$

The key application of Equation 4.26 allows engineering of the breakdown voltage based on the material permittivity, ionization coefficient, intrinsic carrier concentration, and doping profile. This expression assumes that the physical width of the multiplication region is larger than the applied depletion width, that is $L>W_D$. For shorter diodes, $W_D$ can become fixed once it becomes equal to L.

For the short diode approximation the breakdown voltage expression becomes,

$$V_B = E_m b + E_d(W_B - b) \quad 4.27$$

where $E_m$ and $E_d$ is the electric field across the multiplication and absorption (drift) region, respectively. The parameter b is the physical length of the multiplication region, and $W_B$ is the total length of the diode with a non-zero electric field. A diagram of a short diode with each of these parameters is shown in Figure 33. The multiplication region electric field can be determined based on the background doping, N, and permittivity of the region of the interest,

$$E_m = \sqrt{\frac{2qNV_{bi}}{\epsilon_s}}. \quad 4.28$$

The electric field across the absorption (drift) region can be approximated by [88],

$$E_d = -\frac{kT}{qW_A}\ln\left(\frac{N_\pi}{N_{P^+}}\right) \quad 4.29$$

where $W_A$ is the length of the absorption region, and $N_{P+}$ and $N_\pi$ are the doping concentration of the heavy doped charge ($P^+$) and lightly doped absorption ($\pi$) regions, respectively. Application

of Equation 4.27 with 4.28 and 4.29 allow the breakdown voltage to be calculated based on the doping concentration and layer width. Additionally, the doping profile could be determined by experimental measurement of the breakdown voltage of a fabricated device.

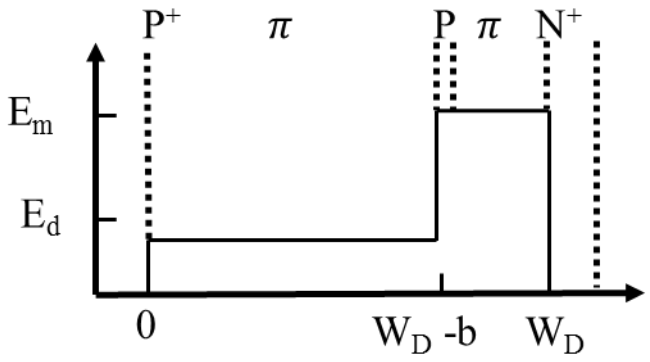


Figure 33: Parameters used in the short diode approximation of a separate absorption and charge multiplication avalanche photodiode.

### 4.3 Photodetector Figures of Merit

Spectral response and responsivity provide useful insights into detector photoresponse for material based characterizations, but for a complete picture of detector performance the detectivity needs to be measured. Detectivity is the figure of merit established to quantify the response and noise of a detector based on a normalized surface area and bandwidth. This measurement allows comparison of detector performance across different material platforms and detection regions. The highest $D^*$ in the SWIR region is for InGaAs, which has a maximum $D^*$ at 1.6 μm due to the high responsivity of the material in that region and the low noise operation. In order for $Ge_{1-x}Sn_x$ to be shown as a competing technology, the a baseline detectivity will need to be established on which material and fabrication improvements can be measured against.

4.3.1 Spectral Response

The spectral response and long wavelength cut-off of a detector is determined by the absorption coefficient of the active region. The absorption coefficient, α, is a numerical value calculated from the extinction coefficient, k, $\alpha = \left(4\pi k\right)/\lambda$. The extinction coefficient and refractive index are traditionally measured using ellipsometry. However, the absorption coefficient or detector cut-off can be directly determined experimentally from photoresponse measurements under illumination from a calibrated light source [89]. Near the bandgap of the material the absorption coefficient follows [90],

$$\alpha \propto \left(h\nu - E_g \pm E_p\right)^{\gamma} \tag{4.30}$$

where $E_p$ is the phonon energy for indirect transitions and γ is a constant. For direct transitions γ equals ½; it equals 2 for indirect transitions. The absorption coefficient and band edge define the spectral response of the detector.

Absorption coefficient is the thickness of material needed to absorb $e^1$ of the light entering the sample. The intensity of light within the material follows the standard Beers law absorption. The intensity of light, I, follows the relation, $I = I_o \exp\left(-\alpha_\lambda x\right)$ where Io is the initial light intensity, α is absorption coefficient, and x is the depth. The generation rate, $g_{optical}$, due to the spectral absorption coefficient is then,

$$g_{optical} = I_o \alpha \exp(-\alpha_\lambda x)\,. \tag{4.31}$$

$I_o$ in units of photons/$cm^2$/second allows direct calculation of the electron-hole pairs (ehp) to be determined within the material at a depth, x.

4.3.2 Responsivity and Photoconductor Gain

The responsivity of a detector is the change in current due to the incident radiation divided by the incident power. To further define the parameters within the device that affect the overall responsivity, first start with the change in conductivity in a semiconductor due to optical absorption,

$$\Delta\sigma = q(\Delta n\mu_n + \Delta p\mu_p) \tag{4.32}$$

where σ is the conductivity, n and p are the electron and hole carrier concentrations, and $\mu_n$ and $\mu_p$ are the electron and hole mobilities, respectively. Under high optical absorption, $\Delta n = \Delta p$. Also, assume that for Ge and $Ge_{1-x}Sn_x$ the hole mobility is large compared to electron mobility, $\mu_p >> \mu_n$. Applying these parameters to Equation 4.32 gives,

$$\Delta\sigma = q\Delta p\mu_p . \tag{4.33}$$

The change in carrier concentration due to optical excitation is related to the generation rate and effective lifetime,

$$\Delta p = g_{optical}\tau_{eff} \tag{4.34}$$

The optical generation rate is defined as,

$$g_{optical} = \left(\frac{\eta\phi(\lambda)\lambda}{ALhc}\right) \tag{4.35}$$

where η is the quantum efficiency, ϕ(λ) is the wavelength dependent intensity, λ is the free space wavelength, A is the cross sectional area, L is the length between contacts under optical generation, h is Planck's constant, and c the speed of light. Combining Eq. 4.33-4.35 and Ohm's current law, $J = \sigma E$ gives,

$$J_{photo} = \frac{q\eta\phi(\lambda)\lambda\tau_{eff}\mu_p E}{ALhc} . \tag{4.36}$$

Applying $J_{photo} = I_{photo} / A$ and $E = V_{bias} / \mathrm{L}$ to Eq. 4.36 gives,

$$I_{photo} = \frac{q\eta\phi(\lambda)\lambda\tau_{eff}\mu_p}{L^2 hc} V_{bias} . \quad 4.37$$

Dividing by the incident optical power yields the responsivity of a photoconductor,

$$\mathrm{R}\left(\frac{A}{W}\right) = \frac{q\eta\lambda\tau_{eff}\mu_p}{L^2 hc} V_{bias} . \quad 4.38$$

The total quantum efficiency, η is defined as,

$$\eta = \eta_{internal}(1-\mathbb{R})(1-\exp(-\alpha d)) \quad 4.39$$

where $\eta_{internal}$ is the internal quantum efficiency, $\mathbb{R}$ is the surface reflectance, α is the wavelength dependent absorption coefficient, and d is the film thickness. The optical constants, n and k, measured by ellipsometry allow $\mathbb{R}$ and α to be determined. Assume that each photon absorbed creates one electron-hole pair, thus giving an internal quantum efficiency of 1 [87]. Substituting Eq. 4.39 into Eq. 4.38,

$$\mathrm{R}\left(\frac{A}{W}\right) = \frac{\mathrm{q}(1-R)(1-\exp(-\alpha d))\lambda\tau_{eff}\mu_p}{L^2 hc} V_{bias} . \quad 4.40$$

Photoconductor gain, G, is equal to the effective carrier lifetime, $\tau_{eff}$, of the photo-generated carriers divided by the carrier transit time, $\tau_{tr}$, $G \equiv \tau_{eff} / \tau_{tr}$ . Equivalently, it is the rate of electrons flowing in the external circuit to the rate of electrons generated due to light absorption, $G \equiv I_{photo} / g_{optical}$ . The carrier transit time is determined from the mobility, length between contacts, and applied voltage,

$$\tau_{tr} = \frac{L^2}{\mu_p V_B} \quad 4.41$$

Applying the former definition for gain to Equation 4.41 leads to the expression for photoconductor gain based on the physical parameters of the material and device design,

$$G = \frac{\tau_{eff}\mu_p V_B}{L^2}. \qquad 4.42$$

By examination, the photoconductor gain can be increased by reducing the spacing between the metal contacts or by increasing the bias voltage. Higher mobility or longer effective lifetime will also improve the responsivity of a photoconductor by increasing the gain.

The difference in carrier transit times between the electron, $\tau_n$, and hole, $\tau_p$, explains the increase in gain for applied voltage up to some value that is then followed by a monotonical decrease in gain as bias is further increased. To describe this mathematically, an equivalent expression for the photoconductor gain is applied [90],

$$G = \tau_{eff}\left(\frac{1}{\tau_n} + \frac{1}{\tau_p}\right). \qquad 4.43$$

For a p-type material, the gain continues to increase for increased voltage as the effective lifetime is larger than the hole transit time ($\tau_{eff}>\tau_p$). At lower electric fields the slower moving minority carriers are not replenished as fast. This causes a charge imbalance that is compensated by multiple transits of the optically generated majority carriers. However, if the electric field is further increased, the minority carrier transit time will also become shorter than the effective lifetime ($\tau_{eff}>\tau_n$). At this point a built in space charge region forms around the metal contacts that repels carrier collection, causing a decrease in gain (responsivity) as the applied electric field is further increased.

### 4.3.3 Effective Carrier Lifetime

Effective carrier lifetime describes the length of time an optically generated carrier remains electrically active in a photodetector. In this work, reference to the effective carrier

lifetime is only in context to a photoconductor. This value is a function of the bulk material lifetime, $\tau_B$, and the surface recombination lifetime, $\tau_{sr}$,

$$\frac{1}{\tau_{eff}} = \frac{1}{\tau_B} + \frac{1}{\tau_{sr}}. \tag{4.44}$$

The bulk lifetime is also known as the recombination time of carriers within the material [84]. The dominant bulk recombination mechanisms are Auger, $\tau_{Auger}$, Shockley-Read-Hall (SRH), $\tau_{SRH}$, and radiative recombination, $\tau_{rad}$,

$$\frac{1}{\tau_B} = \frac{1}{\tau_{Auger}} + \frac{1}{\tau_{SRH}} + \frac{1}{\tau_{rad}}. \tag{4.45}$$

Each of the recombination mechanisms in the expression above describe the length of time a minority carrier will remain free in the material before recombining.

Photodetectors require a photo-generated current being higher than the background dark current. The detector generated noise (excluding noise in the electronics) is a function of Auger recombination, Shockley Reed Hall (SRH), surface recombination events, diffusion, and shunt current. Each of these can be suppressed in different ways independently of one another and ultimately the largest will dominate the dark current generation/recombination. Auger is largely the dominant mechanism of dark current in MWIR and LWIR. The carriers lost to Auger recombination are directly dependent on temperature and indirectly dependent on the bandgap,

$$\tau_{Auger} = 8.3\times10^{-13} E_g^{\frac{1}{2}} \left(\frac{q}{kT}\right)^{\frac{3}{2}} \exp\left(\frac{qE_g}{kT}\right). \tag{4.46}$$

Equation 4.46 gives a simplified approximation of the Auger lifetime showing its temperature and bandgap dependence [91]. In order for Auger recombination to not dominate the dark current, the transit time must be shorter than the effective lifetime for the photo-generated

carriers to be collected. Smaller bandgap detectors operating in hot ambient environments will have short Auger lifetimes.

SRH recombination events are linked to the crystal's purity and the epitaxial growth conditions while surface recombination can be quenched with proper passivation and electrical contacts on the device. Each of these two sources of dark current can generally be dealt with by improving manufacturing conditions and source material purity. In SRH, the electron hole pairs generate and recombine randomly on various defects throughout the material. This is a thermal driven process characterized by an activation energy which is temperature dependent. Reducing the SRH portion of the dark current, or reducing the temperature at which they activate, would increase the carrier effective lifetime, thus increasing the detector responsivity.

A photoconductor with an infinitely high recombination rate at the metal contacts (Ohmic contacts) can be used to extract the effective carrier lifetime by way of responsivity measurements. By examination of Equation 4.40, the responsivity of a photoconductor is affected by a change in voltage or electrode spacing. For a plot of responsivity vs applied voltage the slope allows determination of the effective carrier lifetime,

$$\tau_{eff} = \frac{\{slope\ of\ responsivity\} L^2}{\mu_{maj}\eta} \frac{hc}{q\lambda_o} \tag{4.47}$$

A known quantum efficiency, mobility, and length between contacts allow measuring the responsivity vs the applied voltage bias to yield the effective lifetime. The bulk material is unchanged across the devices, thus the bulk lifetime is unaffected by the measurement conditions. For this work, the dominant recombination centers are SRH due to impurities, growth defects, and surface recombination. The activation energy for these trap and surface states is quenched at reduced temperature since these are on the order of 5 to 30 meV [92] giving rise to the large increase in gain across this temperature range.

A general numerical description for the surface recombination lifetime, $\tau_{sr}$, due to a large surface recombination surface is [93],

$$\tau_{sr} = \frac{1}{D}\left(\frac{L}{\pi}\right)^2 \qquad 4.48$$

where D is the diffusion constant of the optically generated carriers and L is the width between metal contacts. For low injection, D is the diffusion of the minority carriers while under high injection, this value then describes the ambipolar carrier diffusion constant. Combining Equation 4.48 and 4.44 results in an expression of the effective lifetime dependent on the square of the electrode spacing and carrier diffusion constant,

$$\frac{1}{\tau_{eff}} = \frac{1}{\tau_B} + \pi^2 D \frac{1}{L^2}\,. \qquad 4.49$$

As the electrode spacing increases, the effective lifetime becomes equal to the bulk lifetime as expected.

### 4.3.4 Photodetector Noise

The unwanted variation in a signal within a detector is noise. An intrinsic semiconductor detector has four main noise mechanisms: thermal, shot, generation-recombination, and 1/f noise. The combined noise current density within a detector is the combined effect of those components,

$$\mathrm{I}_{\mathrm{noise}} = \sqrt{\mathrm{I}_{\mathrm{shot}}^2 + \mathrm{I}_{\mathrm{therm}}^2 + \mathrm{I}_{\mathrm{G-R}}^2 + \mathrm{I}_{1/f}^2}\,. \qquad 4.50$$

Each noise component is further characterized in more detail below.

Shot noise describes the statistical fluctuation in the particle nature of electrons in the detector and circuit. The individual arrival of these charges into the collection circuit generates a fluctuation in the signal,

$$I_{shot} = \sqrt{2qI \times BW} \tag{4.51}$$

where q is elementary charge, I is the dark current, and BW is the measurement bandwidth. The standard measurement bandwidth is often 1 Hz. Since this noise source depends on the fluctuation of charge, the spectral density depends only on the device dark current and is independent of frequency.

Thermal noise is the fluctuations in the electric charges within a material due to random thermal vibrations. This source of noise exists regardless of an applied bias and is largely independent of the operating frequency. Also called Johnson-Nyquist, or white noise, it is described as,

$$I_{therm} = \sqrt{4k_B T \frac{BW}{R}} \tag{4.52}$$

where $k_B$ is Boltzmann constant, T is the absolute temperature, BW is the measurement bandwidth, and R is the DC resistance of the device. The thermal noise of a detector decreases for increasing resistance and decreased temperature.

Generation-recombination (G-R) noise also depends on the total dark current in the device. This source of noise is related to the change in carriers within the semiconductor as they are generated and recombine. This fluctuation in minority charge density is the result of thermal generation at low energy trap sites, G-R across the bandgap for increased temperature, surface recombination, and recombination at the metal contacts. Ideal diffusion limited photodiodes and devices with space-charge regions have a negligible G-R due to the built in field that allows collection of the generated minority carriers. The cumulative G-R noise can be described as [84],

$$I_{G-R} = \sqrt{\frac{KI^2 \tau_{trap} BW}{1 + (\omega \tau_{trap})^2}} \tag{4.53}$$

where K is a constant determined by the trap concentration, $\tau_{trap}$ is the time constant of the trap sites, BW is the bandwidth, I is the device dark current, and ω the operating frequency in radians.

Low frequency (1/f noise) dominates the noise current at low operating frequencies. The accepted expression for the noise current due to 1/f noise is,

$$I_{1/f} = \sqrt{\frac{C \times I^{\alpha} \times BW}{f^{\beta}}} \qquad 4.54$$

where C is a constant, I is the dark current, α is a constant, f is the operating frequency, and β is a constant. The constant C is a proportionality constant dependent on the device. The constants α and β are usually close to 2 and 1, respectively [87].

The large dark current in photoconductors causes the shot noise to become the dominant noise mechanism amongst all other components. This creates a noise floor whereby the noise ceases to decrease for decreasing temperature (when compared at frequencies far from 1/f dominated noise). To illustrate this, the total calculated noise spectrum is plotted in Figure 34 for a device with a 10 μA and 10 nA dark current. This plot compares the effect of temperature and device resistance simultaneously. The 10 nA dark current device shows a decreasing noise spectrum for a decreasing temperature and increasing resistance. However, for a 10 μA dark current, the noise current saturates around $2x10^{-12}$ $A*Hz^{-1/2}$ due to the shot noise limited noise current. By this calculation, the conclusion is made that the photoconductors studied here are all shot noise limited based on the measured dark currents in the μA-mA range. This then allows the noise current to be directly determined from the dark current for calculation of the SNR and specific detectivity ($D^*$).

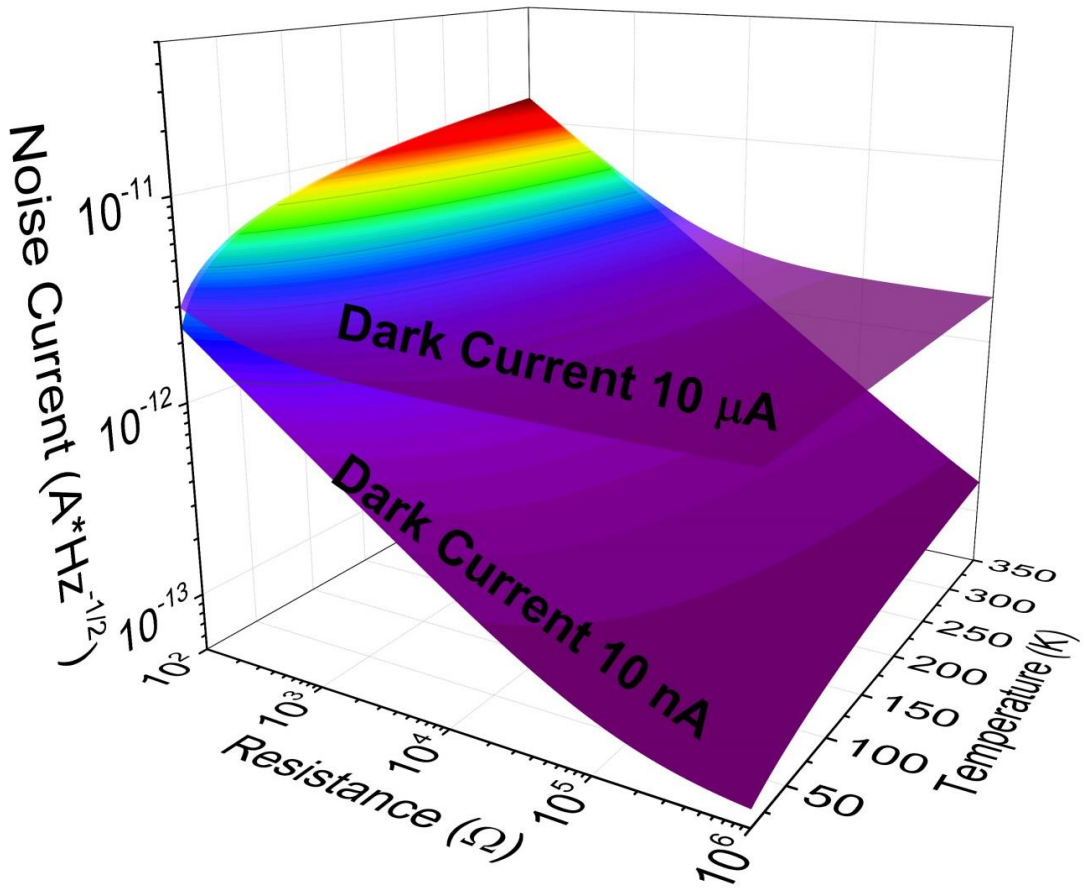


Figure 34: Noise current of a photoconductor with 10 μA and 10 nA dark current plotted for the device resistance and temperature.

4.3.5 Specific Detectivity ($D^*$)

The specific detectivity ($D^*$) is a figure of merit to account for detector noise, responsivity, and normalizes for device size. It is a useful figure of merit for comparing detectors which require low noise operation such as in focal plane arrays or scientific measurement applications. Comparison of $D^*$ between detectors shows a maximum point that balances the gain of photoconductors or APDs with reduction in signal quality by increased dark currents. The specific detectivity ($D^*$) is calculated by,

$$D^*(\lambda) = \frac{R(\lambda)\sqrt{A \times BW}}{i_{noise}} \qquad 4.55$$

where R(λ) is the spectral responsivity, A is the area of the detector, $i_n$ is the noise current, and BW is the bandwidth,. The noise component ($i_n$) is either in terms of current or voltage depending on the method for determining responsivity. If R is measured in A/W then this noise term should be in the noise current. The same applies if R were measured in V/W then the noise component would be the voltage noise measured at that bandwidth. The SI units of $D^*$ are $cm*Hz^{1/2}*W^{-1}$.

The bandwidth (BW) here is the temporal bandwidth over which the measurement collection occurs. In this context, it is also referred to as the equivalent noise bandwidth (ENBW) or the switching bandwidth defined as 1/(2*T), where T is the observational period. This bandwidth (BW) is different from the maximum bandwidth of the device in terms of switching speed (Δf). The speed bandwidth (Δf) is better defined as being the voltage at which the measured response is -3 dB below the DC measured value. This same -3 dB bandwidth ($f_{3dB}$) can be directly calculated based on the junction capacitance and load resistor used, $f_{3dB} = 1/\left(2\pi R_L C_j\right)$. For $D^*$ calculations, a 1 Hz ENBW is a common value used.

The effect of each parameter, on $D^*$, is illustratively shown in Figure 35. In the left panels, two hypothetical devices both have a high responsivity. However, the device with the lower noise will have a much higher $D^*$ due to the lower variation in the signal intensity. Additionally, for detectors with equal noise and responsivity, the large device yields a larger $D^*$. This equal response and noise for differing sizes is less common, because the reduced responsivity and higher noise components trend of larger devices.

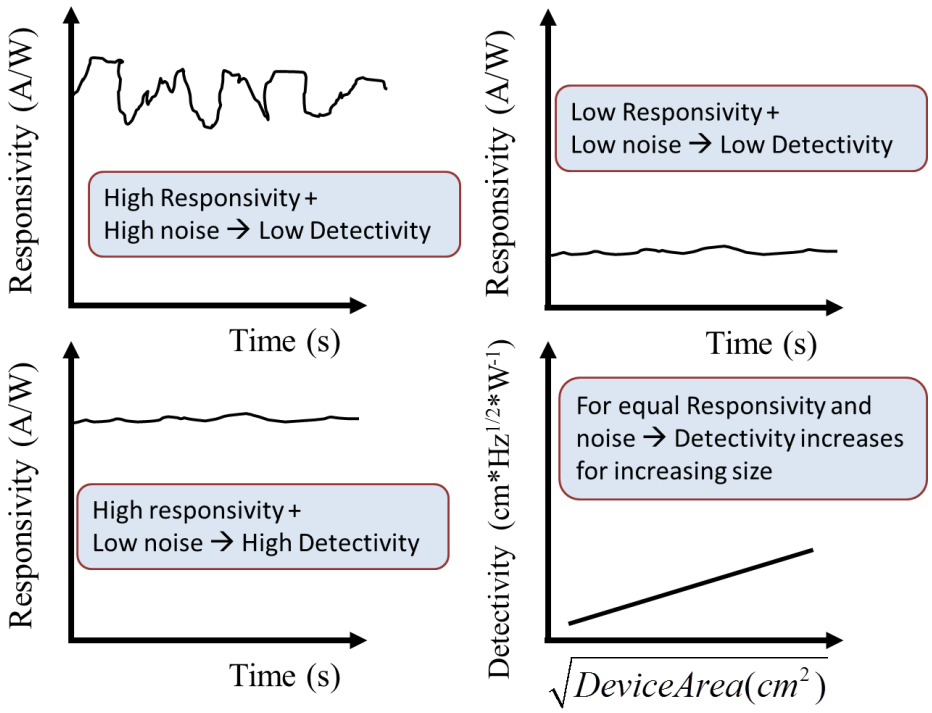


Figure 35: Relative effects of device noise, responsivity, and area have on the detectivity ($D^*$).

## Chapter 5: Fundamental Study of $Ge_{1-x}Sn_x$ Photoconductors

This chapter established a baseline for the spectral response, responsivity, detectivity, and effective carrier lifetime of $Ge_{1-x}Sn_x$ photoconductors grown on Ge buffered Si. This study investigated the efficacy of $Ge_{1-x}Sn_x$ materials as photodetectors in the short-wave infrared (SWIR) region, 1.4 to 3.0 μm. This study covered films with Sn composition and film thickness listed in Table 8. A fabrication methodology was developed using a low complexity and Si CMOS compatible process. The fabrication process developed shows consistency for all Sn compositions. Finally, the figures of merit for an advanced detector are measured for each sample, and in the temperature range of 300 to 77 K. The experimental data showed that the $Ge_{1-x}Sn_x$ material is a promising candidate for extended infrared response on Si and established a baseline for all future $Ge_{1-x}Sn_x$ detectors.

Table 8: Sn composition and film thickness of $Ge_{1-x}Sn_x$ photoconductors

| Sn% | $Ge_{1-x}Sn_x$ Thickness (nm) | Ge Buffer Thickness (nm) |
|---|---|---|
| 0.9 | 327 | 763 |
| 3.2 | 76 | 684 |
| 7.0 | 240 | 755 |
| 8.0 | 90 | 700 |
| 9.0 | 79 | 700 |
| 10.0 | 95 | 700 |

### 5.1 Experimental Setup

#### 5.1.1 $Ge_{1-x}Sn_x$ Growth and Device Fabrication

The $Ge_{1-x}Sn_x$ thin films were grown by ASM America within an ASM Epsilon reduced pressure chemical vapor deposition (RPCVD) reactor. A Ge buffer was first deposited on the 150 or 200 mm Si substrates. The $Ge_{1-x}Sn_x$ epilayers were then deposited on the Ge buffer using $GeH_4$ and $SnCl_4$ precursors at a temperature below 450 °C. Rutherford backscattering, secondary

ion mass spectroscopy, and x-ray diffraction measured the Sn composition and the substitutional lattice incorporation of the Sn atoms within the films.

Square photoconductor mesas were fabricated with side lengths of 2.0, 1.5, 1.0, and 0.5 mm, and the metal contact spacing for each device is 1.6, 1.2, 0.7, and 0.3 mm, respectively. The process flow for the fabrication process is illustrated in Figure 36. Before photolithography, the samples were cleaned in an acetone then isopropyl alcohol ultra-sonic bath for 5 minutes each to remove organic residue on the surface. The samples were then subjected to a dehydration bake to promote adhesion of the photoresist. Then HMDS adhesion promoter was spin-coated on and followed immediately by AZ4110 photoresist. The photoconductor fabrication was conducted using standard UV photolithography and a chromium pattern on glass mask. The photoconductor mesas were then over etched down to the Si substrate using the dry etch recipe, GeSn_ET, as described in Appendix H. Over etching into the Si substrate was done to improve carrier confinement amongst devices since at reduced temperature the increased effective carrier lifetime can allow for crosstalk between detectors.

A $SiO_2$ layer was then deposited via plasma enhanced chemical vapor deposition (PECVD) as a passivation layer. The oxide thickness was 1300 nm for devices with Sn compositions of 0.9, 3.2, and 7.0%. For devices with increased Sn content, and thus a longer infrared cut-off, a thinner 130 nm oxide was used. The thinner oxide was used to reduce the amount of IR absorption in the oxide film at longer wavelengths. Windows in the oxide were opened up with a buffered oxide etch (BOE), followed immediately by thermal evaporation of 10 nm Cr and 300 nm of Au for Ohmic contacts. The optical image in Figure 37 shows the final fabricated photoconductor after metal lift-off for the 500 and 1000 μm square mesas. The metal

contact pads of each device were wire bonded with 1 mil Au wire and packaged for electrical and optical testing within a low temperature cryostat.

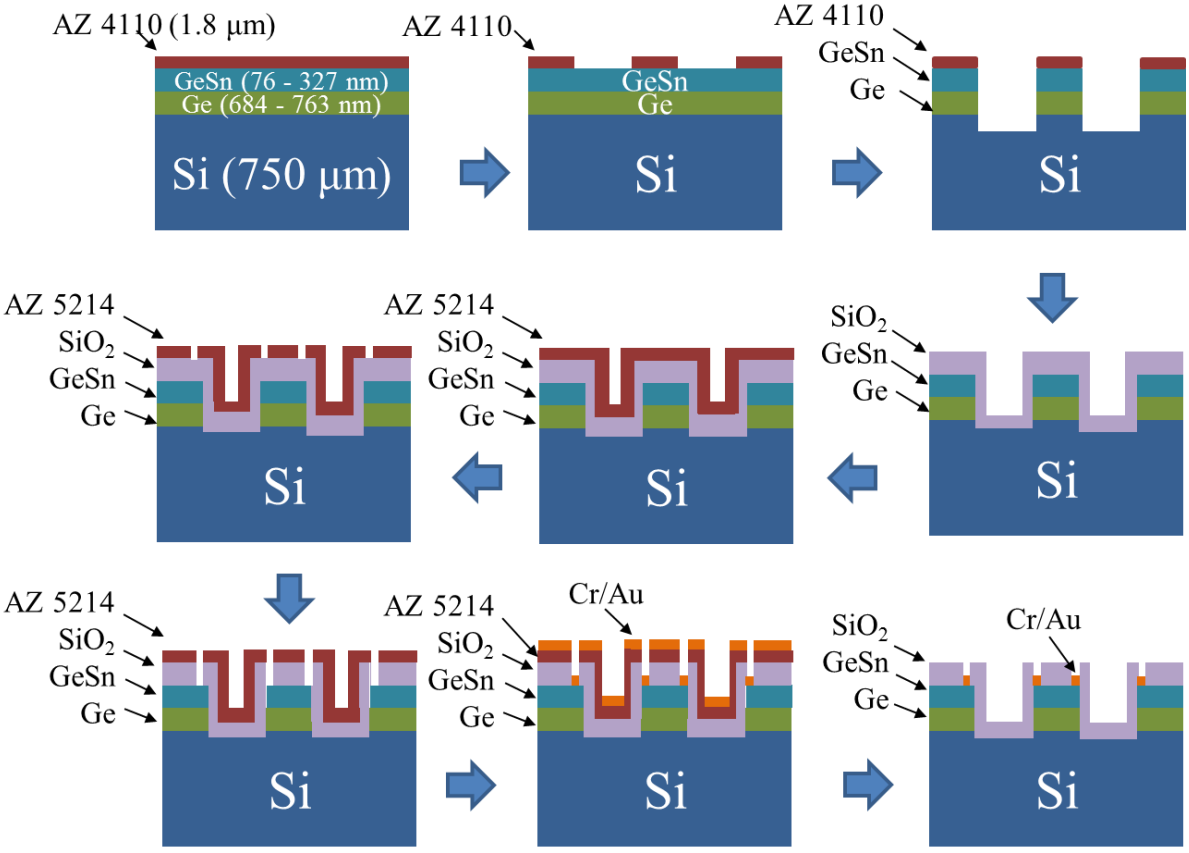


Figure 36: Process flow for fabrication of $Ge_{1-x}Sn_x$ photoconductors grown on Ge buffered Si.

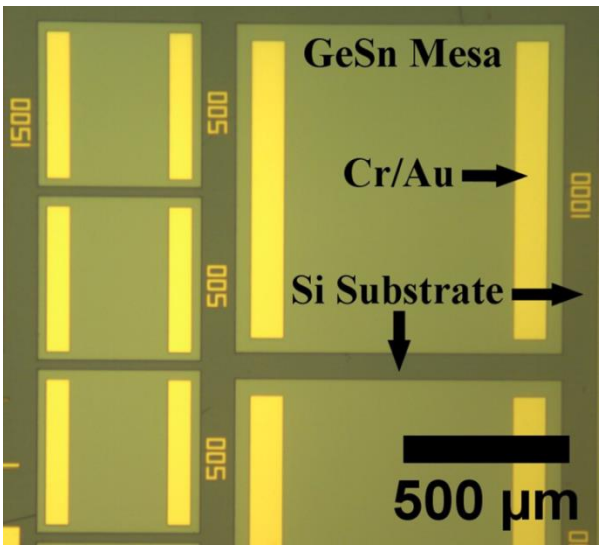


Figure 37: Top view optical image of a fabricated $Ge_{1-x}Sn_x$ photoconductor. This image of the 0.5 and 1.0 mm mesas was taken after the metal lift-off process.

A transmission line measurement (TLM) structure was also fabricated on each photoconductor die as well for measuring the contact and sheet resistance. This structure contains metal pads deposited on the $Ge_{1-x}Sn_x$ surface that had a fixed size but the spacing between the pads was varied from 10 to 70 μm in 10 μm increments as shown in Figure 38. The metal pads were 235 μm wide by 200 μm long. The width of the $Ge_{1-x}Sn_x$ transmission line was 290 μm. Due to the limited isolation between pins on the wire bonded dual in line package (DIP), these structures were not wire bonded. Only room temperature measurements were conducted using on-wafer probes for the TLM measurements to verify Ohmic contacts. As an example, the $Ge_{0.9}Sn_{0.1}$ photoconductor had a measured sheet resistance of 5400 Ω/sq and a contact pad resistance of 130 Ω.

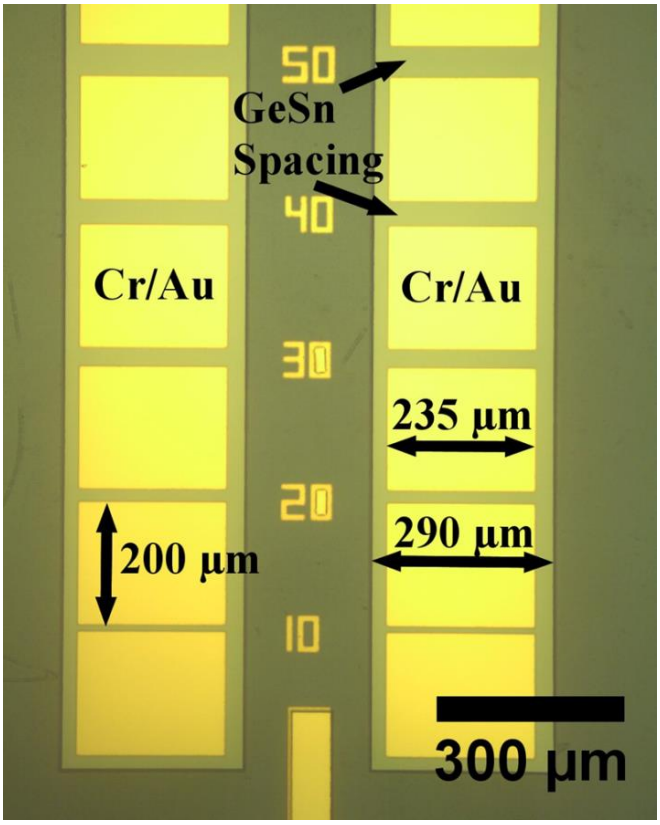


Figure 38: Top view optical image of the transmission line structure fabricated on the photoconductor die.

### 5.1.2 Characterization and Measurement Setup

The experimental testing setup consisted of a Fourier transform infrared (FTIR) spectrometer to measure the spectral response and lock-in amplifier with 1.55 μm laser diode for calibrated responsivity measurements. The spectral response was collected using the FTIR internal tungsten-halogen white light and ETC EverGlo IR source. The IR source has an operating emission temperature of 1140 °C. The DC bias was applied across the detector using a 50 Ω load resistor to measure the AC signal response connected to the FTIR internal electronics. Responsivity measurements using a FTIR or lock-in amplifier with optical chopper allow for a more accurate measurement of photoconductive devices since thermal drift and background light could be misinterpreted for DC measurement conditions.

Current-voltage (I-V) measurements were conducted using a Keithley 237 source measure unit (SMU) and a Keithley 6487 picoammeter/voltage source. The 6487 unit was preferred for its higher level of accuracy, but it has a 2.5 mA current limit for bias greater than 10 V. When measurements greater than 10 volts were applied, the 237 SMU was used. The I-V measurements were made by a LabView program which swept the voltage and measured the current within the device.

The AC responsivity measurements were conducted using a lock-in amplifier with an equivalent noise bandwidth (ENBW) of 1 Hz. The ENBW of the lock-in was adjusted by setting the appropriate time constant and slope roll off of the filter. For the Stanford Research 830 lock-in amplifier, a 100 ms time constant and 18 dB/oct roll-off were used, which corresponds to a 1 Hz ENBW. The dark current within this AC measurement setup was measured for each temperature and device for calculation of the noise current within the entire circuit. The noise current, 1 Hz ENBW, device active area, and responsivity were used to determine the $D^*$ for each device.

### 5.2 Background Carrier Activation Energy

The low temperature I-V measurements in Figure 39 (b) for each device confirmed that the metal contacts on the photoconductor were Ohmic. The 300 K measurements, shown in Figure 39 (a), exhibited a non-linear behavior for each photoconductor at 300 K. This rectifying behavior at elevated temperatures (300 K) is a result of the $Ge_{1-x}Sn_x$ Fermi level near the mid bandgap, close to the intrinsic level of the material. The position of the Fermi level near mid-gap results in a small space charge region around the metal-semiconductor interface. This band bending is due to the alignment of the metal work function and semiconductor Fermi level at the interface. A decrease in the minority carriers as temperature is decreased reduces this pinning effect, allowing the Fermi level to shift closer to the valence band. A similar effect was observed for HgCdTe photoconductors at a lower temperature range due to the smaller bandgap [94].

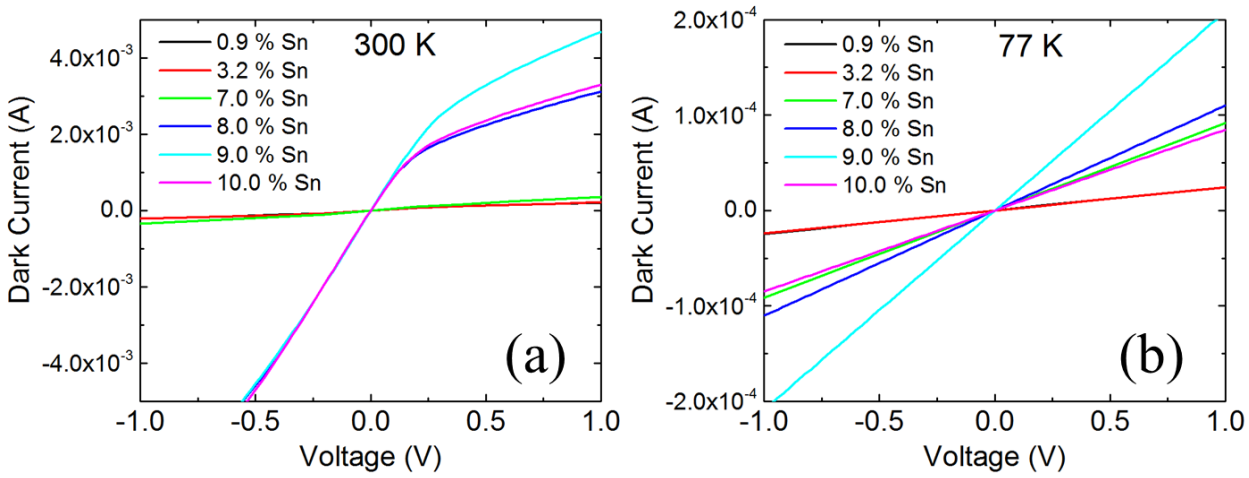


Figure 39: Dark I-V measurements of a 2 mm photoconductor for each $Ge_{1-x}Sn_x$ sample at (a) 300 K and (b) 77 K.

This temperature dependent pinning effect was observed experimentally by comparing the 7 and 10% Sn photoconductors in Figure 40, and comparing the respective dark resistance of each device in Figure 41. The lower Sn content sample [Figure 40 (a)] has an observed rectifying behavior for the 300 K that decreases to zero by 260 K. However, the higher content $Ge_{0.9}Sn_{0.1}$

photoconductor [Figure 40 (b)] shows evidence of a built in electrostatic barrier down to 220 K. The 7.0% Sn sample in Figure 40 (a) has a higher level of activated sites that contribute to a higher p-type background carrier concentration compared to the 10.0% Sn sample in Figure 40 (b). These activated defects (explained in further detail later in this section) allow for the lower content Sn samples to have a reduced metal-semiconductor barrier even at 300 K compared to the 8.0, 9.0, and 10.0% Sn samples.

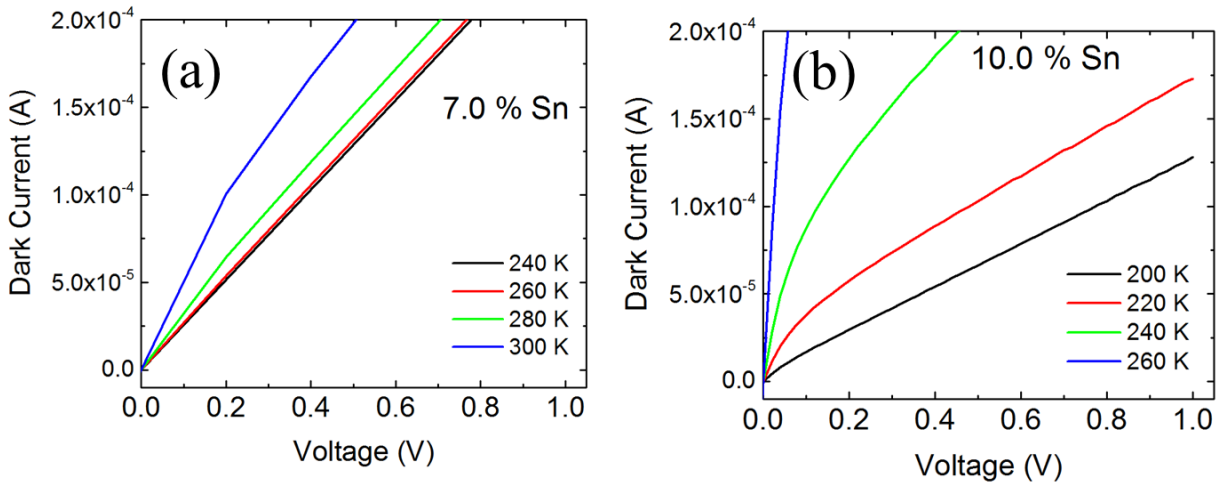


Figure 40: Temperature dependent dark I-V of the (a) $Ge_{0.93}Sn_{0.07}$ and (b)$Ge_{0.9}Sn_{0.1}$ 2 mm photoconductors showed a decreasing metal-semiconductor barrier with decreasing temperature.

The linear I-V region for each device and temperature was used to extract the dark resistance. This dark resistance shows the distinct regions of carrier activation within the material. The plot of dark resistance of the 2 mm photoconductors in Figure 41 showed three regions where the slope of the dark resistance vs temperature changes. Region 1 was the temperature range whereby the shallow dopants within the material are being ionized. This region is typically referred to as the freeze out region since carriers are frozen or inactivated. Within Region 2 all of the shallow dopants were activated. This temperature range, called the extrinsic region, has a small change in the device resistance, which is mostly due to surface traps

and deeper level defects within the material. For samples with 8.0, 9.0, and 10.0% Sn, no statistical difference in the slope was observed between Region 1 and 2. These samples maintained a near constant resistance value from 77 to 200 K. The absence of Region 1 in these samples indicated no ionized dopants were present in those materials and that the background doping level is intrinsic. Region 3 is the high temperature region where the resistance of the material decreased due to carriers being thermally excited across the bandgap. This region is called the intrinsic region since an equal number of holes and electrons exist within the material.

Between the samples plotted in Figure 41, there were distinct similarities between the (Group I) 0.9, 3.2, and 7.0% Sn samples that differ from the (Group II) 8.0, 9.0, and 10.0% Sn samples. The Sn content of Group I was below the indirect-to-direct bandgap crossover point. The conduction band L-valley for these photoconductors remains sufficiently high that phonon assisted indirect generation-recombination is still dominant. For the case of Group II, the bandgap has decreased further due to the increased Sn content. Additionally, the direct Γ-valley was now equal to or lower than the L-valley allowing for direct generation-recombination to occur. These two aspects allow for a lower carrier density, and thus higher dark resistance for the lower Sn content samples.

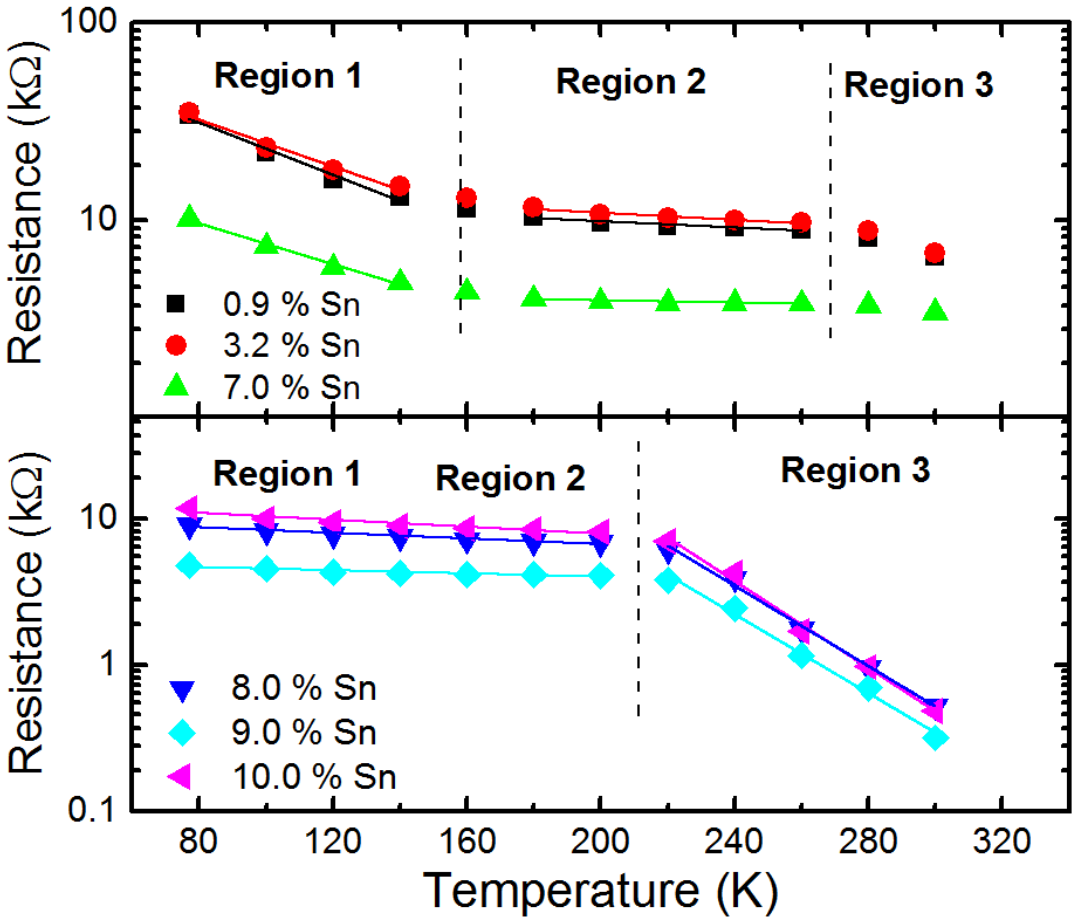


Figure 41: Dark resistance of each 2 mm $Ge_{1-x}Sn_x$ photoconductor measured for varying temperature. Regions 1, 2, and 3 defined the regions of changing slope for each detector set.

The measured dark resistance of a device for varied temperature allowed for extraction of the carrier activation energy. The resistance of a semiconductor is determined by, $\Re = l/(\sigma \times A)$ where σ is the conductivity, l is the material length, A is cross sectional area. The conductivity is defined as, $\sigma = q(\mu_n n + p\mu_p)$. The change in conductivity due to temperature is dominated by the orders of magnitude change in the carrier concentration. As a result, the temperature dependent conductivity can be described using an Arrhenius relationship [90], $\sigma = B_1 \exp(-E_A/[2kT])$ where $B_1$ is a pre-factor constant, k is Boltzmann constant, and $E_A$ is the carrier activation energy. Substituting the Arrhenius relationship into the resistance relationship yields an Arrhenius form of the resistance as a function of temperature,

$$\Re = B_2 \exp\left(\frac{E_A}{2kT}\right) \quad 5.1$$

where $B_2$ is a new pre-factor constant containing the length and area of the semiconductor.

The natural logarithm of the dark resistance [ln(R)] was plotted versus 1/T in Figure 42. The y-axis for both the top and bottom plot was spaced equally to allow for an equal assessment between the two sample sets. From Equation 5.1 the activation energy was calculated, $E_A = Slope \times (2k)$. The activation energy for each Sn composition and region is listed in Table 9. The empty cells in this table were due to the lack of high temperature data points for Group I, and lack of a low temperature freeze-out region for Group II. The carrier activation energy for each region falls within the expected values for each range. For Group II, Region 3 had activation energies around the bandgap energy further confirming that these materials are intrinsic in the high temperature range.

Table 9: Carrier and trap activation energy for 2 mm $Ge_{1-x}Sn_x$ photoconductors

| | Carrier Activation Energy (eV) | | |
|---|---|---|---|
| Sn Composition (%) | Region 1 ±0.002 | Region 2 ±0.0007 | Region 3 ±0.022 |
| 0.9 | 0.028 | 0.006 | - |
| 3.2 | 0.026 | 0.007 | - |
| 7.0 | 0.022 | 0.002 | - |
| 8.0 | - | 0.007 | 0.411 |
| 9.0 | - | 0.003 | 0.410 |
| 10.0 | - | 0.008 | 0.442 |

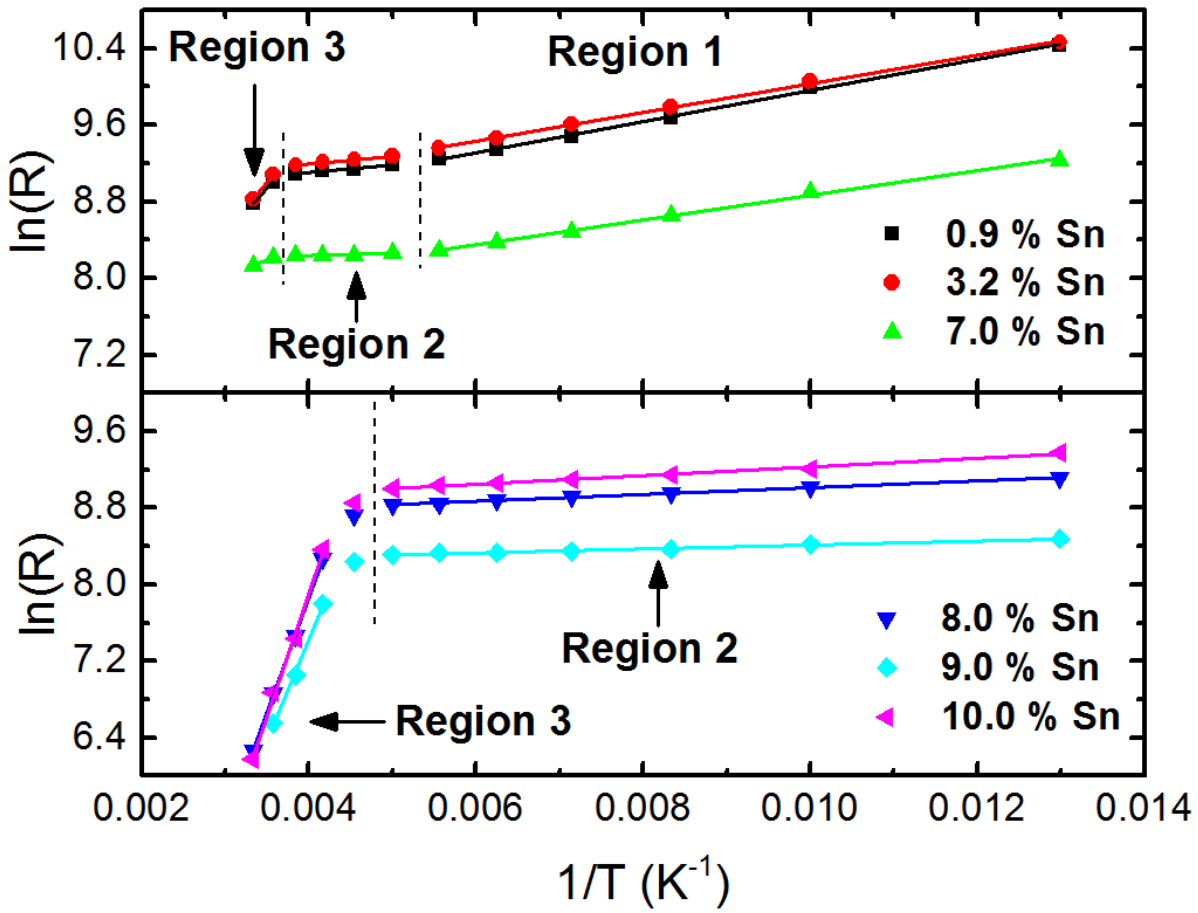


Figure 42: Natural logarithm of the 2 mm photoconductor dark resistance [ln(R)] plotted for 1/T. The slope of each separate region corresponds to the corresponding carrier activation energy ($E_A$).

Identifying the carrier activation energy and background carrier concentration are important steps in material development for device applications. These traps and other defect sites within the material reduce the performance of a device by generating higher dark currents and noise within the detector signal. The source of the defects can then be identified through proper experimental design of the film growth or fabrication procedures followed by subsequent activation energy measurements. This work developed a reliable fabrication procedure for $Ge_{1-x}Sn_x$ devices that produced a background carrier activation limited by the material quality. This is evident by the intrinsic carrier generation of the 8.0, 9.0, and 10.0% Sn photoconductors for temperatures above 200 K.

### 5.3 Long-Wavelength Cut-off of $Ge_{1-x}Sn_x$ Photoconductors

The decreasing bandgap for increasing Sn composition causes the long-wavelength cut-off of these $Ge_{1-x}Sn_x$ based detectors to red-shift. This is well documented for materials at room temperature based on a Vegard's law interpolation between Ge and Sn [28]. The spectral response for Group I photoconductors as measured per temperature in Figure 43 showed the observed red-shift for increasing temperature. The spectral response was normalized to allow comparison of the detector cut-off and only select temperatures were shown here for clarity. A small red-shift in the spectral response for the direct absorption was observed for the 0.9% Sn content from that of Ge in Figure 43 (a). However, the 3.2% Sn was observed to have only absorption for the indirect band from 1.6 to 1.85 μm for the 300 K measurement. The strong absorption for this sample that starts at 1.6 μm for the 300 K measurement is due to the Ge buffer layer. The absorption due to the Ge buffer for the 3.2% sample allows comparison for the red-shift in the absorption edge in the 0.9% Sn sample. This confirms the increased response is due to the 0.9% Sn incorporation. Figure 43 (b) shows the spectral response of the 7.0% Sn sample was extended beyond 2.1 and 1.95 μm for the 260  and 77 K measurement, respectively. The signal-to-noise ratio of the 280 K and 300 K of this sample were too low to be considered reliable.

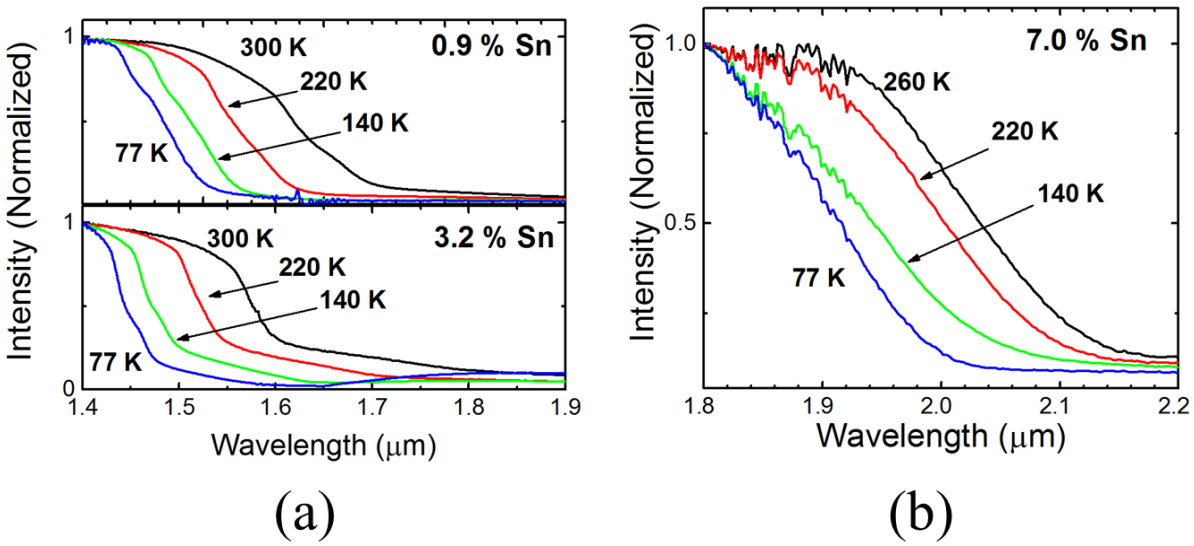


Figure 43: Normalized spectral response of the (a) 0.9, 3.2, and (b) 7.0% Sn photoconductors for different temperatures as a function of wavelength shows the shifting absorption edge for increased Sn composition. © 2014 Optical Society of America [92]

Absorption in the $Ge_{0.93}Sn_{0.07}$ photoconductor sample was to the indirect L conduction band. This was determined by plotting the log of the spectral response intensity versus the photon energy. From Equation 4.30, the slope of this plot at the absorption edge is expected to be ½ for direct bandgaps and 2 for indirect bandgaps. Due to the thermal population of carriers within both the indirect and direct bands at increased temperatures, the 77 K measurement in Figure 44 was used to determine the γ exponent. The $Ge_{0.93}Sn_{0.07}$ has a slope of 2.03 indicating it is an indirect gap transition. Absorption at 1.5 μm has a γ value of 0.51 as expected for the direct absorption edge of the Ge buffer layer.

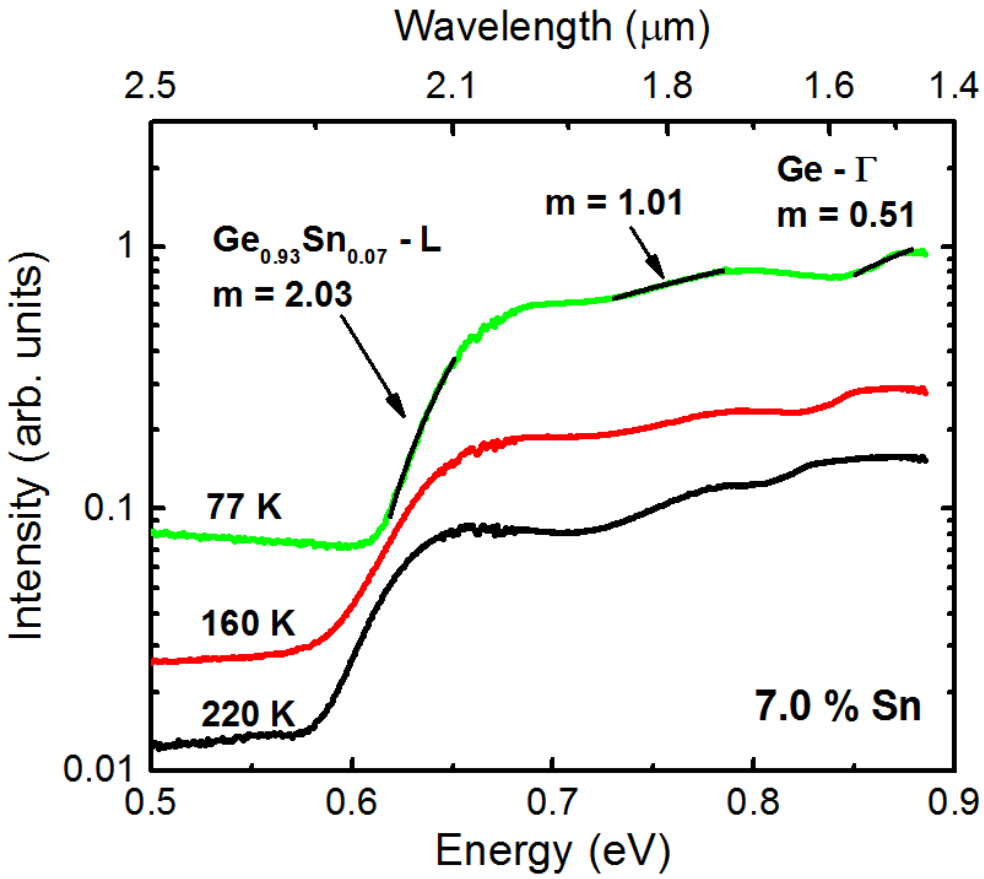


Figure 44: Absolute spectral response temperature profile of the 7.0% Sn photoconductor shows increasing response intensity for decreased temperature. The absorption edge power factor (m) indicates either direct or indirect absorption. © 2014 Optical Society of America [92]

Spectral response for the Group II photoconductors all showed extended red-shift of the long-wavelength cut-off compared to the lower Sn samples. The spectra for these samples in Figure 45 were normalized at 1.8 μm and only some of the intermediate temperatures were plotted for clarity. The longest wavelength response was observed for the 9.0% Sn sample at 300 K, which has a response out to 2.40 μm. The expected longer-wavelength response of the 10% Sn sample could be suppressed by compressive strain in the film, which widens the bandgap. All the spectra in Figure 45 were collected using the IR source within the FTIR, while the white light source was used for measuring the spectra in Figure 43. The spectral radiance of the white light source was insufficient beyond 2.2 μm for an accurate spectral response measurement.

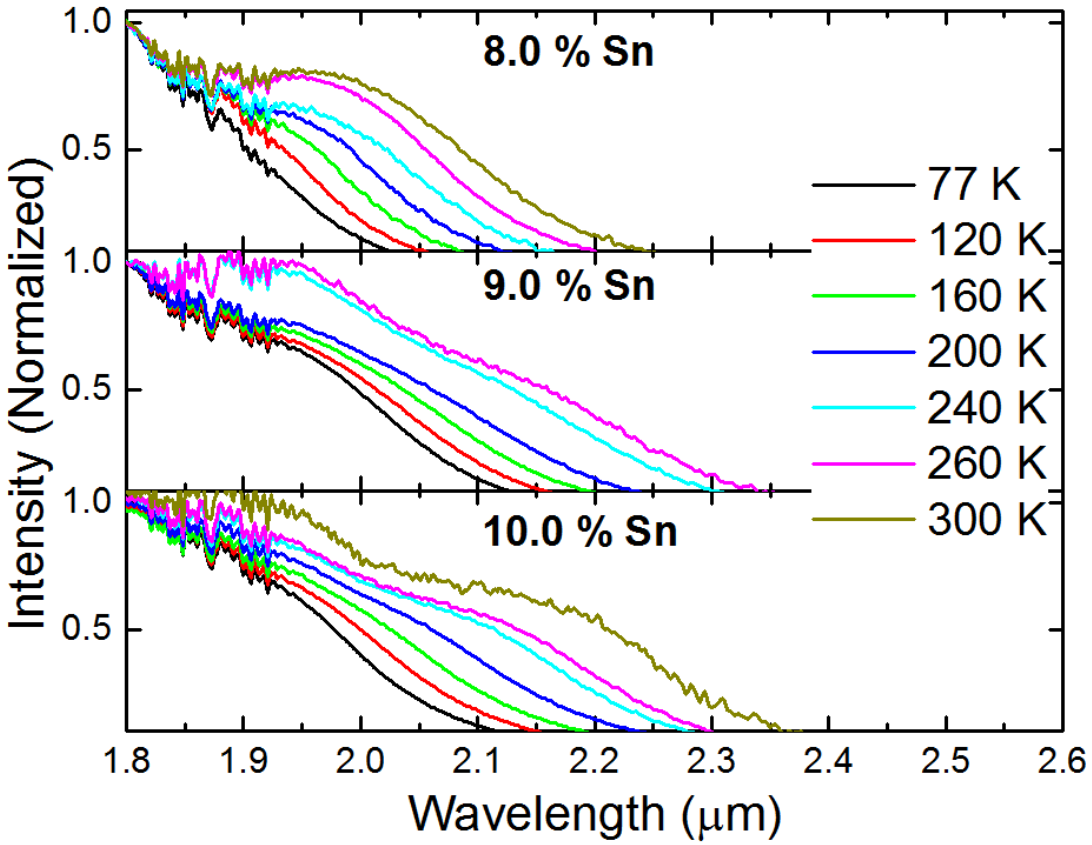


Figure 45: Temperature dependent long-wavelength spectra of $Ge_{1-x}Sn_x$ photoconductors with Sn composition 8.0 – 10.0%.

The long-wavelength cut-off of each detector was extracted by measuring the wavelength at 50% (-3 dB) down from the top of the absorption band of interest [95-98]. For example, the 8.0% Sn absorption edge in Figure 45 of interest had an intensity of 0.7 at 300 K for the leading cut-off band. The 50% cut-off has an intensity of 0.35 which occurs at 2.113 μm. Using this 50% cut-off method the temperature dependent bandgap of each photoconductor was extracted and plotted in Figure 46. The indirect absorption of the 3.2% Sn sample diminishes for reduced temperatures, thus it was not shown here below 260 K. Additionally, the low SNR for the 7.0% Sn above 260 K prevented extraction of the cut-off for those temperatures.

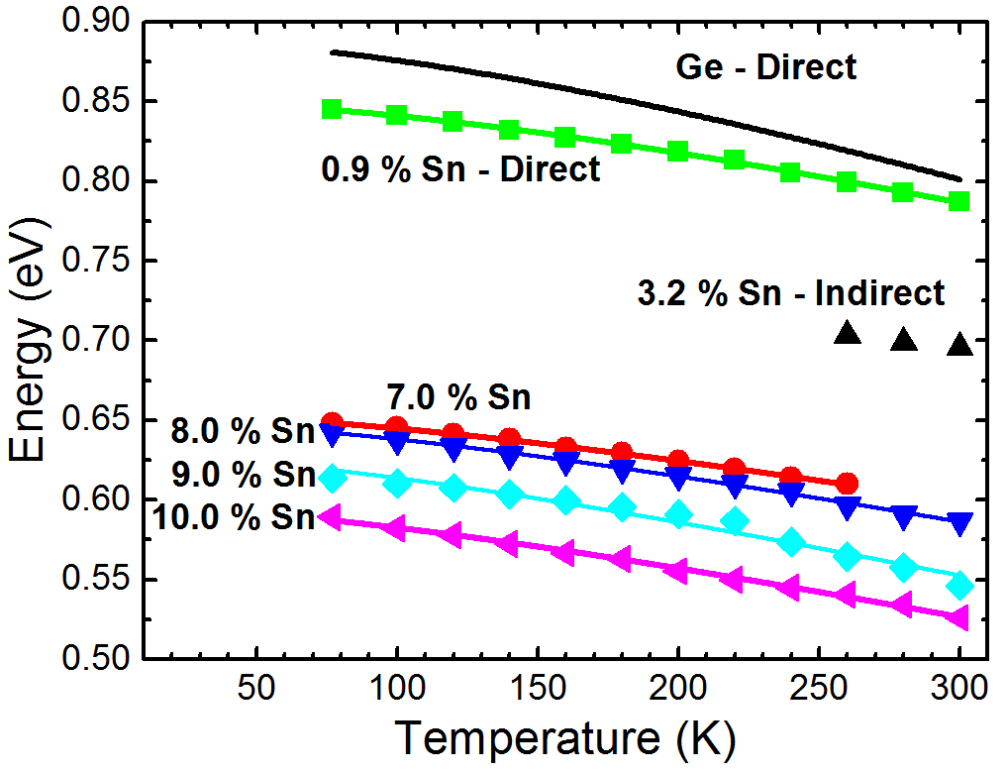


Figure 46: Detector cut-off plotted for each measured temperature and fitted using the Varshni relationship. The Ge-direct line was plotted from ref. [99] and is shown here for comparison.

The detector cut-off wavelengths measured for each temperature were fitted using the Varshni relationship [99],

$$E(T) = E(0) - \frac{(\alpha T^2)}{(\beta + T)} \qquad 5.2$$

where E(T) is the temperature dependent band gap, E(0) is the bandgap at 0 K, and α and β are fitting parameters. The β parameter in the Varshni parameter is generally close to the Debye temperature of the material. The Debye temperature and accepted β parameters for Ge being 374 and 398 K, respectively [99]. For the $Ge_{1-x}Sn_x$ material system, a 7.0 and 8.0% Sn film were fitted with β parameters at 269 and 226 K, respectively, with unconstrained fitting parameters. However the 9 and 10% Sn films were unable to arrive at unconstrained solution. The Debye temperature for α-Sn is 155 K [100], thus it was expected that the β parameter should be between this value and that of Ge. Using this lower limit and the decreasing trend of the 7.0 and 8.0% Sn

film, the β for 9.0 and 10.0% Sn was fixed at 200 K. The compressive strain of these samples obscured these values slightly compared to a relaxed film due to the thermal coefficient mismatches of the $Ge_{1-x}Sn_x$ layer, Ge buffer, and Si substrate [101, 102]. The fitted Varshni parameters and the standard error from the fitting process are listed in Table 10.

Table 10: Fitting parameters for $Ge_{1-x}Sn_x$ temperature dependent bandgap

| Sn Composition (%) (± 0.2%) | | Fitting Parameter | | |
|---|---|---|---|---|
| | | $E_\Gamma(0)$ (eV) | α (eV/K) | β (K) |
| 0.9 | Fitted Value | 0.851 | $5.1 \times 10^{-4}$ | 416 |
| | Standard Error | 0.001 | $0.8 \times 10^{-4}$ | 123 |
| 7.0 | Fitted Value | 0.654 | $3.5 \times 10^{-4}$ | 269 |
| | Standard Error | 0.001 | $0.6 \times 10^{-4}$ | 111 |
| 8.0 | Fitted Value | 0.649 | $3.7 \times 10^{-4}$ | 226 |
| | Standard Error | 0.002 | $0.6 \times 10^{-4}$ | 90 |
| 9.0 | Fitted Value | 0.628 | $4.2 \times 10^{-4}$ | 200 (Fixed) |
| | Standard Error | 0.002 | $0.3 \times 10^{-4}$ | - |
| 10.0 | Fitted Value | 0.595 | $3.8 \times 10^{-4}$ | 200 (Fixed) |
| | Standard Error | 0.0008 | $0.07 \times 10^{-4}$ | - |

Plotting the zero Kelvin bandgap for each of the Sn compositions in Table 10 showed the linear relationship with Sn content. A linear fit of this data resulted in a y-intercept that was expected to equal the $E_\Gamma(0)$ of Ge and a slope equal to the composition dependent bandgap factor. The extracted y-intercept of 0.87 (±0.03) eV was within the margin of error of the expected $E_\Gamma(0)$ for Ge (0.889 eV [99]). The Sn content dependent $E_\Gamma(0)$ was reported for the first time here for $Ge_{1-x}Sn_x$ alloys. The extracted slope in Figure 47 was -0.028 (±0.002) eV/[% Sn]. The 7.0% Sn content photoconductor is the only sample that was far from the linear trend of the remaining samples. This departure from the expected trend was due to the indirect L-valley remaining the dominant absorption edge for this level of Sn composition. The 0.9, 8.0, 9.0, and 10.0% Sn long-wavelength samples are all measurements of the direct, Γ, absorption edge.

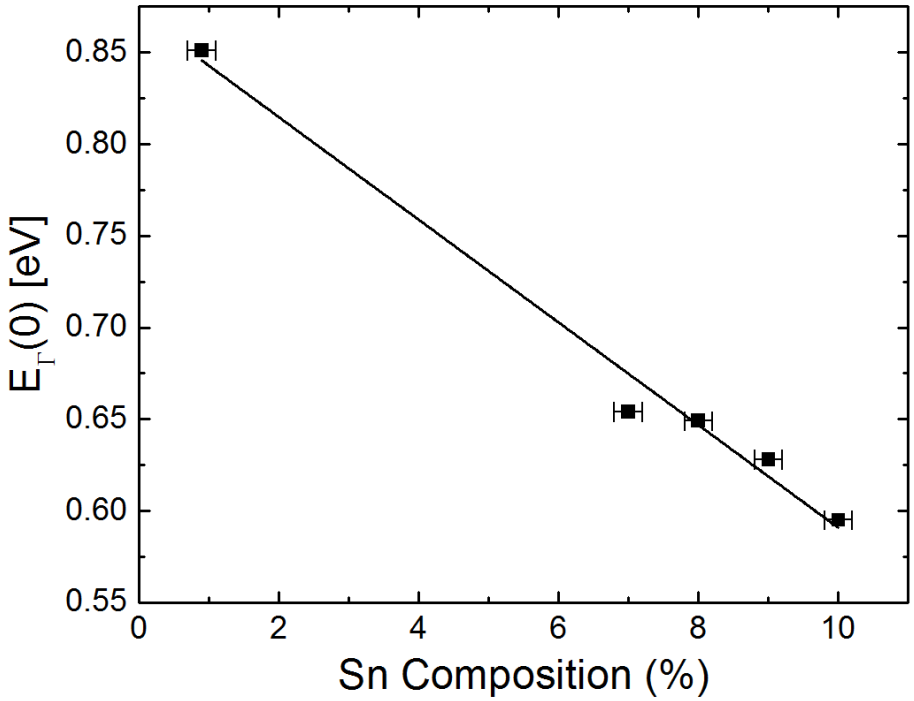


Figure 47: Zero Kelvin bandgap of $Ge_{1-x}Sn_x$ alloys extracted from the temperature dependent photoconductor long wavelength cut-off.

**5.4 Responsivity**

The responsivity maximum for the 0.9 and 3.2% Sn photoconductors occurred at an intermediate temperature, rather than increasing monotonically with decreasing temperature. These 2 mm mesas with 0.9 and 3.2% Sn had a peak at 180 and 160 K, respectively. Although for both of these devices, the dark current reduced for decreasing temperature. This decrease in responsivity at reduced temperature was due to the blue-shifting band edge of these two samples away from the 1.55 μm excitation source. The responsivity increased for decreasing temperature due to the reduced dark current up to the temperature where the absorption coefficient blue-shifts away from 1.55 μm. The linear increase in the responsivity observed for increased DC bias in all samples was indicative of the photoconductive gain and the decreasing carrier transit time for increased bias.

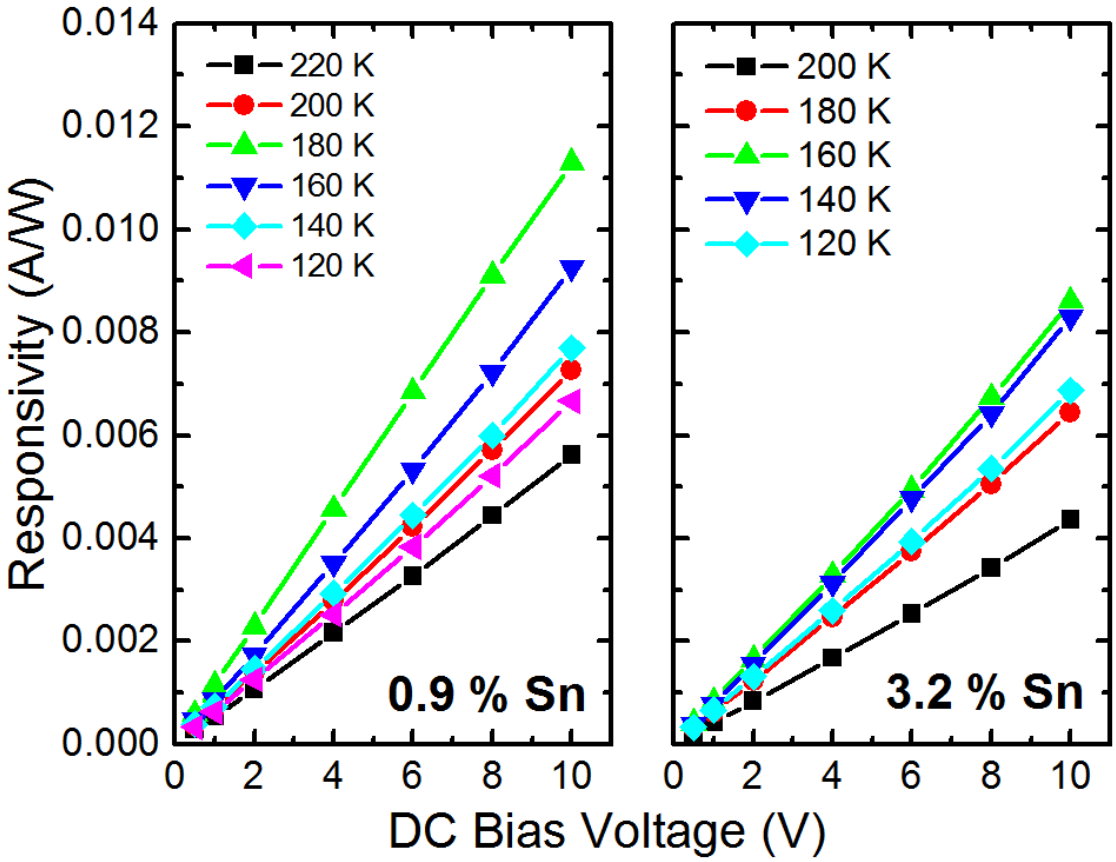


Figure 48: Responsivities of the 0.9 and 3.2% Sn photoconductors measured at 1.55 μm and plotted for the DC bias voltage. The photoconductor mesa size was 2 mm.

Responsivity of the 2 mm $Ge_{0.93}Sn_{0.07}$ photoconductor increased monotonically for decreasing temperature. The lowest temperature measurement in Figure 49 showed an equally maximum responsivity at 77 and 100 K. The absorption edge for this Sn composition as measured in Figure 43 (b) never blue-shifted past the 1.55 μm excitation laser, yielding a responsivity that increased with decreasing temperature due to the decreased dark current. The maximum value obtained for this sample occurred at 10 volts with a responsivity of 0.077 A/W.

A large 3 times increase in the responsivity over the 7% Sn photoconductor was observed for the higher Sn samples. The measured responsivity of the 2 mm mesas for the 8.0, 9.0, and 10.0% Sn samples in Figure 50 showed this large increase in responsivity across all measured temperatures. The highest performance detector at 1.55 μm was the 8.0% Sn sample with a 0.300

A/W responsivity at 77 K and a 10 volt bias. Each sample measured in Figure 50 had an equal Ge buffer thickness and no more than a 16 nm difference in $Ge_{1-x}Sn_x$ thickness. Examination of the full width half max (FWHM) from XRD indicated the crystal quality of each sample was equivalent [8]. Thus the decreasing trend in the responsivity from 8.0 to 10.0% Sn was likely due to surface recombination. The increased Sn content leads to a higher absorption coefficient, α, at 1.55 μm whereby more photons are absorbed closer to the surface and these optically generated carriers recombined before being collected.

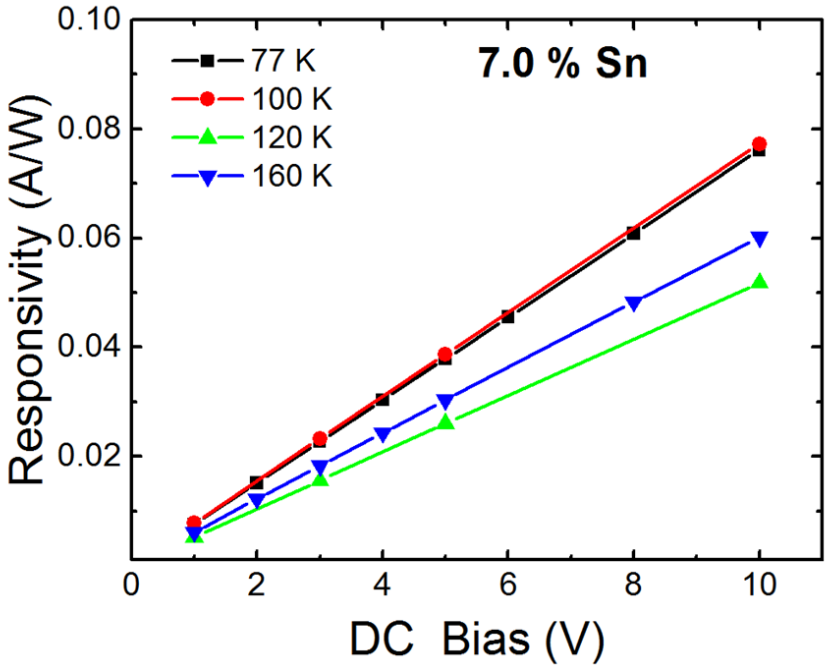


Figure 49: Responsivity of the 7.0% Sn photoconductor at 1.55 μm plotted for the lowest measured temperatures. The photoconductor mesa size was 2 mm.

The trend was observed that detector responsivity increased occurred due to the increased Sn content within the photoconductor film. This is due to a decreased Γ conduction valley with increased Sn content that allows for a higher density of states for the non-phonon assisted transitions. Additionally, the small activation energy of 3 to 7 meV from 200 K down to 77 K for the Group II samples indicated an already depleted active material of background carriers. This

further indicated that the Sn content of these films did not degrade detector responsivity despite the large 1.7% lattice mismatch for $Ge_{0.9}Sn_{0.1}$ when grown on Ge buffered Si.

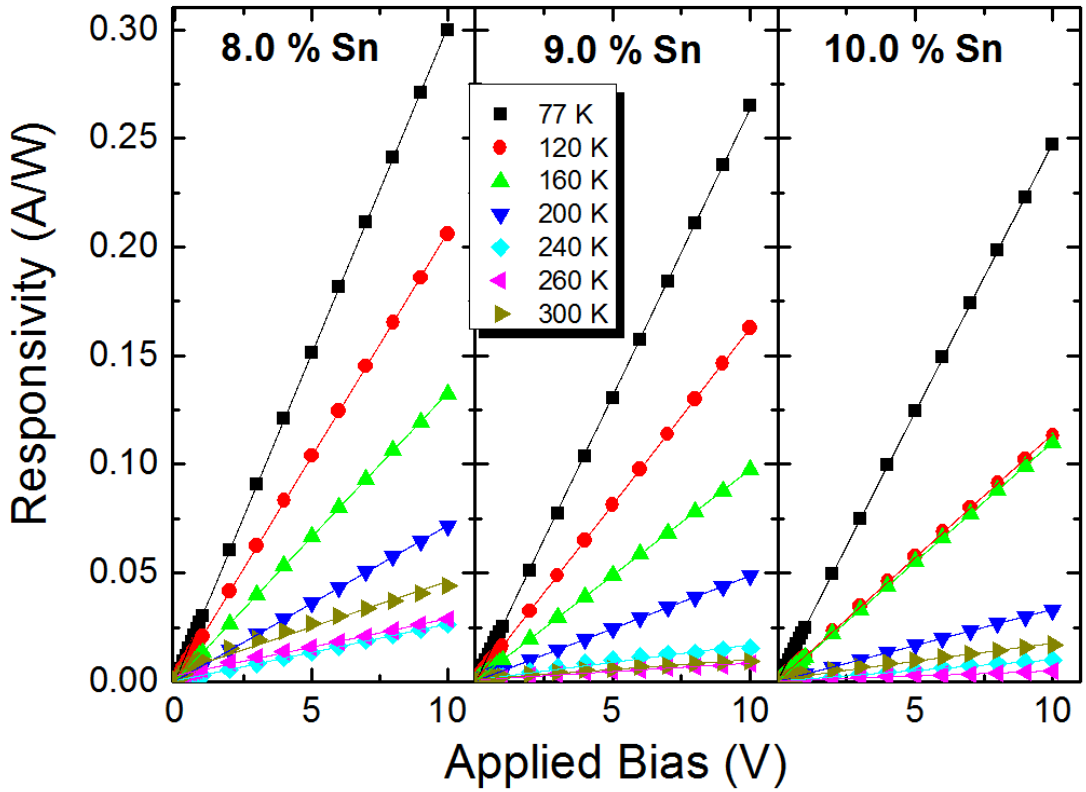


Figure 50: Responsivity of the 2 mm photoconductor mesas with 8.0, 9.0, and 10.0% Sn were measured as a function of applied bias, and across different temperatures.

The responsivity of a higher Sn content sample (from Group II) was further analyzed for the varying photoconductor mesa size. All previous measurements on each photoconductor sample from 0.9 to 10% Sn samples were done on 2 mm square mesas to allow direct comparison of the effect of Sn composition. Further study was done on the effect of photoconductor mesa size on the 8.0% Sn sample. The responsivity at 1.55 μm was measured for each temperature from 77 to 300 K in 20 K increments and as a function of bias voltage with 1 V increments. This was done for 0.5, 1.0, and 2.0 mm square mesas. The responsivity for each of these variables was plotted in a 3D contour plot in Figure 51. The color contours correspond to the responsivity values on the z-axis as marked in the legend.

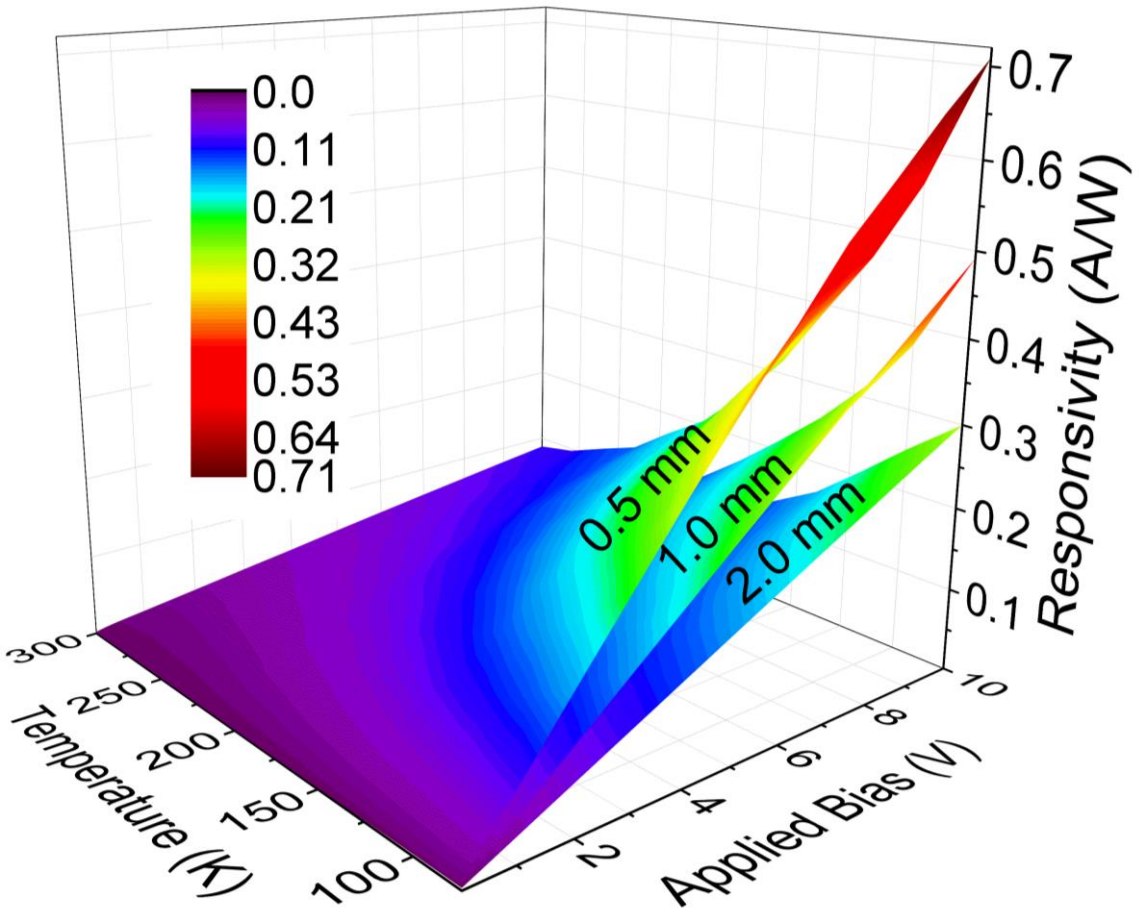


Figure 51: Responsivity at 1.55 μm for the 8.0% Sn photoconductor measured as a function of temperature and applied bias voltage and plotted in a 3D contour plot. This measurement was conducted on 0.5, 1.0, and 2.0 mm square mesas.

A noticeable increase over 2 times from the 2.0 mm mesa to the 0.5 mesa is observed for equal temperature and applied bias. This increase in response was a result of the reduced carrier transit time for the smaller mesa. Spacing between the metal contacts for the 2.0 and 0.5 mm mesas is 1.6 and 0.3 mm, respectively. By examination of Equation 4.41 and the definition of photoconductor gain leads to a linear dependence of photoconductor gain due to the applied bias ($G \propto V_B$), but an inverse squared dependence due to the metal contact spacing ($G \propto 1/L^2$). Based on this relationship, the reduction in metal contact spacing from 1.6 to 0.3 mm should have a 28 time increase in responsivity instead of the observed 2.3 time increase. This large difference could be due to the laser spot being larger than the 0.5 mm photoconductor mesa,

leading to a lower responsivity. The other possible cause is the high surface recombination near the metal contacts causing a reduction in the effective carrier lifetime within the smaller device. The latter effect is studied in more detail in Chapter 6.

The 9.0 and 10.0% Sn samples were measured at 77 K for the effect of decreasing mesa size on the device responsivity. The same trend of increasing responsivity for decreasing mesa size was observed in Figure 52. For the 9.0% Sn sample, the 0.5 mm mesa was measured with the highest responsivity with a two times increase in responsivity over the 2.0 mm mesa device. However, the 10.0% Sn sample showed a 3.8 factor increase in responsivity compared to the 2.0 mm mesa at 10 volts bias for the 0.5 mm mesa. The change from a linear dependence to saturation on the bias voltage was due to the carrier sweep out effect. This effect occurs when the effective lifetime of the minority carriers becomes longer than the transit time. As a result the minority carriers were swept across the length of the device and collected resulting in a charge imbalance that was compensated by an electric field build-up around the metal contacts. The localized dip in the responsivity for the 10.0% Sn with a 0.5 mm mesa size around 2 volts was likely due to an isolated instrument error since this same effect is not observed in other samples. This effect was also not observed when the measurement was repeated in Figure 53 for the same device on a different instrument.

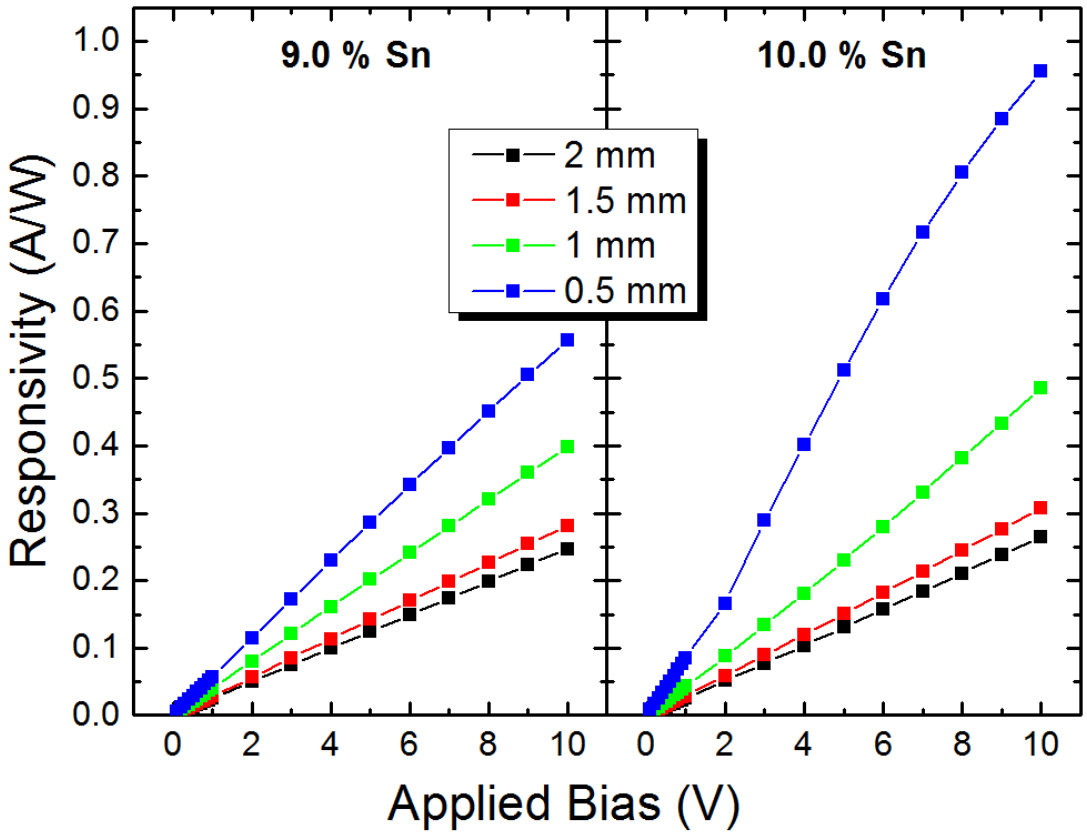


Figure 52: Effect of mesa size on responsivity at 1.55 μm compared for the 9.0 and 10.0% Sn photoconductors at 77 K.

The applied bias of the 10.0% Sn sample at 77 K was further increased beyond 10 volts and the measured responsivity is shown in Figure 53. The increased bias beyond 10 volts resulted in an amplification of this sweep out effect for the 0.5 mm mesa. The responsivity for the 0.5 mm mesa began to saturate at 15 volts. The 1.0 mm mesa had an observed saturation being first observed around 40 volts as indicated by the reduced slope at this point. The transit time for these two devices at this sweep point voltage was calculated using Equation 4.41 and the measured mobility. The Hall mobility for this sample was measured at 77 K to be 1046 $cm^2/(V*s)$. The calculated transit time for the 1.0 and 0.5 mm mesas was $1.2x10^{-7}$ and $5.7x10^{-8}$ s, respectively. Since the sweep out effect occurs when the minority carrier effective lifetime becomes longer than the transit time, then these two transit times provided an estimate of the effective minority carrier lifetime within the sample. The disagreement in these two values is

likely due to the inaccuracy in determining the turning point, or beginning of sweep out by this method.

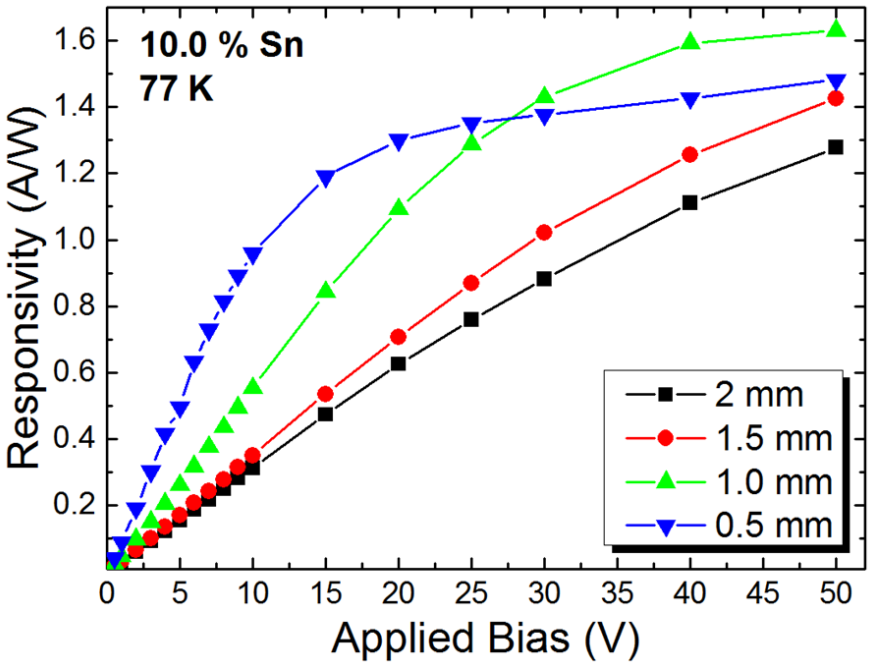


Figure 53: High voltage bias effect on responsivity was measured for 10.0% Sn photoconductor at 77 K. The measurement was made using a 1.55 μm laser source.

The largest observed responsivity occurred for the 10.0% Sn photoconductor with a 1.0 mm mesa size at 77 K. The responsivity at this point, measured at 1.63 A/W, corresponded to quantum efficiency (QE) of 130%. The above 100% QE was due to the photoconductive gain and allows this device to achieve a higher responsivity than commercially available Ge and InGaAs detectors. These two materials have on average a QE of 65 and 80% for photodiodes, respectively. This photoconductive gain is advantageous over detector and electronic amplifier combinations in low flux operations. High electronic amplification requires an increased input impendence that results in a higher Johnson-Nyquist noise in the circuit. However, the power requirements of this high bias operation are a disadvantage of this type of signal amplification.

## 5.5 Effective Carrier Lifetime

A linear fit of the responsivity vs voltage in Figure 50 for the 10.0% Sn photoconductor was performed using Equation 4.47 to find the effective lifetime, $\tau_{eff}$,. This value was calculated and plotted for the 2 mm mesa over temperature in Figure 54. The temperature dependent quantities in Equation 4.47 were $\alpha$ and $\mu_p$. For high Sn compositions where the absorption band edge is far from the incident wavelength of 1.55 μm, the temperature dependent effects on $\alpha$ were expected to be negligible. The mobility was also temperature sensitive in the 77 to 300 K range of interest. Hall effect measurements at 77 and 300 K measured the mobility to be 1046 and 196 $cm^2/(V*s)$, respectively. The mobilities between these two measured values was extrapolated using the temperature dependent mobility model, [103] $\mu = \beta T^{-1.5}$ where the fitting parameter $\beta$ was fitted as $7.12x10^5$ based on the measured Hall mobility values.

The effective carrier lifetime remains mostly unchanged above 260 K, then increases with decreasing temperature. Under low injection, the dominant recombination process was Shockley-Read-Hall and surface recombination. Thus, the increase in lifetime was due to reduced number of activated recombination centers as temperature was decreased. The decrease in lifetime for the 77 K measurement was due to the increased minority carrier lifetime observed in the responsivity measurements to incur a sweep out effect at the device contacts. The small space charge region around the metal contacts as a result of the longer minority carrier lifetime caused a decrease in the effective carrier lifetime of the majority carrier.

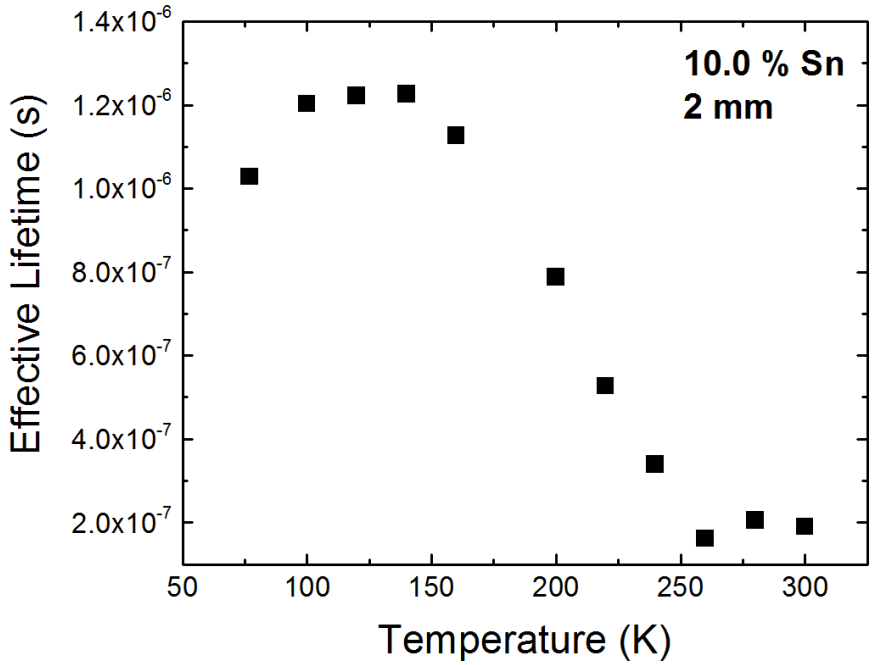


Figure 54: Effective lifetime of the 10.0% photoconductor with 1.6 mm electrode spacing (2 mm square mesa) calculated for each measured temperature.

The effective lifetime for each mesa size was also measured at 77 K for comparison between device sizes in Figure 55. The lifetime here was calculated using the measured electrode spacing with the measured Hall mobility at 77 K. A linear increase is observed for the effective carrier lifetime versus electrode spacing. The trend of increasing effective lifetime for increased electrode spacing indicates that the increased responsivity for decreasing spacing is due to the reduced transit time. In fact, the increasing lifetime with increasing electrode spacing adds evidence to the previous hypothesis that closer spaced electrodes were more negatively affected by surface recombination sites than larger devices. However, another possible explanation is that the increased lifetime for larger electrode spacing was related to the mesa size, not the ratio of metal on the semiconductor surface. This implied that the effective lifetime of the larger mesa was moving closer to the bulk lifetime due to a lower surface area to volume ratio. If this was the case, then improved surface passivation and etching recipes would allow for a longer effective carrier lifetime.

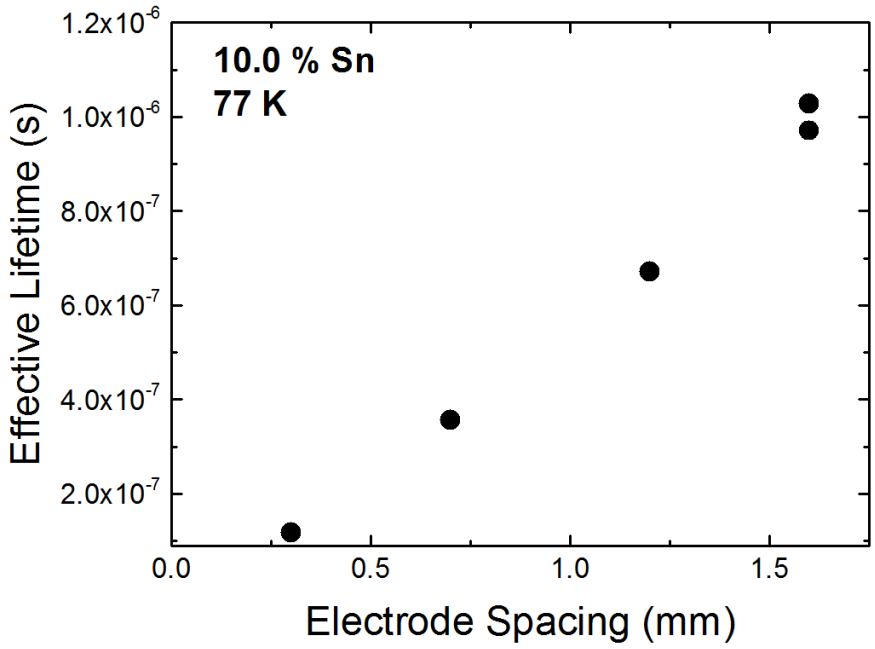


Figure 55: Effective lifetime for the 10.0% Sn photoconductor measured at 77 K versus the photoconductor electrode spacing. Two separate detectors with 1.6 mm spaced electrode spacing were measured.

### 5.6 Specific Detectivity ($D^*$)

The dark current was measured for each device, temperature, and measurement condition to allow the noise current within the device to be calculated as outlined in Section 4.3.4. The device area, responsivity and noise current were then used to calculate the specific detectivity ($D^*$). The $D^*$ for the Group I photoconductors plotted in Figure 56 were from the temperatures that yielded the highest $D^*$ for each device. The $D^*$ value for the 0.9 and 3.2% Sn samples does not occur for the lowest temperature due to the blue-shifted absorption edge away from the 1.55 μm laser wavelength. The temperature of the peak $D^*$ occurred at different temperatures from the peak responsivity temperature for the 3.2% Sn sample due to the reduced noise current. The lower noise current at 120 K allowed for a higher $D^*$ at this value even though the peak responsivity was observed at 160 K.

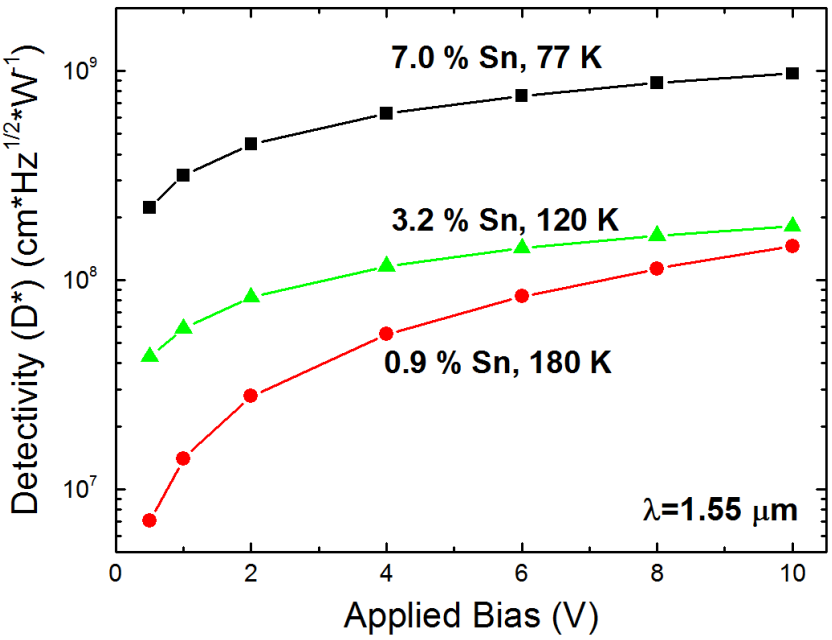


Figure 56: Detectivity at 1.55 μm for the 0.9, 3.2, and 7.0% Sn photoconductors as measured versus the applied bias voltage. The values were for the temperatures with the maximum detectivity of each device.

Detectivity for the Group II photoconductors measured at 1.55 μm for each temperature in Figure 57 shows that each had an increase of $D^*$ over Group I photoconductors. For these 2 mm mesas, the maximum $D^*$ observed occurred all at 77 K as expected since this temperature has the lowest background carrier concentration for reduced noise operation. At 77 K, the peak $D^*$ for all 2 mm mesa photoconductors under a 10 volt bias observed was $3.2 \times 10^9$ cm*Hz$^{1/2}$*W$^{-1}$ which was measured for both the 8.0 and 10.0% Sn samples. The peak $D^*$ at 300 K operation was measured at $1.3 \times 10^8$ cm*Hz$^{1/2}$*W$^{-1}$ for the 8.0% Sn sample. This was 10 times larger than the $D^*$ for the 10.0% Sn sample at 300 K. As discussed previously for the responsivity measurement of these high Sn content samples at 1.55 μm, the shallower absorption of 1.55 μm light near the surface of the 9.0 and 10.0% Sn sample reduced their signal-to-noise ratio (SNR). At 300 K, this effect was more pronounced since all surface traps are expected to be activated, while at 77 K the $D^*$ are almost equivalent due to a reduced noise mechanism.

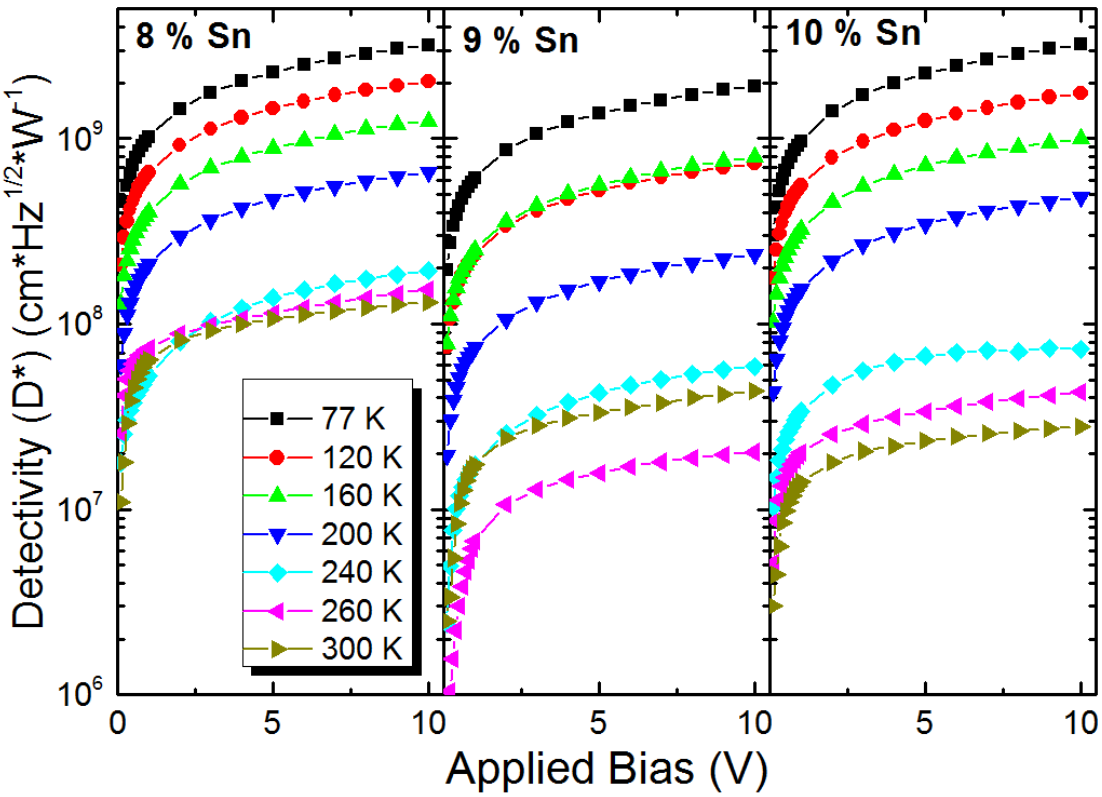


Figure 57: Specific detectivity of the 2 mm photoconductors with 8.0, 9.0, and 10.0% Sn. Measurement conducted using a 1.55 μm laser source.

The $D^*$ for the 10.0% Sn photoconductor measured for varying square mesa size and high bias voltage in Figure 58 shows that the peak $D^*$ was observed for the 2 mm mesa. Although the 0.5 and 1.0 mm mesas had a higher measured responsivity, the device size and noise included within the calculation of $D^*$ showed that for these materials and device design, the 2 mm mesa had the highest SNR compared to smaller mesas. In the low bias region, $D^*$ increased, but then saturated and decreased at higher applied bias.

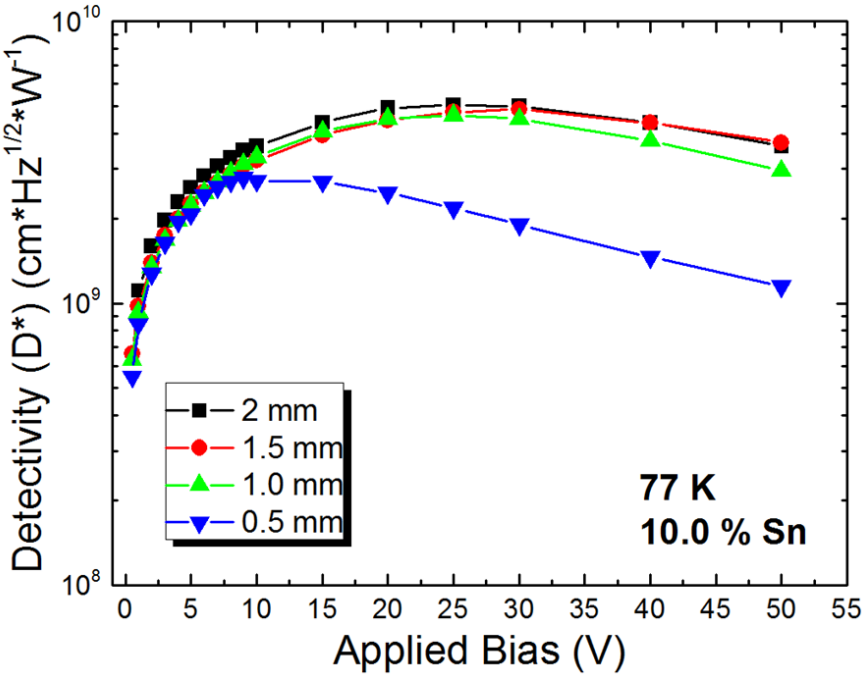


Figure 58: Detectivity of 10.0% Sn photoconductor at 77 K for the 2.0, 1.5, 1.0, and 0.5 mm square mesa sizes measured at 1.55 μm.

Since these devices are Ohmic with a classical $V = IR$ relationship, an examination of Equations 4.55 and 4.51 leads to a deduction that $D^*$ should increase at a rate close to $\sqrt{V_{bias}}$ in the low bias regions. In this low bias region responsivity increased linearly with $V_{bias}$ and noise increases as $\sqrt{V_{bias}}$. The decrease in slope of $D^*$ at higher bias was a result of the noise current still increasing proportional to $\sqrt{V_{bias}}$ while sweep out effect quenched the increase in responsivity. This was confirmed by performing a fit of $D^*$ from 0 to 10 volts on the 2 mm mesa in Figure 58. The fitted power factor was 0.514±0.006 following well with an Ohmic photoconductor in a region where the power factor was expected to follow this square root dependence. The 0.5 mm mesa in the voltage range from 20 to 50 volts was also fitted to measure the power factor for the high voltage region under increased carrier sweep out. A power factor of -0.79±0.06 was calculated from this fit. This was steeper than the expected -0.5 power factor that would occur for a device with constant responsivity and increasing noise current.

Sample heating due to the increased current density may have contributed to this larger decrease in SNR.

The spectral detectivity was calculated using the measured spectral response and calibrated based on the measured responsivity at 1.55 μm. The spectral response for each device and temperature was conducted at a 10 volt applied bias, thus the responsivity and dark current measurements used to calculate $D^*$ at 1.55 μm could then be used to perform this spectral calibration. The other boundary condition used was setting the spectral response to zero for each detector at 3.0 μm, which is a valid assumption based on the bandgap of these detectors. From these calculations the spectral detectivity for the highest responsivity detectors is shown in Figure 59. The $D^*$ for each detector was highest at 77 K and decreased with increasing temperature to 300 K.

The $D^*$ for the 8.0, 9.0, and 10.0% Sn detectors at 77 K are plotted together with the $D^*$ values for commercially available detectors in Figure 60. The $D^*$ of InGaAs, Ge, InAs, and PbS are plotted using data from reference [78]. Dotted lines were used to distinguish the referenced detectors from this work. Although the $D^*$ of the $Ge_{1-x}Sn_x$ detectors at 77 K was lower than Ge and InGaAs at 295 K, the thickness of the $Ge_{1-x}Sn_x$ detectors were all less than 100 nm. The thickness of the commercialized detectors is typically much thicker to achieve higher quantum efficiencies. Thus it is expected that several orders of magnitude increase in D* can still be improved upon for the $Ge_{1-x}Sn_x$ detectors by thicker film growth and optimized growth conditions.

The combination of spectral response and SNR into the spectral D* figure is a key milestone in the development of $Ge_{1-x}Sn_x$ photodetector technology. It allows for direct comparison of these detectors to other commercially available detectors in equivalent units.

Additionally, further device and material improvements will now have a baseline performance metric in which to assess future $Ge_{1-x}Sn_x$ detectors.

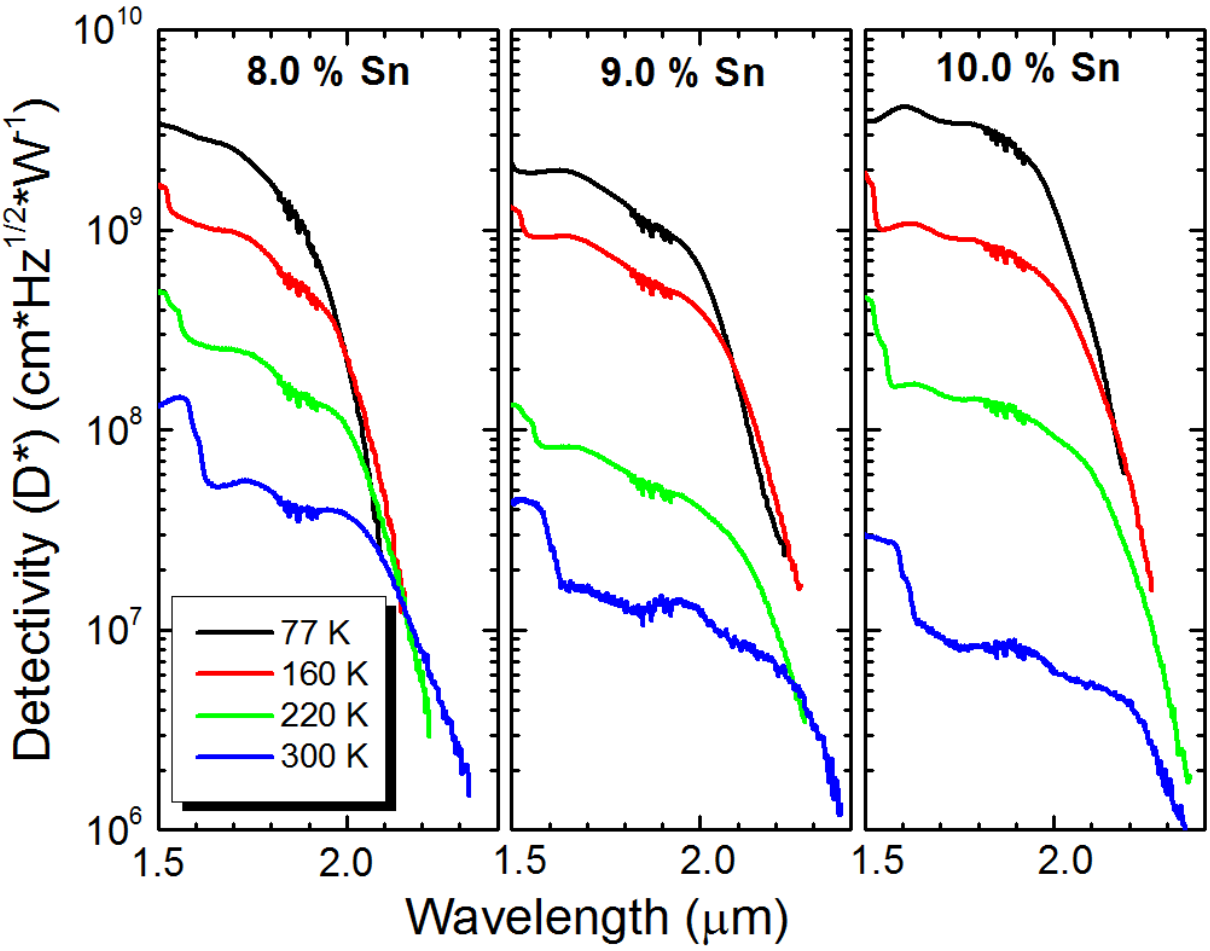


Figure 59: Spectral detectivity for the 2 mm square photoconductors with 8.0, 9.0, and 10.0% Sn composition. Each measurement was conducted with a 10 volt applied bias.

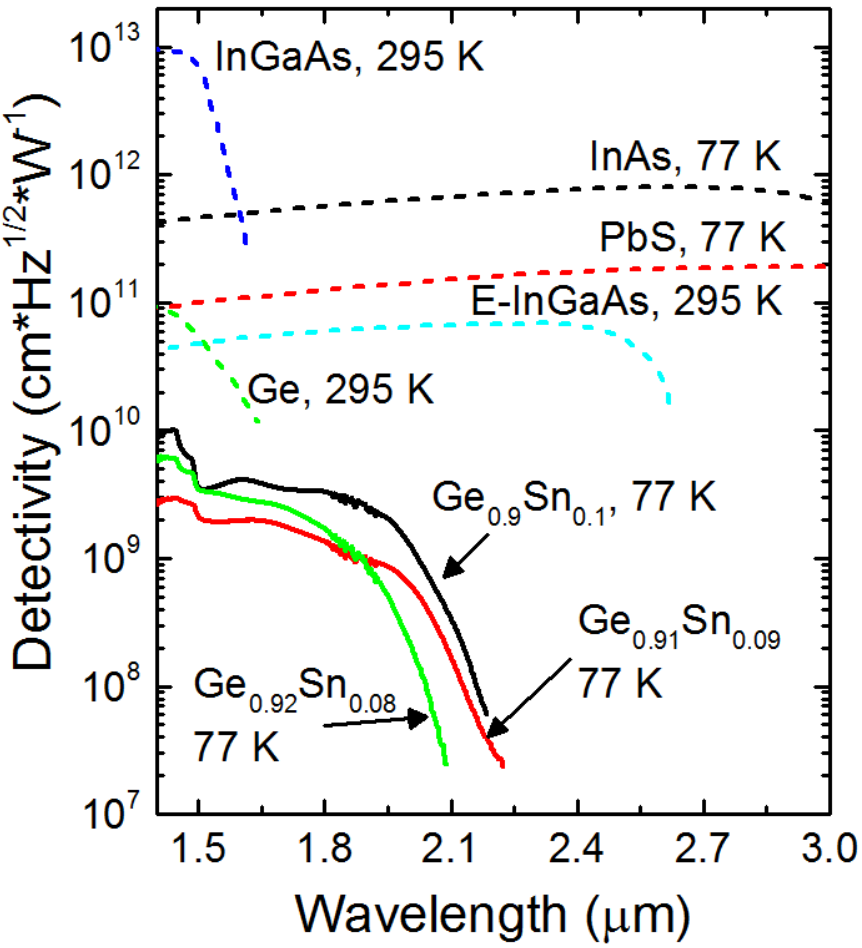


Figure 60: Spectral $D^*$ of the 8.0, 9.0, and 10.0% Sn photoconductors at 77 K plotted versus wavelength. Also plotted are the $D^*$ values of currently available detectors in the SWIR. The $D^*$ of InGaAs, extended-InGaAs, Ge, InAs, and PbS are plotted using data from references [78, 79].

## Chapter 6: Advanced Photoconductive Devices with Interdigitated Electrodes

Increased photoconductive gain can be achieved by increasing the effective carrier lifetime. This was demonstrated in Chapter 5 by decreasing the device operating temperature and reducing the number of available trap or active recombination sites. Increased gain was also demonstrated in those $Ge_{1-x}Sn_x$ photoconductors by reducing the transit time. This was achieved by increasing the applied bias, which allowed each photo-generated carrier to achieve a higher drift velocity. Chapter 6 will investigate enhanced gain due to a reduction in electrode spacing by the use of interdigitated electrodes. Square photoconductor mesas with 0.5 and 1.0 mm side lengths were fabricated. The interdigitated electrodes on these two different sized mesas were fabricated with a metal-to-active area ratio of two. The electrode width was 3, 6, and 12 μm with a corresponding electrode gap of 6, 12, and 24 μm, respectively. Each 0.5 and 1.0 mm device was also fabricated without interdigitated electrodes, with only co-planer contacts, as a control. The change in responsivity due to the varied electrode spacing as well as for variable temperature was measured. The effective carrier lifetime and enhanced gain are discussed.

### 6.1 Interdigitated Electrode Device Fabrication

The sample used in this study was the $Ge_{0.93}Sn_{0.07}$ sample grown on Ge buffered Si with a $Ge_{0.93}Sn_{0.07}$ epilayer thickness of 240 nm and a 755 nm Ge buffer layer thickness. The total fabrication was done using a three step mask process with standard UV lithography and is outlined in Figure 61. A positive AZ4110 photoresist was used for the first mask to define the mesa. Dry etching was done using the GeSn_ET etch recipe down to the Si substrate.

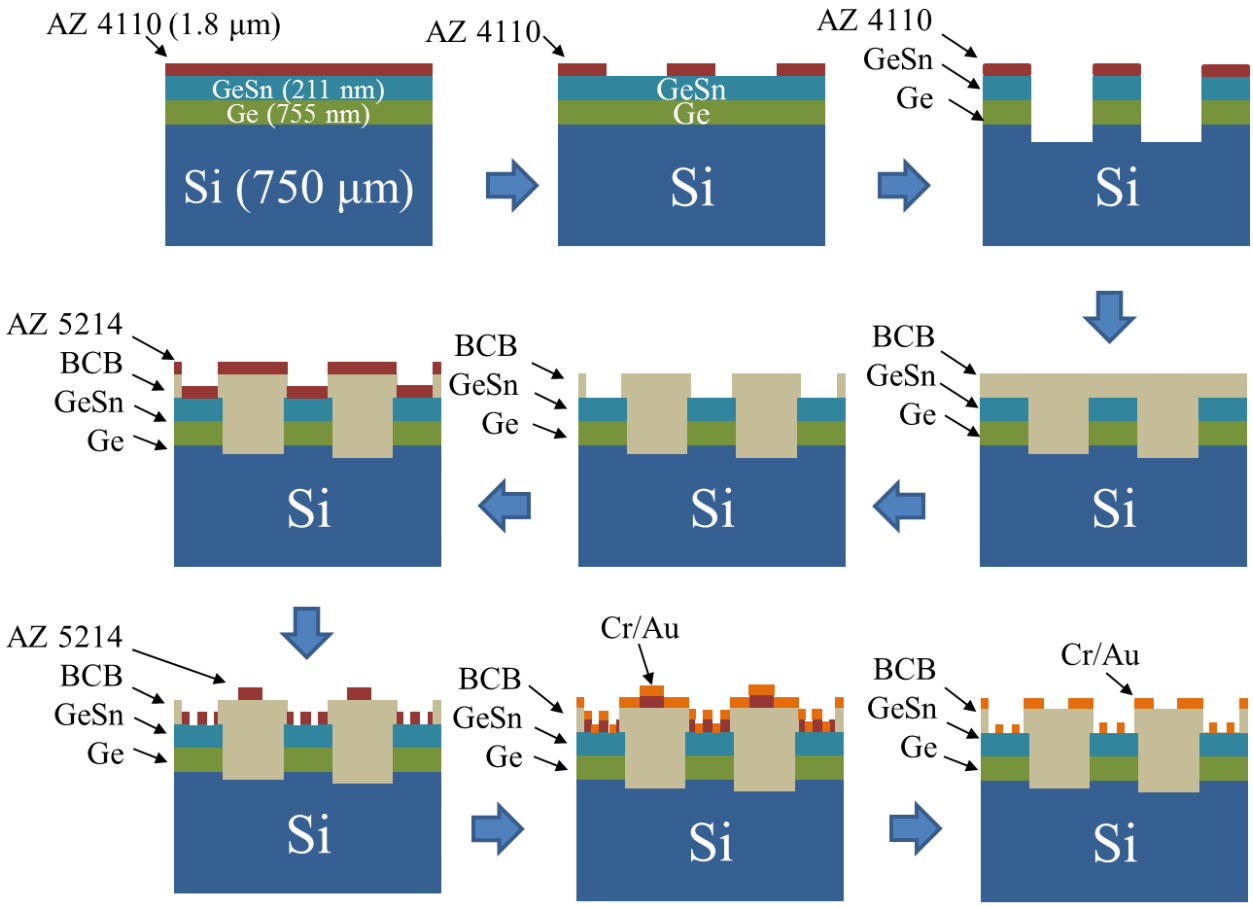


Figure 61: Fabrication process flow for fabricating a $Ge_{1-x}Sn_x$ photoconductor with interdigitated electrodes used a photoactive BCB layer as a dielectric and passivation.

The second mask was used to open a square window in the passivation layer, leaving a $Ge_{1-x}Sn_x$/air interface. Initially a thin 100 nm $SiO_2$ layer was used as passivation to ensure the 300 nm thick metal trace from the interdigitated electrodes up to the metal bonding pads would remain connected across that vertical interface. However, the I-V characteristics of the wire bonded device compared to the on-wafer I-V test indicated that the Au ball bonding for this fabrication process resulted in a short through the $SiO_2$. The pressure and force due to the ball bonding process cracked and shorted the metal pad through the underlying semiconductor. Current-voltage measurement of an open circuit test structure in Figure 62 showed this shorting effect even when 1000 nm of $SiO_2$ is used.

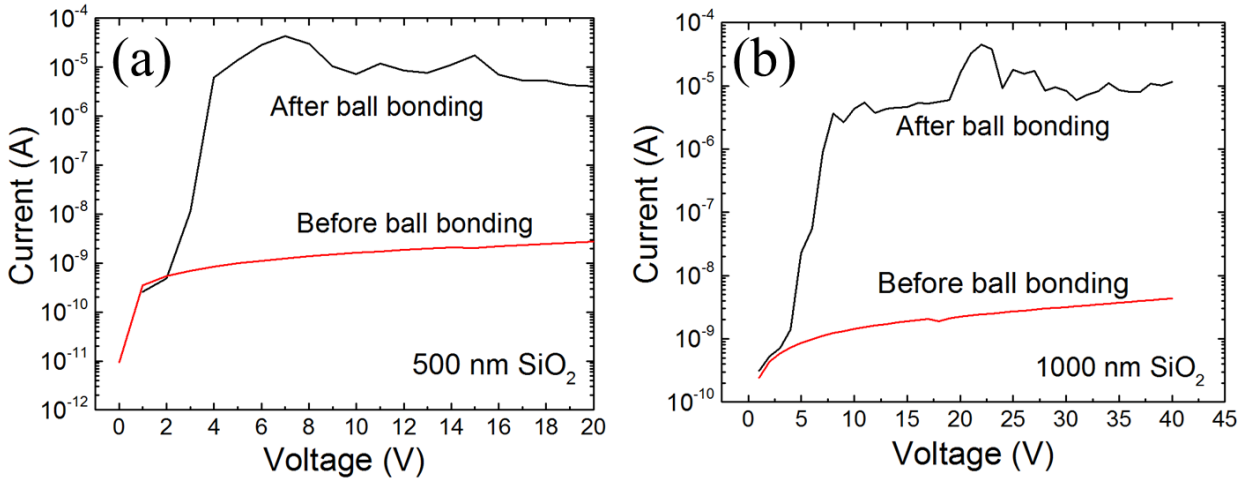


Figure 62: Current-voltage measurement before and after ball wire bonding on a 500 nm thick Au pad with (a) 500 nm and (b) 1000 nm thick $SiO_2$ passivation layer.

Furthermore, a thickness as low as 500 nm of $SiO_2$ proved to be too thick for the 500 nm of deposited Au traces to remain connected between the interdigitated electrodes on the $Ge_{1-x}Sn_x$ surface up to the metal pads on top of the passivation layer. The SEM images in Figure 63 show the metal trace disconnected when (a) 500 nm and (b) 1000 nm thick $SiO_2$ layer was used as a passivation layer. The steep vertical sidewall that resulted from a buffered oxide etch (BOE) of $SiO_2$ created a metal disconnect when the metal thickness was equal to or less than this vertical step. Deposition of thicker metal layer is not possible because the increased heat of a thicker metal film resulted in a photoresist that became impenetrable by solvents for the lift-off process.

Benzocyclobutene (BCB) was used for this device instead of $SiO_2$ because the curing process leaves the BCB sidewalls sloped. The entire sample was baked in an oven at 250 °C for 5–6 hours to cure the BCB layer. The type of BCB, spin speed, and curing process used resulted in a final cured thickness of 3.6 μm. The photoconductor mesa height was etched a total depth of 1.6 μm, thus the BCB was 2 μm above the $Ge_{1-x}Sn_x$ mesa. The SEM images of the final device with BCB passivation layer in Figure 64 (a) shows the top view of the full 0.5 mm square photoconductor mesa with the two metal contact pads and interdigitated electrodes on the

$Ge_{0.93}Sn_{0.07}$ surface. The image in Figure 64 (b) was a zoomed in view from the red box region in (a) that shows the transition of the evaporated metal across the 2 μm thick BCB layer. This image shows the metal remains connected across the sloped BCB sidewall. An additional advantage of the BCB process was the resistance to acid. This allowed the sample to be dipped in BOE to remove the $Ge_{1-x}Sn_x$ native oxide prior to metal deposition.

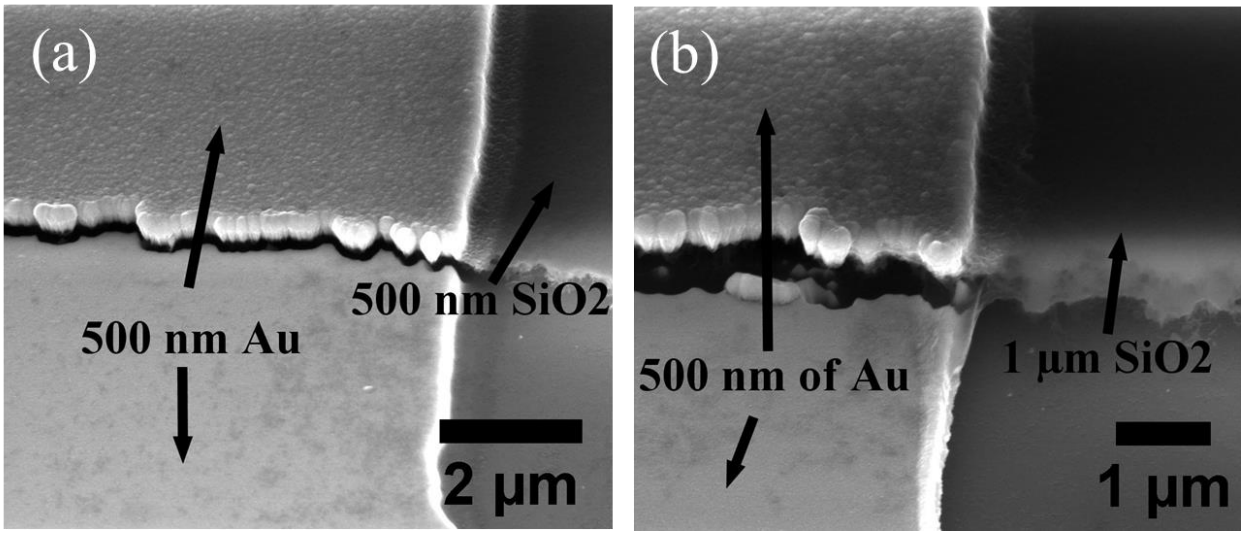

Figure 63: SEM image of a metal trace test structure going up a vertical $SiO_2$ passivation layer with (a) 500 nm and (b) 1000 nm $SiO_2$ thickness.

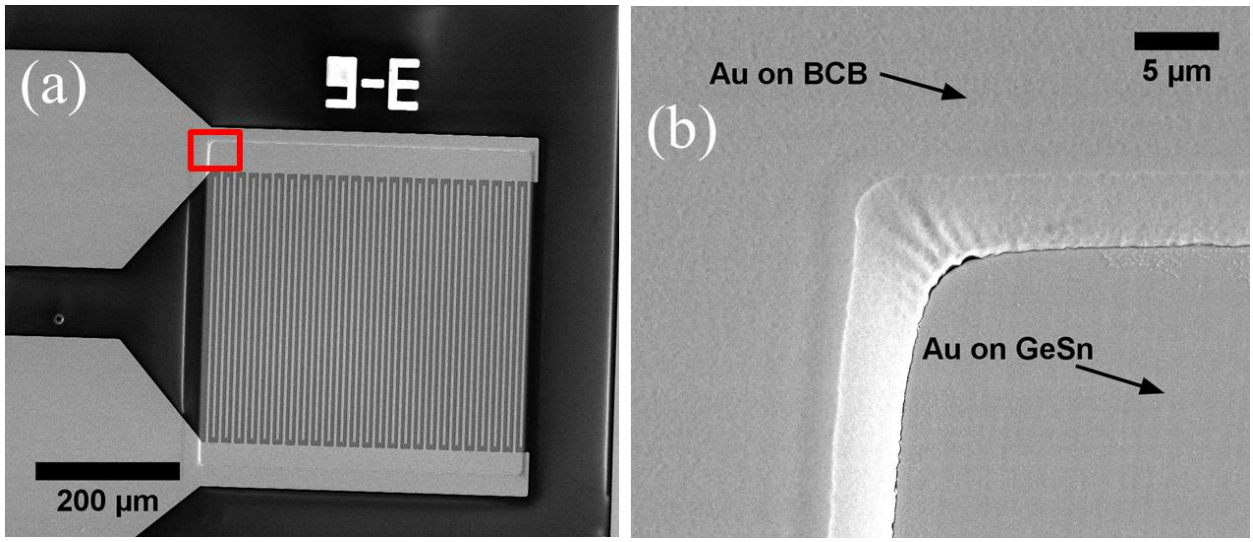

Figure 64: SEM image of fabricated interdigitated photoconductor with BCB passivation layer. Image (b) is a zoomed in view of the metal trace transition down to the device surface from the highlighted red box in (a) the device full view perspective.

The interdigitated metal electrodes, metal traces, and metal contact pads were patterned with the third mask using AZ5214 reversible resist. Metal evaporation of 10 nm Cr followed by 300 nm of Au was performed, followed by lift-off using heated acetone to remove the AZ5214 resist. The top view optical image of a final device with a designed 3 μm electrode width and 6 μm spacing is shown in Figure 65 (a). The width and spacing of the electrodes for the fabricated device was measured using SEM. The 3 μm wide, 6 μm spaced electrode was the only structure with dimensions different from the designed specifications. The SEM image in Figure 65 (b) shows the fabricated device to have electrodes with a 3.5 μm width and 5.2 μm spacing. For labeling convention only, these photoconductors will continue to be labeled based on the designed size, 3–6 μm. Calculations based on the device dimensions were done using the measured width of the fabricated device.

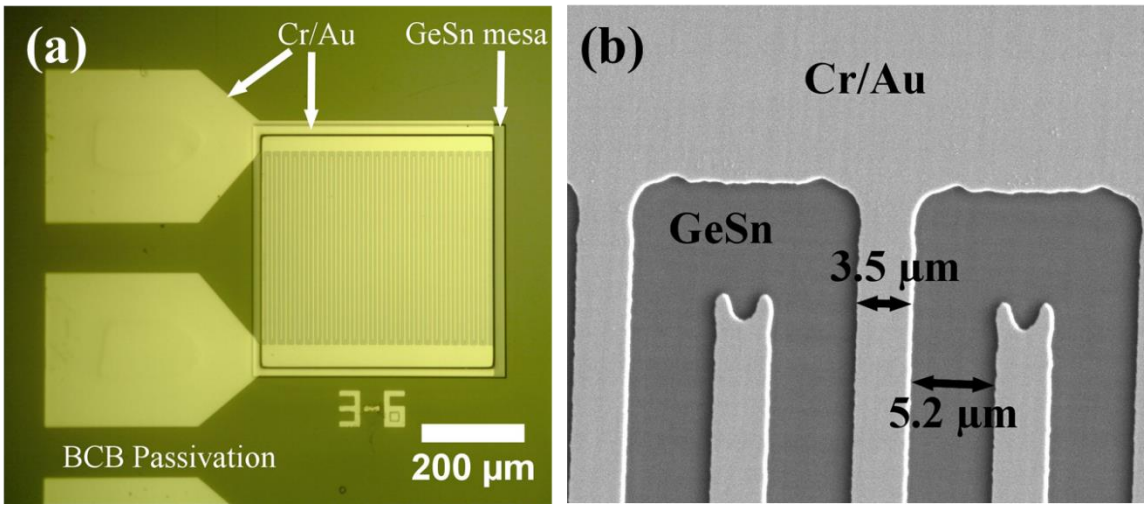


Figure 65: (a) Top view optical image of a fabricated $Ge_{0.93}Sn_{0.07}$ photoconductor with interdigitated electrodes. (b) SEM image measured the electrode dimensions of a fabricated device with expected 3 μm electrode width and 6 μm spacing.

The fabricated die containing several of each size detector and electrode spacing was mounted in a ceramic dual in line package (DIP). Wire bonding from the metal pads to the package outputs was performed using a standard Au ball bonding process. Current-voltage

measurements in Figure 66 for each photoconductor were linear indicating good Ohmic contacts were made. These measurements also confirm that each interdigitated electrode is connected to the metal pads across the sloped BCB-to-semiconductor interface.

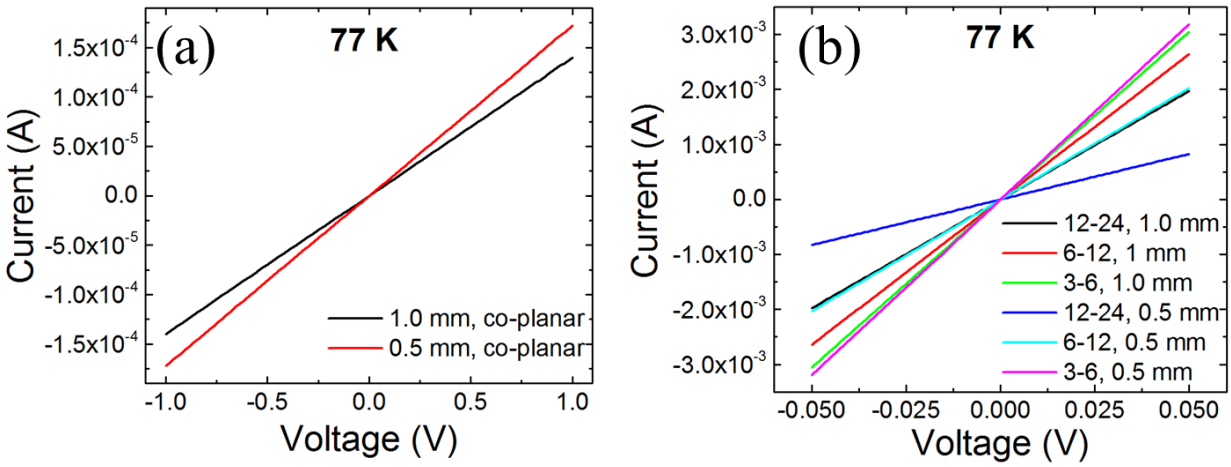


Figure 66: Current-voltage measurement of the (a) co-planar and (b) interdigitated electrode photoconductors at 77 K.

The dark resistance of each photoconductor mesa was extracted from the I-V measurements at each temperature. The dark resistance of the two different sized co-planar photoconductors in Figure 67 (a) show that the 1 mm mesa had the largest resistance across the temperature range. This is expected since the distance between the electrodes for the 0.5 and 1.0 mm mesas was 375 and 850 μm, respectively. This trend continued for the interdigitated electrodes, with the resistance of the interdigitated electrodes increasing for increasing distance of the electrode gap. However, the 1-to-2 ratio of metal-to-semiconductor coverage on the sample makes interpreting the difference between the mesa sizes versus dark resistance unclear. The significant increase in the resistance of all devices from the 100 to 77 K measurement was due to the carrier freeze out of the background doping within this sample. This was discussed and shown previously in Figure 42.

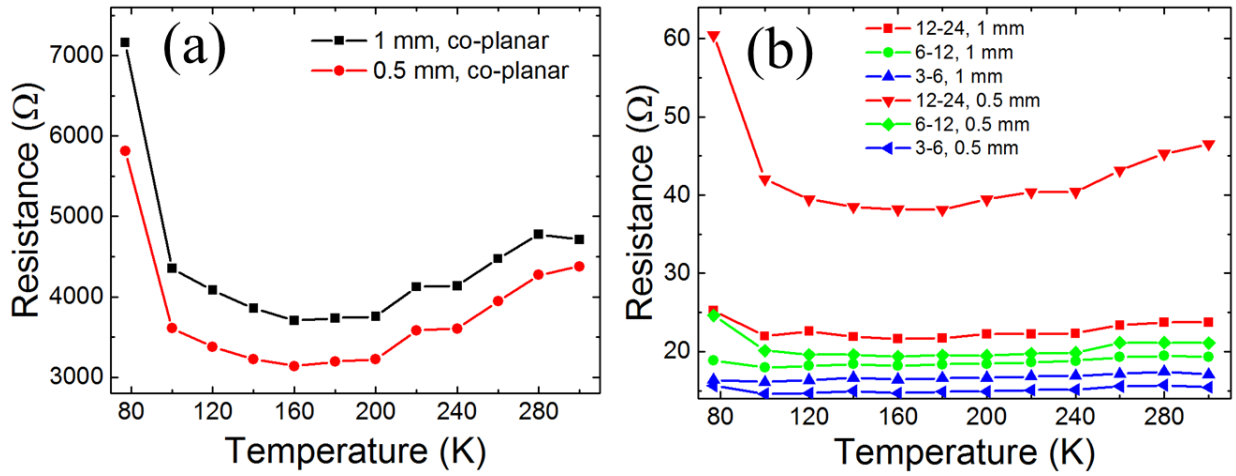


Figure 67: Dark resistance of the (a) co-planar photoconductors and (b) interdigitated electrodes were plotted for each measured temperature.

### 6.2 Enhanced Photoconductive Gain

The responsivity of the interdigitated devices was measured at 1.55 μm from 77 to 300 K, in 20 K increments. The responsivity for each device at 300, 260, 100, and 77 K in Figure 68 show that for each measured temperature the two devices with the highest responsivity were the 0.5 mm mesa with electrode width-spacing of 12-24 μm and 6-12 μm. In fact, it was observed that for a given mesa size the responsivity increased for increasing interdigitated electrode spacing. The 3-6 μm interdigitated detector with a 1 mm mesa was the only device to show a decrease in responsivity for any measured temperature below that of the corresponding co-planar detector.

The decreasing electrode spacing was expected to increase the photoconductive gain by reduction of the carrier transit time. However, a decreasing responsivity with decreasing electrode spacing for all devices was observed. This reduction in overall gain was due to a corresponding decrease in the effective carrier lifetime as the electrode spacing was decreased. The increased metal surface perimeter on the device for the decreasing electrode spacing led to an increased surface recombination velocity near the contacts. Since the recombination at an

Ohmic contact approaches the maximum carrier velocity for that material, the minority carrier surface recombination velocity was increased leading to an overall reduction in the effective carrier lifetime. These surface recombination losses can be reduced in next generation devices by design of higher doped regions under the metal contacts or with passivation of the exposed semiconductor surface.

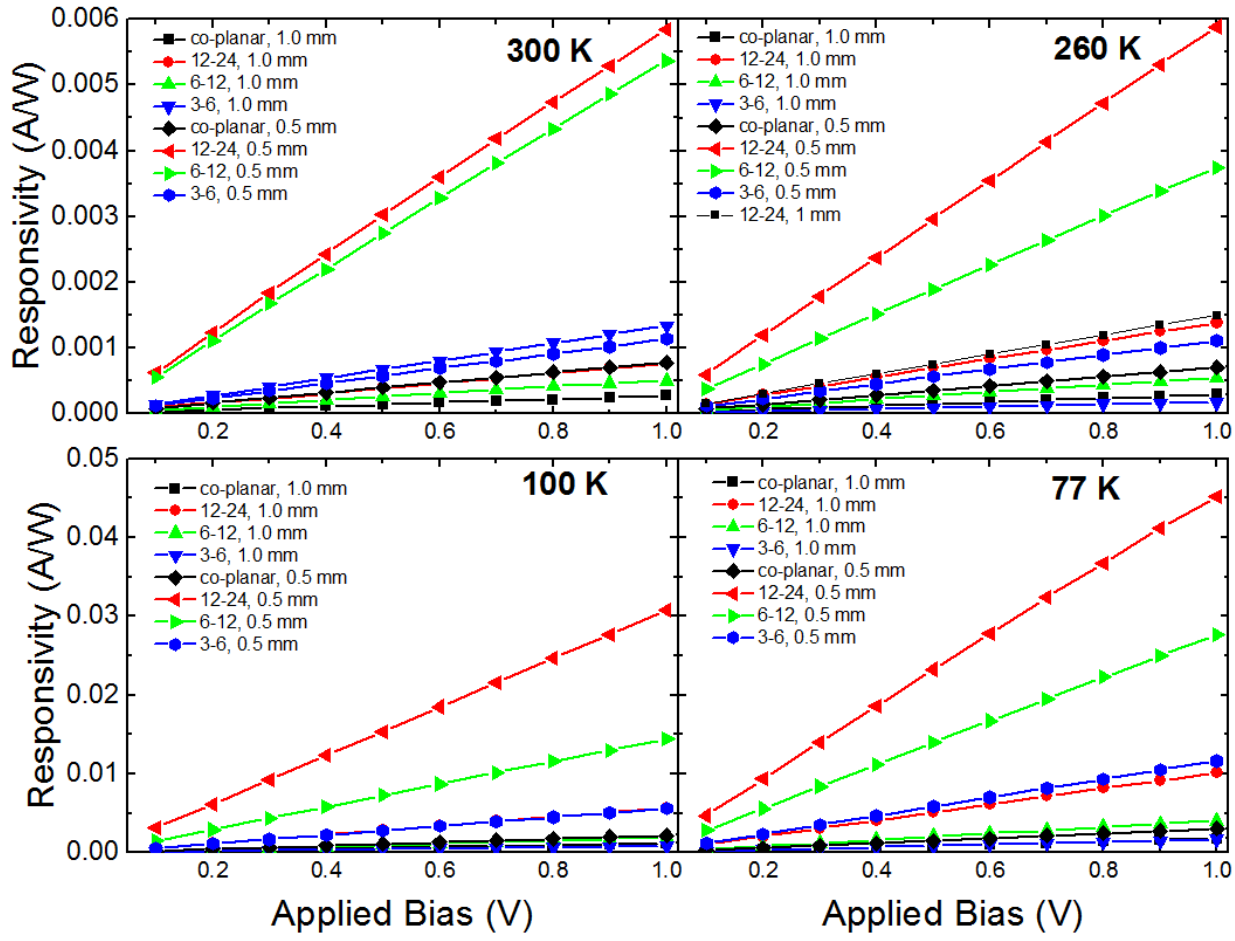


Figure 68: Responsivity measured for the $Ge_{0.93}Sn_{0.07}$ interdigitated photoconductor devices at 1.55 μm for device temperatures of 300, 260, 100, and 77 K.

### 6.3 $Ge_{1-x}Sn_x$ Bulk Lifetime

The effective carrier lifetime was extracted from the linear slope of the responsivity versus applied voltage as previously described in Section 5.5. The mobility for the $Ge_{0.93}Sn_{0.07}$ sample was measured at 77 and 300 K as 578 and 352 $cm^2/(V*s)$, respectively. These two

temperature measurements do not follow a $T^{1.5}$ relationship, thus interpolating the mobility for temperatures other than the measured values was not possible. The effective lifetime for this sample was only calculated for the 77 and 300 K measurements. To determine the external quantum efficiency the optical constants n and k for this sample were measured by Ellipsometry at 300 K. These values were measured to be, n=4.37 and k=0.12 at 1.55 μm. This equated to a $Ge_{1-x}Sn_x$/air reflectivity of 0.385 and an absorption coefficient 13629 $cm^{-1}$. The effective carrier lifetime was plotted in Figure 69 per interdigitated electrode spacing and mesa size. The relative error for the effective lifetime calculations was calculated based on the propagation of error and was determined to be 40%. The 0.5 mm mesa had a longer effective lifetime at both measured temperatures compared to the 1.0 mm mesa. The available data does not provide sufficient evidence to investigate that result further and would have to be accomplished in future work.

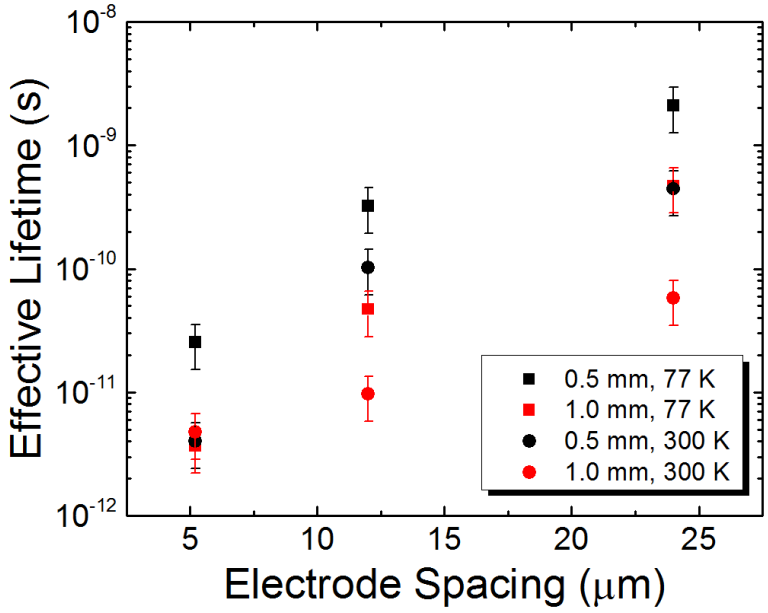


Figure 69: Effective carrier lifetime for the $Ge_{0.93}Sn_{0.07}$ photoconductor measured per interdigitated electrode spacing.

Since each device was fabricated on the same thin film with the only difference between devices was the interdigitated electrode spacing and mesa size. This allowed the $Ge_{1-x}Sn_x$ thin

film bulk lifetime to be extracted by this change in electrode spacing. Examination of Equation 4.49 for the effective lifetime permitted the bulk lifetime, $\tau_B$, to be determined from a plot of $1/\tau_{eff}$ vs $1/L^2$, where L is the space between the interdigitated metal electrodes. A device with a linear responsivity for applied voltage indicated the device was still under low injection. Thus D in this case is the minority carrier diffusion constant. A linear fit of this plot equates the y-intercept to $1/\tau_B$ and the slope equal to $\pi^2 D$. The measured effective lifetime for the devices measured at 77 and 300 K were plotted in this $1/\tau_{eff}$ vs $1/L^2$ format in Figure 70. Both plots were in log-log scale for clarity, but the fitting line used was linear. The devices measured at 77 K were well fitted within the margin of error of the effective lifetime calculation. The 0.5 and 1.0 mm devices were plotted and fitted separately because the differing surface area and carrier volume between these two mesa sizes was expected to affect the minority carrier diffusion constant. The fit line for the devices measured at 300 K were outside the margin error for both mesa sizes with the 0.5 farther outside the expected fit.

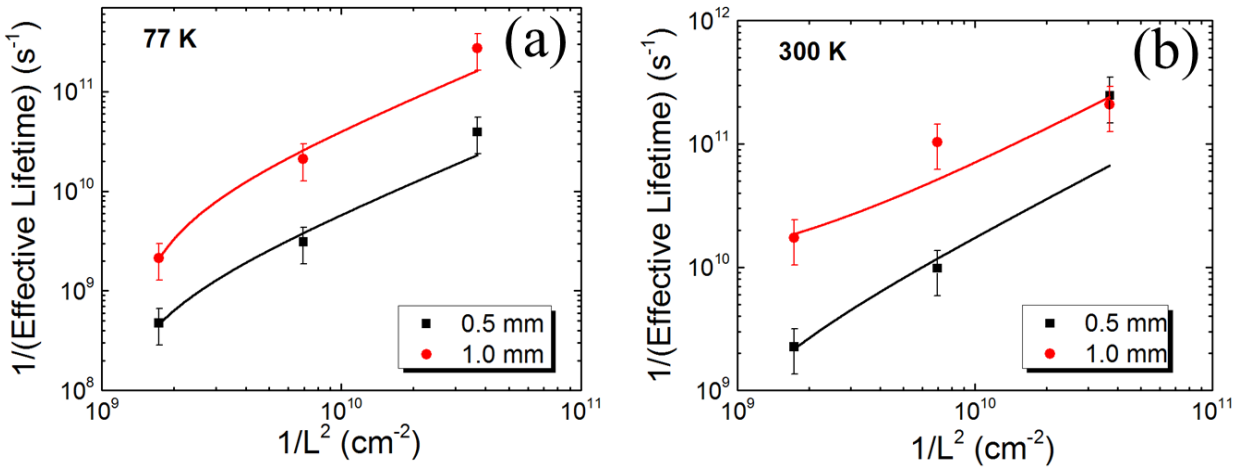


Figure 70: Inverse of effective carrier lifetime plotted against the inverse of the squared electrode spacing at (a) 77 K and (b) 300 K. Linear fitting was performed for the 0.5 and 1.0 mm mesas.

The bulk lifetime and minority carrier diffusion calculated from the linear fit in Figure 70 (a) are listed in Table 11. The fit from the 300 K were not included here due to the disagreement

in the data with the theoretical model. The minority carrier diffusion constant had an increase for the 1.0 mm mesa compared to the 0.5 mm mesa. This was expected since the larger mesa had a larger volume for which diffusion could occur. The small difference in the bulk lifetime of this sample at 77 K for the 0.5 and 1.0 mm photoconductor mesas could be due to the difference in the co-planar metal traces at the edges of the photoconductors. Since the 1.0 mm had a larger metal surface area per device along this edge, the increased surface recombination here was not accounted for in the Figure 70 fitting.

Table 11: Bulk lifetime and minority carrier diffusion of $Ge_{0.93}Sn_{0.07}$ thin films at 77 K

| Mesa Size (mm) | Bulk Lifetime (s) | Standard Error of Bulk lifetime (s) | Minority Carrier Diffusion ($cm^2/s$) | Standard Error of Minority Carrier Diffusion ($cm^2/s$) |
|---|---|---|---|---|
| 0.5 | $1.5x10^{-9}$ | $1.2x10^{-9}$ | 650 | 250 |
| 1.0 | $1.7x10^{-10}$ | $0.9x10^{-10}$ | 4600 | 1700 |

The spontaneous radiative emission rate for this sample was expected to dominate over Auger and Shockley-Read-Hall mechanisms at 77 K. The radiative emission rate for $Ge_{0.94}Sn_{0.06}$ within a double heterostructure design with $Si_{1-x-y}Ge_xSn_y$ barriers was calculated at $6x10^{25}$ $s/cm^3$ for 77 K [51]. The photon flux on the sample from the 1.55 μm laser with an optical power of 1.2 mW was $9.2x10^{15}$ $s^{-1}$. The background carrier concentration for this sample and temperature was measured by Hall as $4x10^{16}$ $cm^{-3}$. This means that the sample is still under lower injection. Using the background carrier concentration measured by Hall and the radiative emission rate calculated by Sun, *et al.* at 77 K; the radiative lifetime was predicted to be $7x10^{-10}$ s. This calculated bulk lifetime falls within the measured experimental values in Table 11.

# Chapter 7: $Ge_{1-x}Sn_x$ Avalanche Photodiode

An avalanche photodiode (APD) structure with a $Ge_{1-x}Sn_x$ active layer was grown on Ge buffered Si using the separate charge and multiplication (SACM) design described in Section 4.2.2. An additional APD with a Ge active layer was grown and fabricated with identical conditions as the $Ge_{1-x}Sn_x$ APD for the control sample. The electrical characterization of these two devices was measured as a function of temperature to establish a baseline dark current and measure the temperature dependent breakdown voltage. Within the SACM design, the region where breakdown and multiplication occur was confirmed based on the temperature dependent breakdown voltage. The gain within the multiplication region was then measured to determine the region of dominant generation of photo-generated and amplified carriers.

## 7.1 Fabrication

The growth of $Ge_{1-x}Sn_x$ APD was carried out using the previously described growth process within an ASM Epsilon RPCVD reactor. The thin film cross section and fabricated detector is shown in Figure 71. The substrate used was an n-type Si substrate to serve as the ground n-type contact. On the substrate an intrinsic Si multiplication region was grown, followed by a high doped p-type Si charge layer. Next a high doped p-type Ge buffer layer was grown to serve as an extended charge layer as well as provide the virtual substrate for the $Ge_{1-x}Sn_x$ epilayer. The $Ge_{1-x}Sn_x$ active layer was grown unintentionally doped to improve the lifetime of the photo-generated carriers within this region. The Sn composition of this layer was expected to be within the 6–7% Sn range based on the growth parameters used. Finally, a p-type Ge layer was grown on top of the $Ge_{1-x}Sn_x$ epilayer as the p-type contact.

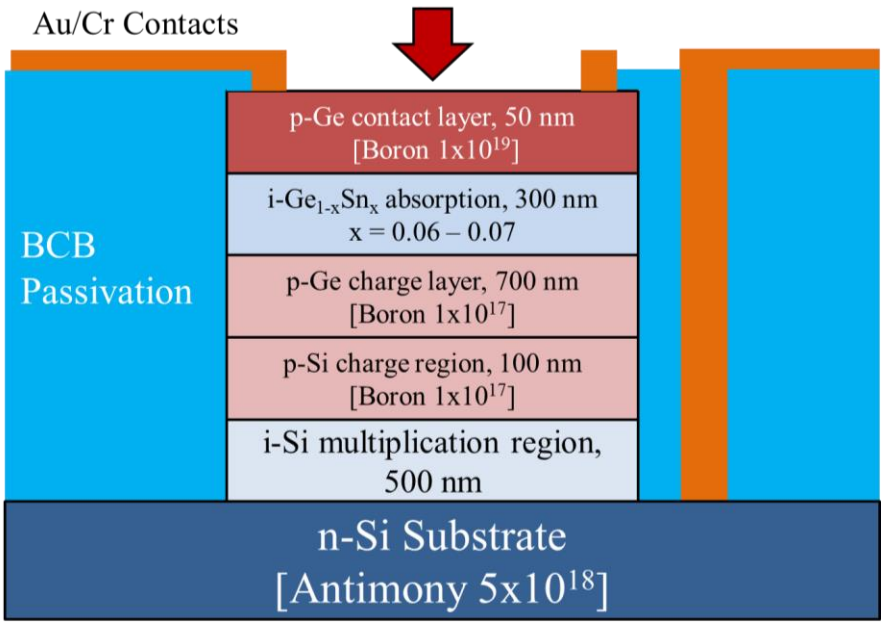


Figure 71: Cross section of the $Ge_{1-x}Sn_x$ avalanche photodiode shows the final fabricated detector with a top illuminated design.

The samples were fabricated into circular photodiodes with a ground-signal-ground contact design. The photodiode mesas were fabricated into 100, 250, and 500 μm diameters with top and bottom ring contacts for the signal and ground, respectively. A top view SEM image of a fabricated 250 μm diameter photodiode is shown in Figure 72 (a). The small size of each photodiode required wire bonding in order to perform the temperature dependent measurements. For this reason, the same process flow with BCB passivation was used as described in Section 6.1. The SEM image in Figure 72 (b) shows the connected metal trace across the $Ge_{1-x}Sn_x$/BCB interface.

The only difference between the interdigitated fabrication and the APD was the device mask design and mesas etch depth. The remaining fabrication process flow for these devices was the same as described in Section 6.1. For the photoconductor designs, the mesa etch depth was only required to isolate the photo-generated carriers and restrict current spreading between the top contacts. For this device, the mesa etch depth was critical so that the metallization layer for the ground contact was deposited on the n-Si substrate.

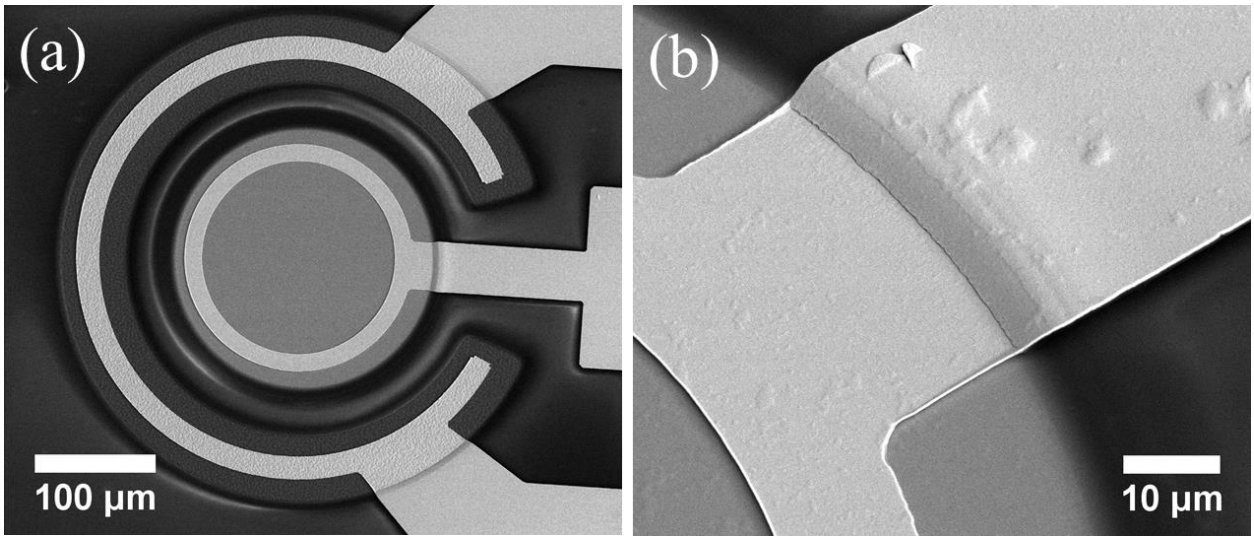

Figure 72: Top view SEM image of (a) 250 µm diameter $Ge_{1-x}Sn_x$ APD shows the top signal contact on the $Ge_{1-x}Sn_x$ epilayer and the ground ring contact on the Si n-type substrate. (b) Enlarged view shows the metal trace across the BCB to $Ge_{1-x}Sn_x$ interface.

The layer thicknesses listed in Figure 71 were the designed thickness. The final growth sample thickness was estimated by fabrication of a test APD structure and dry etching with the GeSn_ET recipe for maximum time the photoresist could sustain. For a 1.9 µm thick AZ4110 resist, this etch time used was 75 minutes. The average depth measured by the Dektak profilometer was 2.58±0.01 µm due to this RIE etch process.

The sample was then cleaved so that the cross section of the etched mesa would be exposed. The SEM image of this cross section device allowed further confirmation of the etch depth, and the approximate thickness of each epilayer. The side view and cross sectional SEM image from this etch test structure are shown in Figure 73. From these images the total etch depth was estimated at 2.28 µm. This method is not as precise as transmission electron microscopy due to the lower magnification and lower angle accuracy. Since a SEM image is a stereoscopic image of a 3D surface, a misalignment of the sample to normal incidence will result in an error of the thickness measurement. These SEM images show the increased lateral etching on the $Ge_{1-x}Sn_x$ and Ge layers compared to the Si layers. Energy dispersive x-ray (EDX)

spectroscopy was used to identify the elements within each layer. The cross sectional SEM image in Figure 73 (b) was scanned by the EDX sensor within the SEM. The result of this EDX in Figure 74 confirms the identity of the $Ge_{1-x}Sn_x$/Ge layers compared to the underlying Si layers.

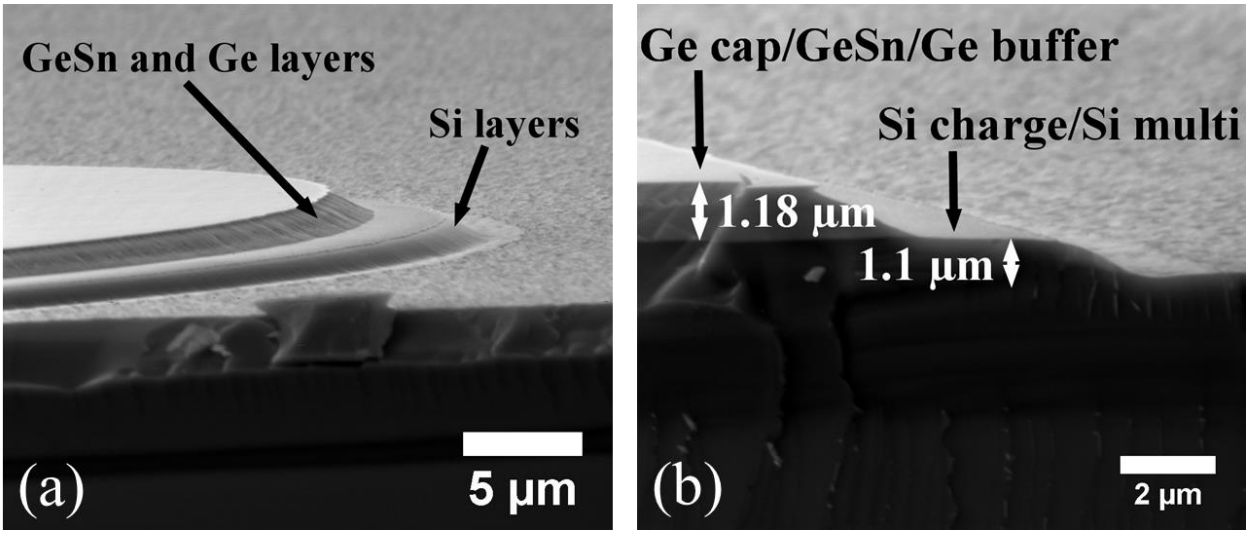

Figure 73: SEM image the $Ge_{1-x}Sn_x$ APD after mesa dry etching. (a) Side view of a device and (b) cross sectional view allows the total etch depth to be determined.

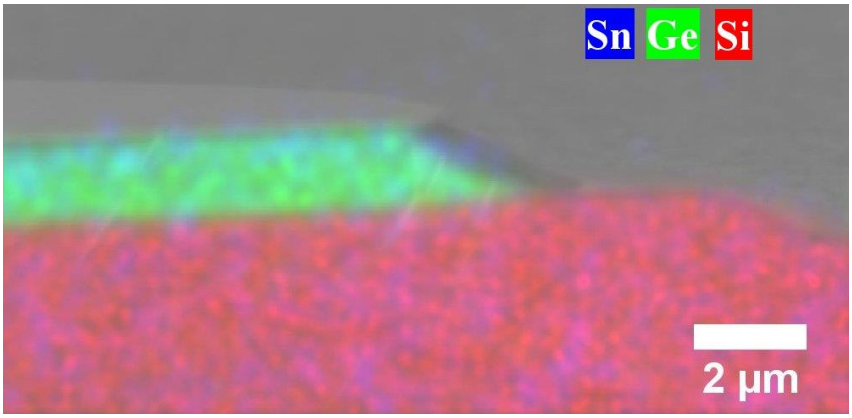

Figure 74: Energy dispersive x-ray spectroscopy of the APD device cross section identifies the elemental presence defining the epitaxial layers with Sn (blue), Ge (green), or Si (red).

### 7.2 Electrical Characterization

Current-voltage measurements were done on the 100, 250, and 500 µm diameter $Ge_{1-x}Sn_x$ diodes from 340 to 77 K. The measurements of each device and temperature in Figure 75

showed the breakdown voltage decreasing with decreasing temperature. This follows with the predicted breakdown voltage of an APD as modeled in Equation 4.26. The increasing breakdown voltage for increasing temperature further indicated that the breakdown was due to impact ionization. A Zener type breakdown due to heavy doping is characterized by decreasing breakdown voltage for increasing temperature. For all three devices the dark current remained lower than 100 nA for all temperatures prior to breakdown. This indicated a high shunt resistance as a result of good passivation. This was an additional indication that the mesa etching was sufficiently deep to allow the ground metal pad to be deposited onto the p-type Si substrate. The constant slope of the dark current in the reverse bias voltage prior to breakdown has negligible tunneling at high voltage. This indicated that the dark current within the device was limited by diffusion and not generation-recombination within the depletion regions.

For the 500 μm diameter device, a shoulder in the avalanche region was noticed around 0.1 after the onset of avalanche within the device. The slope of the dark current changed once at 100 nA due to the onset of avalanche, then changes again just prior to 100 μA. This second change could be due to the 'punch through' effect where the depletion region has widened enough to include the $Ge_{1-x}Sn_x$ active region.

Breakdown voltage was defined as the voltage that resulted in a current greater than $1x10^{-5}$ A. The temperature dependent breakdown voltage for each device was extracted and plotted in Figure 76. By linear fit, the temperature dependent breakdown voltage was extracted. The breakdown voltage for the 100, 250, and 500 μm diameter mesas had a temperature dependent breakdown voltage (±0.2 mV/K) of 10.4, 10.1, and 10.1 mV/K, respectively. This corresponded to a thermal coefficient, $\delta = (\Delta V_{BR}/V_{BR})/\Delta T$, of 0.05 %/K. The smaller 100 and 250 μm diameter mesas had a reduced standard error and more closely followed the linear

breakdown behavior versus temperature compared to the 500 µm diameter device. This was due to the more uniform current spreading in those smaller diameter devices. The ionization coefficient in Figure 76, α, was determined by solving Equation 4.26 and using the experimentally determined breakdown voltage for each measured temperature.

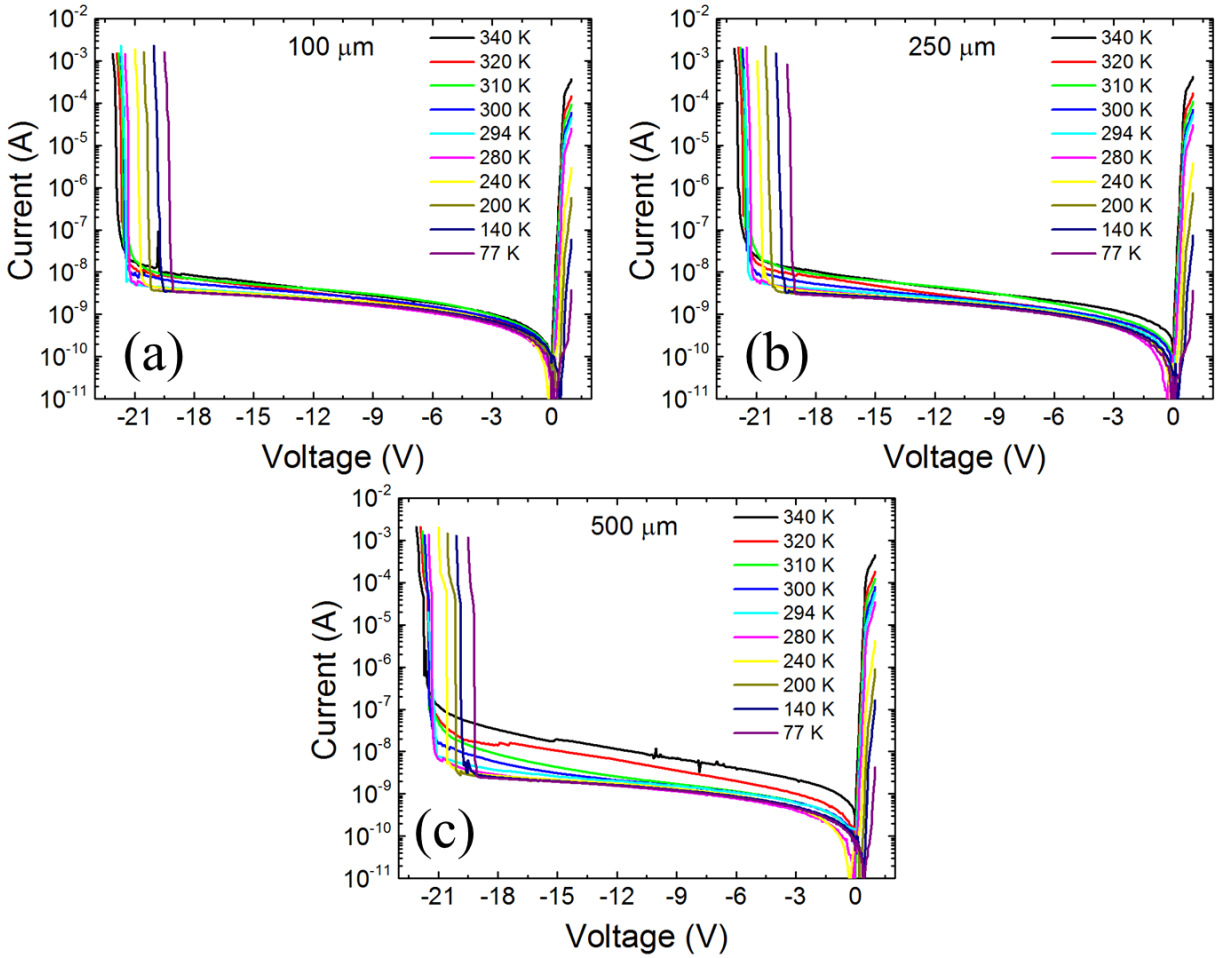


Figure 75: Dark I-V measurement of the (a) 100 µm, (b) 250 µm, and (c) 500 µm diameter $Ge_{1-x}Sn_x$ APDs measured for temperatures from 340 to 77 K.

Carrier scattering due to lattice and phonons increases as temperature increases. This is the fundamental cause for the increase in breakdown voltage for increasing temperature. For that reason, the breakdown voltage temperature coefficient can be used to identify the multiplication or breakdown region. This thermal coefficient reported here is lower than that of APDs with Si

incorporated multiplication regions [104, 105] indicating that the high field region and multiplication occurred in the Si multiplication region. As a reference, the known temperature dependent breakdown voltage for a Ge APD is 19.5 mV/K [88].

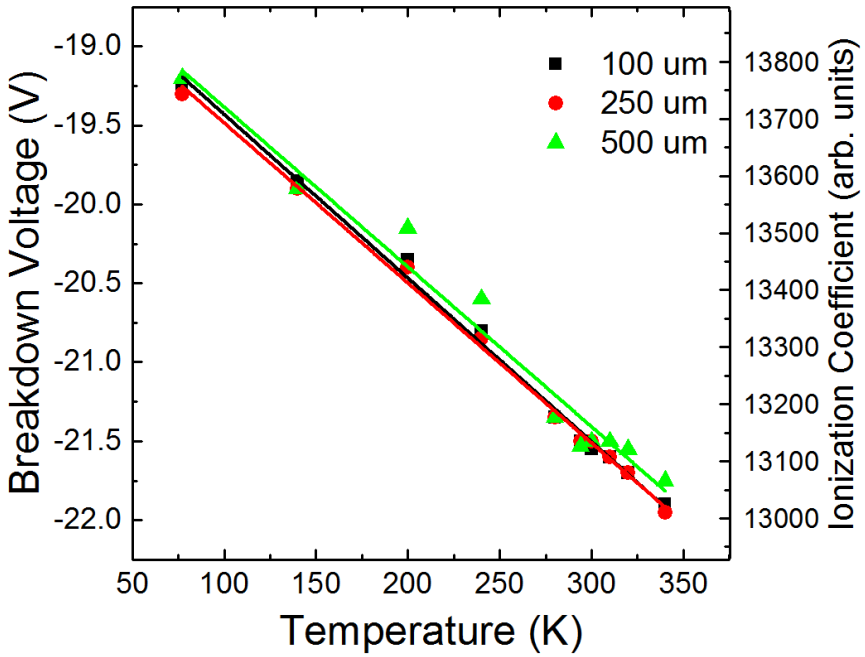


Figure 76: Breakdown voltage for each measured temperature plotted for the $Ge_{1-x}Sn_x$ 100, 250, and 500 μm diameter APDs. The right axis is the corresponding ionization coefficient.

The dark I-V relationship was measured for the Ge APD at room temperature. The large dark current and lack of a significant knee in the dark I-V relationship in Figure 77 (a) means this device was not operating under avalanche mode. The large dependence of the dark current with the bias voltage indicates that the dark current in the Ge APD is limited by generation-recombination within the depletion region. The widening depletion region width per increasing bias showed a proportionate increase in the dark current. Increased dark current and large voltage dependent dark current within this device indicated that the high field region was not applied across the Si multiplication region. This was confirmed by the dark I-V of a 500 μm diameter APD at 77 K in Figure 77 (b). The dark and laser illuminated I-V in this figure show rectifying

behavior of a diode characteristic of Zener breakdown. Examination of the laser illuminated current showed no evidence of IR absorption within this device.

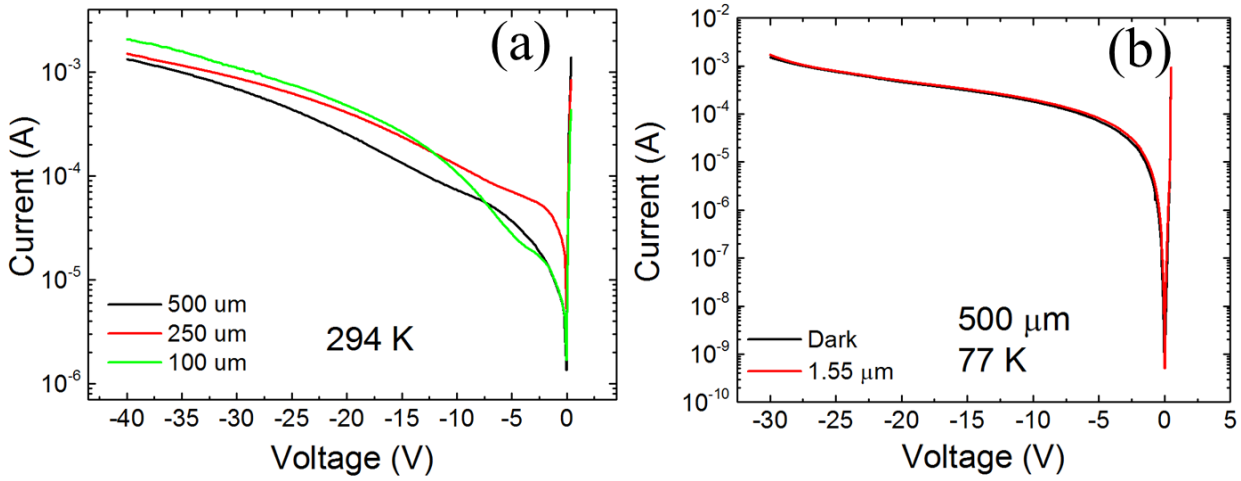


Figure 77: (a) Current-voltage measurement of the Ge APD at room temperature. (b) Current-voltage of a 500 μm diameter Ge APD at 77 K under dark and 1.55 μm laser illumination.

### 7.3 Optical Characterization

The spectral response of the $Ge_{1-x}Sn_x$ APD was measured for different temperatures from 77 to 340 K. A reverse bias within 1 volt of the breakdown voltage for each measured temperature was used for the spectra measurement. Spectra in Figure 78 of a 500 μm diameter device show absorption edge for Si red-shifting from 1.0 to 1.2 μm. However, no absorption due to the $Ge_{1-x}Sn_x$ active layer was observed. A peak in the measurement was observed from 1.2 to 1.4 μm, but it does not follow the profile characteristic of band-to-band absorption. This peak in the 1.2 to 1.4 μm was due to multiplication noise from the Si absorption peak that distorts the Fourier transform of the measured signal within the FTIR. The absence of IR absorption by these devices at the measured temperatures was confirmed by the zero response to a 1.55 μm laser in Figure 79.

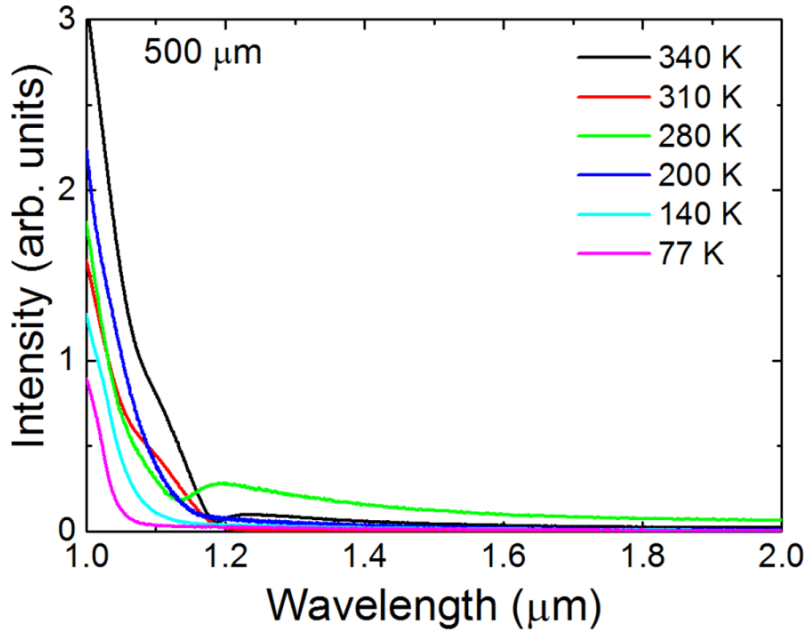


Figure 78: Spectral response of a 500 μm diameter $Ge_{1-x}Sn_x$ APD measured for varying device temperatures from 77 to 340 K.

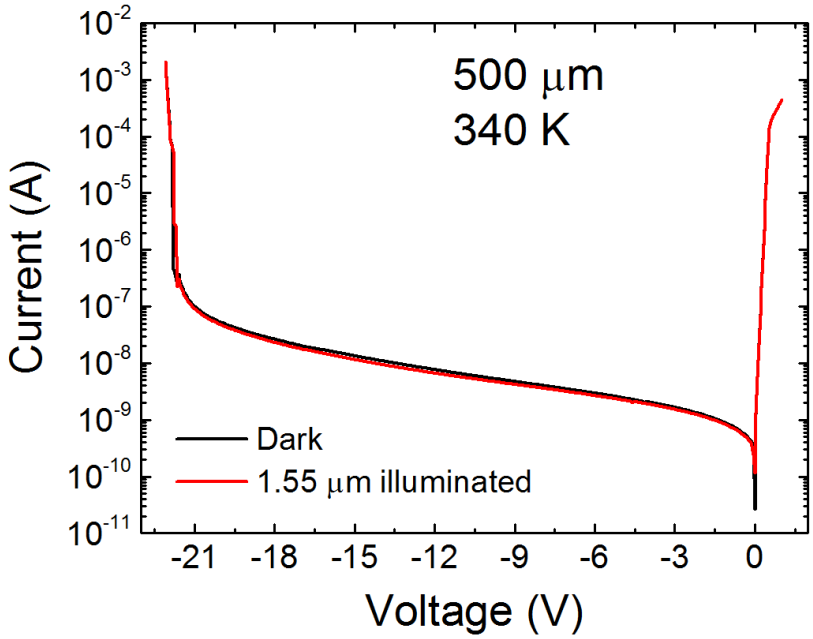


Figure 79: Dark and 1.55 μm laser illuminated I-V of a $Ge_{1-x}Sn_x$ APD with a 500 μm diameter.

The voltage dependent intensity of the spectral response was measured at room temperature (294 K) for a 500 μm diameter $Ge_{1-x}Sn_x$ APD. The spectra from each applied voltage are plotted in Figure 80. The peak intensity as a function of applied bias in Figure 80 (b)

shows the intensity increased non-linearly up to the breakdown voltage, followed by a decrease in response beyond the breakdown voltage. Photo-generated carriers absorbed within the Si substrate or directly within the Si multiplication region were multiplied due to impact ionization creating the voltage dependent gain. The drop off of intensity beyond the breakdown voltage was the result of increased dark current due to impact ionization of thermally generated carriers that start to dominate the signal current.

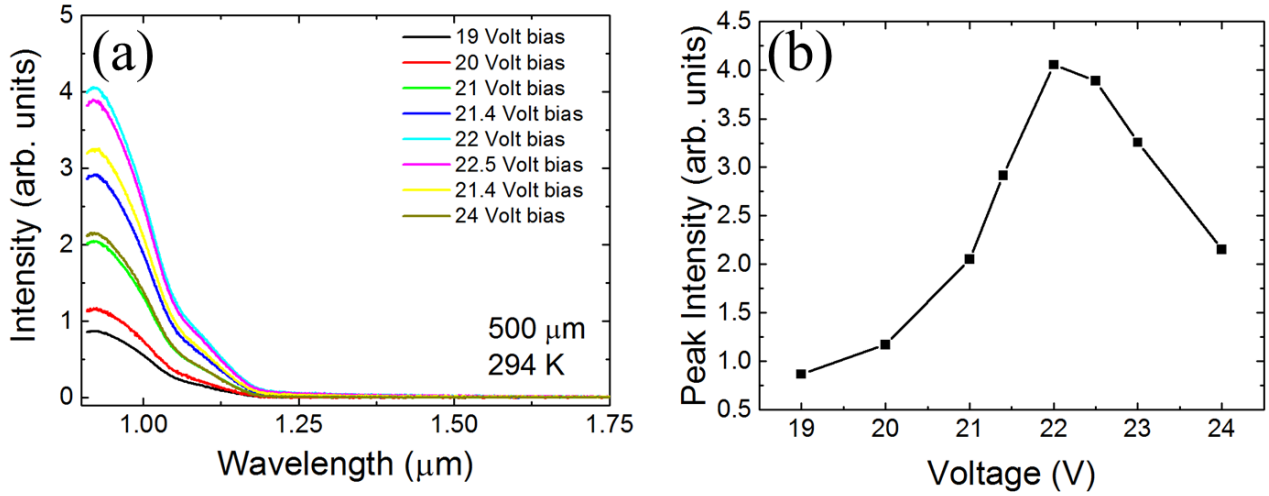


Figure 80: (a) Spectral response of a 500 µm diameter $Ge_{1-x}Sn_x$ APD measured at room temperature for different applied bias near the breakdown voltage. (b) Peak intensity from each spectrum plotted for each applied voltage.

Due to the lack of photoresponse in the SWIR spectrum, I-V measurements were made on the 100, 250, and 500 µm diameter $Ge_{1-x}Sn_x$ APDs under dark and white light condition in Figure 81. These measurements made for 77, 140, 200, and 300 K showed the large photocurrent due to white light absorption. The photocurrent at each temperature and device was the saturated photocurrent to achieve the maximum gain within the devices. The light current for all devices and temperatures was constant in the region from 0 to -15 volts. This region behaves as a reverse bias photodiode with a diffusion limited current and gain of ~1. As the bias approached the breakdown voltage for each temperature, the onset of avalanche of the photo-generated carriers

was observed as a change in the illumination current approximately 3–5 volts prior to breakdown.

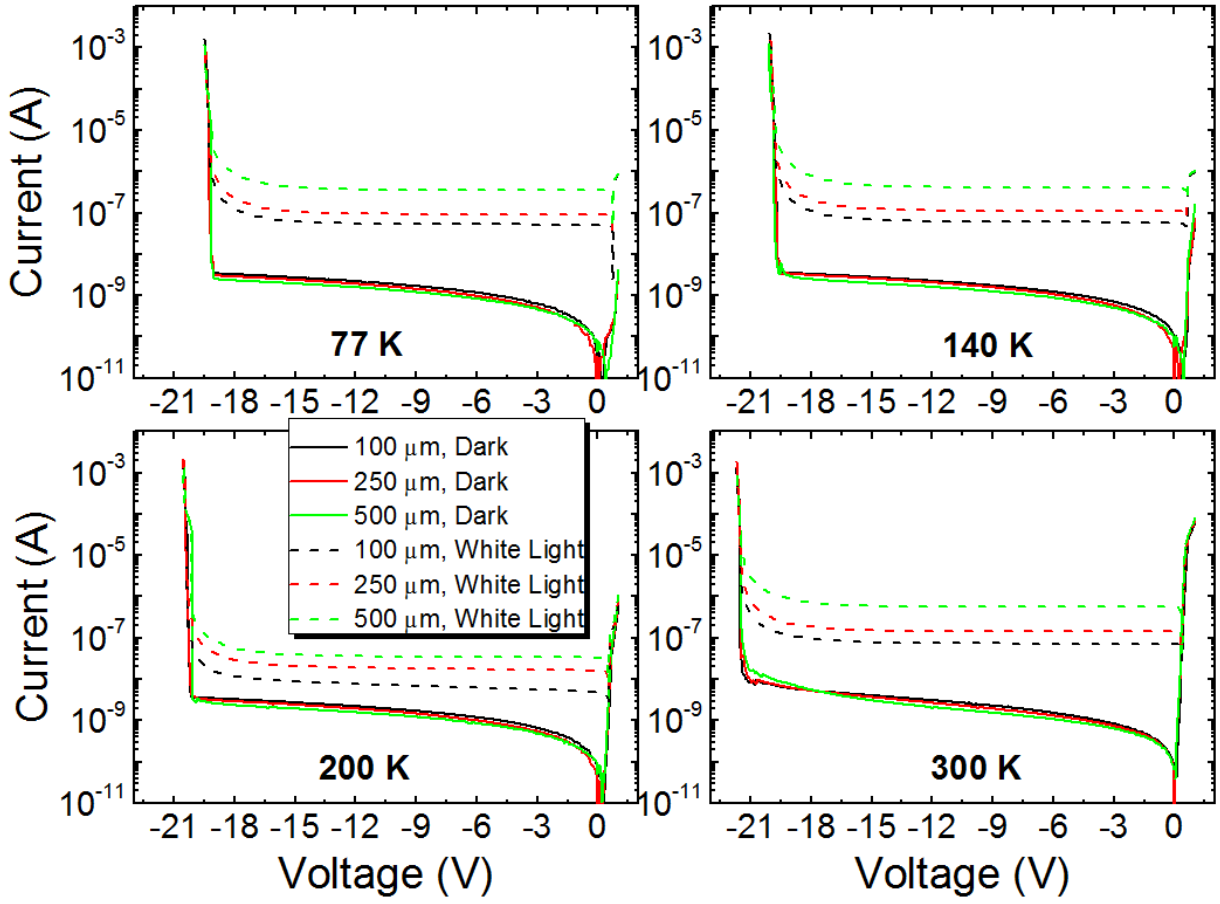


Figure 81: Dark (solid lines) and white light (dashed lines) I-V were measured for $Ge_{1-x}Sn_x$ APDs with 100, 250, and 500 µm diameters at 77, 140, 200, and 300 K.

The multiplication gain from the I-V measurements were calculated by normalizing a gain of one within the constant photocurrent region from 0 to -15 volts. The gain for each device and measured temperature is shown in Figure 82. The high gain of these devices under white light illumination was larger than 10 at 300 K and reached a maximum of over 1000 for operation at 140 K. Each device showed an increase in gain for decreased temperature that reached a maximum at 140 K operation, and then decreased at 77 K. This increase was due to the suppression of the trap assisted generation-recombination up to 140 K. Below this temperature

the ionized dopants start to become inactivated, reducing the depletion region and built in electric field. For voltages beyond the breakdown voltage the gain rapidly decreased and became negative (negative values not shown on log plot). This decrease was due to the increased multiplication noise as the dark current exponentially increased larger than the photocurrent.

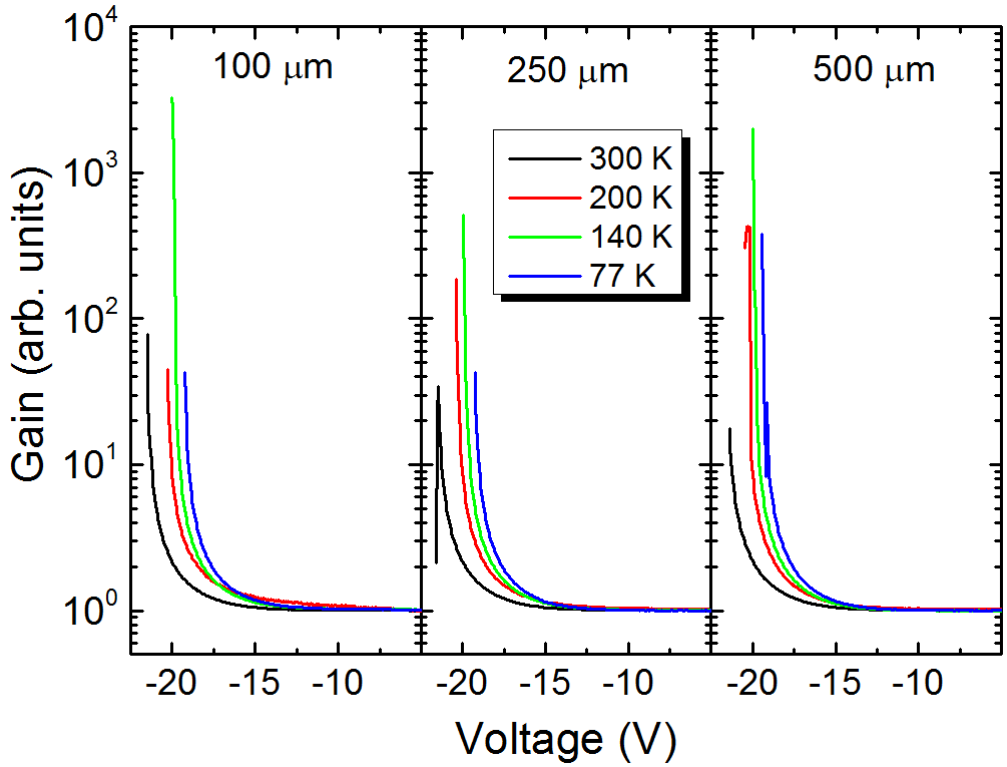


Figure 82: Experimentally multiplication gain of $Ge_{1-x}Sn_x$ APDs measured per applied bias. Devices with diameters of 100, 250, and 500 μm were measured at temperatures of 300, 200, 140, and 77 K.

The reason for the lack of multiplication of $Ge_{1-x}Sn_x$ generated carriers could be due to the band offset of holes entering the Si multiplication region as shown in Figure 32. To investigate this, future studies on the band offset for $Ge_{1-x}Sn_x$/Ge/Si will be needed. Other possible areas of exploration are reducing the Ge buffer layer within the SACM structure and increasing the doping concentration within the charge layer. This is expected to reduce the breakdown voltage, but allow 'punch through' of the depletion region into the $Ge_{1-x}Sn_x$ layer.

# Chapter 8: Summary and Future Work

## 8.1 Summary

This research studied the optoelectronic aspects of $Ge_{1-x}Sn_x$ thin films grown on Ge buffered Si. Up until now, research in the field of $Ge_{1-x}Sn_x$ materials focused primarily on the dynamics of film growth and material properties. Initial prototype detectors and emitters were further extensions of basic material physics; they lacked a deeper study of the device physics for these materials. Thus, the strategy for this work was to first establish compatibility of these materials with back end of the line (BEOL) Si CMOS processing by annealing at and below the critical 450 °C. The efficacy of a $Ge_{1-x}Sn_x$ laser on Si was then investigated by development of a high-Q cavity microdisk resonator. Next, the device characterization of $Ge_{1-x}Sn_x$ photoconductors with Sn content up to 10% demonstrated both a high responsivity and detectivity. These detectors proved that detection of SWIR up to 2.4 μm on a Si platform is possible with $Ge_{1-x}Sn_x$ films. The effective carrier and bulk lifetime for these films were estimated for the first time in this work at various Sn contents and temperatures. Finally, an avalanche photodiode (APD) with a $Ge_{1-x}Sn_x$ active layer was fabricated and tested as the next phase in the state-of-the art for this material.

Although $Ge_{1-x}Sn_x$ films were grown below 450 °C, thereby being compatible with any embedded CMOS components already incorporated, prior to this work investigation of the effects of BEOL processing on the $Ge_{1-x}Sn_x$ film were not considered. Films of increasing Sn content have a decreasing thermal budget, thereby making this a nontrivial question. Thin films deposited on Ge buffered Si were cycled at elevated temperatures above the growth temperature to measure the Sn segregation on films up to 7% Sn. Additionally, films were annealed at 400 and 450 °C and compared for film quality as a result of subsequent processing. For BEOL

compliant temperatures, each film showed initial degradation for annealing times on order of 30–60 seconds due to the initial relaxation of the film. Continued annealing on order of 1–5 minutes, restored the material quality equal to the as-grown film. These experiments demonstrate that $Ge_{1-x}Sn_x$ films are both forward and backwards compatible with Si CMOS processes.

Development of a Si based laser is one top interest of the microelectronics industry because it would enable high speed optical communication in a revolutionary way. This technology would enable data centers to operate with lower power consumption, more condensed processing power, and with lower cooling requirements. This work sought to explore a $Ge_{1-x}Sn_x$ based laser by way of a high-Q cavity. A microdisk cavity modeled with $Ge_{1-x}Sn_x$ optical parameters showed enhanced whisper gallery modes (WGM) around the circumference of the disk. These resonant modes allow increased optical fields to overcome material losses and enable stimulus emission of laser light. This work developed a simple one-mask approach for the fabrication of $Ge_{1-x}Sn_x$ microdisks on Si. Low temperature photoluminescence measured a resonant enhancement within the microdisk compared to the bulk $Ge_{1-x}Sn_x$ film with a three mode hop resonance. However, these microdisks did not exhibit stimulus emission.

A reliable fabrication process for $Ge_{1-x}Sn_x$ photoconductors was developed. Photoconductors with Sn concentrations of 0.9, 3.2, 7.0, 8.0, 9.0, and 10.0% Sn were fabricated and tested as a broad range study of the device physics for these films. The temperature dependent electrical and optical experiments on these films determined that increased Sn content samples up to 10% Sn did not reduce the device performance. This result goes against the increasing lattice mismatch of high Sn content films and the Ge buffer layer, showing that the quality of these films has improved. The experimental space in this work will allow engineering of a detector with a cut-off up to 2.4 μm based on the desired operating temperature or Sn

content. Additionally, carrier activation energies and dark current mechanisms were identified and provide a baseline for future device performance improvements.

Testing of each $Ge_{1-x}Sn_x$ photodetector was done within a temperature controlled cryostat. In order to efficiently test the electrical and optical properties of these detectors, the process flow for mounting and testing these devices on a commercially available chip carrier was developed. The standard fabrication process from as-grown thin films on a substrate to packaged $Ge_{1-x}Sn_x$ prototypes was developed in this work and is now available for future researchers.

One fundamental property of any electronic or photonic device is the carrier lifetime. This work sought to measure this value based on experimental performance metrics of the fabricated photoconductor devices. From the simple co-planar photoconductors, the effective carrier lifetime of the devices were calculated as a function of the operating temperature. Since this effective carrier lifetime is device dependent, the bulk carrier lifetime is the preferred quantity. Interdigitated electrode photoconductors with varying distance between the electrodes allowed the bulk lifetime and minority carrier diffusion constant to be measured. These values have never before been experimentally calculated for a $Ge_{1-x}Sn_x$ film.

The high gain, low noise, and low temperature sensitivity of Si based APDs with a $Ge_{1-x}Sn_x$ thin film were explored in this work. The established viability of $Ge_{1-x}Sn_x$ for SWIR detection in this work, and the previous success by other researchers using Ge absorption layer with a Si multiplication APD led this work to explore a $Ge_{1-x}Sn_x$ based APD on Si. A separate absorption charge multiplication (SACM) was designed based the available $Ge_{1-x}Sn_x$ growth limitations. The thin film samples were packaged and tested for their SWIR response, breakdown voltage, gain, and temperature dependent behavior. All indications from the fabrication to the electrical and optical testing show that the fabrication was successful in creating an APD.

However, the inactive $Ge_{1-x}Sn_x$ region indicates that either the APD design or growth must be adjusted.

### 8.2 Future Work

Photoconductors with high dark currents are more susceptible to noise mechanisms dependent on current within the device. Thus, a method for noise reduction is needed to decrease the dark current. This could be accomplished by reducing the amount of dangling bonds and surface states with improved surface passivation. As the size of the detector reduces, leakage current becomes dominated by surface recombination. Thus surface passivation becomes increasingly important as the detector size decreases. This effect could then be measured using the photodetector testing setup and analysis process flow established in this work.

The next step in developing a $Ge_{1-x}Sn_x$ laser based on the microdisk design should include an etch process with reduced surface roughness such as a $BCl_3$ based dry etch. After fabrication of the microdisk, passivation by way of $SiO_2$ or BCB could be used to reduce the density of states and non-radiative recombination at the surface.

The next step in the $Ge_{1-x}Sn_x$ development roadmap should be a detector array on Si with an appropriate read out integrated circuit (ROIC). The design in Figure 83 depicts a simple schematic for how this monolithic integration method could be applied for a $Ge_{1-x}Sn_x$ based FPA on Si. Since the $Ge_{1-x}Sn_x$ deposition process complies with current CMOS design rules, no major design rule modifications would be required for this device. For this design the ROIC transistors are fabricated using standard front end of the line (FEOL) methods, and then a $SiO_2$ isolation layer is deposited. A window would then be opened up in the oxide, exposing the Si substrate for a Ge buffer and $Ge_{1-x}Sn_x$ active pixel deposition process. Following this deposition, the connecting metal stacks and oxide separation layers are deposited to allow readout of the

accumulated charge. This design would allow for either front or back-side illuminated mounting. Direct growth of $Ge_{1-x}Sn_x$ on Si could then be used to detect in the SWIR at the same level of pixel density and low cost as current Si CMOS imagers that are in everything from smart phones to DSLR cameras.

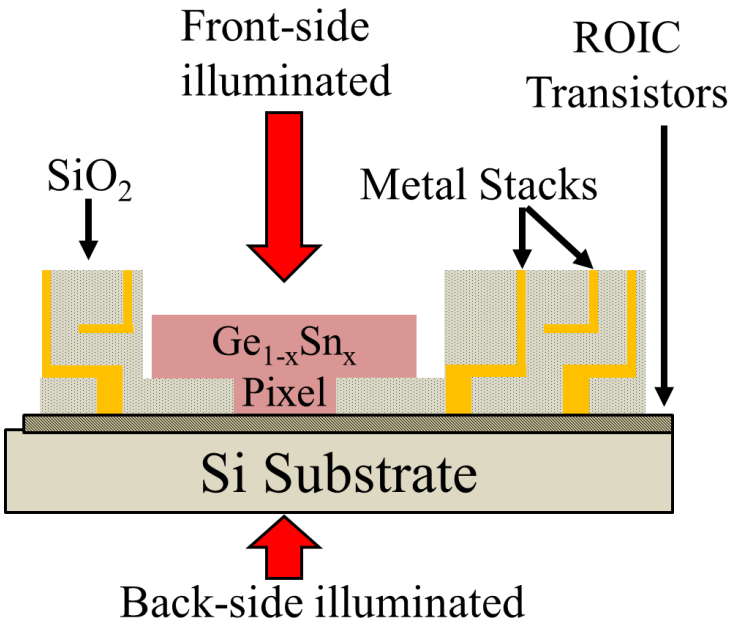


Figure 83: Design for monolithic integration of epitaxial $Ge_{1-x}Sn_x$ pixels with a Si read out integrated circuit (ROIC). Not drawn to scale.

The compositional dependent absorption cut-off and fabrication methodology demonstrated in this work would directly allow for multi-spectral imaging using $Ge_{1-x}Sn_x$ materials. This can be applied for single element detectors or for low cost lab-on-a-chip spectral measurement applications. This design could also be used for $Ge_{1-x}Sn_x$ pixels within a detector array for multi-spectral imaging in the SWIR. The increasing Sn content design of each subsequent $Ge_{1-x}Sn_x$ layer would also allow a lower lattice mismatch for the higher Sn content films allowing for a lower defect interface.

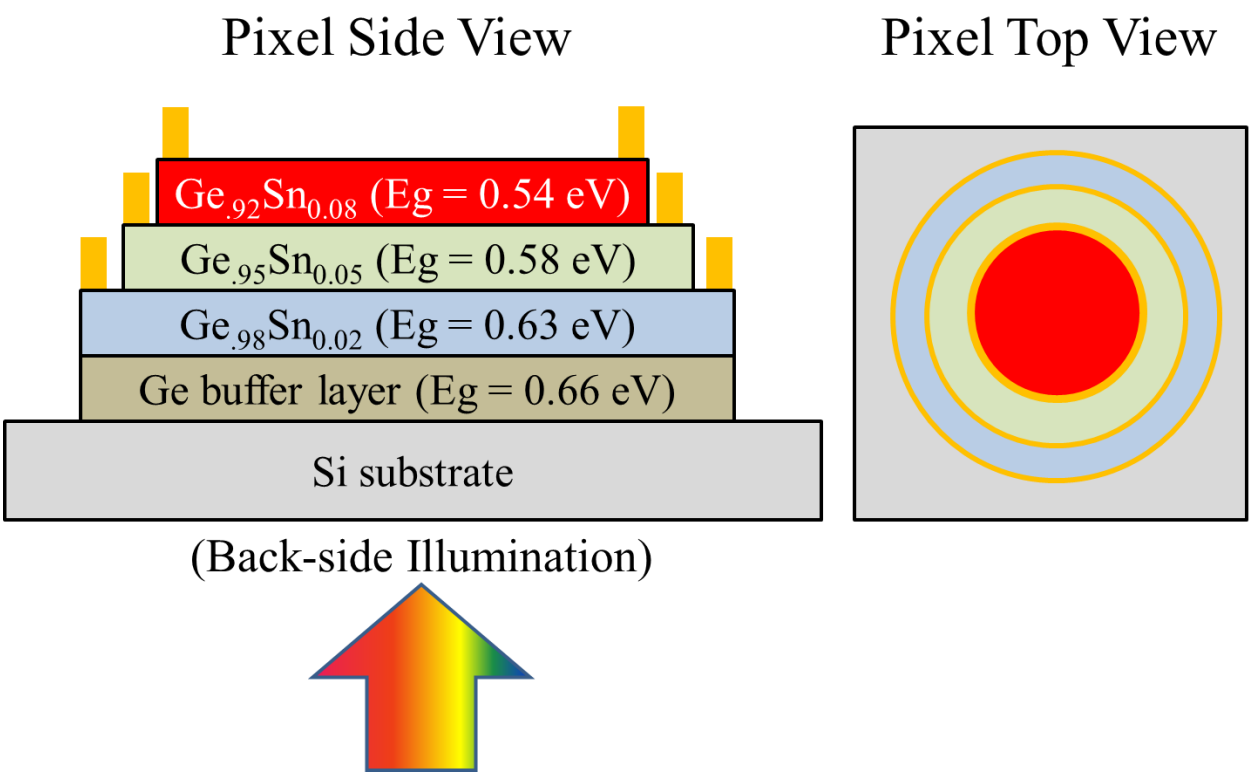


Figure 84: Cross sectional side view of a multi-spectral detection design using $Ge_{1-x}Sn_x$ films can be accomplished by increasing the Sn content of each subsequent film. This design would be back-side illuminated. Top view of the pixel shows a simple geometry for the metal contacts of each layer. Not drawn to scale.

## References


[1] A. Georgakilas, G. Deligeorgis, E. Aperathitis, D. Cengher, Z. Hatzopoulos, M. Alexe, *et al.*, "Wafer-scale integration of GaAs optoelectronic devices with standard Si integrated circuits using a low-temperature bonding procedure," *Appl. Phys. Lett.*, vol. 81, pp. 5099-5101, 2002.

[2] G. Roelkens, J. Van Campenhout, J. Brouckaert, D. Van Thourhout, R. Baets, P. R. Romeo, *et al.*, "III-V/Si photonics by die-to-wafer bonding," *Mater. Today*, vol. 10, pp. 36-43, 2007.

[3] R. A. Soref, "Silicon-based optoelectronics," *Proc. IEEE*, vol. 81, pp. 1687-1706, 1993.

[4] J. Michel, J. Liu, and L. C. Kimerling, "High-performance Ge-on-Si photodetectors," *Nat. Photon.*, vol. 4, pp. 527-534, 2010.

[5] J. Liu, X. Sun, R. Camacho-Aguilera, L. C. Kimerling, and J. Michel, "Ge-on-Si laser operating at room temperature," *Opt. Lett.*, vol. 35, pp. 679-681, 2010.

[6] J. Liu, L. C. Kimerling, and J. Michel, "Monolithic Ge-on-Si lasers for large-scale electronic–photonic integration," *Semicond. Sci. Technol.*, vol. 27, p. 094006, 2012.

[7] V. D'Costa, C. Cook, A. Birdwell, C. Littler, M. Canonico, S. Zollner, *et al.*, "Optical critical points of thin-film $Ge_{1-y}Sn_y$ alloys: A comparative $Ge_{1-y}Sn_y$/$Ge_{1-x}Si_x$ study," *Phys. Rev. B*, vol. 73, p. 125207, 2006.

[8] S. A. Ghetmiri, W. Du, J. Margetis, A. Mosleh, L. Cousar, B. R. Conley, *et al.*, "Direct-bandgap GeSn grown on Silicon with 2230 nm photoluminescence," *Appl. Phys. Lett.*, vol. 105, p. 151109, 2014.

[9] B. R. Conley, A. Mosleh, S. A. Ghetmiri, H. A. Naseem, J. Tolle, and Y. Shui-Qing, "CVD growth of $Ge_{1-x}Sn_x$ using large scale Si process for higher efficient multi-junction solar cells," in *Photovoltaic Specialists Conference (PVSC), 2013 IEEE 39th*, 2013, pp. 1346-1349.

[10] J. Taraci, J. Tolle, J. Kouvetakis, M. R. McCartney, D. J. Smith, J. Menendez, *et al.*, "Simple chemical routes to diamond-cubic germanium–tin alloys," *Appl. Phys. Lett.*, vol. 78, p. 3607, 2001.

[11] O. Gurdal, P. Desjardins, J. R. A. Carlsson, N. Taylor, H. H. Radamson, J. E. Sundgren, *et al.*, "Low-temperature growth and critical epitaxial thicknesses of fully strained metastable $Ge_{1-x}Sn_x$ ($x <\sim 0.26$) alloys on Ge(001)2 x 1," *J. Appl. Phys.*, vol. 83, pp. 162-170, 1998.

[12] V. R. D'Costa, J. Tolle, R. Roucka, C. D. Poweleit, J. Kouvetakis, and J. Menéndez, "Raman scattering in $Ge_{1-y}Sn_y$ alloys," *Solid State Commun.,* vol. 144, pp. 240-244, 2007.

[13] M. Oehme, M. Schmid, M. Kaschel, M. Gollhofer, D. Widmann, E. Kasper, *et al.*, "GeSn p-i-n detectors integrated on Si with up to 4% Sn," *Appl. Phys. Lett.,* vol. 101, p. 141110, 2012.

[14] M. Oehme, E. Kasper, and J. Schulze, "GeSn Heterojunction Diode: Detector and Emitter in One Device," *ECS J. of Solid State Sci. and Technol.,* vol. 2, pp. R76-R78, 2013.

[15] F. Gencarelli, B. Vincent, J. Demeulemeester, A. Vantomme, A. Moussa, A. Franquet, *et al.*, "Crystalline Properties and Strain Relaxation Mechanism of CVD Grown GeSn," *ECS J. of Solid State Sci. and Technol.,* vol. 2, pp. 134-137, 2013.

[16] B. Vincent, F. Gencarelli, H. Bender, C. Merckling, B. Douhard, D. H. Petersen, *et al.*, "Undoped and in-situ B doped GeSn epitaxial growth on Ge by atmospheric pressure-chemical vapor deposition," *Appl. Phys. Lett.,* vol. 99, p. 152103, 2011.

[17] V. R. D'Costa, Y. Fang, J. Mathews, R. Roucka, J. Tolle, J. Menéndez, *et al.*, "Sn-alloying as a means of increasing the optical absorption of Ge at the C- and L-telecommunication bands," *Semicond. Sci. Technol.,* vol. 24, p. 115006, 2009.

[18] A. Mosleh, S. Ghetmiri, B. Conley, M. Hawkridge, M. Benamara, A. Nazzal, *et al.*, "Material Characterization of $Ge_{1-x}Sn_x$ Alloys Grown by a Commercial CVD System for Optoelectronic Device Applications," *J. Electron. Mater.,* vol. 43, pp. 938-946, 2014.

[19] R. Loo, B. Vincent, F. Gencarelli, C. Merckling, A. Kumar, G. Eneman, *et al.*, "$Ge_{1-x}Sn_x$ Materials: Challenges and Applications," *ECS J. of Solid State Sci. and Technol.,* vol. 2, pp. 35-40, 2013.

[20] S. Wirths, D. Buca, G. Mussler, A. T. Tiedemann, B. Holländer, P. Bernardy, *et al.*, "Reduced Pressure CVD Growth of Ge and $Ge_{1-x}Sn_x$ Alloys," *ECS J. of Solid State Sci. and Technol.,* vol. 2, pp. 99-102, 2013.

[21] R. Soref, "Group IV photonics for the mid infrared," *SPIE Silicon Photonics VIII,* vol. 8629, 2013.

[22] J. Xie, J. Tolle, V. R. D'Costa, C. Weng, A. V. G. Chizmeshya, J. Menendez, *et al.*, "Molecular approaches to p- and n-nanoscale doping of $Ge_{1-y}Sn_y$ semiconductors: Structural, electrical and transport properties," *Solid-State Electron.,* vol. 53, pp. 816-823, 2009.

[23] J. Taraci, S. Zollner, M. McCartney, J. Menendez, M. Santana-Aranda, D. Smith, *et al.*, "Synthesis of silicon-based infrared semiconductors in the Ge-Sn system using molecular chemistry methods," *J. Am. Chem. Soc.,* vol. 123, pp. 10980-10987, 2001.

[24] M.-Y. Ryu, T. R. Harris, Y. K. Yeo, R. T. Beeler, and J. Kouvetakis, "Temperature-dependent photoluminescence of Ge/Si and $Ge_{1-y}Sn_y$/Si, indicating possible indirect-to-direct bandgap transition at lower Sn content," *Appl. Phys. Lett.,* vol. 102, p. 171908, 2013.

[25] R. Roucka, Y. Y. Fang, J. Kouvetakis, A. Chizmeshya, and J. Menéndez, "Thermal expansivity of $Ge_{1-y}Sn_y$ alloys," *Phys. Rev. B,* vol. 81, 2010.

[26] H. Li, Y. X. Cui, K. Y. Wu, W. K. Tseng, H. H. Cheng, and H. Chen, "Strain relaxation and Sn segregation in GeSn epilayers under thermal treatment," *Appl. Phys. Lett.,* vol. 102, p. 251907, 2013.

[27] R. Chen, Y.-C. Huang, S. Gupta, A. C. Lin, E. Sanchez, Y. Kim, *et al.*, "Material characterization of high Sn-content, compressively-strained GeSn epitaxial films after rapid thermal processing," *J. of Crys. Growth,* vol. 365, pp. 29-34, 2013.

[28] P. Moontragoon, R. A. Soref, and Z. Ikonic, "The direct and indirect bandgaps of unstrained $Si_xGe_{1-x-y}Sn_y$ and their photonic device applications," *J. Appl. Phys.,* vol. 112, p. 073106, 2012.

[29] R. Beeler, R. Roucka, A. Chizmeshya, J. Kouvetakis, and J. Menéndez, "Nonlinear structure-composition relationships in the $Ge_{1-y}Sn_y$/Si(100) ($y<0.15$) system," *Phys. Rev. B,* vol. 84, 2011.

[30] E. Kasper, M. Kittler, M. Oehme, and T. Arguirov, "Germanium tin: silicon photonics toward the mid-infrared [Invited]," *Photon. Res.,* vol. 1, pp. 69-76, 2013.

[31] B. R. Conley, A. Mosleh, S. A. Ghetmiri, W. Du, G. Sun, R. Soref, *et al.*, "Stability of Pseudomorphic and Compressively Strained Ge1-XSnx Thin Films under Rapid Thermal Annealing," *ECS Transactions,* vol. 64, pp. 881-893, August 12, 2014 2014.

[32] R. Cheng, W. Wang, X. Gong, L. Sun, P. Guo, H. Hu, *et al.*, "Relaxed and Strained Patterned Germanium-Tin Structures: A Raman Scattering Study," *ECS J. of Solid State Sci. and Technol.,* vol. 2, pp. 138-145, 2013.

[33] D. Shaw, "Self- and impurity diffusion in Ge and Si," *Phys. Status Solidi B,* vol. 72, pp. 11-39, 1975.

[34] D. Liang and J. E. Bowers, "Recent progress in lasers on silicon," *Nat. Photon.,* vol. 4, pp. 511-517, 2010.

[35] Y. A. Vlasov, "Silicon Integrated Nanophotonics: Road from Scientific Explorations to Practical Applications," presented at the Conference on Lasers and Electro-Optics (CLEO), San Jose, CA, 2012.

[36] J. Liu, "Monolithically Integrated Ge-on-Si Active Photonics," in *Photonics*, 2014, pp. 162-197.

[37] D. Liang and J. E. Bowers, "Photonic integration: Si or InP substrates?," *Electron. Lett.*, vol. 45, pp. 578-581, 2009.

[38] R. Soref, "The past, present, and future of silicon photonics," *IEEE J. Sel. Top. Quant. Electron.*, vol. 12, pp. 1678-1687, 2006.

[39] A. V. Krishnamoorthy, K. W. Goossen, W. Jan, Z. Xuezhe, R. Ho, L. Guoliang, *et al.*, "Progress in Low-Power Switched Optical Interconnects," *IEEE J. Sel. Topics Quantum Electron.*, vol. 17, pp. 357-376, 2011.

[40] R. A. Soref, S. J. Emelett, and W. R. Buchwald, "Silicon waveguided components for the long-wave infrared region," *J. Opt. A-Pure Appl. Op.*, vol. 8, p. 840, 2006.

[41] Z. Cheng, X. Chen, C. Y. Wong, K. Xu, and H. K. Tsang, "Mid-infrared Suspended Membrane Waveguide and Ring Resonator on Silicon-on-Insulator," *IEEE Photonics J.*, vol. 4, pp. 1510-1519, 2012.

[42] G. T. Reed, G. Mashanovich, F. Y. Gardes, and D. J. Thomson, "Silicon optical modulators," *Nat. Photon.*, vol. 4, pp. 518-526, 2010.

[43] L. Tsybeskov, D. J. Lockwood, and M. Ichikawa, "Silicon Photonics: CMOS Going Optical," *Proc. IEEE*, vol. 97, pp. 1161-1165, 2009.

[44] L. Ansheng, L. Ling, Y. Chetrit, J. Basak, N. Hat, D. Rubin, *et al.*, "Wavelength Division Multiplexing Based Photonic Integrated Circuits on Silicon-on-Insulator Platform," *IEEE J. Sel. Top. Quant. Electron.*, vol. 16, pp. 23-32, 2010.

[45] B. G. Lee, C. Xiaogang, A. Biberman, L. Xiaoping, I. W. Hsieh, C. Cheng-Yun, *et al.*, "Ultrahigh-Bandwidth Silicon Photonic Nanowire Waveguides for On-Chip Networks," *IEEE Photon. Technol. Lett.*, vol. 20, pp. 398-400, 2008.

[46] R. Halir, A. Maese-Novo, A. Ortega-Monux, I. Molina-Fernandez, J. G. Wanguemert-Perez, P. Cheben, *et al.*, "Compact broadband directional coupler," in *Group IV Photonics (GFP), 2012 IEEE 9th International Conference on*, 2012, pp. 177-179.

[47] X. Chen, C. Li, and K. Tsang Hon, "Device engineering for silicon photonics," *NPG Asia Mater*, vol. 3, pp. 34-40, 2011.

[48] A. Mekis, S. Gloeckner, G. Masini, A. Narasimha, T. Pinguet, S. Sahni, *et al.*, "A Grating-Coupler-Enabled CMOS Photonics Platform," *IEEE J. Sel. Top. Quant. Electron.*, vol. 17, pp. 597-608, 2011.

[49] A. W. Fang, H. Park, O. Cohen, R. Jones, M. J. Paniccia, and J. E. Bowers, "Electrically pumped hybrid AlGaInAs-silicon evanescent laser," *Opt. Express*, vol. 14, pp. 9203-9210, 2006.

[50] R. E. Camacho-Aguilera, Y. Cai, N. Patel, J. T. Bessette, M. Romagnoli, L. C. Kimerling, *et al.*, "An electrically pumped germanium laser," *Opt. Express*, vol. 20, pp. 11316-11320, 2012.

[51] G. Sun, R. A. Soref, and H. H. Cheng, "Design of an electrically pumped SiGeSn/GeSn/SiGeSn double-heterostructure midinfrared laser," *J. of Appl. Phys.*, vol. 108, p. 033107, 2010.

[52] G. Sun, R. A. Soref, and H. H. Cheng, "Design of a Si-based lattice-matched room-temperature GeSn/GeSiSn multi-quantum-well mid-infrared laser diode," *Opt. Express*, vol. 18, pp. 19957-19965, 2010.

[53] S. L. McCall, A. F. J. Levi, R. E. Slusher, S. J. Pearton, and R. A. Logan, "Whispering-gallery mode microdisk lasers," *Appl. Phys. Lett.*, vol. 60, pp. 289-291, 1992.

[54] J. Van Campenhout, L. Liu, P. R. Romeo, D. Van Thourhout, C. Seassal, P. Regreny, *et al.*, "A Compact SOI-Integrated Multiwavelength Laser Source Based on Cascaded InP Microdisks," *Photon. Technol. Lett, IEEE*, vol. 20, pp. 1345-1347, 2008.

[55] G. Shambat, S.-L. Cheng, J. Lu, Y. Nishi, and J. Vuckovic, "Direct band Ge photoluminescence near 1.6 μm coupled to Ge-on-Si microdisk resonators," *Appl. Phys. Lett.*, vol. 97, p. 241102, 2010.

[56] A. Ghrib, M. E. Kurdi, M. d. Kersauson, M. Prost, S. Sauvage, X. Checoury, *et al.*, "Tensile-strained germanium microdisks," *Appl. Phys. Lett.*, vol. 102, p. 221112, 2013.

[57] S. Cho, R. Chen, S. Koo, G. Shambat, H. Lin, N. Park, *et al.*, "Fabrication and Analysis of Epitaxially Grown $Ge_{1-x}Sn_x$ Microdisk Resonator with 20-nm Free-Spectral Range," *IEEE Photon. Technol. Lett.*, vol. 23, pp. 1535-1537, 2011.

[58] K. R. Williams, K. Gupta, and M. Wasilik, "Etch rates for micromachining processing-Part II," *J. Microelectromech. S.*, vol. 12, pp. 761-778, 2003.

[59] L. Bing-Jing and L. Pao-Lo, "Numerical analysis of the whispering gallery modes by the finite-difference time-domain method," *IEEE J. Quantum Electron.*, vol. 32, pp. 1583-1587, 1996.

[60] V. R. D'Costa, C. S. Cook, J. Menéndez, J. Tolle, J. Kouvetakis, and S. Zollner, "Transferability of optical bowing parameters between binary and ternary group-IV alloys," *Solid State Commun.*, vol. 138, pp. 309-313, 2006.

[61] S. L. Chuang, *Physics of photonic devices*, 2nd ed.: Wiley, 2009.

[62] X. Li, F. Ou, Y. Huang, and S.-T. Ho, "Micro-resonator loss computation using conformal-transformation and active-lasing FDTD approach and applications to tangential/radial output waveguide optimization II: FDTD approach," *Opt. Commun.*, vol. 291, pp. 447-454, 2013.

[63] H. Y. Y. T. S. Kim, Y. H. Ku, T. S. Jeong, S. Kang, K. H. Shim, "Dry Etching of Germanium by Using Inductively Coupled $CF_4$ Plasma," *Journal of Korean Physical Society*, vol. 54, pp. 2290-2296, June 2009 2009.

[64] G. S. Oehrlein, T. D. Bestwick, P. L. Jones, M. A. Jaso, and J. L. Lindström, "Selective Dry Etching of Germanium with Respect to Silicon and Vice Versa," *J. Electrochem. Soc*, vol. 138, pp. 1443-1452, 1991.

[65] G. S. Oehrlein, T. D. Bestwick, P. L. Jones, and J. W. Corbett, "Selective dry etching of silicon with respect to germanium," *Appl. Phys. Lett.*, vol. 56, pp. 1436-1438, 1990.

[66] H. Seidel, L. Csepregi, A. Heuberger, and H. Baumgärtel, "Anisotropic Etching of Crystalline Silicon in Alkaline Solutions: I . Orientation Dependence and Behavior of Passivation Layers," *J. Electrochem. Soc.*, vol. 137, pp. 3612-3626, 1990.

[67] L. Vivien, M. Rouvière, J.-M. Fédéli, D. Marris-Morini, J. F. Damlencourt, J. Mangeney, *et al.*, "High speed and high responsivity germanium photodetector integrated in a Silicon-On-Insulator microwaveguide," *Opt. Express*, vol. 15, pp. 9843-9848, 2007.

[68] D. Ahn, C.-y. Hong, J. Liu, W. Giziewicz, M. Beals, L. C. Kimerling, *et al.*, "High performance, waveguide integrated Ge photodetectors," *Opt. Express*, vol. 15, pp. 3916-3921, 2007.

[69] T. Yin, R. Cohen, M. M. Morse, G. Sarid, Y. Chetrit, D. Rubin, *et al.*, "31 GHz Ge n-i-p waveguide photodetectors on Silicon-on-Insulator substrate," *Opt. Express*, vol. 15, pp. 13965-13971, 2007.

[70] S. Dongwoo, K. Sanghoon, J. Jiho, and K. Gyungock, "36-GHz High-Responsivity Ge Photodetectors Grown by RPCVD," *IEEE Photon. Technol. Lett.*, vol. 21, pp. 672-674, 2009.

[71] Y. Kang, H.-D. Liu, M. Morse, M. J. Paniccia, M. Zadka, S. Litski, *et al.*, "Monolithic germanium/silicon avalanche photodiodes with 340 GHz gain–bandwidth product," *Nat. Photon.*, vol. 3, pp. 59-63, 2008.

[72] S. Assefa, F. Xia, and Y. A. Vlasov, "Reinventing germanium avalanche photodetector for nanophotonic on-chip optical interconnects," *Nature*, vol. 464, pp. 80-4, Mar 4 2010.

[73] L. Zhiwen, K. Yimin, H. Chong, Z. Qiugui, L. Han-Din, and J. C. Campbell, "Geiger-Mode Operation of Ge-on-Si Avalanche Photodiodes," *IEEE J. Quantum Electron.*, vol. 47, pp. 731-735, 2011.

[74] S. Su, B. Cheng, C. Xue, W. Wang, Q. Cao, H. Xue, *et al.*, "GeSn p-i-n photodetector for all telecommunication bands detection," *Opt. Express*, vol. 19, pp. 6400-6405, 2011.

[75] R. Roucka, J. Mathews, C. Weng, R. Beeler, J. Tolle, J. Menendez, *et al.*, "High-Performance Near-IR Photodiodes: A Novel Chemistry-Based Approach to Ge and Ge–Sn Devices Integrated on Silicon," *IEEE J. Quantum Electron.*, vol. 47, pp. 213-222, 2011.

[76] R. T. Beeler, C. Xu, D. J. Smith, G. Grzybowski, J. Menendez, and J. Kouvetakis, "Compositional dependence of the absorption edge and dark currents in $Ge_{1-x-y}Si_xSn_y$/Ge(100) photodetectors grown via ultra-low-temperature epitaxy of $Ge_4H_{10}$, $Si_4H_{10}$, and $SnD_4$," *Appl. Phys. Lett.*, vol. 101, p. 221111, 2012.

[77] A. Gassenq, F. Gencarelli, J. Van Campenhout, Y. Shimura, R. Loo, G. Narcy, *et al.*, "GeSn/Ge heterostructure short-wave infrared photodetectors on silicon," *Opt. Express*, vol. 20, pp. 27297-27303, 2012.

[78] A. Rogalski, "Progress in focal plane array technologies," *Prog. Quant. Electron.*, vol. 36, pp. 342-473, 2012.

[79] A. Rogalski, "Infrared detectors: an overview," *Infrared Phys. Techn.*, vol. 43, pp. 187-210, 2002.

[80] Y. Takeda, A. Sasaki, Y. Imamura, and T. Takagi, "Electron mobility and energy gap of $In_{0.53}Ga_{0.47}As$ on InP substrate," *J. Appl. Phys.*, vol. 47, pp. 5405-5408, 1976.

[81] (2011). *The International Technology Roadmap for Semiconductors (ITRS)*. Available: itrs.net

[82] C. Rafferty, C. King, B. Ackland, J. O'Neill, I. Aberg, T. S. Sriram, *et al.*, "Monolithic germanium SWIR imaging array," in *Technologies for Homeland Security, 2008 IEEE Conference on*, 2008, pp. 577-582.

[83] V. L. Rideout, "A review of the theory and technology for ohmic contacts to group III–V compound semiconductors," *Solid State Electron.*, vol. 18, pp. 541-550, 1975.

[84] D. K. Schroder, *Semiconductor material and device characterization*. Hoboken, New Jersey: John Wiley & Sons, 2006.

[85] F. Capasso, "Chapter 1 Physics of Avalanche Photodiodes," in *Semiconductors and Semimetals*. vol. Volume 22, Part D, W. T. Tsang, Ed., ed: Elsevier, 1985, pp. 1-172.

[86] E. Yu, E. Croke, D. Chow, D. Collins, M. Phillips, T. McGill, *et al.*, "Measurement of the valence band offset in novel heterojunction systems: Si/Ge (100) and AlSb/ZnTe (100)," *J. Vac. Sci. Technol. B,* vol. 8, pp. 908-915, 1990.

[87] A. Rogalski, *Infrared Detectors*. Boca Raton, FL: CRC Press, 2011.

[88] T. Kaneda, "Chapter 3 Silicon and Germanium Avalanche Photodiodes," in *Semiconductors and Semimetals*. vol. Volume 22, Part D, W. T. Tsang, Ed., ed: Elsevier, 1985, pp. 247-328.

[89] M. Coppinger, J. Hart, N. Bhargava, S. Kim, and J. Kolodzey, "Photoconductivity of germanium tin alloys grown by molecular beam epitaxy," *Appl. Phys. Lett.*, vol. 102, p. 141101, 2013.

[90] S. M. Sze and K. K. Ng, *Physics of Semiconductor Devices*: John Wiley & Sons, 2006.

[91] M. A. Kinch, "Fundamental physics of infrared detector materials," *J. Electron. Mater.*, vol. 29, pp. 809-817, 2000.

[92] B. R. Conley, A. Mosleh, S. A. Ghetmiri, W. Du, R. A. Soref, G. Sun, *et al.*, "Temperature dependent spectral response and detectivity of GeSn photoconductors on silicon for short wave infrared detection," *Opt. Express,* vol. 22, pp. 15639-15652, 2014.

[93] A. B. Sproul, "Dimensionless solution of the equation describing the effect of surface recombination on carrier decay in semiconductors," *J. Appl. Phys.*, vol. 76, pp. 2851-2854, 1994.

[94] M. A. Kinch, M. J. Brau, and A. Simmons, "Recombination mechanisms in 8–14 - $\mu$ HgCdTe," *J. Appl. Phys.*, vol. 44, pp. 1649-1663, 1973.

[95] J. M. Arias, J. G. Pasko, M. Zandian, S. H. Shin, G. M. Williams, L. O. Bubulac, *et al.*, "Planar p - on - n HgCdTe heterostructure photovoltaic detectors," *Appl. Phys. Lett.*, vol. 62, p. 976, 1993.

[96] H. Mohseni, A. Tahraoui, J. Wojkowski, M. Razeghi, G. J. Brown, W. C. Mitchel, *et al.*, "Very long wavelength infrared type-II detectors operating at 80 K," *Appl. Phys. Lett.*, vol. 77, p. 1572, 2000.

[97] J. D. Phillips, D. D. Edwall, and D. L. Lee, "Control of very-long-wavelength infrared HgCdTe detector-cutoff wavelength," *J. Electron. Mater.*, vol. 31, pp. 664-668, 2002.

[98] A. Rogalski, "Infrared detectors: status and trends," *Prog. Quant. Electron.*, vol. 27, pp. 59-210, 2003.

[99] Y. P. Varshni, "Temperature dependence of the energy gap in semiconductors," *Physica,* vol. 34, pp. 149-154, 1967.

[100] R. W. Hill and D. H. Parkinson, "XXV. The specific heats of germanium and grey tin at low temperatures," *The London, Edinburgh, and Dublin Philosophical Magazine and Journal of Science,* vol. 43, pp. 309-316, 1952/03/01 1952.

[101] R. Hull, *Properties of crystalline silicon*: IET, 1999.

[102] D. F. Gibbons, "Thermal Expansion of Some Crystals with the Diamond Structure," *Phys. Rev.,* vol. 112, pp. 136-140, 1958.

[103] J. Bardeen and W. Shockley, "Deformation Potentials and Mobilities in Non-Polar Crystals," *Phys. Rev.,* vol. 80, pp. 72-80, 1950.

[104] Y. Kang, P. Mages, A. R. Clawson, P. K. L. Yu, M. Bitter, Z. Pan, *et al.*, "Fused InGaAs-Si avalanche photodiodes with low-noise performances," *Photon. Technol. Lett, IEEE,* vol. 14, pp. 1593-1595, 2002.

[105] Y. Kang, M. Zadka, S. Litski, G. Sarid, M. Morse, M. J. Paniccia, *et al.*, "Epitaxially-grown Ge/Si avalanche photodiodes for 1.3 μm light detection," *Opt. Express,* vol. 16, pp. 9365-9371, 2008.

## Appendix A: Description of Research for Popular Publication

The average person can see all colors within the visible light spectrum. Imagine however only being able to see purple, blue, and green; completely excluding yellow, orange, and red. While this color vision defect is not a problem for most, everyone lacks the ability to see colors beyond red. This region of the spectrum, known as infrared, is also beyond the viewing range of image sensors in all consumer electronics such as smart phones and digital cameras. With this infrared range comes the ability to see through fog, smoke, and most dust particles. It would also allow for seeing and detecting objects in the dark, thus adding a new level of development to self-driving cars that are limited by their night time abilities. Such cameras would also allow for better passive security such as seeing down a dark alley way using only your cell phone camera.

Visible imaging sensors detect light using silicon, which is the dominant material responsible for allowing such cheap and prolific computers and other electronic devices. Imaging infrared light currently requires exotic elements (such as indium, arsenic, and mercury) that are more expensive to process into final imagers and cameras. A germanium and tin alloy is one promising solution to incorporate infrared imaging into a low cost platform. This material was already been successfully incorporated on a silicon platform using a method that wouldn't damage any existing electronics. This means that the process used for fabricating the visible image sensors in high definition cameras and smart devices can be simply 'upgraded' to include these germanium tin materials. Mr. Ben Conley, a researcher at the University of Arkansas, says that, "this level of mass production alongside consumer electronics would allow a dramatic reduction in cost for seeing the infrared."

Researchers at the University of Arkansas have been working with this new germanium tin material for over five years and have become one of the world leaders in germanium tin based

devices. Their work has developed the some of the fabrication and testing methods needed to bring this technology to a commercialized level. They were the first to measure the lifetime of the electrical carriers within this material. Mr. Conley said, “By understanding how long the infrared generated carriers remain in the detector will allow for a much better refinement of the device design.”

Thus far they have demonstrated single-pixel detectors using a simple fabrication process. These proof-of-concept detectors have already proven to be highly sensitive to the infrared light of interest. Dr. Shui-Qing Yu and Mr. Conley have already measured the highest responsivity of any other germanium tin based detector. The development so far will allow these devices to be directly incorporate on silicon electronics in the near future. In the next stage of their work they plan to begin fabrication of imaging arrays with germanium tin pixels.

## Appendix B: Executive Summary of Newly Created Intellectual Property

The following list of new intellectual property items were created in the course of this research project and should be considered from both a patent and commercialization perspective.

1. Bulk lifetime of a $Ge_{1-x}Sn_x$ thin film at 77 K.
2. A method for measuring the photoresponse and responsivity of photodetectors was developed using a Fourier Transform Infrared (FTIR) spectrometer, single wavelength lasers, and lock-in amplifier.
3. An etch recipe was developed using a $CF_4$ chemistry within a reactive ion etching tool to etch $Ge_{1-x}Sn_x$ thin films anisotropically. This simple recipe provides vertical etching profile of $Ge_{1-x}Sn_x$ and Ge thin films.
4. A method for fabricating and packaging $Ge_{1-x}Sn_x$ photodetectors into a commercially available dual in line (DIP) package for testing and prototype devices as future proof-of-concept devices.

## Appendix C: Potential Patent and Commercialization Aspects of listed Intellectual Property Items

### C.1 Patentability of Intellectual Property (Could Each Item be Patented)

The three items listed were considered first from the perspective of whether or not the item could be patented.

1. A measured value could not be patented.
2. The method for testing photodetectors used in this work cannot be patented. The measurement process is adopted from known standard measurement methods. It is unique only in regard of compatibility with the low temperature measurements of the packaged $Ge_{1-x}Sn_x$ and other fabricated detectors.
3. The etch recipe used in etching the $Ge_{1-x}Sn_x$ thin films could be patented. This etch method is compatible with Si CMOS processing and presents a known method for processing these $Ge_{1-x}Sn_x$ films once they are incorporated into modern fabrication facilities.
4. The packaging method is not patentable. The commercially available packages in combination with the wire bonding process are well known. The intellectual property is only unique to the specific fabrication methods used in creating the $Ge_{1-x}Sn_x$ photodetectors.

### C.2 Commercialization Prospects (Should Each Item Be Patented)

The three items listed were then considered from the perspective of whether or not the item should be patented.

1. Not applicable

2. Not applicable
3. The $Ge_{1-x}Sn_x$ etch recipe developed here should not be patented. Although the work here was sufficient in initial device study and prototype detectors, the recipe should be further optimized and is unlikely to meet patent standards for significant improvement over the prior art.
4. Not applicable

**C.3 Possible Prior Disclosure of IP**

The following items were discussed in a public forum or have published information that could impact the patentability of the listed IP.

1. Not applicable
2. Not applicable
3. Not applicable
4. Not applicable

## Appendix D: Broader Impact of Research

### D.1 Applicability of Research Methods to Other Problems

The method used in this dissertation that resulted in the a reliable processing method for creating $Ge_{1-x}Sn_x$ devices can be applied to directly applied to many other disciplines. The starting point for solving any potential challenge or unknown was to investigate the state of the art or methods used for a similar process and apply the known physical parameters of the material of interest. Eventual optimization of the device design and fabrication was accomplished by single variable modification and measurement of the resulting change. The general philosophy was strict adherence to the scientific method.

### D.2 Impact of Research Results on U.S. and Global Society

The camera and photodetector market in the U.S. and globally is saturated with low cost and high quality sensors for imaging and video recording in the visible spectrum. This work would enable the same low cost and scalable platform to detect into the short-wave infrared. A large market opportunity for this technology that would impact society the most would be security sectors, 3D imaging, self-driving vehicles, and greater incorporation of smart sensors and automation to improve everyday life.

### D.3 Impact of Research Results on the Environment

The absorption of infrared light that is currently uncaptured by Si solar cells is absorbed by these $Ge_{1-x}Sn_x$ films. The increased long-wavelength cut-off absorption edge can be tuned based on the Sn composition and operating temperature for improved multi-junction solar cell designs whilst adding little to the total fabrication cost.

# Appendix E: Microsoft Project for MS MicroEP Degree Plan

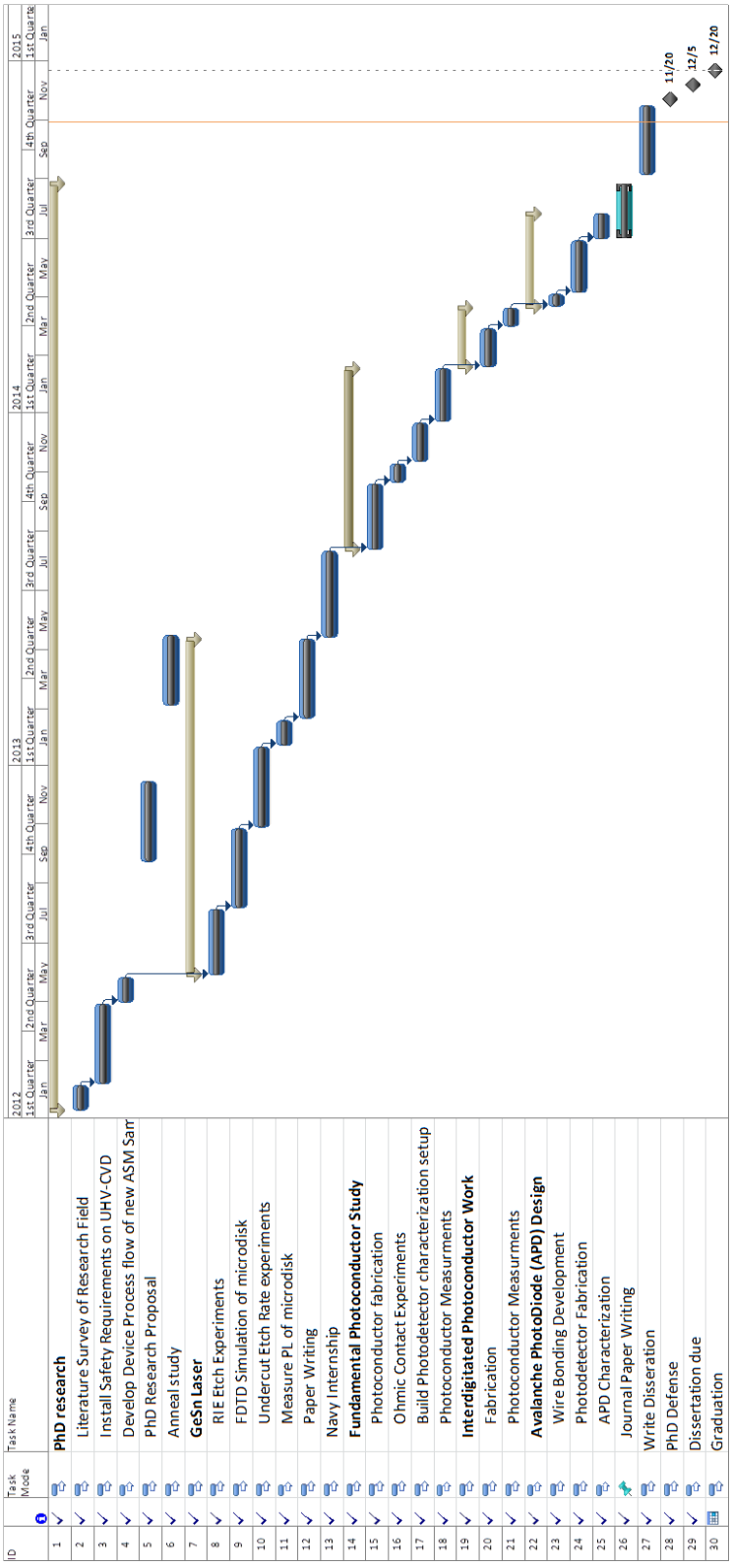

## Appendix F: Identification of All Software Used in Research and Dissertation Generation

Computer #1:
- Model Number: Antec
- Serial Number: Gigabyte – BG5027 00838
- Location: Personal PC
- Owner: Benjamin Conley

Software #1:
- Name: Microsoft Office 2010
- Purchased by: Benjamin Conley

Software #2:
- Name: Origin Pro Student Version
- Purchased by: Benjamin Conley

Software #3:
- Name: Microsoft Project 2010
- Purchased by: MSDN Academy Alliance through Engineering

Software #4:
- Name: Matlab R2012a Student Version
- Purchased by: Benjamin Conley

Software #5:
- Name: EndNote X6
- Purchased by: Benjamin Conley

Software #6:
- Name: MathType 6.9
- Purchased by: Benjamin Conley

Computer #2:
- Model Number: Dell Vostro
- Serial Number: 52M6XK1
- Location: ENRC Room 2993
- Owner: Dr. Shui-Qing Yu

Software #1:
- Name: OMNIC
- Purchased by: Dr. Shui-Qing Yu

Software #2:
- Name: LabVIEW 2012
- Purchased by: Electrical Engineering Department, University of Arkansas

Computer #3:
- Model Number: Corsair
- Serial Number: Gigabyte – 1/H/CGC22900355
- Location: ENRC Room 2993
- Owner: Dr. Shui-Qing Yu

Software #1:
- Name: Rsoft
- Purchased by: Dr. Shui-Qing Yu

## Appendix G: All Publications Published, Submitted and Planned

### G.1 List of peer reviewed published works


[1] B. R. Conley, A. Mosleh, S. A. Ghetmiri, W. Du, R. A. Soref, G. Sun, *et al.*, "Temperature dependent spectral response and detectivity of GeSn photoconductors on silicon for short wave infrared detection," *Opt. Express*, vol. 22, pp. 15639-15652, 2014.

[2] B. R. Conley, A. Mosleh, S. A. Ghetmiri, W. Du, G. Sun, R. Soref, *et al.*, "Stability of Pseudomorphic and Compressively Strained $Ge_{1-x}Sn_x$ Thin Films under Rapid Thermal Annealing," *ECS Transactions*, vol. 64, pp. 881-893, August 12, 2014 2014.

[3] S. A. Ghetmiri, W. Du, J. Margetis, A. Mosleh, L. Cousar, B. R. Conley, et al., "Direct-bandgap GeSn grown on Silicon with 2230 nm photoluminescence," Appl. Phys. Lett., vol. 105, p. 151109, 2014.

[4] S. A. Ghetmiri, W. Du, B. R. Conley, A. Mosleh, A. Nazzal, G. Sun, et al., "Shortwave-infrared photoluminescence from $Ge_{1-x}Sn_x$ thin films on silicon," J. Vac. Sci. Technol. B, vol. 32, pp. -, 2014.

[5] A. Mosleh, S. Ghetmiri, B. Conley, M. Hawkridge, M. Benamara, A. Nazzal, et al., "Material Characterization of $Ge_{1-x}Sn_x$ Alloys Grown by a Commercial CVD System for Optoelectronic Device Applications," J. Electron. Mater., vol. 43, pp. 938-946, 2014.

[6] A. Mosleh, S. A. Ghetmiri, B. R. Conley, H. H. Abu-Safe, M. Benamara, Z. Waqar, et al., "Investigation of Growth Mechanism and Role of H2 in Very Low Temperature Si Epitaxy," ECS Transactions, vol. 64, pp. 967-975, August 12, 2014 2014.

[7] A. Mosleh, M. Benamara, S. A. Ghetmiri, B. R. Conley, M. A. Alher, W. Du, et al., "Investigation on the Formation and Propagation of Defects in GeSn Thin Films," ECS Transactions, vol. 64, pp. 895-901, August 12, 2014 2014.

[8] J. Margetis, S. A. Ghetmiri, W. Du, B. R. Conley, A. Mosleh, R. Soref, et al., "Growth and Characterization of Epitaxial $Ge_{1-x}Sn_x$ Alloys and Heterostructures Using a Commercial CVD System," ECS Transactions, vol. 64, pp. 711-720, August 12, 2014 2014.

[9] W. Du, S. A. Ghetmiri, B. R. Conley, A. Mosleh, A. Nazzal, R. A. Soref, et al., "Competition of optical transitions between direct and indirect bandgaps in $Ge_{1-x}Sn_x$," Appl. Phys. Lett., vol. 105, p. 051104, 2014.

[10] W. Du, Y. Zhou, S. A. Ghetmiri, A. Mosleh, B. R. Conley, A. Nazzal, et al., "Room-temperature electroluminescence from Ge/ $Ge_{1-x}Sn_x$ /Ge diodes on Si substrates," Appl. Phys. Lett., vol. 104, p. 241110, 2014.

## G.2 List of conference proceedings and publications


[11] W. Du, S. A. Ghetmiri, A. Mosleh, B. Conley, L. Huang, A. Nazzal, et al., "Investigation of Photoluminescence from $Ge_{1-x}Sn_x$: A CMOS-Compatible Material Grown on Si via CVD," in CLEO: 2014, San Jose, California, 2014, p. JW2A.57.

[12] B. Conley, L. Huang, S. A. Ghetmiri, A. Mosleh, W. Du, G. Sun, *et al.*, "Extended Infrared Absorption to 2.2 μm with $Ge_{1-x}Sn_x$ Photodetectors Grown on Silicon," in *CLEO: 2014*, San Jose, California, 2014, p. SM2H.5.

[13] S. A. Ghetmiri, B. Conley, A. Mosleh, L. Huang, W. Du, A. Nazzal, *et al.*, "Photoluminescence from GeSn/Ge Heterostructure Microdisks with 6% Sn Grown on Si via CVD," in *CLEO: 2014*, San Jose, California, 2014, p. AW1H.2.

[14] B. R. Conley, A. Mosleh, S. A. Ghetmiri, W. Du, H. Naseem, S.-Q. Yu, *et al.*, "Temperature Dependent Spectral Response and Responsivity of GeSn Photoconductor on Si," in IEEE Photonics Summer Topical, Montreal, CA, 2014.

[15] T. Pham, B. R. Conley, L. Huang, W. Du, R. Soref, G. Sun, et al., "Enhanced responsivity by integration of interdigitated electrodes on $Ge_{0.93}Sn_{0.07}$ infrared photodetectors," presented at the IEEE Photonics Conference, San Diego, CA, 2014.

[16] A. Mosleh, S. A. Ghetmiri, B. R. Conley, W. Du, S.-Q. Yu, H. Naseem, et al., "Strain Relaxation and Material Quality Improvement of Compressively Strained GeSn Epitaxial Films Through a Cyclic Rapid Thermal Annealing Process," in IEEE Photonics Summer Topical, Montreal, CA, 2014.

[17] B. R. Conley, A. Mosleh, S. A. Ghetmiri, H. A. Naseem, J. Tolle, and Y. Shui-Qing, "CVD growth of Ge1-xSnx using large scale Si process for higher efficient multi-junction solar cells," in Photovoltaic Specialists Conference (PVSC), 2013 IEEE 39th, 2013, pp. 1346-1349.

[18] H. Naseem, Y. Shui-Qing, S. El-Ghazaly, Z. Waqar, H. Abu-Safe, S. Adcock, et al., "Safety Considerations in Building Ultra-High Vacuum Plasma Enhanced Chemical Vapor Deposition System for Low Temperature Group IV Epitaxy," in University/Government/Industry, Micro/Nano Symposium (UGIM), 2012 19th Biennial, 2012, pp. 1-1.

[19] A. Mosleh, S. A. Ghetmiri, B. R. Conley, S. Yu, H. Naseem, M. Benamara, et al., "Strain engineering of high quality CVD grown GeSn films for optoelectronic devices," in Electronic Materials Conference, 2013.

[20] A. Mosleh, S. A. Ghetmiri, B. R. Conley, H. Abu-Safe, Z. Waqar, M. Benamara, et al., "Nucleation-step study of silicon homoepitaxy for low-temperature fabrication of Si solar

cells," in Photovoltaic Specialists Conference (PVSC), 2013 IEEE 39th, 2013, pp. 2646-2650.

[21] Z. Hui, H. Abu-Safe, A. Hickerson, B. R. Conley, H. Naseem, and Y. Shui-Qing, "Crystallization of patterned amorphous si and ge thin films for 3D integrated optoelectronics," in Group IV Photonics (GFP), 2013 IEEE 10th International Conference on, 2013, pp. 53-54.

[22] B. R. Conley, H. Naseem, G. Sun, P. Sharps, and S.-Q. Yu, "High efficiency MJ solar cells and TPV using SiGeSn materials," in Photovoltaic Specialists Conference (PVSC), 2012 38th IEEE, 2012, pp. 001189-001192.

**G.3 List of submitted works**

[23] B. R. Conley, J. Margetis, W. Du, H. Tran, A. Mosleh, S. A. Ghetmiri, *et al.*, "Si based high performance GeSn photoconductor with 1.63 A/W peak responsivity and 2.4 μm long wavelength cut-off," Submitted to *Appl. Phys. Lett.*, 2014.

[24] B. R. Conley, W. Du, R. A. Soref, G. Sun, J. Margetis, J. Tolle, B. Li, S.-Q. Yu, "Enhanced gain of GeSn photoconductors by interdigitated electrodes for mid-infrared detection," Accepted to *SPIE Photonics West Conference*, 2015

**G.4 List of planned works**

[25] B. R. Conley, *et al*., "Effective and bulk lifetime of $Ge_{1-x}Sn_x$ photoconductors by interdigitated photoconductor method." *Appl. Phys. Lett.* 2015

## Appendix H: Device Fabrication Methods and Recipes

This appendix details process steps and recipes used in the High Density Electronics Center (HiDEC) to fabricate these $Ge_{1-x}Sn_x$ devices.

### H.1 Thin Film Processing

When etching $SiO_2$ from the plasma enhanced chemical vapor deposition (PECVD) with buffered oxide etch (BOE), first dip the sample in water to wet the surface. Otherwise the smaller features opened up in the photoresist are do not chemically react with the BOE to etch the oxide. This wetting dip should be done quite vigorously so to ensure all the small features are adequately wetted. Additionally, it was noticed that poor etching using BOE occurs when the BOE bottle is near empty. This bottom layer of BOE might also contain many particulates and plastics that have settled out of the solution with time that can then collect on the sample during etching. It is recommended to use a fresh bottle of BOE once only 0.25 liters remain in a given bottle. Oxide etch was performed using the premixed BOE 5:1 solution. An etch rate of PECVD grown $SiO_2$ was on order of 50 nm/second.

The PECVD and reactive ion etch (RIE) recipes used in this work are listed in Table 12 and Table 13, respectively.

Table 12: Plasma enhanced chemical vapor deposition recipes used for $SiO_2$ and $Si_3N_4$ thin film deposition

| Recipe Name | Deposited Film | $SiH_4$ (sccm) | $N_2O$ (sccm) | $N_2$ (sccm) | $NH_3$ (sccm) | He (sccm) | Deposition Rate (nm/min) |
|---|---|---|---|---|---|---|---|
| SiO2Alan | $SiO_2$ | 32 | 900 | 400 | 0 | 0 | 45 |
| Si3N4Ge | $Si_3N_4$ | 40 | 0 | 200 | 4 | 800 | 10 |

Table 13: Reactive ion etch recipes used to remove $Ge_{1-x}Sn_x$ and $Si_3N_4$ thin films

| Recipe Name | Film Etched | Ar (sccm) | CF4 (sccm) | O2 (sccm) | Power (watts) | Pressure (mtorr) | Etch Rate (μm/min) |
|---|---|---|---|---|---|---|---|
| GeSn_ET | Ge1-xSnx | 30 | 30 | 0 | 100 | 200 | 0.04 – 0.07 |
| Si3N4Ge | Si3N4 | 0 | 40 | 5 | 80 | 500 | 0.145 |

## H.2 Fabrication Methods

The resolution limit of AZ4110 is not sufficient for small features that must be subsequently dry etched. Even for moderate thicknesses (~2.0 μm) the higher intensity plasma on the center of a disk structure allows punch through of the photoresist. This leaves a ring structure instead of the desired disk structure. This was observed in some disks of sample 01233 and the SEM image in Figure 85 shows the clear opening in the center of disk after removal from the RIE process. Resist thicker than 2.0 μm reduces the resolution of the resist.

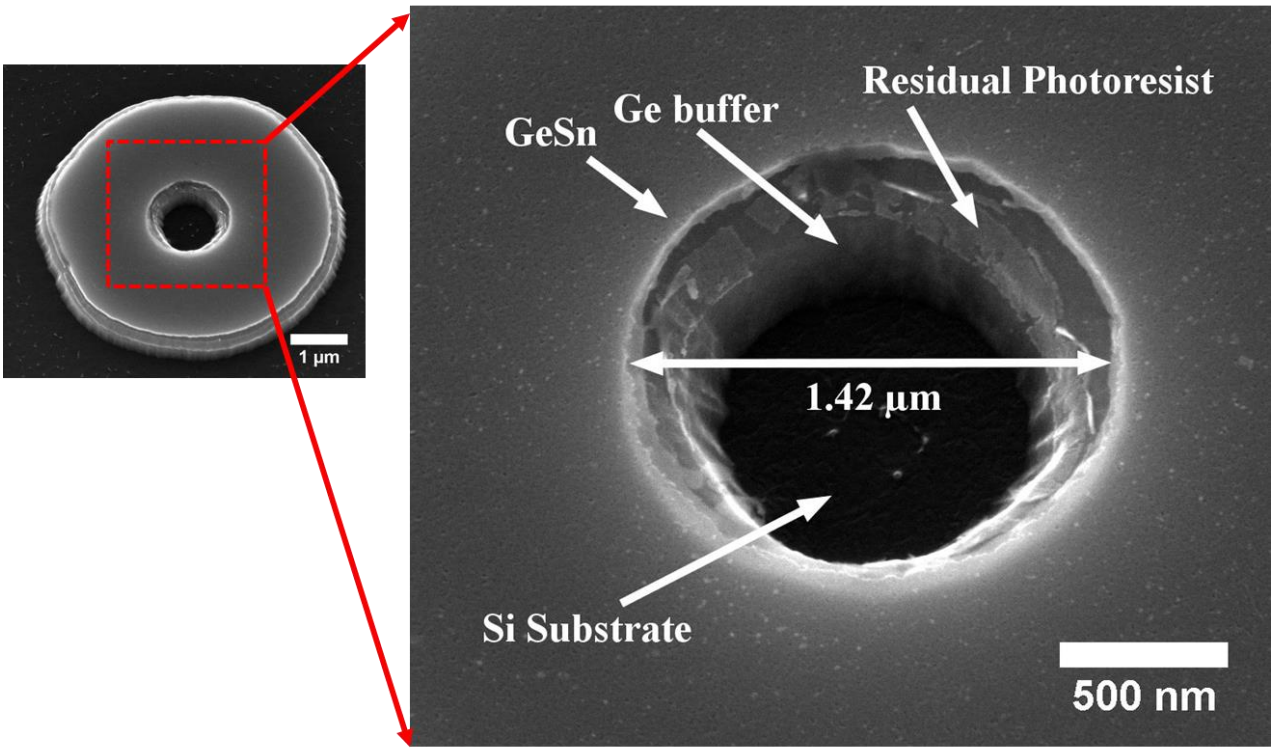


Figure 85: $Ge_{1-x}Sn_x$ ring formed by etching punch through of the photoresist within the RIE process.

For high resolution structures that must be dry etched, a hard mask such as aluminum should be used. For this process, Al would be evaporated, and then patterned using standard photolithography. The Al pattern is then defined using a wet etch such as Al Etchant Type D. Finally, the photoresist is removed leaving only an Al mask.

### H.3 Gold Bold Ball Bonding to Metal on BCB

Wire bonding to the thin metal (Au/Cr) pads for these devices requires a low power and force ball bonding process to reduce pealing of the metal pads. The settings listed in Table 14 are those that produce the most consistent bonding with little tearing of the metal pads. Although these settings are not robust to withstand pull-away of the ball from the pad, they are light enough to not significantly damage the sample. For more robust ball bonds, a thicker metal pad should be used to allow for higher power ball bonding processes. The power here refers to the ultra-sonic power of the bonding tip. Time and force are quantities describing the time of the bond and amount of force pressed onto the pad. The search column is more user preference as this is a relative height of the bonding tip above the sample while searching for the location to make the bond. The 1st and 2nd bonds refer to the order of the bond, with the sample pad being first then to the package. The difference in the power, time, and force settings show the large difference in bonding a thin film metal and that of a thicker plated ceramic. Gold ball bonding to samples with thin metal pads directly on a semiconductor allows for a higher power, force, and time settings to create a more robust ball bond. In this case, there is less tearing of the metal pad due to the stronger adhesion of metal on semiconductor compared to metal on BCB.

Table 14: Gold ball bond settings for wire bonding to thin Au/Cr pads on BCB

| | Power | Time | Force | Search |
|---|---|---|---|---|
| 1st Bond | 0.5 | 3.0 | 0.4 | 4.2 |
| 2nd Bond | 4.5 | 9.0 | 8.1 | 4.4 |

Additional general settings for the ball bonder tool are listed in Table 15. These settings for the ball bonding tool should be used as a starting point for gold ball bonding to thin metal pads. Loop is the vertical rise in the ball tip after the first bond. This setting should be varied per bond to allow enough slack in the wire when going from the thin film pad to the pad on the

ceramic package. Not enough slack in the wire after this first bond could result in the ball being ripped off as the tip is moved to the pad on the ceramic. The 2nd bond to the pad on the package is a wedge bond. The tail setting specifies the amount of wire used in this wedge bond. The ball setting is size of the ball in the 1st bond. Tear is related to the tearing process of the wire after the 2nd wedge bond is made. The speed setting is the rate of movement for the tip during the automated portion of the bonding process. Finally, temperature refers to the stage on which the sample sits. For Au ball bonding on these thin film samples a temperature of 85 °C was used with the best results. However, for samples with thicker gold pads a temperature of 120 °C produces a more robust ball bond with less tearing or separation from the sample.

Table 15: Global settings on the ball bonding tool for samples with thin film metal contacts

| Loop | Tail | Ball | Tear | Speed | Temperature (°C) |
|---|---|---|---|---|---|
| 8.0 | 5.2 | 6.5 | 4.0 | 4.1 | 85 |

## Appendix I: Design of Experiments Matrix and Results of Rapid Thermal Annealing

The data presented in Table 16 lists the full list of experimental parameters and measured data used in the design of experiments (DOE) analysis within Chapter 2. All data to the left of the solid vertical line are the input experimental parameters. To the right of this line are the measured quantities. Number of cycles is the repeated number of times the sample was subjected to annealing at the corresponding temperature and length of time. The photoluminescence (PL) full width half max (FWHM), peak location, and intensity were the measurable outputs of this DOE. The PL peak location was the center wavelength of the PL signal and intensity was the y-axis intensity of this peak.

Table 16: Design of Experiments Matrix for Rapid Thermal Annealing of $Ge_{1-x}Sn_x$ Thin Films

| Sample No. | Temperature ( C ) | Time (seconds) | Sn Mole Fraction | Number of Cycles | PL FWHM (nm) | PL Peak Location (nm) | PL Peak Intensity (uV) |
|---|---|---|---|---|---|---|---|
| 0007-A1 | 450 | 120 | 0.06 | 1 | 376 | 1992 | 56.7 |
| 0007-A2 | 400 | 120 | 0.06 | 3 | 364 | 2004 | 125.3 |
| 0001-B2 | 450 | 120 | 0.026 | 5 | 149 | 1715 | 97.6 |
| 0008-A1 | 450 | 120 | 0.07 | 5 | 243 | 2151 | 45 |
| 0008-A2 | 400 | 120 | 0.07 | 1 | 264 | 2165 | 93 |
| 0008-B1 | 450 | 30 | 0.07 | 1 | 329 | 2113 | 67.1 |
| 0001-A2 | 400 | 120 | 0.026 | 1 | 112 | 1739 | 94.1 |
| 0008-B2 | 450 | 120 | 0.07 | 3 | 338 | 2102 | 162.3 |
| 0001-A1 | 450 | 120 | 0.026 | 1 | 123 | 1726 | 26.4 |
| 0007-A3 | 400 | 120 | 0.06 | 5 | 403 | 1990 | 155 |
| 0007-A4 | 400 | 30 | 0.06 | 1 | 344 | 1995 | 395.3 |
| 0008-A3 | 400 | 120 | 0.07 | 5 | 258 | 2138 | 109 |
| 0008-A4 | 400 | 30 | 0.07 | 3 | 291 | 2126 | 145.4 |
| 0001-B1 | 450 | 30 | 0.026 | 3 | 191 | 1706 | 67.2 |
| 0001-A4 | 400 | 30 | 0.026 | 5 | 120 | 1730 | 53.6 |
| 0007-B2 | 450 | 120 | 0.06 | 3 | 271 | 2013 | 274.1 |
| 0007-B1 | 450 | 30 | 0.06 | 5 | 298 | 1998 | 33.6 |
| 0001-A3 | 400 | 120 | 0.026 | 3 | 115 | 1733 | 88.8 |

As a result of the DOE input experimental parameters and output measured quantities the statistical significance of each was determined. As an example, the direct statistical effect of anneal time on the PL peak location can be predicted from this experimental design if sufficient data falls within the predicted variance of the system. The plot in Figure 86 shows the PL peak location actual versus the PL peak location predicted. The statistical dependence of this output on an input is significant as indicated by the fit line having a slope different from zero. Additionally, the P<.0001 indicates that this significance is well below the generally accepted 5% level. This plot and significance level indicates that one of the input variables has a significant effect on this output. Thus, from here the statistical significance of each input can be assessed for the effect on the PL peak location.

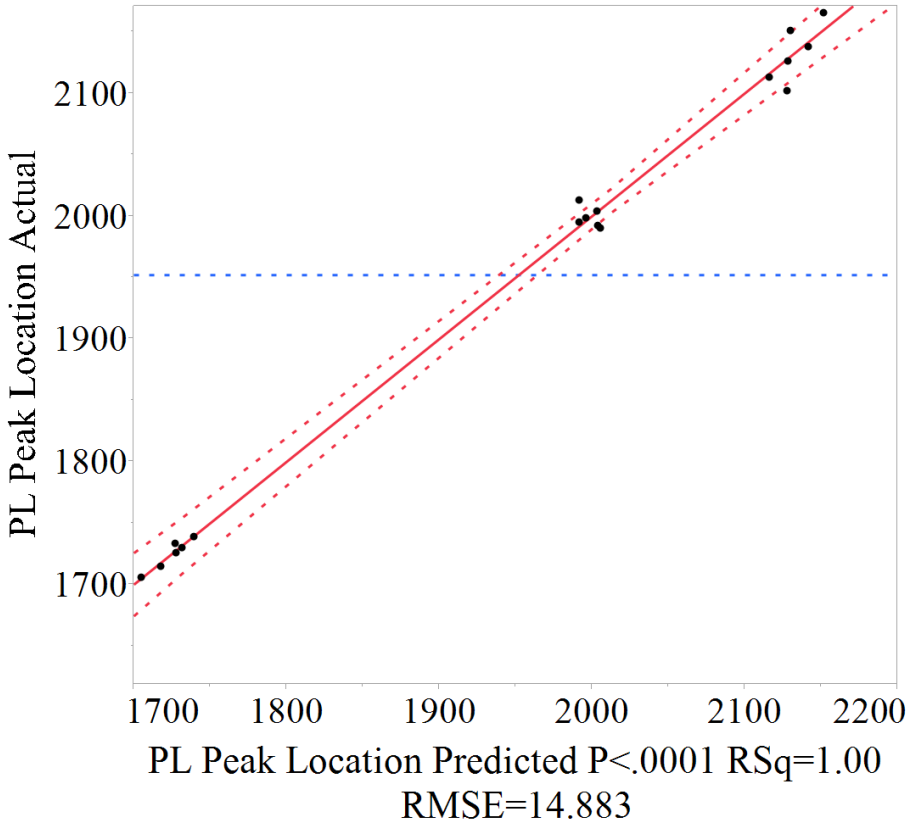


Figure 86: Actual vs predicted plot of the PL Peak location using standard least squares on DOE matrix of variables and measured outputs in Table 16.

## Appendix J: Copyright Permissions

Copyright permissions were obtained for reprint of Table 2, Figure 5, Figure 6, and Figure 7 from The Electrochemical Society. Permissions were received from an authorized agent on November 4, 2014 via email communications.

Copyright permissions were obtained for reprint of Figure 43 and Figure 44 from The Optical Society. Permissions were received from an authorized agent on October 27, 2014 via email communications.